

ACTIVE VIBRATION CONTROL OF BEAMS AND CYLINDRICAL
STRUCTURES USING PIEZOELECTRIC PATCHES

A THESIS SUBMITTED TO
THE GRADUATE SCHOOL OF NATURAL AND APPLIED SCIENCES
OF
MIDDLE EAST TECHNICAL UNIVERSITY

BY

CANER GENÇOĞLU

IN PARTIAL FULFILLMENT OF THE REQUIREMENTS
FOR
THE DEGREE OF MASTER OF SCIENCE
IN
MECHANICAL ENGINEERING

JANUARY 2014

Approval of the thesis:

**ACTIVE VIBRATION CONTROL OF BEAMS AND CYLINDRICAL
STRUCTURES USING PIEZOELECTRIC PATCHES**

submitted by **CANER GENÇOĞLU** in partial fulfillment of the requirements for
the degree of **Master of Science in Mechanical Engineering Department, Middle
East Technical University** by,

Prof. Dr. Canan Özgen
Dean, Graduate School of **Natural and Applied Sciences** _____

Prof. Dr. Süha Oral
Head of Department, **Mechanical Engineering** _____

Prof. Dr. H. Nevzat Özgüven
Supervisor, **Mechanical Engineering Dept., METU** _____

Examining Committee Members

Prof. Dr. Tuna Balkan
Mechanical Engineering Dept., METU _____

Prof. Dr. H. Nevzat Özgüven
Mechanical Engineering Dept., METU _____

Prof. Dr. Yavuz Yaman
Aerospace Engineering Dept., METU _____

Asst. Prof. Dr. Gökhan Özgen
Mechanical Engineering Dept., METU _____

Asst. Prof. Dr. Yiğit Yazıcıoğlu
Mechanical Engineering Dept., METU _____

Date: 24.01.2014

I hereby declare that all information in this document has been obtained and presented in accordance with academic rules and ethical conduct. I also declare that, as required by these rules and conduct, I have fully cited and referenced all material and results that are not original to this work.

Name, Last name: Caner Gençođlu

Signature:

ABSTRACT

ACTIVE VIBRATION CONTROL OF BEAMS AND CYLINDRICAL STRUCTURES USING PIEZOELECTRIC PATCHES

Gençoğlu Caner

M. Sc., Department of Mechanical Engineering

Supervisor: Prof. Dr. H. Nevzat Özgüven

January 2014, 202 pages

Airborne structures are required to be lightweight in today's designs. However this lowers the overall stiffness of the structure and causes low frequency vibration problems for which passive vibration control techniques are inadequate. Active vibration control using piezoelectric patches is a promising technology to solve vibration problems of aerospace structures. Many studies were done on beam and plate geometries, however studies on cylinder geometry which is used extensively as engineering structure, is relatively rare.

In this study, first a cantilever beam is studied to verify the analysis, modeling and control concepts to be used in the cylinder structure since cantilever beam has simpler dynamics. Finite element model of the beam with piezoelectric patch is generated. Control simulations are done on the mathematical model of the cantilever beam derived from the finite element model. Experimental works are carried out on the beam to verify the controller designed in the simulation stage.

The second structure studied is a hollow cylinder with piezoelectric patch actuator and sensor pair. This study is an extension of the beam study with the addition of determining the optimal piezoelectric patch placement. Optimal location of piezoelectric patch actuator is determined based on a method that uses the

controllability Gramian of the system with piezoelectric patch for the target modes to be controlled. After patch placement control simulations are made to design the controller and verify the placement of actuator. Experimental works are also made over the cylinder to verify the designed controller and the patch placement.

Keywords: Active vibration control, vibration control with piezoelectric patch, hollow cylinder structure, piezoelectric patch actuator and sensor, optimum patch placement, modal test

ÖZ

PİEZOELEKTRİK YAMALAR KULLANILARAK KİRİŞLERİN VE SİLİNDİRİK YAPILARIN AKTİF TİTREŞİM KONTROLÜ

Gençoğlu Caner

Yüksek Lisans, Makine Mühendisliği Bölümü

Tez Yöneticisi: Prof. Dr. H. Nevzat Özgüven

Ocak 2014, 202 sayfa

Günümüzün tasarımlarında havacılık yapılarının hafif olması gerekmektedir. Fakat bu durum yapının toplam direngenliğini düşürmekte ve pasif titreşim kontrolü yöntemlerinin yetersiz kaldığı düşük frekanslı titreşim problemlerine yol açmaktadır. Piezoelektrik yamalarla aktif titreşim kontrolü havacılık ve uzay yapılarının titreşim problemlerinin çözümede geleceği olan bir teknolojidir. Kiriş ve plaka geometrisindeki yapılarda çok sayıda çalışma yapılmış olsa da mühendislik yapılarında sıklıkla kullanılan silindir geometrisi üzerindeki çalışmalar görece enderdir.

Bu çalışmada silindir yapıda kullanılacak analiz, modelleme ve kontrol kavramlarını doğrulamak için önce ankastre kiriş üzerinde çalışılmıştır. Bunun nedeni ankastre kirişin silindire göre daha basit bir dinamiğinin oluşudur. Üzerinde piezoelektrik yama bulunan kirişin sonlu elemanlar modeli oluşturulmuştur. Ankastre kirişin sonlu elemanlar yöntemiyle elde edilen modeli üzerinde kontrol simülasyonları yapılmıştır. Simülasyon aşamasında tasarlanan kontrolcüyü doğrulamak için deneysel çalışmalar yapılmıştır.

Çalışılan ikinci yapı, üzerinde piezoelektrik yama eyleyici ve sensör çifti bulunan içi boş silindirdir. Bu çalışma kiriş çalışmasının optimum piezoelektrik yama yerleşimi

konusu eklenmiş bir uzantısıdır. Optimum piezoelektrik yama eyleyici konumu, kontrol edilecek hedef modlar için farklı konumlarda piezoelektrik yamaya sahip sistemlerin kontrol edilebilirlik Gramian'larını kullanan bir yöntemle göre hesaplanmıştır. Yama yerleşiminden sonra, kontrolcü tasarımı için ve eyleyici yerleşimini doğrulamak amacıyla kontrol simülasyonları yapılmıştır. Tasarlanan kontrolcüyü ve yama yerleşimini doğrulamak için silindir üzerinde deneysel çalışmalar yapılmıştır.

Anahtar Kelimeler: Aktif titreşim kontrolü, piezoelektrik yama ile titreşim kontrolü, içi boş silindir yapı, piezoelektrik yama eyleyici ve sensör, en uygun yama yerleşimi, modal test

to my family

ACKNOWLEDGEMENTS

First of all I would like to express my sincere appreciation to my thesis supervisor Prof. Dr. H. Nevzat ÖZGÜVEN for his guidance throughout my thesis study.

I appreciate Asst. Prof. Dr. Gökhan ÖZGEN for his efforts in the preparation of test setups and his help with the test processes.

I wish to express my gratitude to Asst. Prof. Dr. Yiğit YAZICIOĞLU for his guidance and help in control concepts.

I would like to thank my manager Bayındır KURAN in ROKETSAN Inc. for giving me the opportunity to work with piezoelectric materials.

I am in debt of gratitude to my unit leader Bülent ACAR in ROKETSAN Inc. for his friendly support with the finite element analysis method and his patience.

I also owe thanks to my colleagues in my unit in ROKETSAN Inc. who helped me in every subject throughout the years of my study.

I am thankful to Doğan TAŞÇI in ROKETSAN Inc. for supplying and preparing computers used in the test setup.

I am grateful to my friend Levent BEKER for his encouragement of me from time to time during my thesis study.

Finally I wish to express my sincere thanks to my father Adil GENÇOĞLU, my mother Fatma GENÇOĞLU and my brother Cihangir GENÇOĞLU and his wife Cansu GENÇOĞLU for their endless support.

TABLE OF CONTENTS

ABSTRACT	v
ÖZ	vii
ACKNOWLEDGEMENTS	x
TABLE OF CONTENTS	xi
LIST OF FIGURES	xiii
LIST OF TABLES	xx
CHAPTERS	
1 INTRODUCTION	1
1.1 Literature Survey	1
1.2 Objective and Scope of Thesis	10
2 ACTIVE VIBRATION CONTROL USING PIEZOELECTRIC MATERIALS ..	
.....	13
2.1 Piezoelectric Materials and Piezoelectric Actuators	13
2.1.1 Definition of Piezoelectricity	13
2.1.2 Piezoelectric Materials	13
2.1.3 History of Piezoelectric Materials.....	13
2.1.4 Poling Process	14
2.1.5 Piezoelectric Actuators.....	16
2.2 Piezoelectric Properties and Modeling of Piezoelectric Actuators by ANSYS.....	25
2.3 Modeling Plant in State Space.....	29
2.4 Concepts of Controllability and Observability.....	31
2.4.1 Concept of Controllability.....	31
2.4.2 Concept of Observability	32
2.5 Placement of Piezoelectric Patches by Controllability.....	32
2.6 Placement of Sensors by Observability.....	34
2.7 State Feedback, Observer Design and Pole Placement	34

3	ACTIVE VIBRATION CONTROL OF BEAM	39
3.1	Introduction	39
3.2	Finite Element Modeling and Analysis of the Beam.....	42
3.2.1	Beam Model	42
3.2.2	Static Analysis for Applied Voltage Load	47
3.2.3	Modal Analysis	54
3.2.4	Mathematical Model Using State Space Matrices	56
3.3	Test and Data Acquisition Over the Beam	63
3.3.1	Test Setup.....	63
3.3.2	Static Deflection for Applied Voltage Load	69
3.3.3	Measurement of Voltage FRFs	80
3.4	Updating FEM and State Space Model Using Test Data	94
3.5	Controller Design and Simulations for the Updated Model.....	102
3.6	Implementation of Controller to Beam Structure	114
4	ACTIVE VIBRATION CONTROL OF CYLINDER.....	117
4.1	Introduction	117
4.2	Finite Element Modeling of Cylinder with Piezoelectric Patches.....	119
4.3	Finite Element Analysis of the Cylinder Structure.....	121
4.3.1	Modal Analysis	121
4.3.2	Static Analysis.....	125
4.4	Placement of Piezoelectric Patches by Controllability Concepts.....	126
4.5	Mathematical Model Using State Space Matrices.....	130
4.6	Controller Design and Simulations.....	133
4.7	Verification by Tests	140
5	SUMMARY AND CONCLUSIONS	159
	REFERENCES.....	163
	APPENDIX A QUARTER BRIDGE STRAIN GAGE MEASUREMENT WITH SINGLE STRAIN GAGE	171
	APPENDIX B MATERIAL PROPERTIES	173
	APPENDIX C ANSYS APDL CODES.....	175
	APPENDIX D IMAC 2013 PAPER	187

LIST OF FIGURES

FIGURES

Figure 1-1. LANTIRN pods and ventral fins of F-16 aircraft [9].....	2
Figure 1-2. Ventral fin failure [9]	3
Figure 1-3. Test fin with piezoelectric patches [9]	4
Figure 1-4. On board active vibration control system [9].....	4
Figure 1-5. First flight test helicopter with active flaps [11]	5
Figure 1-6. Amplified piezoelectric stack actuator controlling the flaps at the helicopter rotor blade trailing edge [6,12].....	5
Figure 1-7. Open rotor aircraft engine composite blades with piezoelectric elements [7].....	6
Figure 1-8. Payload of a launch vehicle [5]	9
Figure 1-9. MFC piezoelectric actuators on an aluminum shell [15]	10
Figure 2-1. Unit cell of PZT crystal [16]	15
Figure 2-2. Difference between single crystal and poly crystal piezoelectric materials [16].....	15
Figure 2-3. Poling process of piezoelectric ceramics [16].....	16
Figure 2-4. Operation modes of piezoelectric material after poling [22]	17
Figure 2-5. Typical force and displacement values for piezoelectric actuators.....	18
Figure 2-6. Piezoelectric patch actuator [25]	19
Figure 2-7. Photo of piezoelectric patch actuators [26]	19
Figure 2-8. Bimorph bender actuators [27].....	20
Figure 2-9. Piezo stack actuator [28]	21
Figure 2-10. Photo of piezo stack actuators [29]	21
Figure 2-11. Mechanically amplified stack actuator [30]	22
Figure 2-12. Internal structure of MFC [31]	23
Figure 2-13. Photo of MFC [31]	23
Figure 2-14. An illustration of piezo tube actuators [32].....	24
Figure 2-15. Working process of piezo inchworm motor [33]	25

Figure 2-16. Axis system of a piezoelectric material, polarized in axis 3 [37].....	27
Figure 2-17. SOLID 226 element in ANSYS [38].....	28
Figure 2-18. Poles of a vibratory system in s-domain [49].....	36
Figure 2-19. Block diagram of system with observer [50]	37
Figure 3-1. Cantilevered beam as the test structure	39
Figure 3-2. Piezoelectric patches at the root of the beam	40
Figure 3-3. Strain gages at the opposite side of piezoelectric patches.....	40
Figure 3-4. Controller design approach for beam structure	41
Figure 3-5. Dimensions of the beam with piezoelectric patches.....	42
Figure 3-6. Locations of strain gages at the back side of the beam	42
Figure 3-7. Thickness of the beam, glue layer and piezoelectric patches	43
Figure 3-8. Cantilevered boundary condition modeled in ANSYS	43
Figure 3-9. Beam with sensors and root block, ready to be held by the clamp	44
Figure 3-10. Test beam held by clamp mechanism.....	45
Figure 3-11. Deformation of beam in Z direction in mm for 70V applied at piezo #1	47
Figure 3-12. Strain of beam in X direction in mm for 70V applied at piezo #1	48
Figure 3-13. Deformation of beam in Z direction in mm for 70V applied at piezo #2	48
Figure 3-14. Strain of beam in X direction in mm for 70V applied at piezo #2	49
Figure 3-15. Deformation of beam in Z direction in mm for -70V applied at piezo #1	49
Figure 3-16. Strain of beam in X direction in mm for -70V applied at piezo #1	50
Figure 3-17. Deformation of beam in Z direction in mm for -70V applied at piezo #2	50
Figure 3-18. Strain of beam in X direction in mm for -70V applied at piezo #2.....	51
Figure 3-19. Deformation of beam in Z direction in mm for 70V applied at piezo #1 and -70V applied at piezo #2	51
Figure 3-20. Strain of beam in X direction in mm for 70V applied at piezo #1 and -70V applied at piezo #2	52
Figure 3-21. Deformation of beam in Z direction in mm for -70V applied at piezo #1 and 70V applied at piezo #2.....	53

Figure 3-22. Strain of beam in X direction in mm for -70V applied at piezo #1 and 70V applied at piezo #2.....	53
Figure 3-23. 1 st bending mode shape, natural frequency 9.865 Hz.....	55
Figure 3-24. 2 nd bending mode shape, natural frequency 56.65 Hz.....	55
Figure 3-25. 3 rd bending mode shape, natural frequency 150.96 Hz.....	55
Figure 3-26. 1 st lateral bending mode shape, natural frequency 206.14 Hz.....	56
Figure 3-27. 1 st torsion mode shape, natural frequency 236.29 Hz.....	56
Figure 3-28. Comparison of full harmonic analysis and frequency response of state space model.....	58
Figure 3-29. Relationship between viscous damping and Rayleigh damping [54]....	60
Figure 3-30. ANSYS transient analysis results vs Simulink result.....	61
Figure 3-31. Comparison of full and reduced model for first 5 seconds.....	62
Figure 3-32. Comparison of full and reduced model for the first second of simulation.....	62
Figure 3-33. Test setup scheme.....	64
Figure 3-34. A photo of the test equipments in METU.....	64
Figure 3-35. Test beam and laser displacement sensor heads.....	65
Figure 3-36. Keyence laser displacement sensor and controller unit.....	65
Figure 3-37. Micro Measurement Model A2 Strain gage conditioning unit.....	66
Figure 3-38. APC SVR 350-bip piezoelectric voltage amplifier.....	67
Figure 3-39. Simulink blocks for NI PCI card.....	68
Figure 3-40. Simulink model on the Host PC used in static tests part 1.....	71
Figure 3-41. Simulink model on the Host PC used in static tests part 2.....	71
Figure 3-42. Data acquired at test 1.1, Tip displacement and voltage load.....	72
Figure 3-43. Data acquired at test 1.2, Tip displacement and voltage load.....	72
Figure 3-44. Data acquired at test 1.3, Tip displacement and voltage load.....	73
Figure 3-45. Data acquired at test 1.4, Tip displacement and voltage load.....	73
Figure 3-46. Data acquired at test 1.5, Tip displacement and voltage load.....	74
Figure 3-47. Data acquired at test 1.6, Tip displacement and voltage load.....	74
Figure 3-48. Data acquired at test 1.7, Tip displacement and voltage load.....	75
Figure 3-49. Data acquired at test 1.8, Tip displacement and voltage load.....	75
Figure 3-50. Data acquired at test 2.1, strain gage data #1 and #2 load.....	76

Figure 3-51. Data acquired at test 2.2, strain gage data #1 and #2 load.....	77
Figure 3-52. Data acquired at test 2.3, strain gage data #1 and #2 load.....	77
Figure 3-53. Data acquired at test 2.4, strain gage data #1 and #2 load.....	78
Figure 3-54. Data acquired at test 2.5, strain gage data #1 and #2 load.....	78
Figure 3-55. Data acquired at test 2.6, strain gage data #1 and #2 load.....	79
Figure 3-56. Data acquired at test 2.7, strain gage data #1 and #2 load.....	79
Figure 3-57. Data acquired at test 2.8, strain gage data #1 and #2 load.....	80
Figure 3-58. Simulink model on the Host PC used in dynamic tests part 1.....	82
Figure 3-59. Simulink model on the Host PC used in dynamic tests part 2.....	82
Figure 3-60. Tip displacement data acquired for H_{p1d} test.....	85
Figure 3-61. Voltage applied to piezo patch#1 in the test for H_{p1d}	86
Figure 3-62. Chirp input voltage signal for first 20 seconds of H_{p1d} test.....	86
Figure 3-63. Voltage FRF between tip displacement and applied voltage to patch#1 (H_{p1d}).....	87
Figure 3-64. Voltage FRF between tip displacement and applied voltage to patch #1 (H_{p1d}) using 10 averages.....	88
Figure 3-65. Voltage FRF between tip displacement and applied voltage to patch #2	89
Figure 3-66. Voltage FRF between tip displacement and applied voltage to patch #2 using 10 averages	90
Figure 3-67. Voltage FRF between strain gage#1 and applied voltage to patch#1 ...	91
Figure 3-68. Voltage FRF between strain gage#2 and applied voltage to patch#1 ...	92
Figure 3-69. Voltage FRF between strain gage#1 and applied voltage to patch#2 ...	92
Figure 3-70. Voltage FRF between strain gage#2 and applied voltage to patch#2 ...	93
Figure 3-71. Simulink model used in data acquisition to test the model in time domain.....	95
Figure 3-72. Simulink model used to test the simulation model to compare with the test data.....	96
Figure 3-73. Voltage input used in simulation model and real life test model	96
Figure 3-74. Comparison of results for the initial model and test result.....	97
Figure 3-75. Comparison of results for the initial model and test result, detailed view	98

Figure 3-76. Comparison of test data with simulation of updated model.....	99
Figure 3-77. Comparison of test data with simulation of updated model, detailed view.....	100
Figure 3-78. Comparison of test data with simulation of updated model with added noise.....	100
Figure 3-79. Data measured from strain gage #1 in the test.....	101
Figure 3-80. Plant model.....	103
Figure 3-81. Simulink model of the PID controller simulation.....	103
Figure 3-82. Block diagram of moving average.....	104
Figure 3-83. Beam simulation result without control.....	105
Figure 3-84. Beam simulation with control.....	106
Figure 3-85. Beam simulation with control and with added noise.....	106
Figure 3-86. Simulink model for full state feedback control simulation.....	108
Figure 3-87. Observer model for full state feedback controller.....	108
Figure 3-88. Uncontrolled plant poles and controlled system poles on s-domain...	110
Figure 3-89. Observer poles, uncontrolled plant poles and controlled system poles on s-domain.....	110
Figure 3-90. Frequency responses of uncontrolled and controlled models.....	111
Figure 3-91. Simulation result without added noise.....	112
Figure 3-92. Simulation result without added noise, detailed view.....	112
Figure 3-93. Simulation result with added noise.....	113
Figure 3-94. Simulation result with added noise, detailed view.....	113
Figure 3-95. Simulink model used in PID control implementation.....	114
Figure 3-96. Result of PID implementation, test data.....	114
Figure 3-97. Control with piezo1 for disturbance from piezo2 with different controller gains.....	115
Figure 4-1. Dimensions of the cylinder.....	117
Figure 4-2. Photo and 3-D model of the cylinder.....	118
Figure 4-3. PI Dura Act type piezoelectric patch [55].....	119
Figure 4-4. Finite element mesh over the 3-D cylinder model.....	120
Figure 4-5. 1 st and 2 nd mode shapes.....	123
Figure 4-6. 3 rd and 4 th mode shapes.....	123

Figure 4-7. 5 th and 6 th mode shapes.....	124
Figure 4-8. 7 th and 8 th mode shapes.....	124
Figure 4-9. 9 th and 10 th mode shapes.....	125
Figure 4-10. Result of static analysis over the cylinder	126
Figure 4-11. Cylinder structure with divided volumes and a patch actuator	127
Figure 4-12. Example of the difference between mode shapes and deflection shapes in cylinder, a) 1st mode shape, b) 1st deflection shape for F_x	129
Figure 4-13. Piezoelectric patch actuator placement criteria according to coordinates	130
Figure 4-14. Relative tangential motion of the nodes corresponding to piezo sensor	131
Figure 4-15. Pole-Zero plot of the plant.....	132
Figure 4-16. Frequency response of the system.....	132
Figure 4-17. Pole zero plot of the plant, observer and the controlled system	134
Figure 4-18. Frequency response on uncontrolled and controlled systems	134
Figure 4-19. Simulink block diagram of the system with PPF control	136
Figure 4-20. Simulation of PPF control	136
Figure 4-21. Simulation for piezoelectric actuators at different locations.....	137
Figure 4-22. FFT of the response for different actuator locations	138
Figure 4-23. FFT of the response for different actuator locations, 1 st and 2 nd mode zoomed	139
Figure 4-24. FFT of the response for different actuator locations, 5 th and 6 th mode zoomed	139
Figure 4-25. Test setup and the cylinder in Roketsan	140
Figure 4-26. Piezoelectric patch on the outer surface of the cylinder.....	141
Figure 4-27. Piezoelectric patch on the inner surface of the cylinder.....	142
Figure 4-28. Accelerometer placed at the corner of the piezoelectric actuator.....	143
Figure 4-29. PCB model 480E09 signal conditioning unit	143
Figure 4-30. Voltage applied to piezoelectric patch actuator from the amplifier as drive voltage.....	144
Figure 4-31. Voltage read from piezoelectric patch sensor	145
Figure 4-32. Voltage read from accelerometer	145

Figure 4-33. TF between piezoelectric patch sensor and actuator 147

Figure 4-34. TF between accelerometer and piezoelectric patch actuator 147

Figure 4-35. Time data acquired by LMS 148

Figure 4-36. TF between piezoelectric patch sensor and actuator using 200 averages, LMS result 148

Figure 4-37. B&K 8200 impact hammer 149

Figure 4-38. Accelerometers placed on the cylinder for modal test 149

Figure 4-39. 1st mode shape, test result 150

Figure 4-40. 2nd mode shape, test result 150

Figure 4-41. 5th mode shape, test result 151

Figure 4-42. 6th mode shape, test result 151

Figure 4-43. Auto MAC values of modes obtained from LMS 152

Figure 4-44. Simulink block diagram of the cylinder test model 154

Figure 4-45. 1st mode shape from analysis, 2nd mode shape from test 155

Figure 4-46. 2nd mode shape from analysis, 1st mode shape from test 155

Figure 4-47. 5th mode shape from analysis, 6th mode shape from test 156

Figure 4-48. 6th mode shape from analysis, 5th mode shape from test 156

Figure 4-49. Controller started in the middle of cylinder motion 157

Figure 4-50. Cylinder sensor measurements for control off and control on 157

Figure 4-51. Cylinder sensor measurements for different actuator locations 158

LIST OF TABLES

TABLES

Table 3-1. Material properties of steel	45
Table 3-2. Material properties of APC 850	45
Table 3-3. Material properties of epoxy layer	46
Table 3-4. Summary of static analysis results	54
Table 3-5. Results of modal analysis	54
Table 3-6. Summary of input and output channels for part 1 of the tests	69
Table 3-7. Summary of input and output channels for part 2 of the tests	70
Table 3-8. List of measured FRFs	81
Table 3-9. Comparison of resonant frequencies found by test	89
Table 4-1. Material properties of steel	120
Table 4-2. Material properties of PIC 255	121
Table 4-3. Analysis results of the cylinder model	122
Table 4-4. Comparison of natural frequencies from test and analysis	153

CHAPTER 1

INTRODUCTION

1.1 Literature Survey

Reduction of the weight has the key importance with the increasing speed and performance requirements in today's design of aerospace structures. As a result of the efforts to reduce the weight of the airborne structures, the structural members are weakened and this reduced the overall stiffness of the structure. Reduced stiffness of the structure caused low frequency oscillation problems to arise. Together with that increasing speed and maneuverability of modern airborne structures cause many types of aerodynamic problems to solve. Due to interactions of the inertia and stiffness of the airborne structure with the aerodynamic loads, dynamic instability problems of the airborne structure may arise. The interactions between inertial, elastic and aerodynamic forces on the airborne structure are studied under aeroelasticity [1].

Dynamic instability problems cause unwanted vibrations on an airborne structure. Control of vibrations for the aerospace systems such as aircraft wings, helicopter rotor blades and propellers of turboprop engines have the key importance for satisfactory operation of the aircraft [2]. Many types of aerospace structure namely fighter aircrafts, missiles, satellite launch vehicles, helicopters and turboprop engine propellers suffer from vibration problems [3-7]. There are many ways to tackle with the structural vibration problems, but these methods can be gathered under two topics: passive vibration control methods and active vibration control methods. Engineers and scientists may apply different passive or active vibration control technique, or they may utilize an hybrid method as a semi-active vibration control technique.

Buffet and flutter are two big problems of today's high performance fighter aircrafts. Buffet is caused by unsteady separating flows striking on the structural surfaces and exciting vibration modes of the airborne structure [3,8]. Flutter, on the other hand is usually caused by coupling of two or more structural vibration modes of the system, i.e. wing bending and torsion. In this type of dynamic instability, the vibratory energy is gathered from the flow stream [8]. For high performance twin tail fighter aircraft such as F-14, F-15, F/A-18 and F22, tail buffeting can be a serious problem reducing the service life and limiting the maneuvers in the flight envelope of the aircraft. This was the case for F-15 and F/A-18 when tail buffeting caused fatigue cracks shortly after the aircrafts were in service. These cracks led serious inspection and maintenance costs, and many researchers studied the effects of tail buffets on high performance twin tail aircrafts [3,9]. Not only twin tail aircrafts but also ventral fins of F-16 aircraft suffered from buffet. After F-16 aircrafts were equipped with LANTIRN pods, the wake induced by those pods caused more buffeting problems for ventral fins and increased the number of ventral fin failures. A photo of F-16 aircraft with LANTIRN pods is given in Figure 1-1 and a ventral fin failure is given in Figure 1-2 [9].



Figure 1-1. LANTIRN pods and ventral fins of F-16 aircraft [9]



Figure 1-2. Ventral fin failure [9]

For the F-16 example, altering the flow direction can be attempted but this could only solve the problem for limited flight cases [9]. For F/18-A example methods to change the flow direction reduced the peak vibration levels at tail wing tips, however this caused a 3% loss in lift and was not very effective at higher angles of attack [10]. On the other hand structural strengthening will increase the weight of the aircraft. Considering the great potential of piezoelectric materials, active vibration control technique can solve tail buffet problem without increasing the weight [9].

In the study of Browning [9], an active vibration control system is designed to reduce the vibrations of the ventral fins of F-16 aircraft. Piezoelectric patch actuators are mounted on a test fin of the aircraft are given in Figure 1-3. On board active control system composed of a controller and a piezoelectric amplifier is built and placed on the aircraft is given in Figure 1-4. The system reduced the vibrations according to the flight test data.



Figure 1-3. Test fin with piezoelectric patches [9]

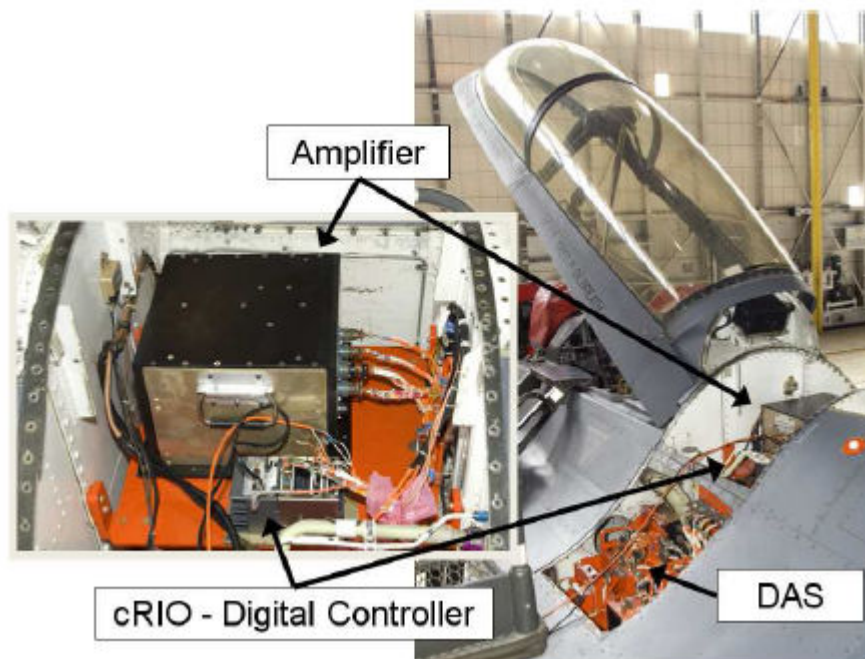


Figure 1-4. On board active vibration control system [9]

Another air vehicle suffering from mechanical vibrations is the helicopter. Low passenger comfort due to cabin noise and vibration are still the problem of today's helicopters [11]. Main rotor induced vibration has the key importance in helicopter vibrations. Therefore effort is focused on developing systems to tackle with main rotor vibrations [6,11,12]. There are many concepts, active and passive vibration control and isolation methods to solve this problem. One of the concept is active trailing edge, in which the flaps at the ends of the helicopter rotor blades are

controlled by mechanically amplified piezoelectric actuators controlled by an electronic system placed on top of the helicopter hub [11]. A picture of first flight test helicopter with active trailing edge is given in Figure 1-5 and the illustration and photo of the piezoelectric actuator controlling the trailing edge flap is given in Figure 1-6. Note that the hub electronics on the helicopter in Figure 1-5 is planned to be made smaller for better aerodynamics [6,11,12].



Figure 1-5. First flight test helicopter with active flaps [11]

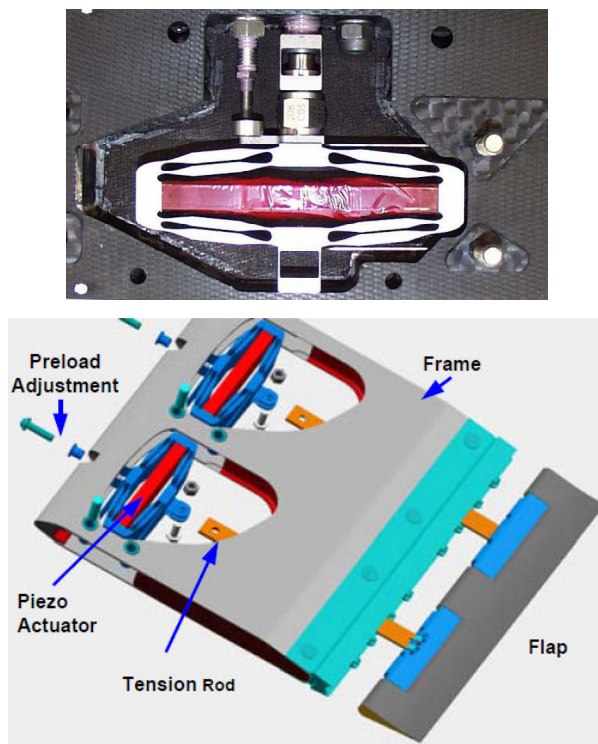


Figure 1-6. Amplified piezoelectric stack actuator controlling the flaps at the helicopter rotor blade trailing edge [6,12]

Other type of aerospace structures upon which piezoelectric actuators are used to reduce the vibrations are the blades of aircraft engines. In the thesis study of Bachmann [7], piezoelectric elements are used as shunt dampers to reduce the vibrations of open rotor aircraft engine blades. This is a passive way of reducing vibrations. In this method blade vibrations are damped by converting vibration energy to electrical energy via piezoelectric elements. Piezoelectric elements are placed at the highest strain energy locations to maximize the converted energy. Composite rotor blades with piezoelectric elements in this study are given in Figure 1-7 [7].



Figure 1-7. Open rotor aircraft engine composite blades with piezoelectric elements [7]

Missiles and rockets are also airborne structures which are subject to vibration and shock loads. As all the airborne structures with wings and/or fins, missiles are also susceptible to aeroelastic instabilities such as flutter and buffet. Yet, missile body vibration modes can also get excited from the loads of flow stream. Missiles contain high valued electronic guidance and/or navigation systems that are extremely important for missiles that follow a specified path and hit the specific target. Those electronic systems could be damaged if the vibration and shock loads are transmitted to them by the missile airframe [4].

There are many types of loads on a missile to cause unwanted vibrations. The divert thrust from propulsion system can cause the lateral bending modes of the missile to excite, which causes missile seeker to move off its line of sight and this reduces the performance of the seeker. All the missiles need to know its own position accurately to hit the target. For this purpose missiles have Inertial Measurement Unit (IMU) to determine its position and orientation. IMU is a very delicate instrument which should be attached missile airframe very rigidly and precisely so that IMU does not make a wrong measurement due to the flexibility of the airframe. Making the airframe rigid is advantageous for IMU measurements since IMU can measure the missile position and orientation correctly without suffering from airframe flexibility issues. However making a rigid missile airframe requires a heavy airframe. Most importantly a rigid airframe causes all the vibration and shock loads on the missile due to motor ignition, aerodynamic buffet, stage separation and acoustic loads to be transmitted to the high valued electronics at guidance section. Then IMU can fail due to these vibration and shock loads. IMU should be isolated from the missile airframe by some rubber dampers. At this stage a compromise should be made between isolating the IMU from destructive shock and vibration loads from the missile, and keeping the rigidity between IMU and the missile for the functionality of the IMU [4].

As a result of missile flexible body vibrations, IMU may be effected and may measure these vibratory motions and interpret them as rigid body motion. Since the IMU is connected to the control surfaces of the missile by the control system, it may try to command the wings to move the missile in the opposite direction. As a result of this missile wings will begin to oscillate, which finally and catastrophically move the missile out of its trajectory. This is the destabilizing effect of missile body flexible modes on the IMU and missile control system. To solve this problem, some filters are designed at the natural frequencies of the missile airframe and implemented at missile's electronic control system. This will cancel the destabilizing effect to the flexible modes of the missile, however those filters will reduce the performance of the electronic devices on missile at these frequency bands. Tuning the missile airframe and the airframe-IMU connection to solve this dynamic problem

is a long and iterative approaches and requires many detailed finite element analysis [4,13]. At this stage, design of an active vibration isolation system between the IMU and missile airframe is promising.

Launch vehicles, which are used in delivering payloads to orbits are the environments that high levels of shock and vibrations are encountered. Isolating the payload from the vibration loads coming from the launch vehicle is the key design parameter. Payloads can be damaged by the excessive vibrations and shocks resulting from motor ignition, engine shutdown, stage separations, fairing separations and so on. Therefore the payload should be isolated from the launch vehicle. Payload attachment fitting is the part on which payload is sitting and it connects the payload to the launch vehicle. There are some passive isolation dampers on the payload attachment fitting to protect the payload. However, those passive dampers lack two important design request. The damper in fitting is required to provide low stiffness in the vertical axis to absorb the effects of thrust load and high rigidity in lateral axis to prevent rocking and tilting of the payload. Since the distance between the payload and the fairing walls are limited, lateral motion of payload may result in hitting the walls. Active systems have the ability to provide different stiffness for different axis. The second drawback of passive systems is that their characteristics may change with static load. Since the load that payload applies on the isolator changes during launch due to the change of gravitational acceleration, the characteristics of passive isolator alters. Active isolation systems does not have this problem [5]. Payload of a launch vehicle is given in Figure 1-8.

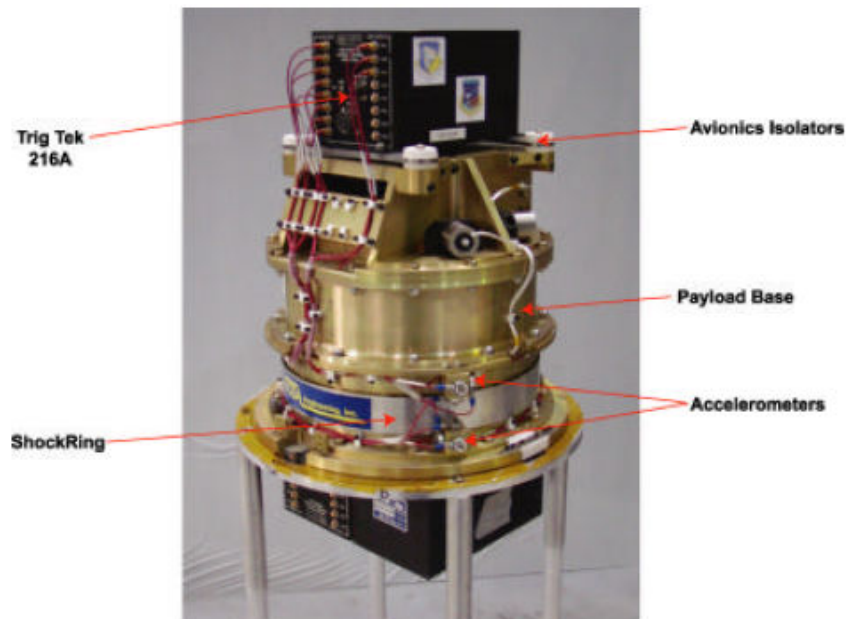


Figure 1-8. Payload of a launch vehicle [5]

All of these aerospace applications of active vibration control require design, installation and implementation of a complete system consisting of sensors, actuators, control computers and amplifiers. These systems can be installed and operated successfully on aerospace vehicles by a team of engineers. Other than the applications on aerospace vehicles, some laboratory research is also done on active vibration control by many researchers. Those kind of researches aim to increase knowledge in the subject. In order to obtain basic knowledge about active vibration control, some simple structures such as beams, plates and shells are studied rather than complex real life engineering structures.

Cylindrical shell structures are used in several engineering structures. Aircraft fuselage, submarines, pressure vessels and pipes can be modeled as hull structures. For the beam and plate geometries a huge amount of research work has been done in active vibration control with piezoelectric sensors and actuators, but studies about active vibration control of cylindrical hull structures with piezoelectric sensors and actuators are relatively rare [14]. A photo of two piezoelectric MFC actuators placed on an aluminum cylinder can be seen in Figure 1-9 [15].

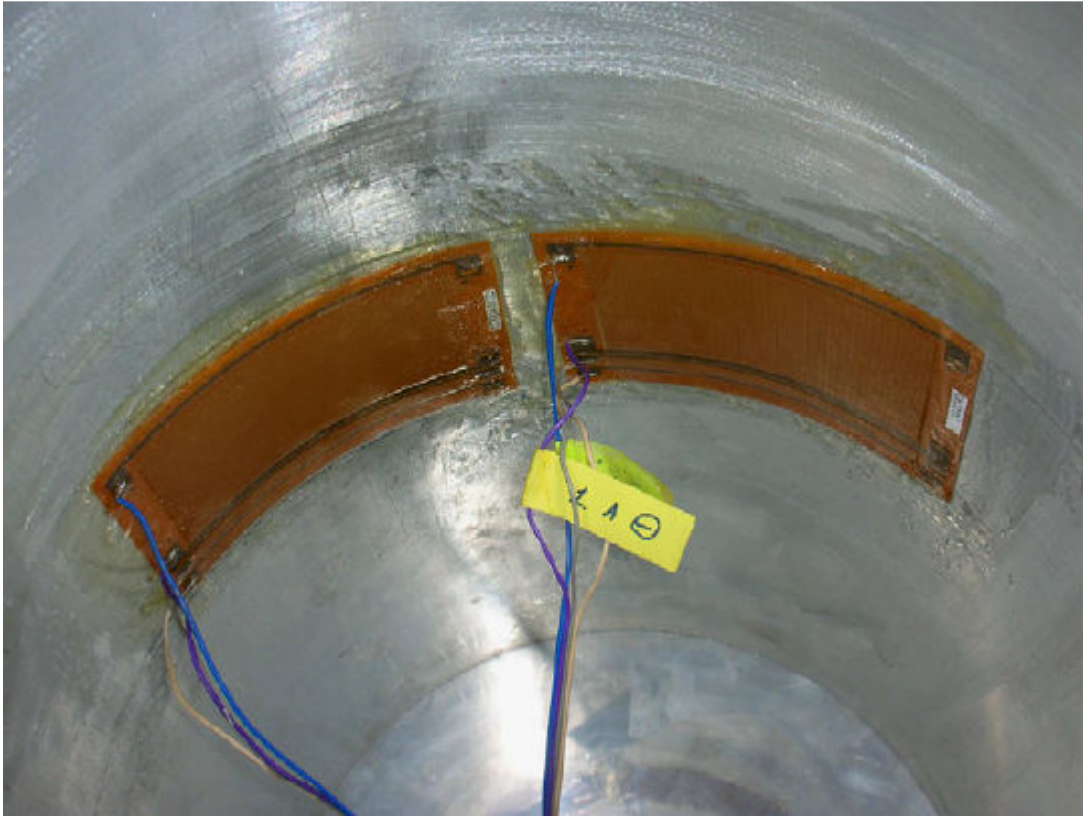


Figure 1-9. MFC piezoelectric actuators on an aluminum shell [15]

1.2 Objective and Scope of Thesis

The purpose of this study is to gain theoretical and practical knowledge about piezoelectric actuators and their usage as actuators in active vibration control systems the ultimate goal being active vibration control in cylindrical structures. The following studies are made in the scope of this thesis:

- A literature survey about active vibration control systems that include piezoelectric elements as actuators and/or sensors is done in Chapter 1.1. In this survey examples of active vibration control by piezoelectric actuators in aerospace platforms such as fighter aircrafts, helicopters, engine propellers, rockets and missiles and launch vehicles are presented. Also example of studies on cylindrical hull structures as a laboratory application is given.

- The background information about piezoelectric materials and state space concepts are given in Chapter 2. Definition of piezoelectric materials and their working principle is explained. Different ways of utilization of piezoelectric materials as actuators is presented. Information about modeling piezoelectric materials is given. Theoretical information about modeling in state space, controllability and observability and controller design in state space are also given in this chapter.
- A beam model is studied in Chapter 3. In this chapter, a beam with piezoelectric elements is modeled in finite element software ANSYS, The system model of the beam generated in ANSYS is transferred to MATLAB and Simulink environment for controller design. Finally the controller is tested and verified on a real life model.
- In Chapter 4, a hollow cylindrical part is studied using a similar approach as in Chapter 3. The cylindrical part is modeled in ANSYS. The location of piezoelectric patch is calculated by considering the vibration modes of the cylinder to control. After selecting the optimal locations, the system model of cylindrical structure with piezoelectric actuators is generated and a controller is designed for this model. Design of the controller is also verified by tests.
- The concluding remarks are presented in Chapter 5 as a conclusion.

CHAPTER 2

ACTIVE VIBRATION CONTROL USING PIEZOELECTRIC MATERIALS

2.1 Piezoelectric Materials and Piezoelectric Actuators

2.1.1 Definition of Piezoelectricity

Piezoelectric effect is defined as the production of electric charge as a response to the applied strain on the material. Generation of strain or dimension change on the material as a response to the applied electric field is called inverse piezoelectric effect [16]. Materials which are said to have the piezoelectric property exhibit both piezoelectric and inverse piezoelectric behavior. Piezoelectricity is a linear reversible phenomenon which allows exchange of electrical and mechanical energy [17,18].

2.1.2 Piezoelectric Materials

Some crystals such as quartz, tourmaline Rochelle salt found in the nature exhibit piezoelectric property. Other than naturally piezoelectric crystals there are manmade ceramic materials such as lead-zirconate-titanate (PZT), lead-titanate (PbTiO_2), lead-zirconate (PbZrO_3), and barium-titanate (BaTiO_3) and polymer material such as Polyvinylidene Difluoride (PVDF) which can be equipped with piezoelectric property. Manmade piezoelectric materials do not exhibit piezoelectric property until they undergo a special process called poling [19].

2.1.3 History of Piezoelectric Materials

Piezoelectric effect was first demonstrated by Pierre and Jacques Curie in 1880 in an experimental study. They were able to produce electric charges as a response to the applied pressure on naturally piezoelectric crystal such as quartz, tourmaline,

Rochelle salt etc. The inverse piezoelectric effect is suggested by Lippmann in 1881 as a result of principles of thermodynamics and confirmed by Curie Brothers. The studies on piezoelectricity continued and in 1910 "Lerbuch der Kristallphysic" published, becoming the first standard reference for piezoelectric crystals [18]. The first application of piezoelectric materials was during World War 1 years. In 1917 Langevin and his colleagues developed first ultrasonic transducer by gluing thin quartz crystal between two steel plates. This device is used as submarine detector and it was the first application of sonar [17,18]. This invention opened the path of using piezoelectric materials as sensors in underwater applications as hydrophones, and in other important applications such as accelerometers, microphones and so on. During the next two decades, studies on the applications of piezoelectric materials with natural crystals continued. However since the piezoelectric properties of natural crystals were limited, commercialization of the technology was also limited [18]. During World War 2 studies on the smart material technology was led by isolated research groups in the United States, Soviet Union and Japan. Studies were focused on improving the piezoelectric properties of the material and building man made materials with piezoelectric property. As a result of these studies, sintered ceramic materials with high dielectric constants and improved piezoelectric properties were developed. Barium Titanate (BaTiO_3) family and Lead-Zirconate-Titanate $\text{Pb}(\text{Zr,Ti})\text{O}_3$ alloy were two important materials developed in this era [18]. Development of Lead Zirconate Titanate (PZT), which is the most commonly used piezoelectric material, was a milestone in the history of smart materials. Around 1965, studies started in Japan which led to the commercialization of piezoelectric material [17].

2.1.4 Poling Process

For any material to have piezoelectric property, it should have unbalanced dipoles in its crystal structure. Piezoelectricity is a result of asymmetric distribution of charge in the unit cell of the material. Below a certain temperature called Curie temperature, piezoelectric crystals have unbalanced dipoles. A unit cell of a PZT ceramic with unbalanced charge is given in Figure 2-1 [16].

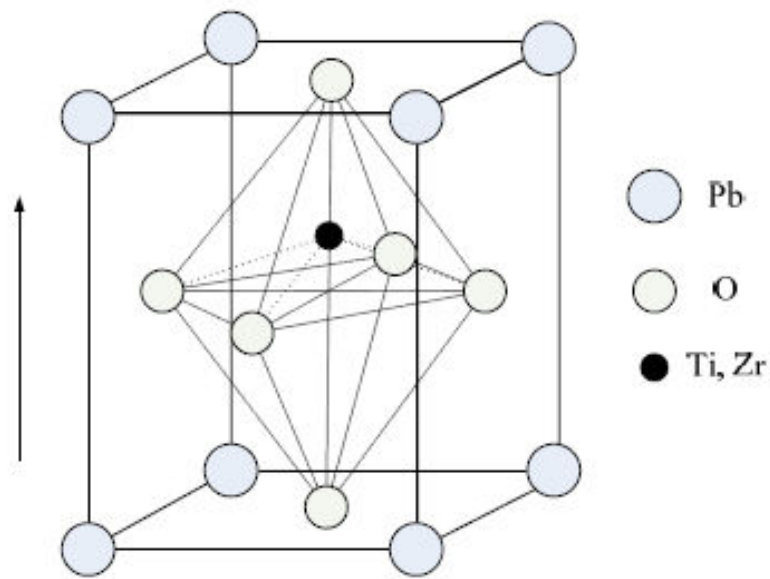


Figure 2-1. Unit cell of PZT crystal [16]

Naturally piezoelectric materials are in single crystal structure and they have single orientation of charge all over the structure. That is why they exhibit piezoelectric property without the need of any further processes. However, manmade piezoelectric materials are in polycrystal structure after sintering process. Since these polycrystal materials are made up of many grains with random orientation of charge, this results in the net cancellation of the macroscopic piezoelectric property of these materials. A figure showing the difference between single crystal and poly crystal piezoelectric material is shown in Figure 2-2 [16].

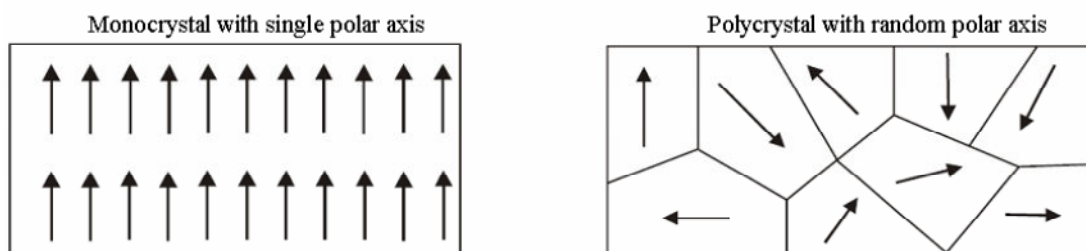


Figure 2-2. Difference between single crystal and poly crystal piezoelectric materials [16]

Above Curie temperature the orientation of unbalanced dipoles in the piezoelectric crystal vanishes and the unit cell becomes symmetric. In order to produce man made piezoelectric material, the piezoelectric material should undergo poling process. In poling process, piezoelectric materials are heated above their Curie temperature and a strong electric field is applied in a direction called polarization direction. By the effect of the strong electric field, the random orientation of dipoles are aligned. Note that it is not a full alignment of all the grains. After the alignment of dipoles in the grains on the material, cooling of material while keeping the electric field is done. Below Curie temperature, the surviving polarity on the material is permanent. By this process a material that exhibits piezoelectric property below Curie temperature is ready to use [16,20,21]. A figure describing the poling process is given in Figure 2-3 [16].

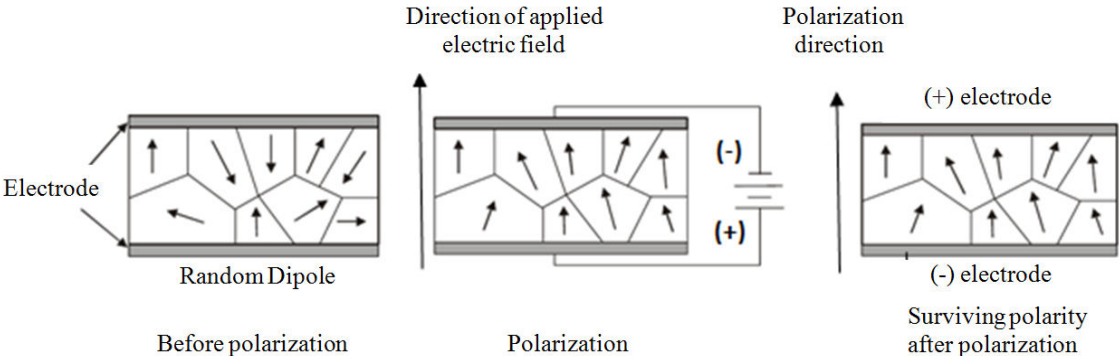


Figure 2-3. Poling process of piezoelectric ceramics [16]

2.1.5 Piezoelectric Actuators

Piezoelectric materials have the ability to deform upon the effect of an applied electric field on them, this makes the use of piezoelectric materials as actuators possible. But piezoelectric materials can be used as sensors at the same time. After poling process, a man-made piezoelectric crystal gains its + and - electrodes. In the sensor/generator mode of application, if the piezoelectric material is compressed in the polarization direction (this also applies to tension in the direction perpendicular to the polarization direction), the generated voltage has the same polarity with the

piezoelectric crystal. If piezoelectric material undergoes tension in the polarization direction (this also applies to compression in the direction perpendicular to the polarization direction), then the voltage generated has the opposite polarity. On the other hand in the actuator/motor mode of piezoelectric material, if the applied voltage has the same polarity with the piezoelectric material, then the piezoelectric material expands in the polarization direction and contracts in the directions perpendicular to the polarization direction. If the applied voltage has the opposite polarity, then the piezoelectric material contracts in the polarization direction and expands in the directions perpendicular to the polarization direction. All of these working principles are summarized in Figure 2-4 [22].

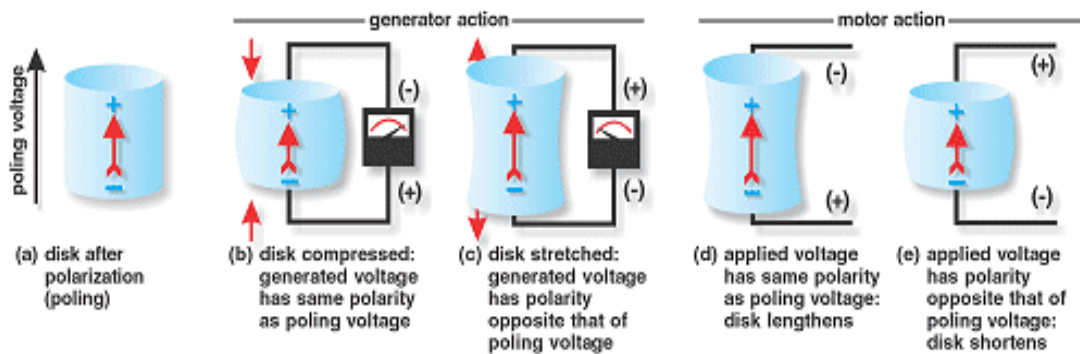


Figure 2-4. Operation modes of piezoelectric material after poling [22]

Piezoelectric actuators enjoy some unique properties such as unlimited resolution of motion, no wear or tear, fast response, no magnetic field effect thanks to their unbalanced dipole structure at unit cell level [21]. The amount of motion generated from piezoelectric actuator depends directly on the applied electric field on the piezoelectric material. However piezoelectric actuators lack the stroke distance since their motion is a result of the deformation of the unit cell structure. Also they cannot be used above temperatures higher than their Curie temperature since they lose their piezoelectric ability at those temperatures [21]. Each piezoelectric material has a specific Curie temperature. PZT materials are commonly used popular piezoelectric materials. Curie temperature of PZT materials ranges from 170 to 360°C [23]. A final drawback of piezoelectric actuators is the requirement of high voltages, in the order of hundreds of Volts. However they do not require high amount of current, it is in the order of miliAmperes. This reduces the amount of power consumed by piezoelectric

actuators. Piezoelectric actuators usually require a high voltage piezoelectric amplifier to operate. This can be a problem when designing an active vibration control system for an aerospace structure due to space limitation.

There are many forms of piezoelectric actuators namely patch actuators, bimorph actuators, stack actuators, mechanically amplified stack actuators, MFC (Macro Fiber Composite) actuators, piezo tube actuators, piezo motors and special design type actuators. An appropriate type of actuator can be selected based on the need of force and the displacement requirement of the application. A quick comparison chart for the typical force and displacement values of different piezoelectric actuator types is given in Figure 2-5.

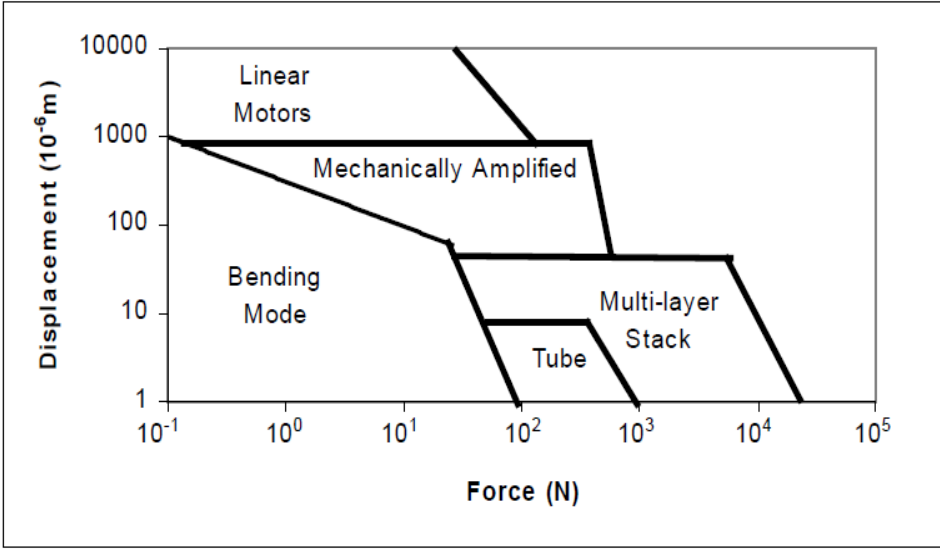


Figure 2-5. Typical force and displacement values for piezoelectric actuators

The piezoelectric phenomenon is exhibited as a result of applied electric field between the electrodes of a piezoelectric actuator. To have high intensity of electric field between the electrode surfaces, the thickness between the electrode surfaces should be small for a fixed voltage since the electric field between two parallel plate is:

$$E = \frac{V}{t} \tag{2.1}$$

where E is the electric field between the electrodes and t is the distance between the electrodes [24]. That explains why building a piezoelectric actuator in the form of a thin plate is advantageous.

A common practice in the application of this scientific fact is the piezoelectric patch actuators. Those actuators are polarized in their thickness direction and exposed to electric field also in their thickness direction. Usually the polarization direction of a piezoelectric actuator is denoted as axis number 3, which is the thickness of a patch actuator as shown in Figure 2-6 [25]. This makes the length and width of the piezo actuator to be named as axis 1 and axis 2. Application of electric field in the direction of axis 3 with the opposite polarity as the piezoelectric actuator contracts the piezo in axis 3 direction and expands in axis 1 and axis 2 directions (see Figure 2-6). A photograph of piezoelectric patch actuators with different sizes is given in Figure 2-7 [26].

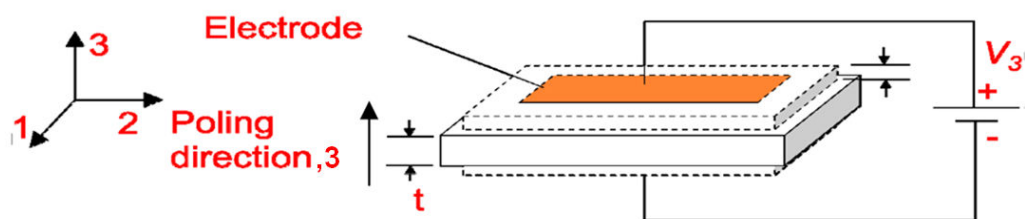


Figure 2-6. Piezoelectric patch actuator [25]

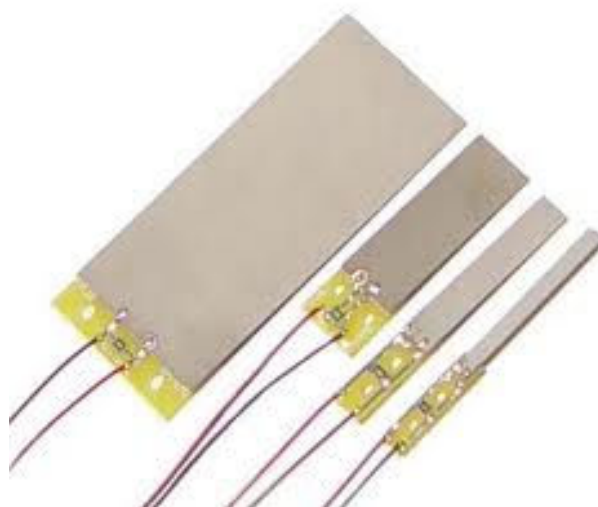


Figure 2-7. Photo of piezoelectric patch actuators [26]

Bimorph piezo actuators are manufactured by placing two piezoelectric patches on top of each other. Bimorph actuators consist of two piezoelectric layers that work in opposite direction. This makes the bending motion possible. Bimorph configuration can be achieved by parallel connection or series connection of piezoelectric layers. A schematic representation of the bimorph bender actuators is given in Figure 2-8 [27].

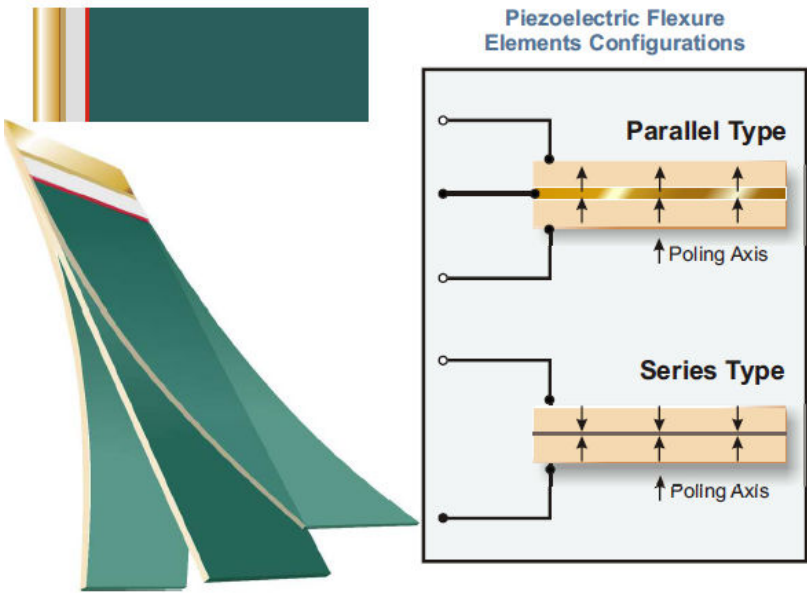


Figure 2-8. Bimorph bender actuators [27]

Another form of piezoelectric actuators is piezo stack actuator. Piezo stack actuators are manufactured by stacking single layer piezo plates on top of each other. The applied voltage to the piezo stack is divided individually for each layer. The electric field applied to each piezo layer is in the polarization axis, namely axis number 3. The motion of the stack is also utilized in the axis number 3. This is called 3-3 operation mode for each piezo layer. The cumulative force/displacement generated from the stack is the summation of the force/displacement coming from each layer. This makes higher force levels and/or displacement levels possible from piezoelectric materials by stacking a number of piezo layers. An illustrative drawing of a piezo stack actuator is given in Figure 2-9 and a photo of piezo stack actuator is given in Figure 2-10 [28-29].

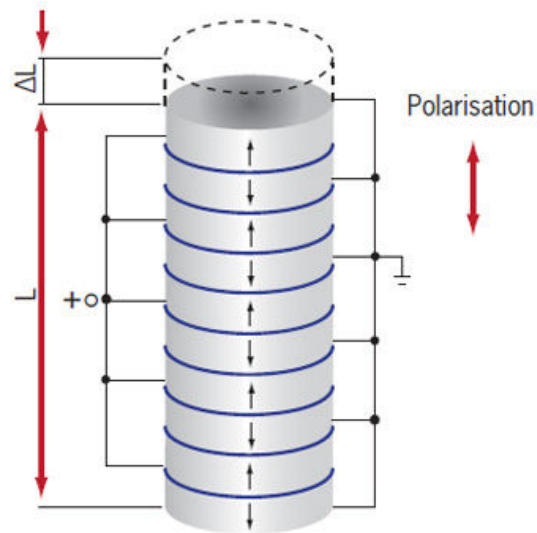


Figure 2-9. Piezo stack actuator [28]

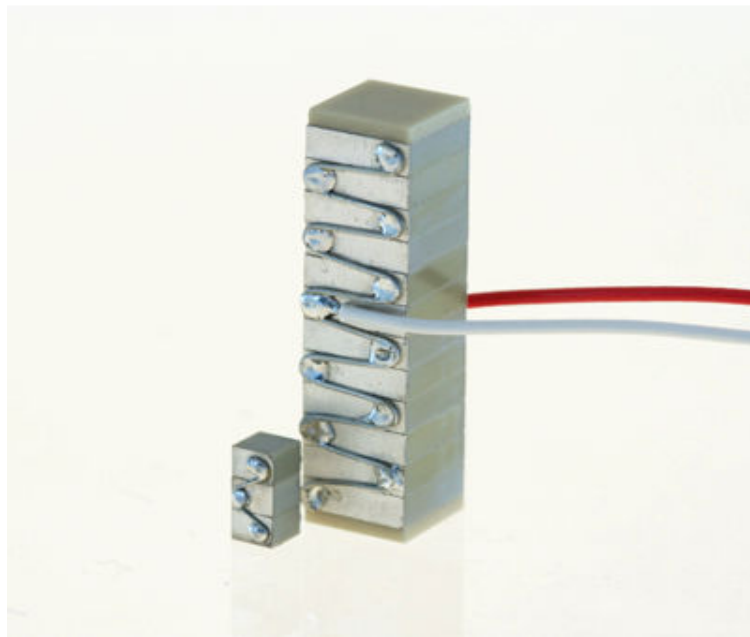


Figure 2-10. Photo of piezo stack actuators [29]

Another enhancement to increase the stroke displacement of piezoelectric actuators is called mechanically amplified piezoelectric actuators. The travel distance of the actuator is enhanced thanks to some specially designed compliant mechanisms. Those mechanism increase the stroke of the actuator in the price of decreased force. A photo of an example piezoelectric actuator with amplification mechanism is given in Figure 2-11 [30].

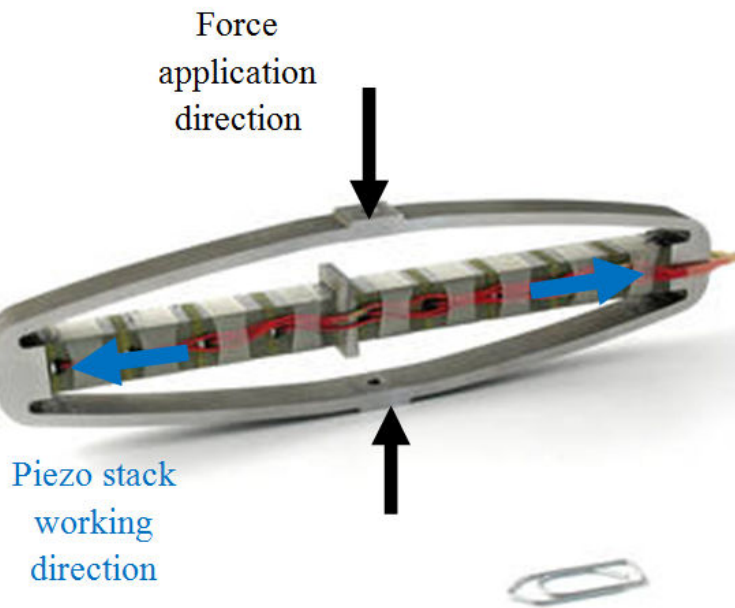


Figure 2-11. Mechanically amplified stack actuator [30]

PZT is the one of the most common material used in the piezoelectric actuators, but since it is in the form of a ceramic, it is brittle. Brittleness of hard piezoelectric materials is a disadvantage in terms of usage. It is impossible to deform and apply a hard PZT plate on the surface of a curved member. PVDF is a polymer type soft piezoelectric material, yet it is soft to be used as actuator and is rather preferred to be used as sensor. Here comes a necessity for a type of material which is hard enough to be used as actuator and soft enough to be bend and applicable to curved surfaces. That is the motivation behind the development of composite piezoelectric actuators. In those actuators PZT fibers are reinforced and supported by some soft layers. That makes application of MCF's to curved surfaces possible. An illustrative drawing of the internal structure of a MCF is given in Figure 2-12 and a photo of a MFC is given in Figure 2-13 [31].

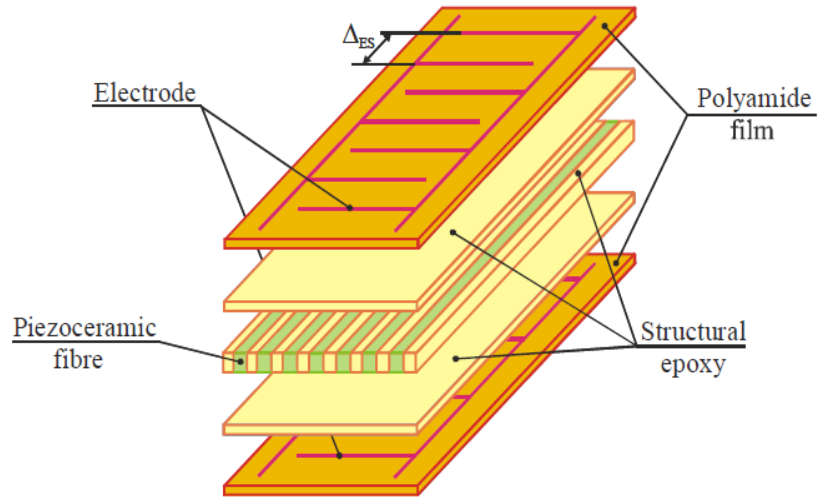


Figure 2-12. Internal structure of MFC [31]

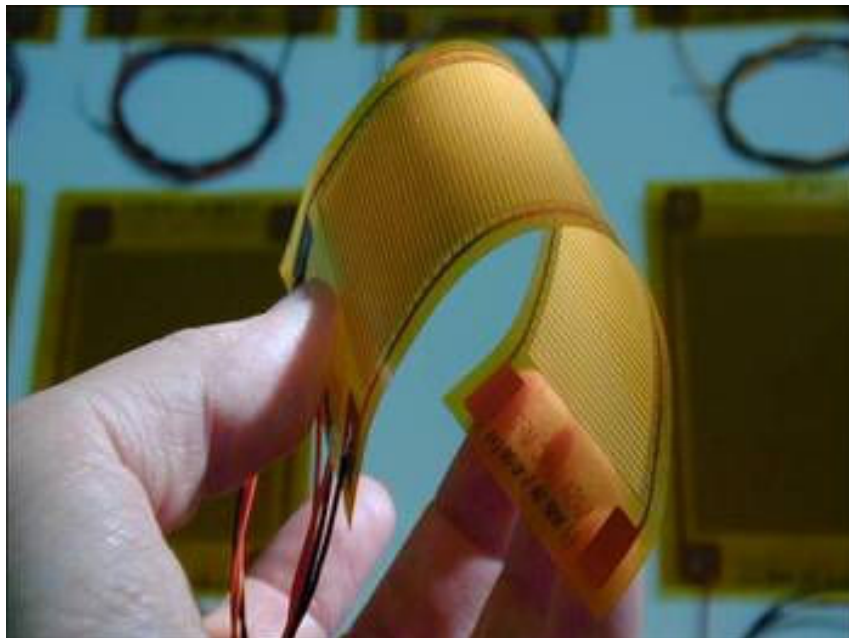


Figure 2-13. Photo of MFC [31]

Piezo tube actuators are in the form of hollow cylinders. Those type of actuators are used in scanning microscopy, ultrasonic applications, piezoelectric pumps, ink jet printers and nano-positioning. The inner and outer surfaces of piezoelectric material are the electrodes. A schematic drawing of a tube actuator is given in Figure 2-14 [32].

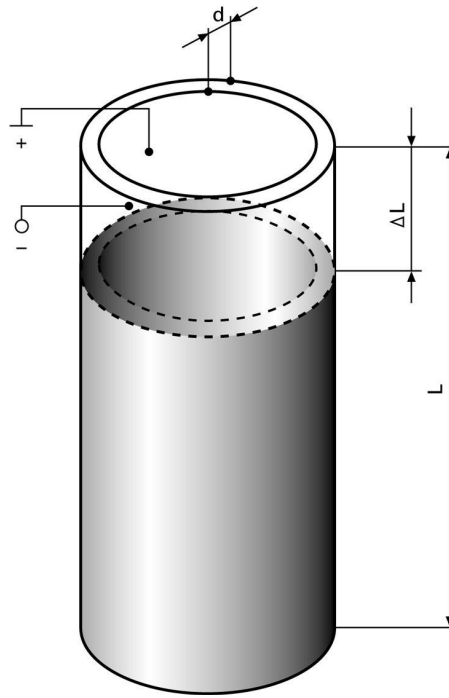


Figure 2-14. An illustration of piezo tube actuators [32]

A different type of piezoelectric actuator is piezoelectric motors. Those type of actuators have moving parts inside, so their motion is not limited to the deformation of piezoelectric material due to electric field. Piezoelectric motors works as a combination of piezoelectric elements with other mechanical parts. There are many different types and designs of piezo motors to generate linear or rotary motion. One example for the illustration of the concept is called piezo inchworm motor whose working process is given in Figure 2-15 [33]. The piezo motor in this example consists of 3 sets of piezo element. In the initialization phase, piezoelectric elements placed on the right side hold the motion rod. In step 1, the piezo elements placed laterally moves the motion rod from left to right. In step 2 piezoelectric elements on the left secure the motion rod. In step 3 piezoelectric elements on the left release the motion rod and on step 4 they are moved back to left by lateral piezoelectric elements. In step 5 piezoelectric elements on the left hold the motion rod again to move it right further and in step 6 piezoelectric elements on right release the motion rod to allow its motion to right. This comes back to the initialization step of the loop of operation of piezo inchworm motor.

Six Step Actuation Processes of the Piezo Inchworm Motor

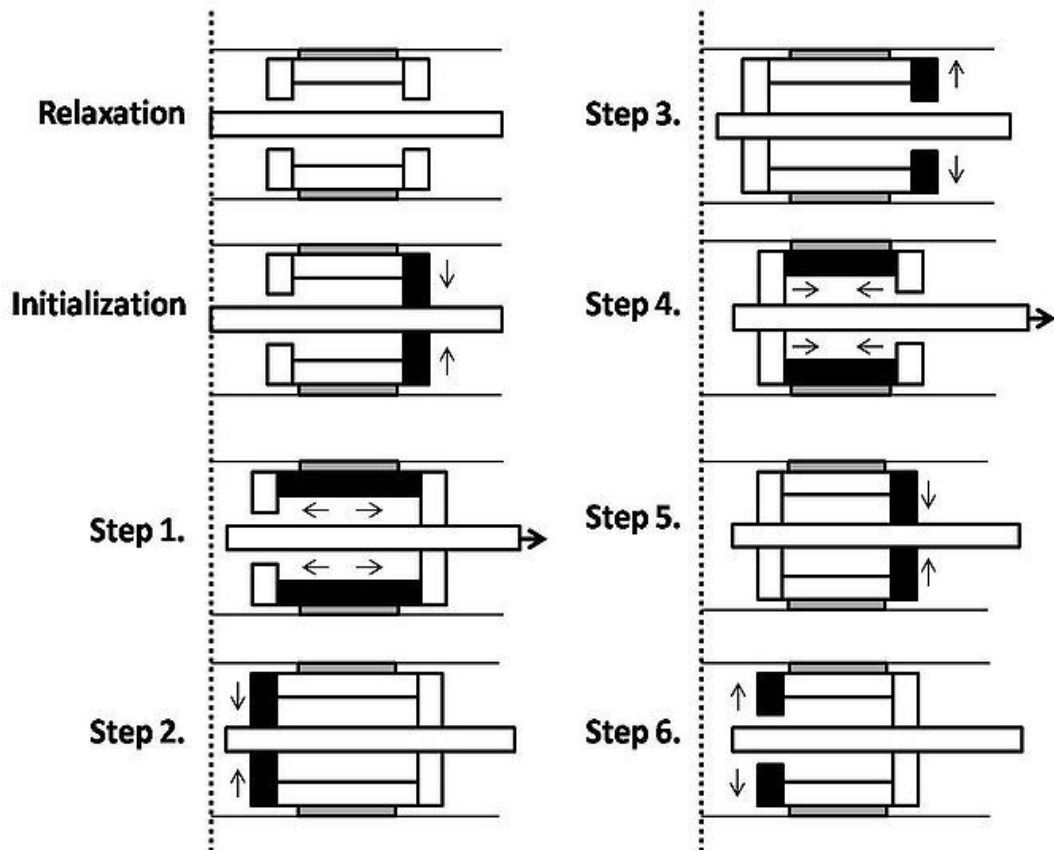


Figure 2-15. Working process of piezo inchworm motor [33]

2.2 Piezoelectric Properties and Modeling of Piezoelectric Actuators by ANSYS

Piezoelectric materials have the ability to generate electric charge as a response to the applied strain. They also have the ability to deform upon an applied electric field [16]. The amount of electric charge generated per unit electrode area of the piezoelectric material as a response to applied strain and the amount of deformation of the piezoelectric material as a response to applied electric field between its electrodes can be computed using piezoelectric constitutive equations. The material properties of piezoelectric materials are the coefficients in those constitutive equations. The piezoelectric constitutive equations are defined in ANSI/IEEE 176 standard [34] in 1987 and presented as follows:

$$\{S\} = [s^E]\{T\} + [d]\{E\} \quad (2.2)$$

$$\{D\} = [d]^t\{T\} + [\varepsilon^T]\{E\} \quad (2.3)$$

In these equations, these terms can be explained as follows [34,35,36]:

$\{S\}$: Mechanical strain vector, unit: m/m

$\{T\}$: Mechanical stress vector, unit: N/m²

$\{E\}$: Electric field vector, unit: V/m

$\{D\}$: Electric displacement (electric flux density), unit: C/m²

$[s^E]$: Compliance matrix evaluated at constant electric field, unit: m²s/N

$[d]$: Piezoelectric constant matrix for strain/electric field, unit: m/V

$[\varepsilon^T]$: Dielectric permittivity matrix evaluated at constant stress, unit: F/m

There is also an alternative form of those equations in which applied strain on the piezoelectric material is linearly related to stress and the electric displacement [34,36]. Piezoelectric materials are anisotropic, so their material properties change with direction [34,35]. If the poling axis of the piezoelectric material is denoted as 3, a coordinate axis as given in Figure 2-16 can be defined [37]. The constitutive piezoelectric equations can be written in this axis system as given by the following equations [19].

$$\begin{Bmatrix} S_1 \\ S_2 \\ S_3 \\ S_4 \\ S_5 \\ S_6 \end{Bmatrix} = \begin{bmatrix} s_{11}^E & s_{12}^E & s_{13}^E & 0 & 0 & 0 \\ s_{12}^E & s_{11}^E & s_{23}^E & 0 & 0 & 0 \\ s_{13}^E & s_{23}^E & s_{33}^E & 0 & 0 & 0 \\ 0 & 0 & 0 & s_{44}^E & 0 & 0 \\ 0 & 0 & 0 & 0 & s_{44}^E & 0 \\ 0 & 0 & 0 & 0 & 0 & s_{66}^E \end{bmatrix} \begin{Bmatrix} T_1 \\ T_2 \\ T_3 \\ T_4 \\ T_5 \\ T_6 \end{Bmatrix} + \begin{bmatrix} 0 & 0 & d_{13} \\ 0 & 0 & d_{13} \\ 0 & 0 & d_{33} \\ 0 & d_{15} & 0 \\ d_{15} & 0 & 0 \\ 0 & 0 & 0 \end{bmatrix} \begin{Bmatrix} E_1 \\ E_2 \\ E_3 \end{Bmatrix} \quad (2.4)$$

$$\begin{Bmatrix} D_1 \\ D_2 \\ D_3 \end{Bmatrix} = \begin{bmatrix} 0 & 0 & 0 & 0 & d_{15} & 0 \\ 0 & 0 & 0 & d_{15} & 0 & 0 \\ d_{13} & d_{13} & d_{33} & 0 & 0 & 0 \end{bmatrix} \begin{Bmatrix} T_1 \\ T_2 \\ T_3 \\ T_4 \\ T_5 \\ T_6 \end{Bmatrix} + \begin{bmatrix} \varepsilon_{11}^T & 0 & 0 \\ 0 & \varepsilon_{22}^T & 0 \\ 0 & 0 & \varepsilon_{33}^T \end{bmatrix} \begin{Bmatrix} E_1 \\ E_2 \\ E_3 \end{Bmatrix} \quad (2.5)$$

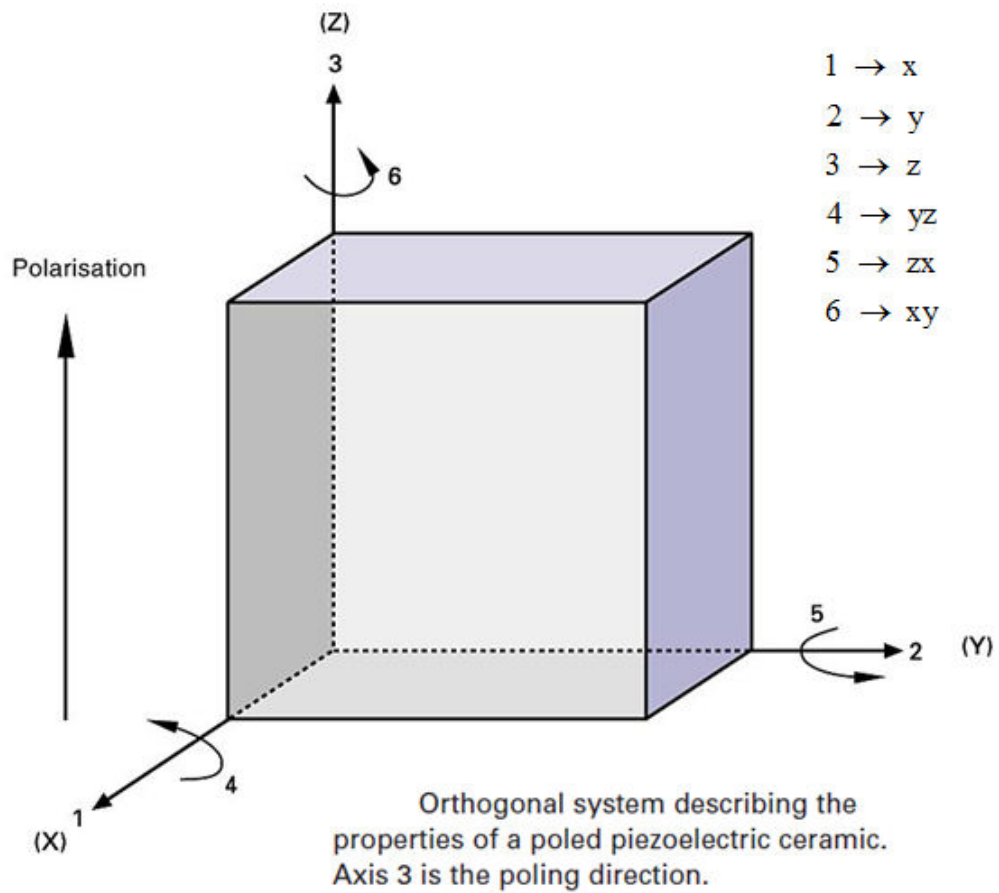


Figure 2-16. Axis system of a piezoelectric material, polarized in axis 3 [37]

ANSYS software has the ability to model piezoelectric materials by SOLID 226, 20 Node Coupled Field solid element [34,38]. In modeling piezoelectric material properties in ANSYS an important point to notice is that the order of vectors of piezoelectric materials in the manufacturer's datasheet is $\{x,y,z,yz,xz,xy\}$. However ANSYS accepts the material properties in the order $\{x,y,z,xy,yz,xz\}$. Therefore equations (2.4) and (2.5) are modified as follows when entering material properties into ANSYS [36].

$$\begin{Bmatrix} S_1 \\ S_2 \\ S_3 \\ S_4 \\ S_5 \\ S_6 \end{Bmatrix} = \begin{bmatrix} S_{11}^E & S_{12}^E & S_{13}^E & 0 & 0 & 0 \\ S_{12}^E & S_{11}^E & S_{23}^E & 0 & 0 & 0 \\ S_{13}^E & S_{23}^E & S_{33}^E & 0 & 0 & 0 \\ 0 & 0 & 0 & S_{66}^E & 0 & 0 \\ 0 & 0 & 0 & 0 & S_{44}^E & 0 \\ 0 & 0 & 0 & 0 & 0 & S_{44}^E \end{bmatrix} \begin{Bmatrix} T_1 \\ T_2 \\ T_3 \\ T_4 \\ T_5 \\ T_6 \end{Bmatrix} + \begin{bmatrix} 0 & 0 & d_{13} \\ 0 & 0 & d_{13} \\ 0 & 0 & d_{33} \\ 0 & 0 & 0 \\ 0 & d_{15} & 0 \\ d_{15} & 0 & 0 \end{bmatrix} \begin{Bmatrix} E_1 \\ E_2 \\ E_3 \end{Bmatrix} \quad (2.6)$$

$$\begin{Bmatrix} D_1 \\ D_2 \\ D_3 \end{Bmatrix} = \begin{bmatrix} 0 & 0 & 0 & 0 & 0 & d_{15} \\ 0 & 0 & 0 & 0 & d_{15} & 0 \\ d_{13} & d_{13} & d_{33} & 0 & 0 & 0 \end{bmatrix} \begin{Bmatrix} T_1 \\ T_2 \\ T_3 \\ T_4 \\ T_5 \\ T_6 \end{Bmatrix} + \begin{bmatrix} \varepsilon_{11}^T & 0 & 0 \\ 0 & \varepsilon_{22}^T & 0 \\ 0 & 0 & \varepsilon_{33}^T \end{bmatrix} \begin{Bmatrix} E_1 \\ E_2 \\ E_3 \end{Bmatrix} \quad (2.7)$$

ANSYS SOLID 226 element is a coupled field element which has piezoelectric option. This element has 20 nodes. Geometry options of this element is given in Figure 2-17. The degree of freedom of this element is translation in x,y and z axes and voltage (UX,UY,UZ and VOLT) if piezoelectric option is selected. In piezoelectric option, force in x,y and z axes and charge (FX,FY,FZ and CHRG) can be applied to the element. This element can be used in static, modal, full harmonic and full transient analyses [38].

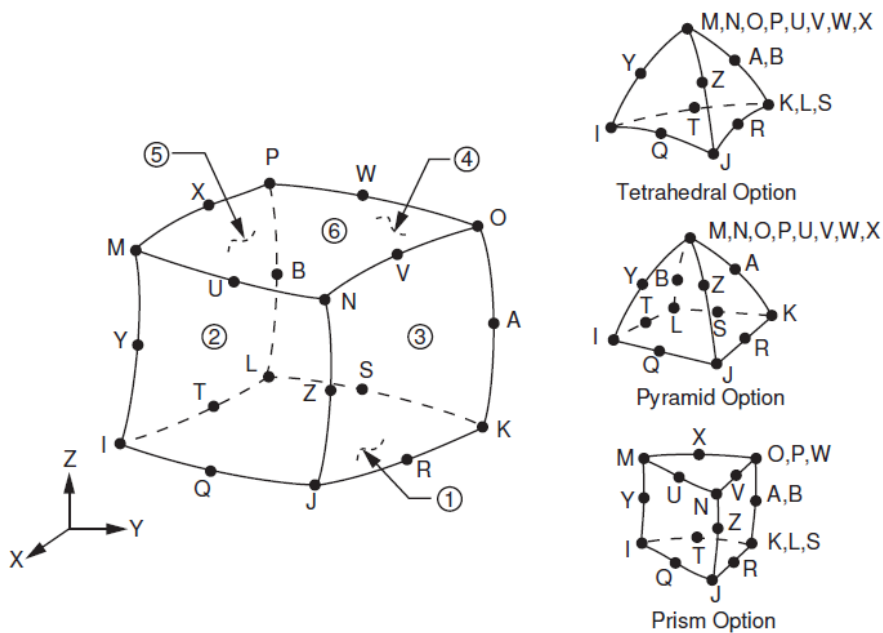


Figure 2-17. SOLID 226 element in ANSYS [38]

2.3 Modeling Plant in State Space

A linear vibratory system can be expressed in state space as a dynamic system. To obtain a state space representation of a linear vibratory system, the equation of motion of the system is written in the first step.

$$\mathbf{M}\ddot{\mathbf{r}} + \mathbf{C}_d\dot{\mathbf{r}} + \mathbf{K}\mathbf{r} = \mathbf{F} \quad (2.8)$$

In this equation, \mathbf{r} is the generalized coordinate vector, \mathbf{M} is mass matrix, \mathbf{C}_d is damping matrix, \mathbf{K} is stiffness matrix of the system. \mathbf{F} is the forcing vector on the system. Note that equation (2.8) can be written in modal domain as follows [39]:

$$\bar{\mathbf{M}}\ddot{\boldsymbol{\eta}} + \bar{\mathbf{C}}_d\dot{\boldsymbol{\eta}} + \bar{\mathbf{K}}\boldsymbol{\eta} = \bar{\mathbf{F}} \quad (2.9)$$

In this equation $\boldsymbol{\eta}$ is the modal coordinate vector, which is a function of time. $\bar{\mathbf{M}}$ is the modal mass matrix, $\bar{\mathbf{C}}_d$ is the modal damping matrix, $\bar{\mathbf{K}}$ is the modal stiffness matrix and $\bar{\mathbf{F}}$ is the modal forcing vector. If the mass normalized modal matrix of the system is $\boldsymbol{\varphi}$, then modal mass, damping, stiffness matrices and the forcing vector can be calculated as follows [39]:

$$\bar{\mathbf{M}} = \boldsymbol{\varphi}^T \mathbf{M} \boldsymbol{\varphi} \quad (2.10)$$

$$\bar{\mathbf{C}}_d = \boldsymbol{\varphi}^T \mathbf{C}_d \boldsymbol{\varphi} \quad (2.11)$$

$$\bar{\mathbf{K}} = \boldsymbol{\varphi}^T \mathbf{K} \boldsymbol{\varphi} \quad (2.12)$$

$$\bar{\mathbf{F}} = \boldsymbol{\varphi}^T \mathbf{F} \quad (2.13)$$

To express the vibratory system in state space, the system states are taken as the modal coordinates and their time derivatives. State space form of a dynamic system is as follows:

$$\dot{\mathbf{x}} = \mathbf{A}\mathbf{x} + \mathbf{B}\mathbf{u} \quad (2.14)$$

$$\mathbf{y} = \mathbf{C}\mathbf{x} + \mathbf{D}\mathbf{u} \quad (2.15)$$

In state space representation, \mathbf{x} is the state vector, \mathbf{u} is the system input vector and \mathbf{y} is the system output vector. If the system input is forcing on definite locations of the system and the system output is the displacement at definite locations of the system, then the state space matrices of the system and the system states can be expressed as follows [39,40]:

$$\mathbf{x} = \begin{bmatrix} \boldsymbol{\eta} \\ \dot{\boldsymbol{\eta}} \end{bmatrix} \quad (2.16)$$

$$\mathbf{A} = \begin{bmatrix} \mathbf{0} & \mathbf{I} \\ -\bar{\mathbf{M}}^{-1}\bar{\mathbf{K}} & -\bar{\mathbf{M}}^{-1}\bar{\mathbf{C}}_d \end{bmatrix} \quad (2.17)$$

$$\mathbf{B} = \begin{bmatrix} \mathbf{0} \\ \bar{\mathbf{M}}^{-1}\boldsymbol{\varphi}^T\mathbf{F}_u \end{bmatrix} \quad (2.18)$$

$$\mathbf{C} = [\mathbf{U}_u\boldsymbol{\varphi} \quad \mathbf{0}] \quad (2.19)$$

$$\mathbf{D} = [\mathbf{0}] \quad (2.20)$$

In the above equation \mathbf{U}_u is a matrix of size number of outputs by number of degree of freedom (dof). The elements at the rows of matrix \mathbf{U}_u is 1 at dof where the output of the system is requested. Other elements of \mathbf{U}_u is zero [40]. As an example if the system has 6 dof and the system output is required to be the 1st and 5th dof of the system, the \mathbf{U}_u matrix will be

$$\mathbf{U}_u = \begin{bmatrix} \mathbf{1} & \mathbf{0} & \mathbf{0} & \mathbf{0} & \mathbf{0} & \mathbf{0} \\ \mathbf{0} & \mathbf{0} & \mathbf{0} & \mathbf{0} & \mathbf{1} & \mathbf{0} \end{bmatrix}$$

For the forcing matrix, \mathbf{F}_u is a matrix of size number of dof by number of input forces. The elements at the columns of \mathbf{F}_u is 1 at dof where a forcing is applied. Other elements of \mathbf{F}_u is zero [40]. To illustrate this with an example, for a 6 dof system if the forces are applied at 1st, 3rd and 4th dof, then \mathbf{F}_u matrix will be

$$\mathbf{F}_u = \begin{bmatrix} \mathbf{1} & \mathbf{0} & \mathbf{0} \\ \mathbf{0} & \mathbf{0} & \mathbf{0} \\ \mathbf{0} & \mathbf{1} & \mathbf{0} \\ \mathbf{0} & \mathbf{0} & \mathbf{1} \\ \mathbf{0} & \mathbf{0} & \mathbf{0} \\ \mathbf{0} & \mathbf{0} & \mathbf{0} \end{bmatrix}$$

Since mode shapes of a linear vibratory system is orthogonal, the following expressions can be written for a system modeled with n modes [40,41].

$$\mathbf{A} = \begin{bmatrix} 0 & 0 & \dots & 0 & 1 & 0 & \dots & 0 \\ 0 & 0 & \dots & 0 & 0 & 1 & \dots & 0 \\ \vdots & \vdots & \ddots & \vdots & \vdots & \vdots & \ddots & \vdots \\ 0 & 0 & \dots & 0 & 0 & 0 & \dots & 1 \\ -\omega_1^2 & 0 & \dots & 0 & -2\zeta_1\omega_1 & 0 & \dots & 0 \\ 0 & -\omega_2^2 & \dots & 0 & 0 & -2\zeta_2\omega_2 & \dots & 0 \\ \vdots & \vdots & \ddots & \vdots & \vdots & \vdots & \ddots & \vdots \\ 0 & 0 & \dots & -\omega_n^2 & 0 & 0 & \dots & -2\zeta_n\omega_n \end{bmatrix} \quad (2.21)$$

$$\mathbf{B} = \begin{bmatrix} 0 \\ \boldsymbol{\varphi}^T \mathbf{F}_u \end{bmatrix} \quad (2.22)$$

For mass normalized eigenvectors $\bar{\mathbf{M}} = \mathbf{I}$. It should be noted that in \mathbf{A} matrix ω_i is the natural frequency and ζ_i is the damping ratio of the i^{th} mode.

2.4 Concepts of Controllability and Observability

2.4.1 Concept of Controllability

A system is said to be controllable if it is possible to move the system from any initial state to any final state by means of the control inputs in a finite time interval [42]. Controllability concept plays an important role of the controller design problem since it is impossible to solve this problem if the system is uncontrollable. Given a linear dynamic system in state space representation with n number of states and r number of inputs, the controllability matrix of this system can be calculated as follows [42]:

$$\mathbf{R} = [\mathbf{B} \quad \mathbf{AB} \quad \mathbf{A}^2\mathbf{B} \quad \dots \quad \mathbf{A}^{n-1}\mathbf{B}] \quad (2.23)$$

The controllability matrix is n by n*r. If the controllability matrix has full rank, i.e $\text{Rank}(\mathbf{R}) = n$ then the system is said to be controllable [42].

2.4.2 Concept of Observability

A system is said to be observable if it is possible to observe all of the states of the system by only observing the system outputs for a finite time interval [42]. The observability and controllability are dual concepts. Given a linear dynamic system in state space representation with n number of states and q number of outputs, the observability matrix of this system can be computed as follows [42]:

$$\mathbf{Q} = \begin{bmatrix} \mathbf{C} \\ \mathbf{CA} \\ \mathbf{CA}^2 \\ \dots \\ \mathbf{CA}^{n-1} \end{bmatrix} \quad (2.24)$$

Dimension of the observability matrix is $n \times q$ by n . If the rank of observability matrix is n , i.e $\text{Rank}(\mathbf{Q}) = n$ then the system is said to be observable [42].

2.5 Placement of Piezoelectric Patches by Controllability

Using controllability matrix, it can only be detected whether a system is controllable or not. Controllability Gramian is used to measure the degree of controllability of a system and it is defined as follows [43,44]:

$$\mathbf{G}_c(t) = \int_0^t e^{\mathbf{A}\tau} \mathbf{B} \mathbf{B}^T e^{\mathbf{A}^T \tau} d\tau \quad (2.25)$$

Controllability Gramian matrix is a way to know the degree of controllability of a system. By changing the locations of the actuator, controllability degree of states of a system can be changed. If determinant of controllability Gramian matrix is maximized, then the energy required to control the vibrations of a system will be minimized. Eigenvalues of controllability Gramian matrix are also important measures of controllability for different states of a system. Since vibration modes of the system are taken as states when modeling vibratory systems, then the eigenvalues of controllability Gramian matrix correspond to the degree of controllability of each vibration mode. Among the eigenvalues of controllability Gramian matrix, if there is

a low eigenvalue, this means the corresponding vibration mode of the system is difficult to control with the existing actuator configuration [43]. Therefore it is possible to generate a placement criteria for piezoelectric actuator placement utilizing the eigenvalues of controllability Gramian matrix. A placement criterion utilizing the eigenvalues of controllability Gramian matrix is given below [44,45,46].

$$J = \frac{1}{\sigma(\lambda_i)} \left(\sum_{i=1}^{2n} \lambda_i \right)^{2n} \sqrt{\prod_{i=1}^{2n} (\lambda_i)} \quad (2.26)$$

In the placement criterion above, λ_i are the eigenvalues of the controllability Gramian matrix of the system and $\sigma(\lambda_i)$ is the standard deviation of the eigenvalues. It is desired to find optimum actuator locations to control modes of the system from $i = 1$ to n by maximizing the parameter J . It is desired to have high eigenvalues for the controllability Gramian matrix, so summation of the eigenvalues is included. It should be avoided to have a mode with very low controllability to ensure stability of the system, so a multiplication term of all the eigenvalues is also included in the criterion. Finally it is preferred to have similar controllability degree for each mode, and this is the reason for having the standard deviation of the eigenvalues in the denominator [45]. Ending up with a high J value means good and balanced actuator placement for all the modes that are included in the calculation of the criterion.

In the study of placement of piezoelectric actuators, one approach is to place a piezoelectric actuator to each possible actuator location and calculate a J value for the corresponding system. Each possible piezoelectric actuator configuration will constitute a different system in state space, thus will have a different controllability Gramian matrix and a different J value. The system with the highest J value will be the best system in terms of piezoelectric actuator placement. It is convenient to use finite element method for this task to compute the structural matrices, modal parameters and other required information for the system matrices required in Gramian calculation [39,47].

2.6 Placement of Sensors by Observability

Observability matrix only determines if a system is observable or not by the existing sensors on it, however a mathematical tool is required to determine the degree of observability of the system in order to develop a method which uses system observability for optimal sensor location. This mathematical tool is called observability Gramian matrix. Similar to controllability Gramian matrix, the eigenvalues of observability Gramian of a vibratory system give information about the observability of specific vibration modes. A similar placement criteria for sensor locations using observability Gramian matrix can be derived from the duality principle between controllability and observability. An expression of observability Gramian matrix is given as follows [45,48]:

$$\mathbf{G}_o(t) = \int_0^t e^{\mathbf{A}^T \tau} \mathbf{C}^T \mathbf{C} e^{\mathbf{A} \tau} d\tau \quad (2.27)$$

Maximizing the eigenvalues of the observability Gramian matrix maximizes the observability of the modes, which are the states of vibratory systems. Similar placement criteria as in the actuator placement can be used for sensor placement using the eigenvalues of the observability Gramian matrix instead of the eigenvalues of the controllability Gramian matrix [45]. Discussion in the placement criteria for the actuators also applies for the sensor placement.

2.7 State Feedback, Observer Design and Pole Placement

For the system given in state space representation as in the equations 2.14 and 2.15, a full state control signal will be chosen as follows [42]:

$$\mathbf{u} = -\mathbf{K}\mathbf{x} \quad (2.28)$$

If equation 2.28 is inserted in equation 2.14, the result will be

$$\dot{\mathbf{x}} = (\mathbf{A} - \mathbf{BK})\mathbf{x} \quad (2.29)$$

Note that by this operation the system is modified and the stability and transient response characteristics of the system is determined by the eigenvalues of $(\mathbf{A} - \mathbf{BK})$ matrix. By choosing a proper \mathbf{K} , the poles of the original system \mathbf{A} can be placed on any desired location on the s-plane if the system is completely state controllable [42]. Pole placement problem is finding a proper \mathbf{K} matrix to place the system poles to desired locations for the desired system performance.

If the controllability of all the states of the system are guaranteed, then any pole of the system can be placed on any desired location on the s-plane. For a vibratory system, the location of poles of the system are determined by the natural frequencies and the damping ratios of the system. For each vibration mode of the system there are two poles placed symmetrically with respect to the real axis of s-plane. Poles of a vibratory system for a mode with a natural frequency ω_n and damping ratio ζ is given in Figure 2-18 [49]. If there exists a vibratory system with actuator configuration that presents full state controllability, then it is theoretically possible to manipulate natural frequencies and damping ratios of each mode of the system. If the poles are far from the origin, this mode has higher natural frequency. If the angle between the negative real axis and the line from pole to the origin increases, then the damping ratio of this mode decreases. To add damping to a vibratory system, poles should be located to positions such that the angle between the negative real axis and the line from pole to the origin should be smaller than the original value. It should be noted that ζ defines the cosine of the angles of the poles. At $\zeta = \cos(\pi/4)$ the system has critical damping for that mode.

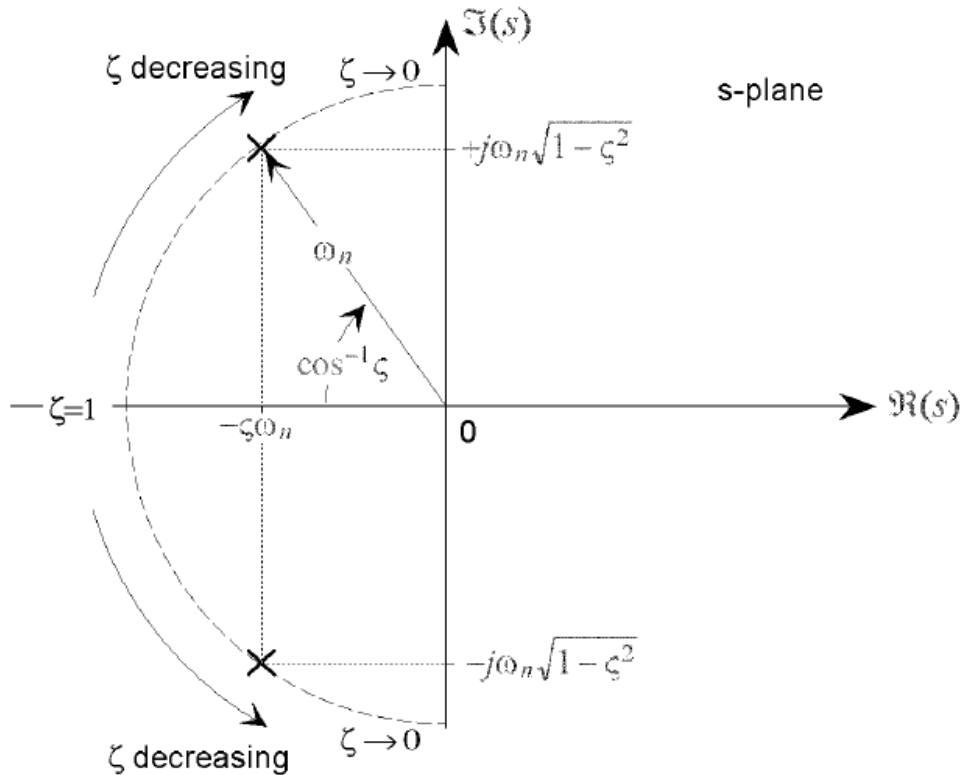


Figure 2-18. Poles of a vibratory system in s-domain [49]

In pole placement the control signal is calculated by using the system states. However, in system models states of the system can be different from the system outputs. In a vibratory system model, the states of the system can be the vibration modes and all of the states may not be available from the system output measurements. Then a dynamic system called observer should be designed to estimate the unavailable system states [42].

Observer estimates the system states based on the control inputs and the system outputs. An observer can be designed if the system is observable. Since the aim of building the observer is to reconstruct the system states, it has a similar structure as the plant except an additional term for the difference between the measures of system output and estimated system output [42]. The block diagram of a system with an observer and full state feedback is given in Figure 2-19 [50]. Estimated states by the observer are denoted by $\hat{\mathbf{x}}$.

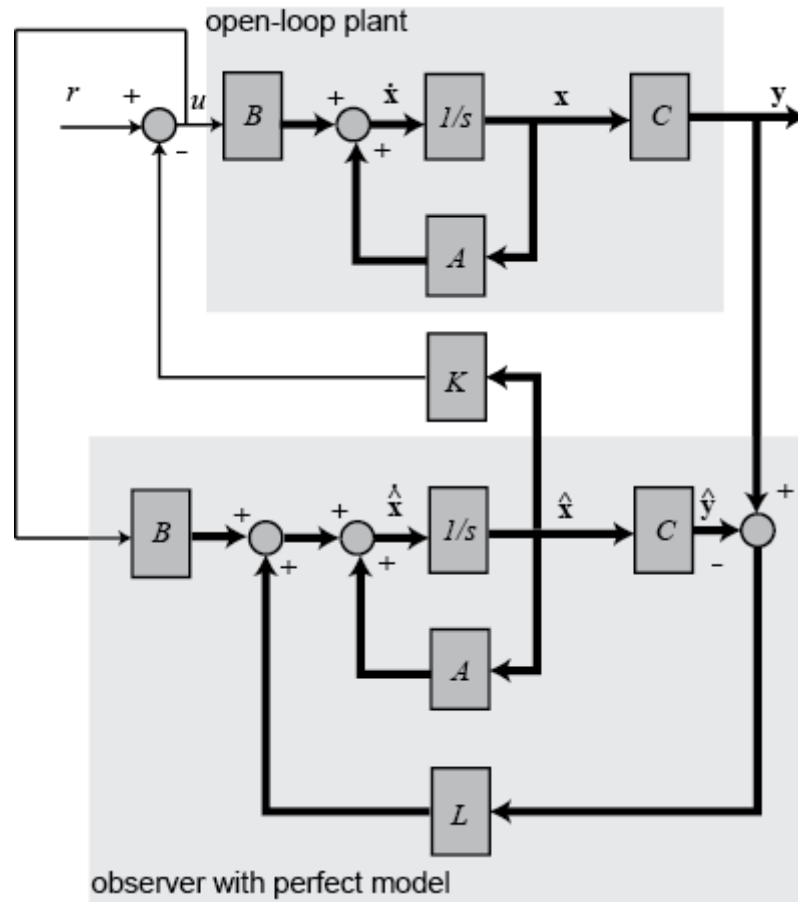


Figure 2-19. Block diagram of system with observer [50]

The equations of the full state observer are as follows [42]:

$$\dot{\hat{\mathbf{x}}} = \mathbf{A}\hat{\mathbf{x}} + \mathbf{B}\mathbf{u} + \mathbf{L}(\mathbf{y} - \mathbf{C}\hat{\mathbf{x}}) \quad (2.30)$$

$$\dot{\hat{\mathbf{x}}} = (\mathbf{A} - \mathbf{L}\mathbf{C})\hat{\mathbf{x}} + \mathbf{B}\mathbf{u} + \mathbf{L}\mathbf{y} \quad (2.31)$$

The observer dynamics is given by equation 2.31. Eigenvalues of $(\mathbf{A} - \mathbf{L}\mathbf{C})$ matrix greatly influence the observer dynamics.

If the reference input to the plant is zero, i.e. $r = 0$, and $\mathbf{u} = -\mathbf{K}\hat{\mathbf{x}}$ then it is possible to write the equation below for the system for which the block diagram is given in Figure 2-19 [42]:

$$\dot{\mathbf{x}} - \dot{\hat{\mathbf{x}}} = \mathbf{A}\mathbf{x} - \mathbf{A}\hat{\mathbf{x}} - \mathbf{L}(\mathbf{C}\mathbf{x} - \mathbf{C}\hat{\mathbf{x}}) \quad (2.32)$$

$$\dot{\mathbf{x}} - \dot{\hat{\mathbf{x}}} = (\mathbf{A} - \mathbf{L}\mathbf{C})(\mathbf{x} - \hat{\mathbf{x}}) \quad (2.33)$$

Difference between $\dot{\mathbf{x}}$ and $\dot{\hat{\mathbf{x}}}$ is called error vector and if $\mathbf{e} = \mathbf{x} - \hat{\mathbf{x}}$ then [42]:

$$\dot{\mathbf{e}} = (\mathbf{A} - \mathbf{L}\mathbf{C})\mathbf{e} \quad (2.34)$$

The dynamics of the error between the system states and the estimated system states is a dynamic system with eigenvalues of $(\mathbf{A} - \mathbf{L}\mathbf{C})$ matrix. If those eigenvalues are stable, then the error will converge to zero and the system will be successfully observed by the designed observer [42].

Observer design problem is a kind of pole placement in which \mathbf{A}^T and \mathbf{C}^T matrices are used instead of \mathbf{A} and \mathbf{B} as in the state feedback controller design [51]. In state feedback controller design with pole placement, eigenvalues of $(\mathbf{A} - \mathbf{B}\mathbf{K})$ matrix is placed by choosing a proper \mathbf{K} . In observer design problem the eigenvalues of $(\mathbf{A} - \mathbf{L}\mathbf{C})$ matrix will be placed by choosing a proper \mathbf{L} . However in state feedback controller design, \mathbf{K} matrix is on the left of \mathbf{B} matrix. To make the observer design problem like the previous one, transpose of $(\mathbf{A} - \mathbf{L}\mathbf{C})$ matrix will be taken [51].

$$(\mathbf{A} - \mathbf{L}\mathbf{C})^T = \mathbf{A}^T - \mathbf{C}^T\mathbf{L}^T \quad (2.35)$$

In observer design, same tools as in the state feedback controller design can be used but \mathbf{A}^T and \mathbf{C}^T matrices should be used instead of \mathbf{A} and \mathbf{B} matrices and the transpose of the resulting \mathbf{K} matrix should be used as \mathbf{L} , i.e. $\mathbf{K}^T = \mathbf{L}$ [51].

In designing a state feedback controller with observer, there are two pole placements that the designer should realize, pole placement for the system by the controller and the pole placement for the observer. There is a rule of thumb for the controlled system poles and the observer poles such that the observer should be 3 to 5 times faster than the system to be observed. Therefore the observer poles should be placed such that the settling time of the observer system should be 1/3 to 1/5 of the settling time of the controlled system [52].

CHAPTER 3

ACTIVE VIBRATION CONTROL OF BEAM USING PIEZOELECTRIC PATCHES

3.1 Introduction

Before studying active vibration control of a cylindrical structure by means of piezoelectric patches, a simpler structure, a cantilevered beam is studied in order to prove the methodology to be used in control of vibrations. In the study a thin, long cantilever beam made of steel is used. A photo of the beam used in the study is given in Figure 3-1.

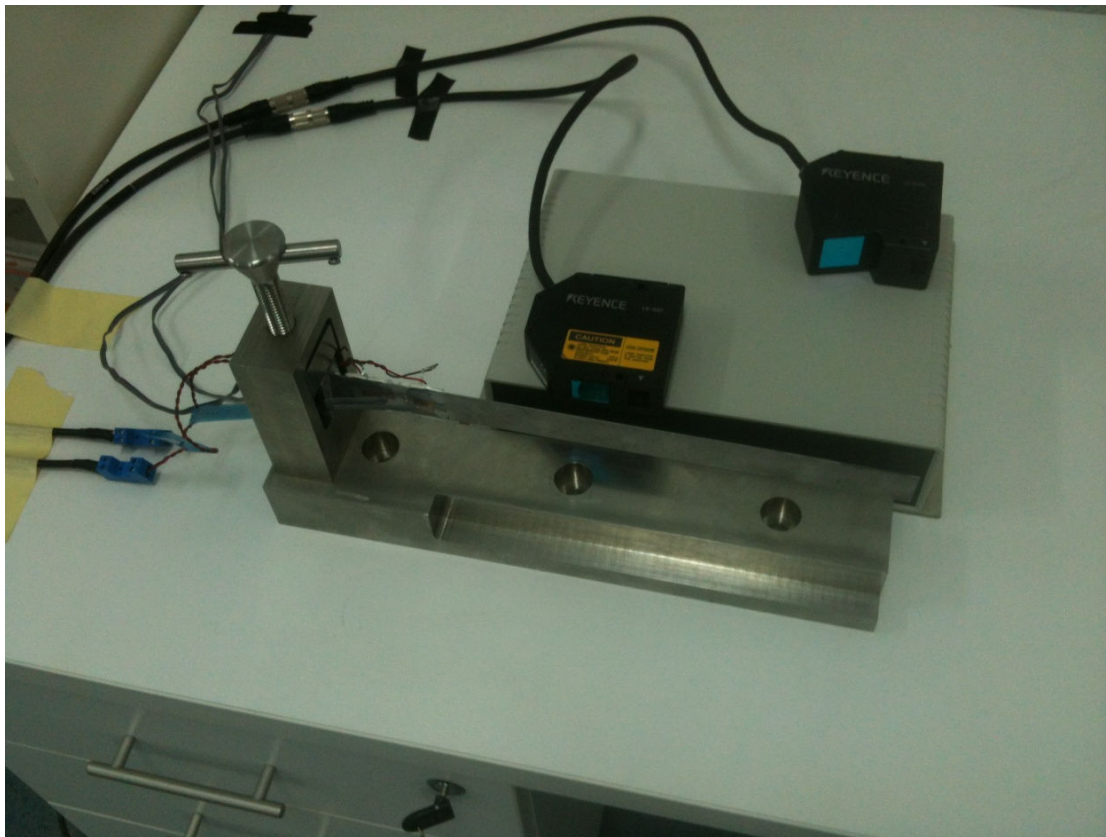


Figure 3-1. Cantilevered beam as the test structure

The beam structure has two American Piezo Company (APC) 850 piezoelectric patches placed side by side at the beam root. On the other side of the beam there are two strain gages located at the center of each piezoelectric patch. A photo of piezoelectric patches bonded at the root of the beam is given in Figure 3-2, and a photo of strain gages bonded at the opposite side of piezoelectric patches is given in Figure 3-3.

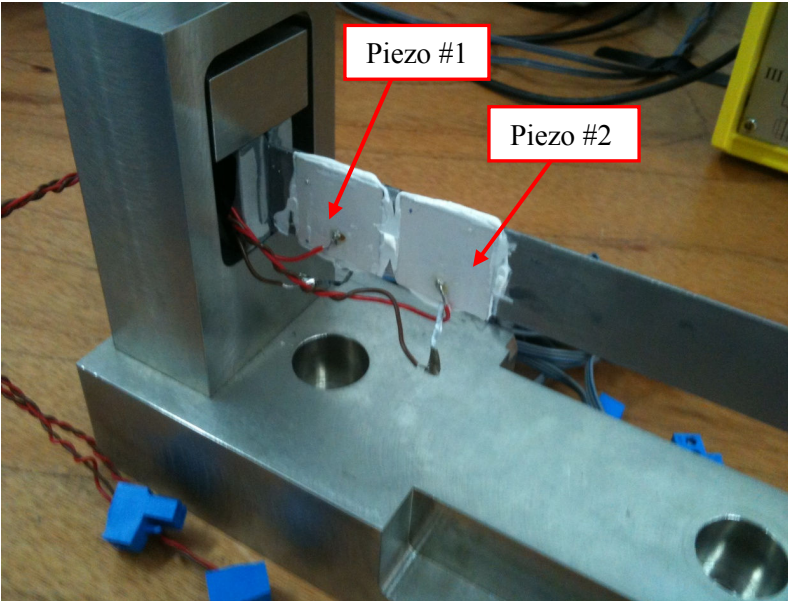


Figure 3-2. Piezoelectric patches at the root of the beam

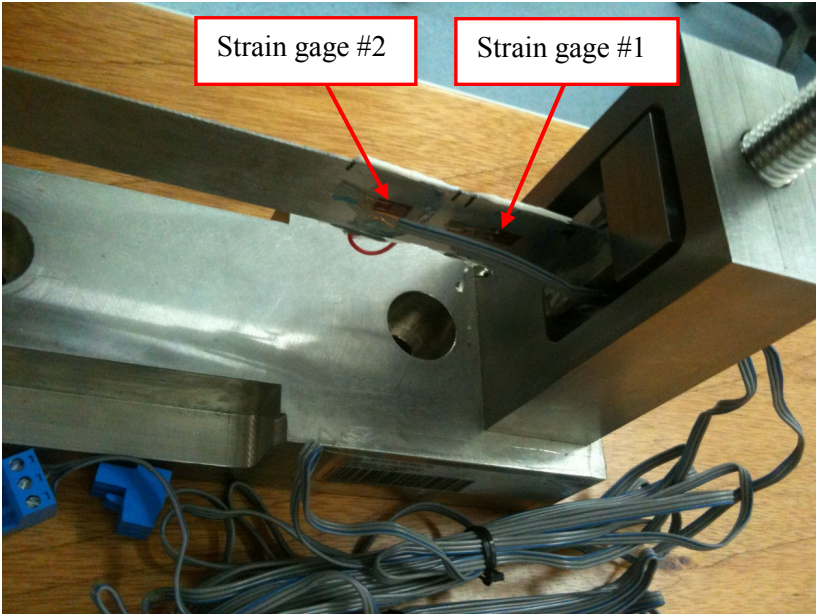


Figure 3-3. Strain gages at the opposite side of piezoelectric patches

In addition to strain gages two laser displacement sensors are also used for data acquisition of vibration of the beam. In designing an active vibration control system for the beam the suggested approach is illustrated in a scheme given in Figure 3-4.

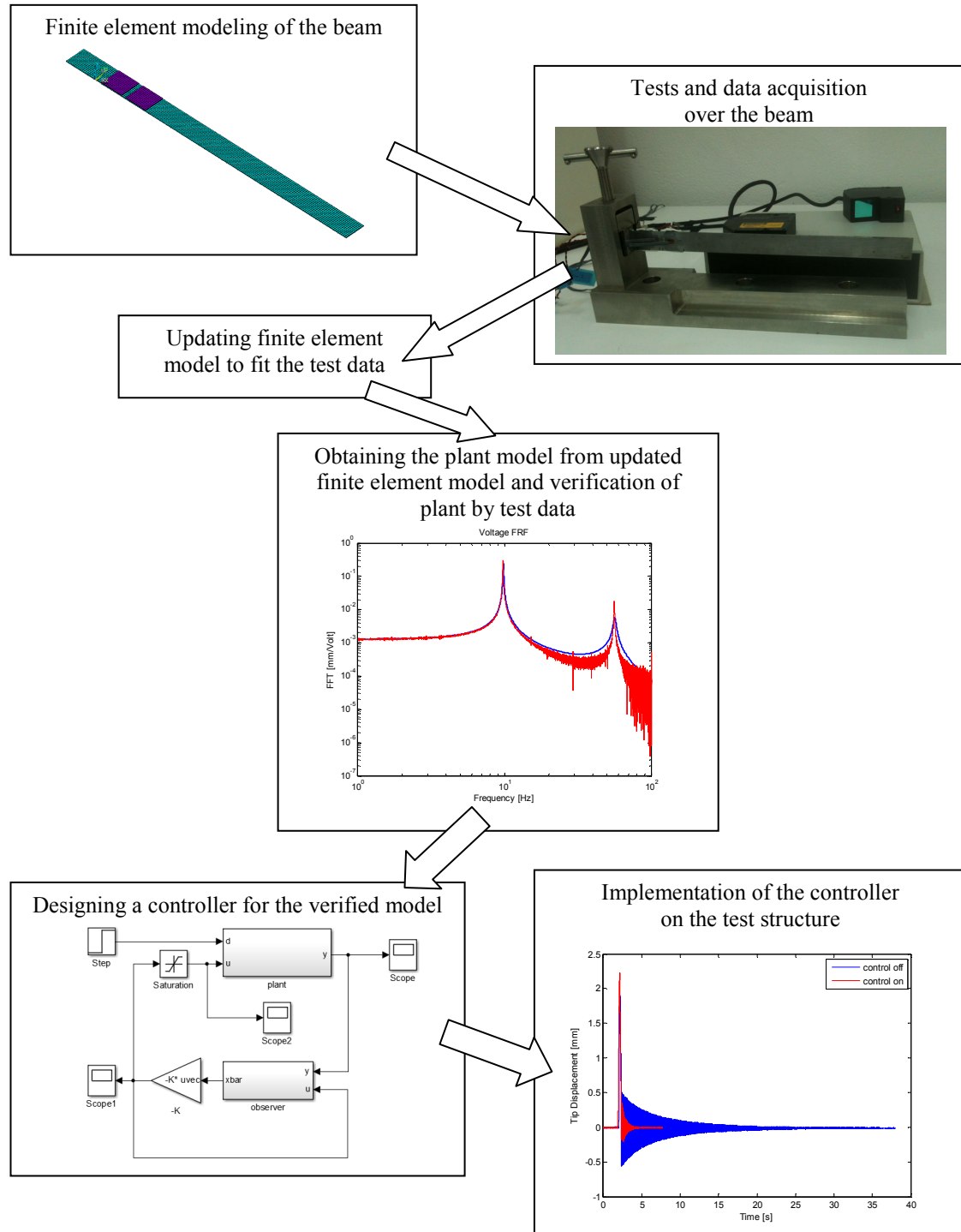


Figure 3-4. Controller design approach for beam structure

3.2 Finite Element Modeling and Analysis of the Beam

3.2.1 Beam Model

A long and thin cantilever beam model is obtained by using in ANSYS finite element software. Dimensions of the beam are 350x24x1 mm. The beam is made of steel. At the cantilevered tip of the beam two root blocks are glued to 35 mm portion of the beam, which makes the active length of the beam 315 mm. Two piezoelectric patches are glued side by side close to the cantilevered end of the beam. On the other face of the beam two strain gages are glued to the locations corresponding to the centers of each piezoelectric patches. Dimensions of the beam are given in Figure 3-5.

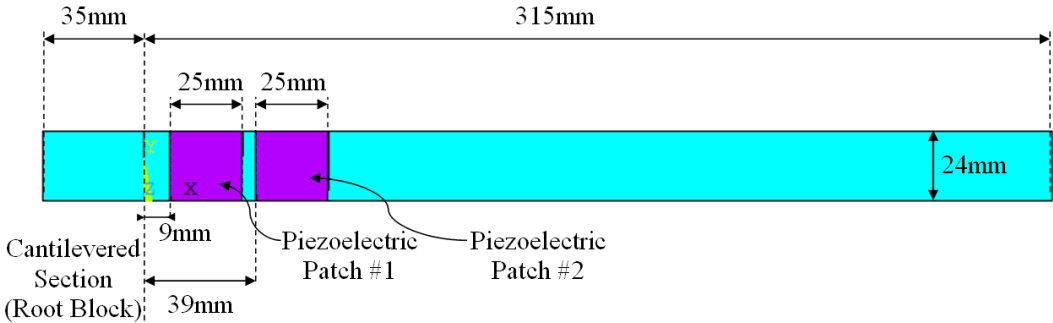


Figure 3-5. Dimensions of the beam with piezoelectric patches

On the front side of the beam, two piezoelectric patches are glued next to each other and at the back side of the beam two strain gages are glued to the locations corresponding to the centers of piezoelectric patches at the front face of the beam. Locations of the strain gages at the back side of the beam measured from the root ($x = 0$) is given in Figure 3-6.

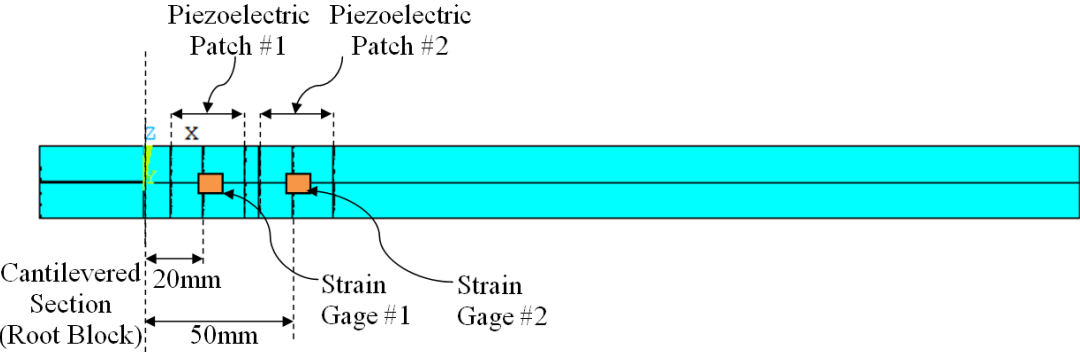


Figure 3-6. Locations of strain gages at the back side of the beam

Thickness of piezoelectric patches are 0.5 mm and the thickness of the glue layer between the beam and the piezoelectric patches is approximately 0.25 mm; which is measured by a micrometer after curing process of the glue. Thickness of the beam, glue layer and the piezoelectric patches is given in Figure 3-7.

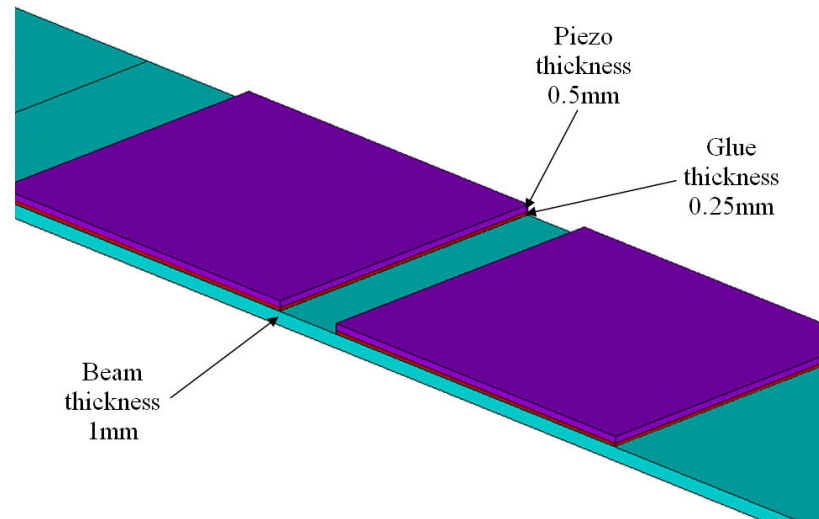


Figure 3-7. Thickness of the beam, glue layer and piezoelectric patches

Beam is secured by a clamp which presses on the top and bottom sides of the root blocks. The portion of the beam with root blocks is considered as the cantilevered portion. In ANSYS, nodes on the areas of the beam where root blocks are glued are fixed in x, y and z directions. Those nodes that are fixed in all 3 directions are showed in Figure 3-8.

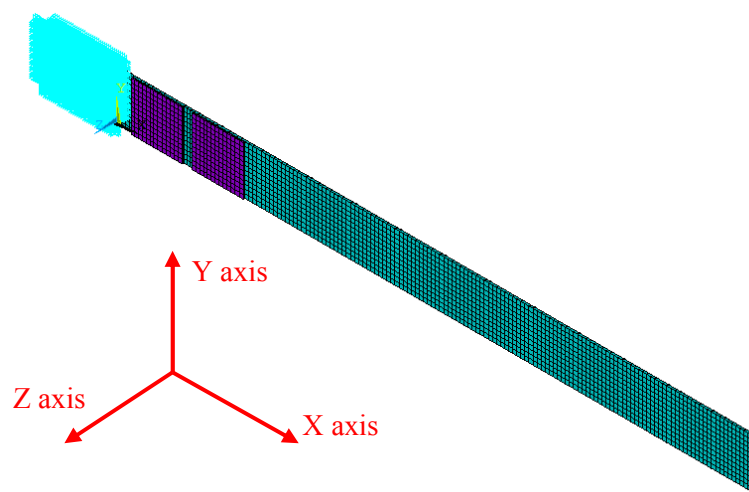


Figure 3-8. Cantilevered boundary condition modeled in ANSYS

As the axes defined on the beam, X axis is the longitudinal direction over the beam. Z axis is the axis normal to the wider surface of the beam. Piezo patches are polarized in thickness direction, which is Z axis. Y axis is the lateral direction of the beam, which is normal to the thinner surface. The defined axes are also shown in Figure 3-8.

Beam is prepared by gluing the root blocks at its fixed end and gluing the piezoelectric patches and the strain gages. Cables of strain gages and piezoelectric patches are secured by sticky tape for strain relief. The electrodes on the top side of the piezoelectric patches are connected by simply soldering. Electrode on the other side is connected to the cable by a thin connecting foil which is glued to the piezo electrode surface with a small portion of Elecolit 325 conductive epoxy at its corner. After gluing the conductive foil to the corner of the bottom electrode of piezo by conductive epoxy, the bottom electrode is covered by 3M DP 760 glue for electrical insulation. After the insulation of the bottom electrode surface, the piezoelectric patch is glued to the beam by 3M DP 760 epoxy. Thus, the beam is electrically insulated from the bottom electrode of the piezo. The bottom electrode is electrically connected by means of a thin foil. This makes each piezoelectric patch electrically independent. The beam ready to be tested is given in Figure 3-9.

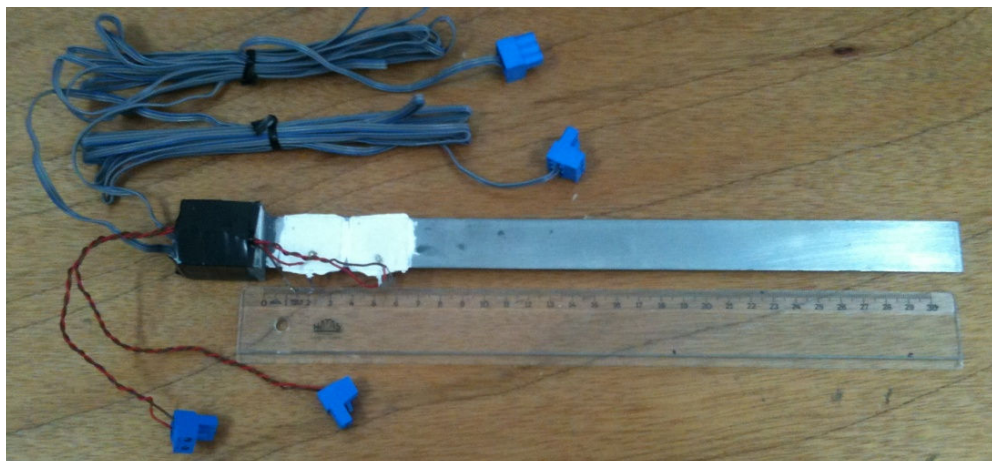


Figure 3-9. Beam with sensors and root block, ready to be held by the clamp

The beam is held by a clamping mechanism by the top and bottom surfaces of the root block. The beam on the clamp mechanism is given in Figure 3-10.

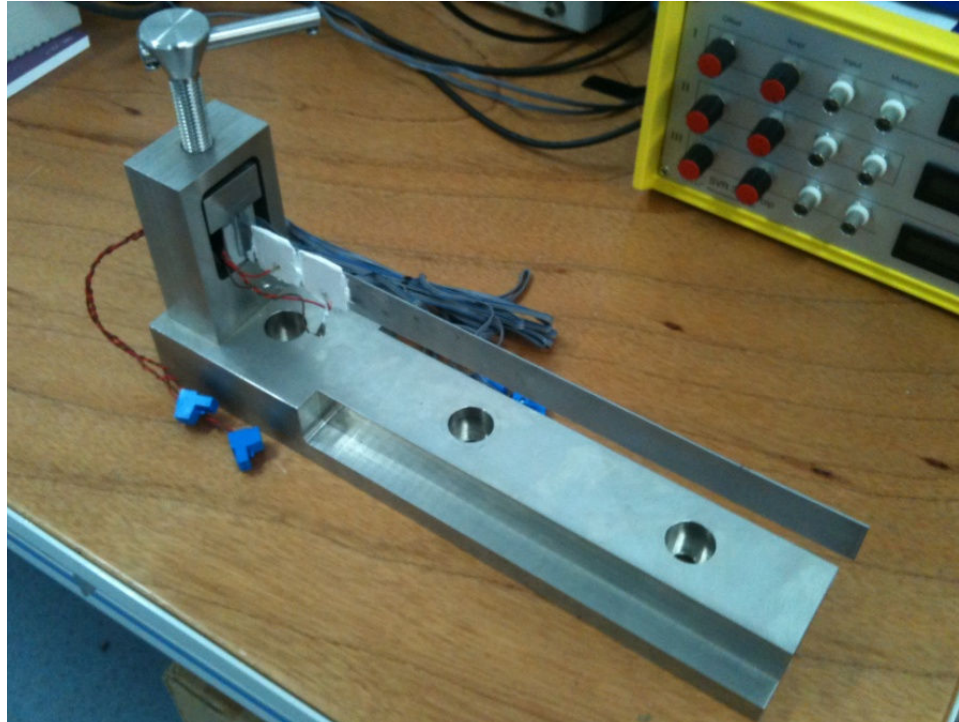


Figure 3-10. Test beam held by clamp mechanism

The material properties of the beam are given in Table 3-1. Note that the material properties of steel are taken as typical values for the beam in the first analyses.

Table 3-1. Material properties of steel

Elastic modulus	210×10^9 Pa
Poisson's ratio	0.3
Density	7.85×10^3 kg/m ³

Piezoelectric patch used on the beam is made of APC 850 material and its properties are given in Table 3-2 below and also given in Appendix B.

Table 3-2. Material properties of APC 850

Density	7.6×10^3 kg/m ³
Piezoelectric constants	
d_{31}	-1.75×10^{-10} m/V
d_{33}	4.00×10^{-10} m/V
d_{15}	5.90×10^{-10} m/V

Table 3-2. Material properties of APC 850 (Continued)

Elastic constants	
S_{11}^E	$1.64 \times 10^{-11} \text{ m}^2/\text{N}$
S_{33}^E	$1.88 \times 10^{-11} \text{ m}^2/\text{N}$
S_{12}^E	$-5.74 \times 10^{-12} \text{ m}^2/\text{N}$
S_{13}^E	$-7.22 \times 10^{-12} \text{ m}^2/\text{N}$
S_{44}^E	$4.75 \times 10^{-11} \text{ m}^2/\text{N}$
S_{66}^E	$4.43 \times 10^{-11} \text{ m}^2/\text{N}$
Dielectric constants	
K_{11}^T	1900
K_{33}^T	1900
ϵ_0	$8.85 \times 10^{-12} \text{ F/m}$

The glue layer between the beam and the piezoelectric patch has a thickness of 0.25 mm and this layer is also modeled. The glue used is 3M DP 760 epoxy. Its material properties are given in Table 3-3 and also given in Appendix B.

Table 3-3. Material properties of epoxy layer

Elastic modulus	$6 \times 10^9 \text{ Pa}$
Poisson's ratio	0.35
Density	$1.2 \times 10^3 \text{ kg/m}^3$

After defining the material properties, element types to be used are selected using ANSYS APDL. For piezoelectric materials SOLID 226 elements are used, while SOLID 186 elements are used for the beam and the epoxy layer. A sweep mesh is generated by APDL using a generic element size of twice the thickness of the beam. The mesh over the beam has a total of 2760 elements and 18709 nodes.

3.2.2 Static Analysis for Applied Voltage Load

Cantilevered beam, piezoelectric patches and the glue layer between them are modeled in ANSYS using ANSYS Parametric Design Language (APDL). A static analysis is done to find out the static deflection of beam upon applying electric potential to the electrodes of piezoelectric patches. A voltage load of 70V is applied to the piezoelectric patch #1 and piezoelectric patch #2 in two separate analyses and the deflection of beam is calculated. The result of a static analysis in which 70V is applied to the first piezo and 0V is applied to the second one is given in terms of the deformation of the beam in Z direction in millimeters in Figure 3-11. Note that the deformation is exaggerated for better understanding. In this analysis, the maximum deflection of the beam is calculated as 0.0936 mm.

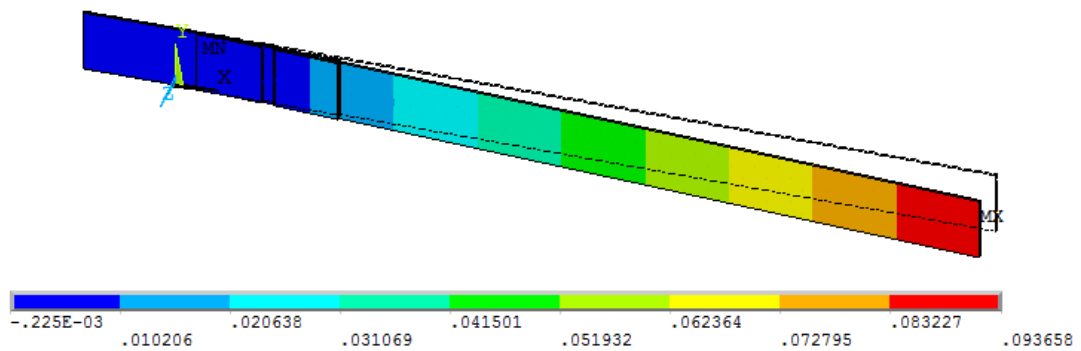


Figure 3-11. Deformation of beam in Z direction in mm for 70V applied at piezo #1

Strain of the beam on the side where piezoelectric patches are not used is given in Figure 3-12. Note that the strain on the beam at the back region of piezoelectric patch#1 is noticeable. It corresponds to the strain that will be read by strain gage #1. From analysis results strain at the node corresponding to strain gage #1 is 7.278 microstrain and strain at node corresponding to strain gage #2 is -0.513 microstrain.

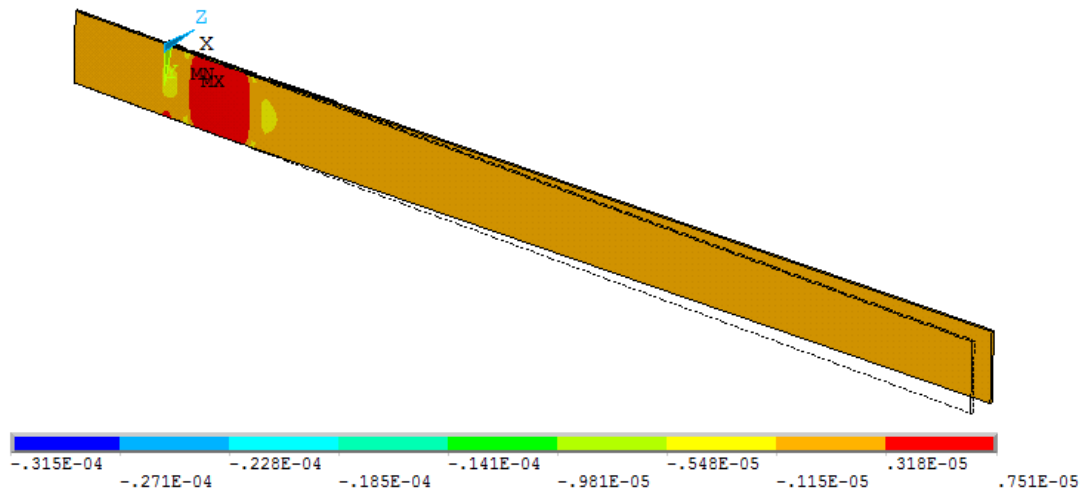


Figure 3-12. Strain of beam in X direction in mm for 70V applied at piezo #1

In the second analysis 0V is applied to the piezo #1 and 70V is applied to piezo #2. The resulting deformation of the beam in Z direction in millimeters is given in Figure 3-13. The maximum tip deflection at this case is 0.0792 mm.

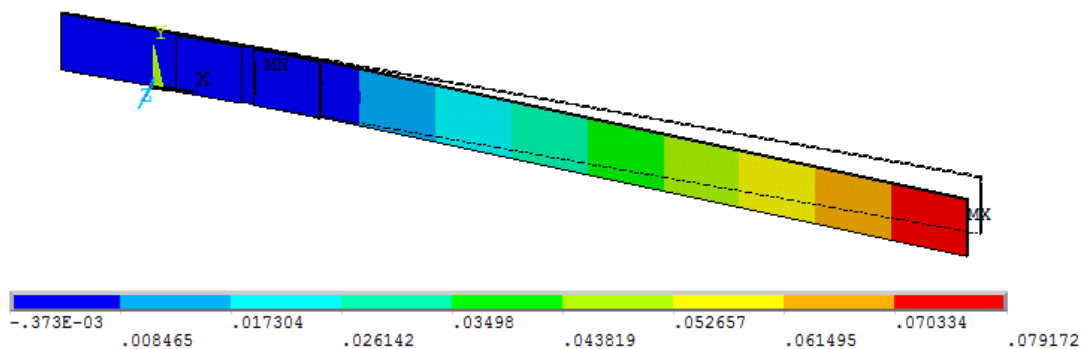


Figure 3-13. Deformation of beam in Z direction in mm for 70V applied at piezo #2

Strain on the beam in X direction for this case is also computed. Strain of the beam on its side without piezo patches is given in Figure 3-14. It is seen from the figure that the portion of the beam under piezo patch#2 which is loaded is the region with the largest strain as expected. In this case the strain on the node of strain gage #1 is -0.357 microstrain and strain on the node of strain gage #2 is 7.131 microstrain.

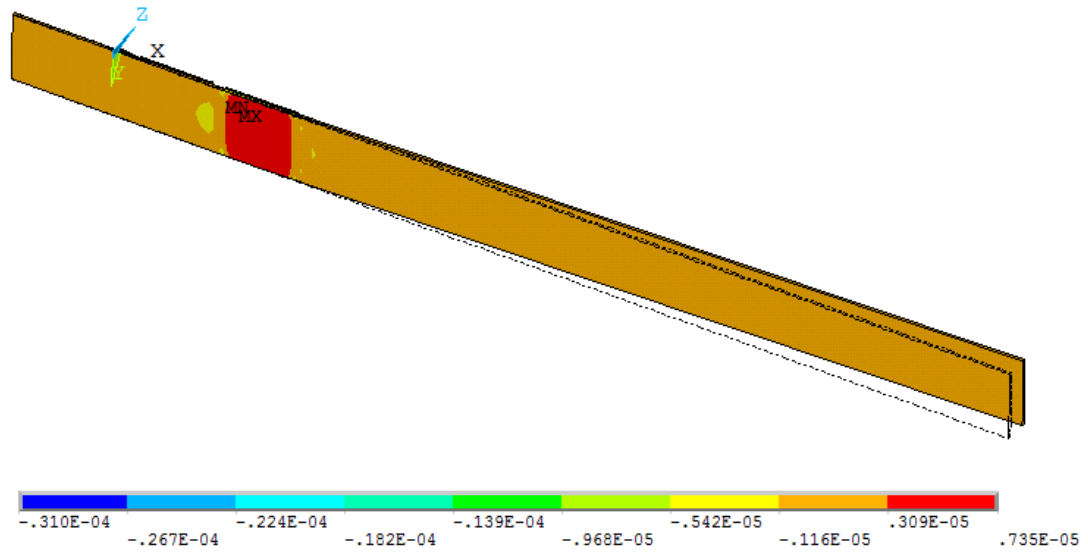


Figure 3-14. Strain of beam in X direction in mm for 70V applied at piezo #2

Piezoelectric patches are glued only at one side of the beam and there is a glue layer between the patches and the beam. This can make the deflection of the beam different for applications of positive and negative voltage loads. However upon making the analyses for the loads of 70 V and -70V it is seen that the difference is small. In the third analysis a -70V load is applied to piezo #1 and the resulting deflection is given in Figure 3-15. The maximum tip deflection at this case is -0.0936 mm.

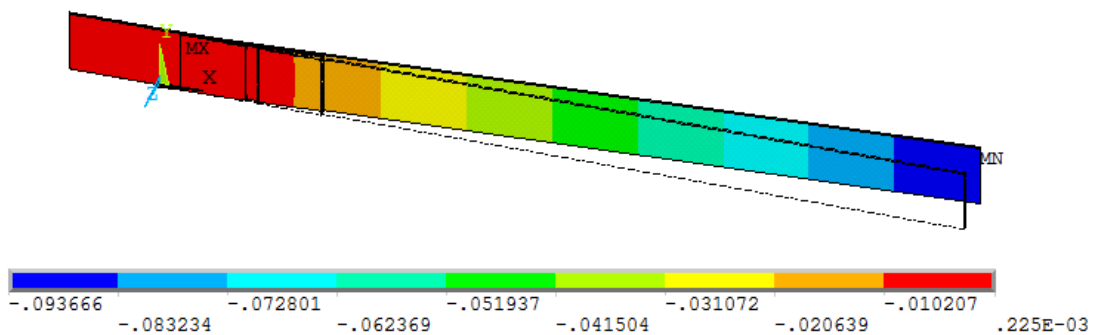


Figure 3-15. Deformation of beam in Z direction in mm for -70V applied at piezo #1

In the case of -70V at piezo patch #1, the resulting strain at the face of beam without piezo patches is given in Figure 3-16. Strain values at the nodes of strain gage #1 and strain gage #2 are -7.273 microstrain and 0.513 microstrain, respectively.

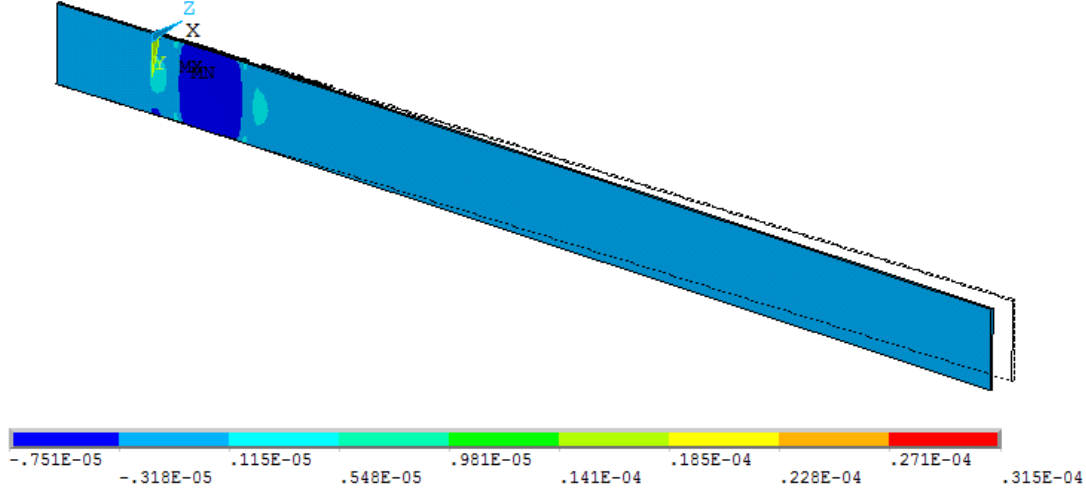


Figure 3-16. Strain of beam in X direction in mm for -70V applied at piezo #1

Similar to the previous case, a -70V load is applied to the second piezo patch and the deformed shape is given in Figure 3-17. The maximum tip deflection is -0.0792 mm for this case.

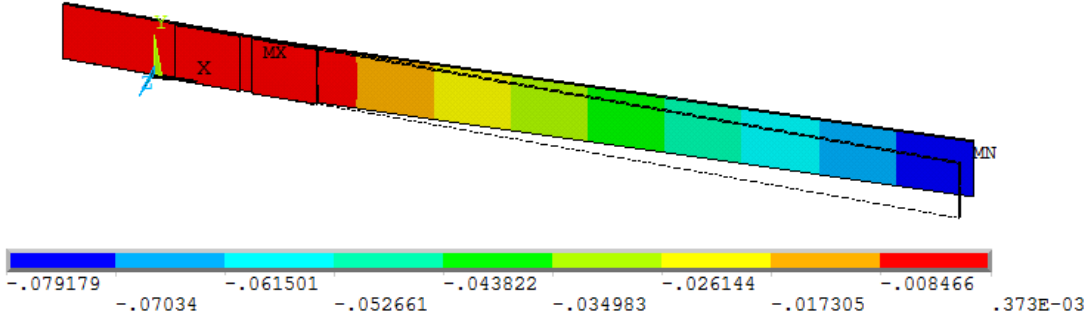


Figure 3-17. Deformation of beam in Z direction in mm for -70V applied at piezo #2

Strain of the beam on its side without piezoelectric patches for the case of -70V applied ap piezo patch#2 is given in Figure 3-18. The strain at the node of strain gage

#1 is 0.357 microstrain and the strain at the node of strain gage #2 is -7.126 microstrain.

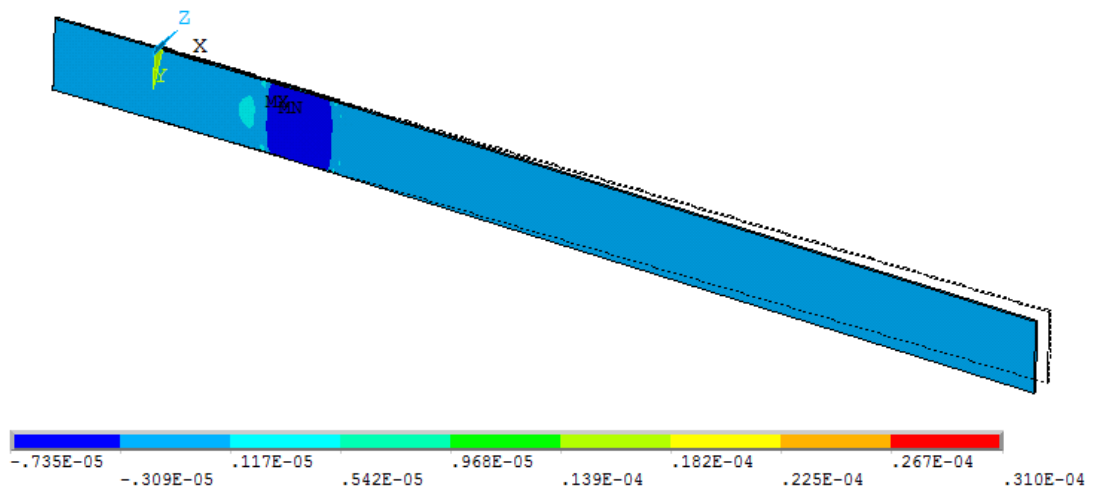


Figure 3-18. Strain of beam in X direction in mm for -70V applied at piezo #2

It would be interesting to see the deformation of the beam for applying positive voltage load on one piezo and negative voltage load on the other. For this purpose, two analyses are done; in the first one 70V is applied to piezo patch #1 and -70V is applied to piezo patch #2. The result of this analysis is given in Figure 3-19. Note that each piezo bend the beam in different directions. The deformation of the beam is given in Figure 3-19 in an exaggerated manner for better understanding. The maximum tip deflection is 0.0145 mm, which is much less than the case that 70V is applied to piezo patch #1 and 0V is applied to piezo patch #2.

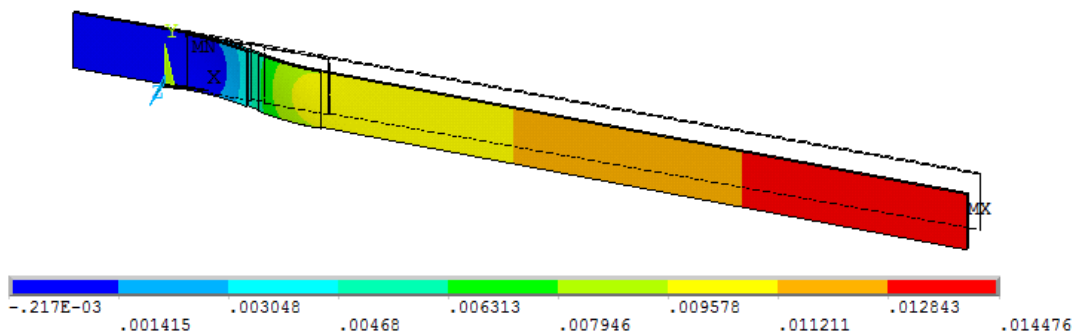


Figure 3-19. Deformation of beam in Z direction in mm for 70V applied at piezo#1 and -70V applied at piezo #2

In the case of 70V applied on piezo patch#1 and -70V applied on piezo patch#2, the strain distribution of the beam on its face without piezo patches is given in Figure 3-20. The strain on the node of strain gage #1 is 7.635 microstrain and -7.639 microstrain on the node of strain gage #2. Note that strain on the electrodes of piezo patches are higher in this case.

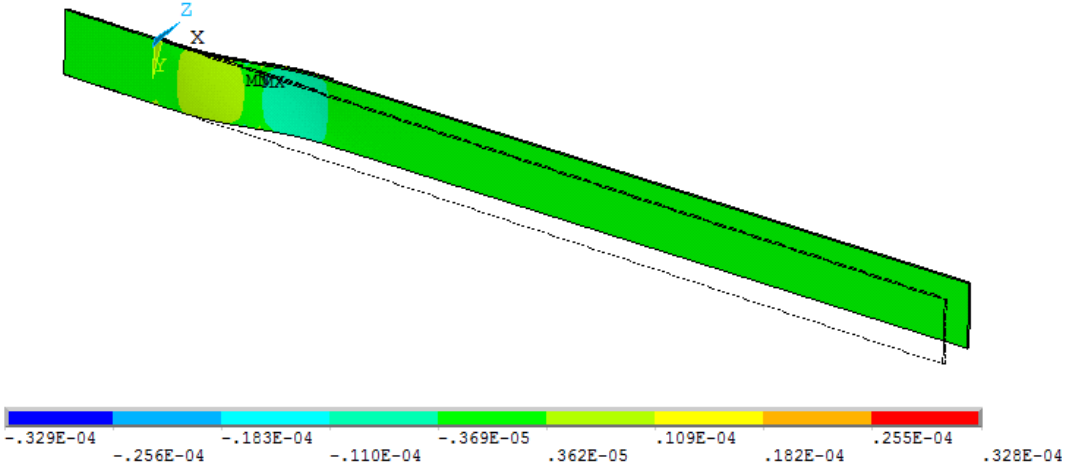


Figure 3-20. Strain of beam in X direction in mm for 70V applied at piezo #1 and -70V applied at piezo #2

As another analysis -70V is applied on piezo patch #1 and 70V is applied on piezo patch #2. The calculated deformation of the beam is given in Figure 3-21. In this the case maximum tip deflection is -0.0145mm.

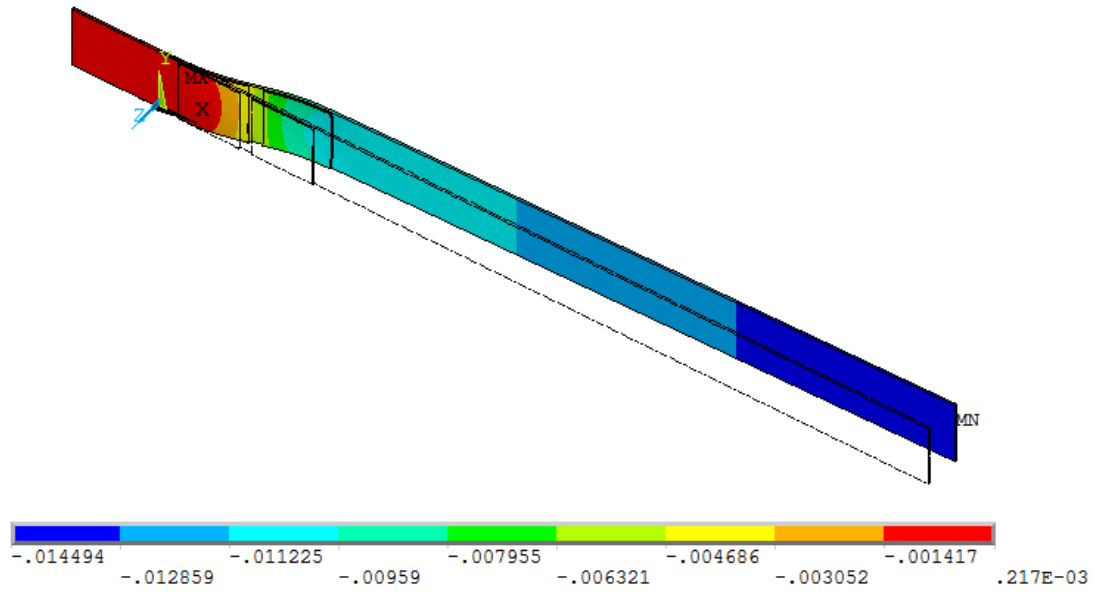


Figure 3-21. Deformation of beam in Z direction in mm for -70V applied at piezo #1 and 70V applied at piezo #2

As a result of this analysis, the strain of the beam on its face without piezo patches are given in Figure 3-22. The strain on the node of strain gage #1 is -7.630 microstrain and the strain on the node of strain gage #2 is 7.644 microstrain. In the case of loading both piezoelectric patches with opposite voltages, like in this case and in the previous one, the strain values are higher than the case of loading single patch at once.

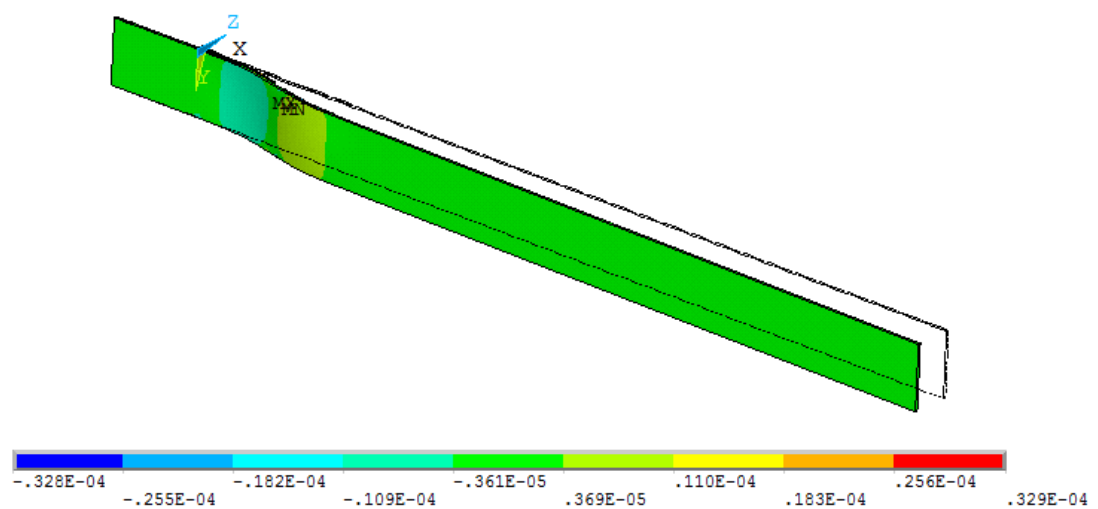


Figure 3-22. Strain of beam in X direction in mm for -70V applied at piezo #1 and 70V applied at piezo #2

A total number of six static analyses are done on the beam, for six different cases. Applied voltage loads on each piezo and resulting tip deflections are summarized in Table 3-4.

Table 3-4. Summary of static analysis results

Analysis number	Load on patch#1	Load on patch#2	Tip deflection	Strain at SG#1 location	Strain at SG#2 location
1	70V	0V	0.0936mm	7.278 μs	-0.513 μs
2	0V	70V	0.0792mm	-0.357 μs	7.131 μs
3	-70V	0V	-0.0936mm	-7.273 μs	0.513 μs
4	0V	-70V	-0.0792mm	0.357 μs	-7.126 μs
5	70V	-70V	0.0145mm	7.635 μs	-7.639 μs
6	-70V	70V	-0.0145mm	-7.630 μs	7.644 μs

3.2.3 Modal Analysis

Modal analysis is done to obtain natural frequencies and mode shapes of the beam with piezoelectric patches. First five modes are obtained and the results are summarized in Table 3-5.

Table 3-5. Results of modal analysis

Mode Number	Definition	Natural Frequency (Hz)
1	1 st bending	9.865
2	2 nd bending	56.650
3	3 rd bending	150.96
4	1 st lateral bending	206.14
5	1 st torsion	236.29

The mode shapes of the beam are given in Figure 3-23, Figure 3-24, Figure 3-25, Figure 3-26, and Figure 3-27.

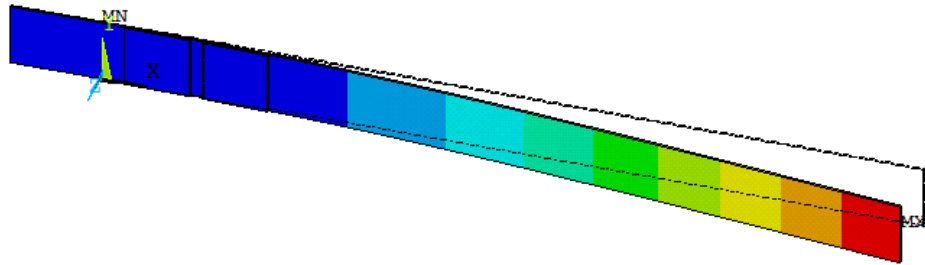


Figure 3-23. 1st bending mode shape, natural frequency 9.865 Hz

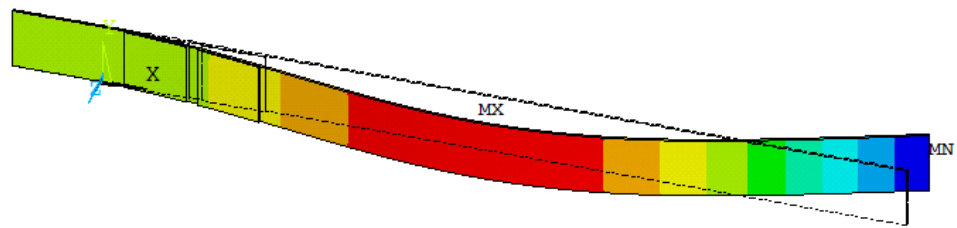


Figure 3-24. 2nd bending mode shape, natural frequency 56.65 Hz

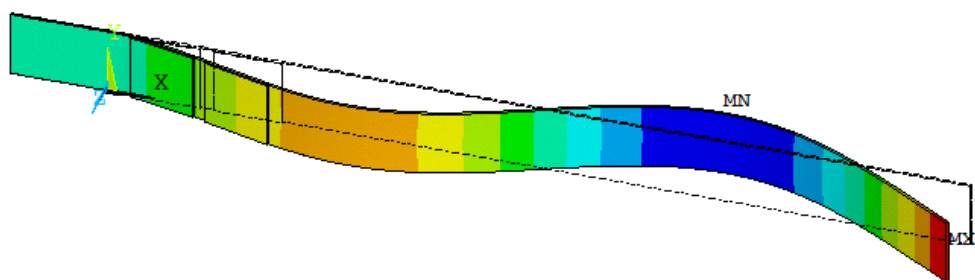


Figure 3-25. 3rd bending mode shape, natural frequency 150.96 Hz

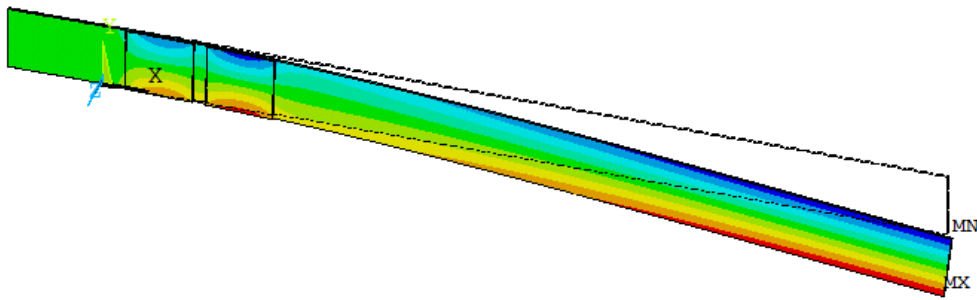


Figure 3-26. 1st lateral bending mode shape, natural frequency 206.14 Hz

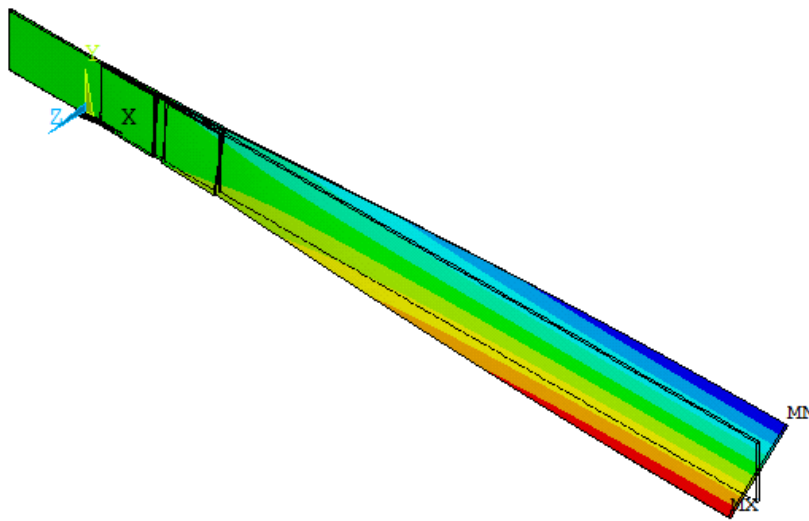


Figure 3-27. 1st torsion mode shape, natural frequency 236.29 Hz

3.2.4 Mathematical Model Using State Space Matrices

In modeling vibratory systems, natural frequencies, mode shapes and damping ratios are the key parameters. By using modal parameters, the mathematical models that show the behavior of the system in frequency domain are easily obtained. Unfortunately it is impossible to know the exact damping behavior of a system without testing. In the first step of modeling the system with analysis, damping behavior will be guessed. Since the model does not have any localized damping elements such as dashpot dampers or mounting block etc., proportional damping model fits to the purpose.

As a first estimate of the damping of the beam, damping ratio will be assumed as $\zeta = 0.001$. Later this value will be updated to fit the calculated results to the test data. Other properties of the structure is kept unchanged.

To obtain a mathematical model of the system, state space matrices are needed. ANSYS SPMWRITE command is a novel way to perform this task [53]. In state space model of the beam as a vibratory system, the voltage applied to the piezoelectric patches is considered as the input to the system. The modes of the system are considered as states and the output is considered as the tip displacement. Modeling of a vibratory system by state space is explained in Chapter 2.3.

By using SPMWRITE command, A,B,C and D matrices are easily obtained. By these matrices transfer functions between the inputs and outputs could be determined. ANSYS APDL codes required for obtaining the system matrices is given in Appendix C.

Once A,B,C and D matrices are obtained, the system model will be complete, then the frequency response and time response of the system to known excitations can be obtained in a very fast way. However, the finite element model contains all the modes of the system, but the state space model contains only the modes of interest which are selected by user. Therefore the state space model is a truncated model of the finite element model. Finite element model contains information about the motion of all the nodes of the system, however its computation time is huge. The state space model considers the motion of the selected dof's only, so it gives instant response in terms of computational time, and it is very suitable for controller design studies. However it is a truncated model and it needs to be verified by means of transient analyses and harmonic analyses done on the full model in ANSYS. Results of full harmonic analysis and full transient analysis are compared with the frequency response and step response of the reduced state space model.

In the harmonic analysis a voltage load of 1V is applied on piezoelectric patch #1 and the results of tip displacement are obtained over the frequency range of 0 to 165

Hz. For the peaks where the modes of the system are located, the frequency resolution is kept much more finer than the rest of the frequency range. Then the results of the harmonic analysis is compared with the frequency response of the state space model. As shown in Figure 3-28, the two models are quite coherent for the first two modes.

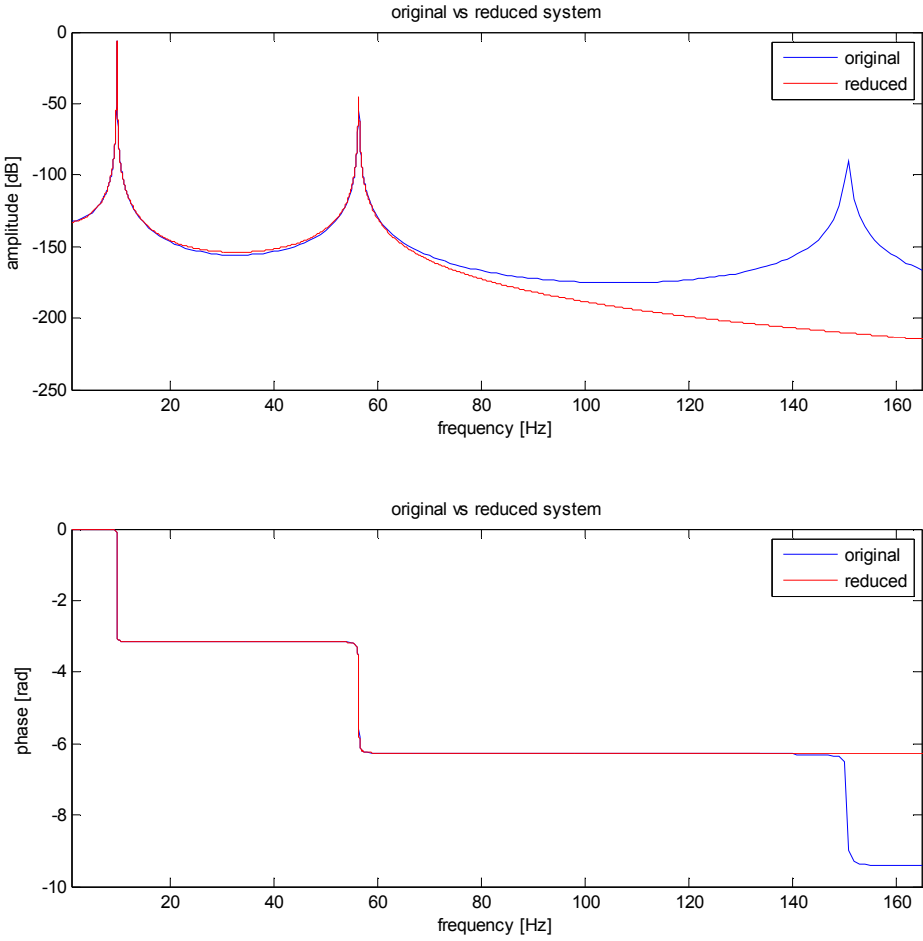


Figure 3-28. Comparison of full harmonic analysis and frequency response of state space model

Comparison of full and reduced model in the frequency domain shows the coherence of the models for the first two modes. However when truncating the dynamic model, it is assumed that the third mode of the structure has no importance when compared to the first two modes. Only way of testing this assumption is

making analysis in time domain. Therefore a transient analysis will be done in ANSYS and its results will be compared to the results of step response of the state space model which will be computed from Simulink.

In the beginning of modeling, a constant damping ratio is assumed as the damping behavior of the system. As a damping ratio an initial value of $\zeta = 0.001$ is taken. In harmonic analysis this damping behavior can be used in the finite element model by DMPRAT command. However this command is not available for the transient analysis. Instead to that Rayleigh damping model should be utilized. This requires a conversion between constant damping ratio and Rayleigh damping [53].

In Rayleigh damping, the damping of a structure is modeled by two coefficient, α and β . In this proportional model the damping matrix of a structure is constructed by its mass and stiffness matrices as follows:

$$\mathbf{C} = \alpha\mathbf{M} + \beta\mathbf{K} \quad (3.1)$$

In the calculation of damping matrix, α is the coefficient of the proportion of the mass matrix and β is the coefficient of the proportion of the stiffness matrix. The viscous damping ratio ζ can be expressed in terms of α and β as a function of frequency which is:

$$\zeta(\omega) = \frac{\alpha}{2\omega} + \frac{\beta\omega}{2} \quad (3.2)$$

The graphical representation of this equation is given in Figure 3-29 [54]. α damping is effective at low frequencies, whereas β damping is more effective at high frequencies. At mid frequencies both α and β damping are effective and the damping in the structure is summation of them.

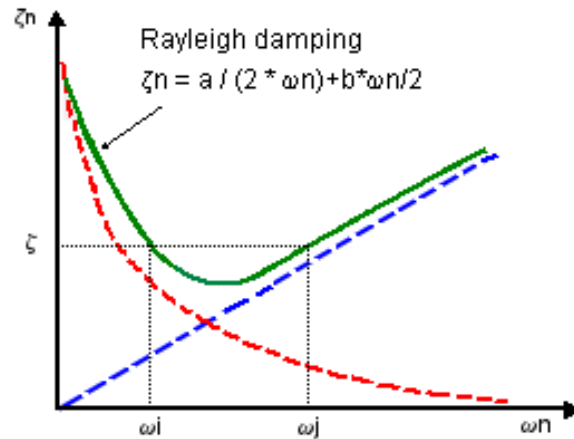


Figure 3-29. Relationship between viscous damping and Rayleigh damping [54]

In a vibratory system the most important frequencies are the natural frequencies, so it is very important to know the damping behavior of the system at its resonant frequencies. Here a constant viscous damping behavior is being converted to α and β damping, since viscous type of damping is not supported by ANSYS transient analysis. Damping curves cover a wide frequency band, however since the most important modes of the system are the first two modes, it is a good approach to calculate α and β values at the natural frequencies of first two modes. To compute corresponding α and β values for a viscous damping ratio of $\zeta = 0.001$, Equation (3.2) will be used at frequencies $f_1 = 9.865$ Hz and $f_2 = 56.65$ Hz which correspond to $\omega_1 = 62$ rad/sec and $\omega_2 = 356$ rad/sec. For two natural frequencies there will be two equations for unknowns α and β .

$$0.001 = \frac{\alpha}{2 * 62} + \frac{\beta * 62}{2} \quad (3.3)$$

$$0.001 = \frac{\alpha}{2 * 356} + \frac{\beta * 356}{2} \quad (3.4)$$

If these two equations are solved simultaneously, the values of α and β are found as 0.1056 and 4.78×10^{-6} respectively. Now a transient analysis can be done with this values in ANSYS.

In the transient analysis a 70V load is applied on the piezo patch #1 on the beam and then the simulation is solved for two time steps where the dynamic effects are turned off. By this steps, the beam has come to steady state. Then at the next time step the voltage load is suddenly released and the dynamic effects are turned on. The step size is taken as 0.001 s and the simulation is run for 5 seconds. The tip displacement is taken as the output of the analysis. The comparison between 5 seconds of transient analysis in ANSYS and the step response of the reduced model computed in Simulink are drawn side by side in Figure 3-30, Figure 3-31 and Figure 3-32. The last two figures are closed versions of the first one.

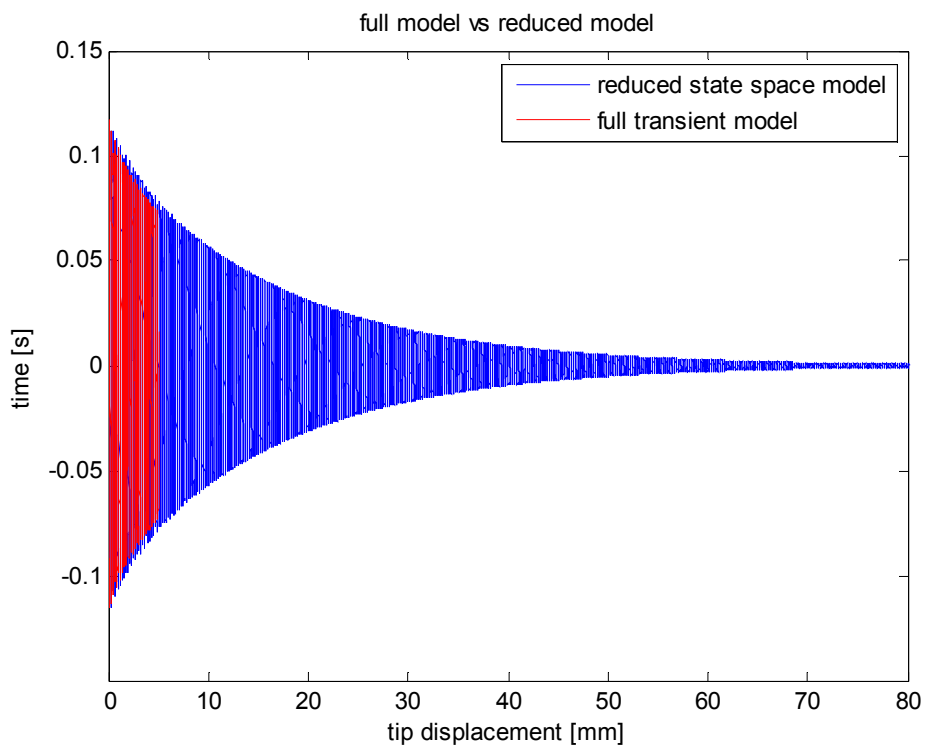


Figure 3-30. ANSYS transient analysis results vs Simulink result

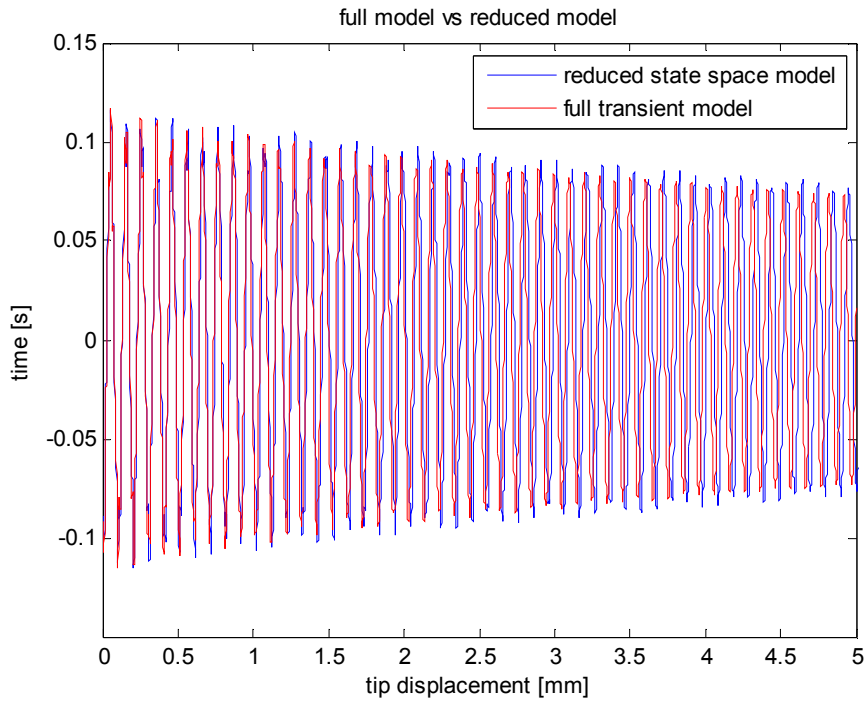


Figure 3-31. Comparison of full and reduced model for first 5 seconds

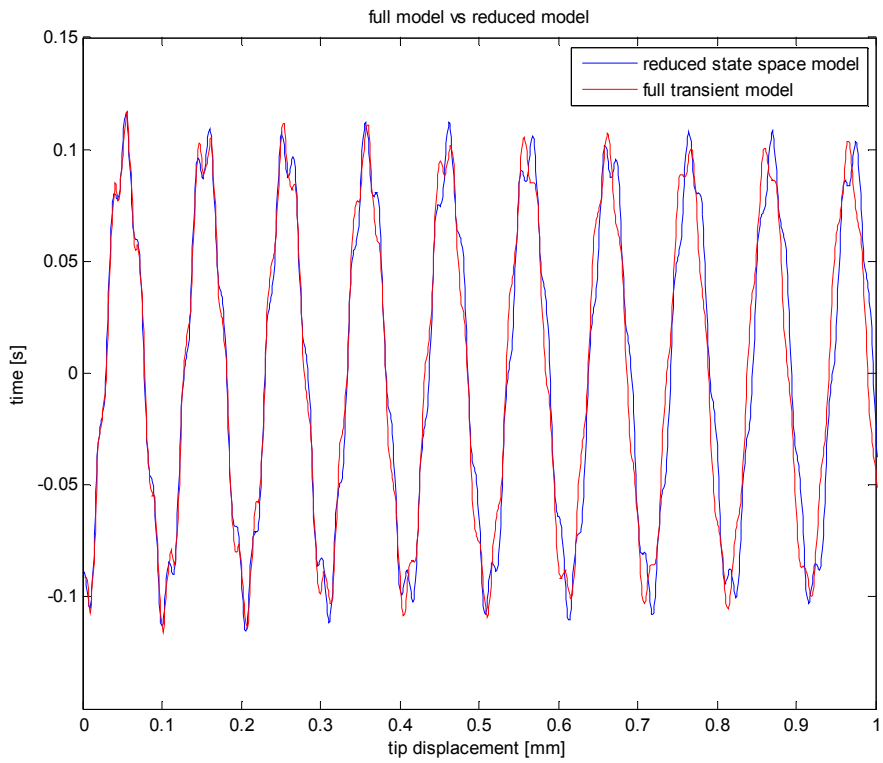


Figure 3-32. Comparison of full and reduced model for the first second of simulation

Examining the results of transient analysis and the Simulink results for the step response to the state space model, it can be seen that the state space model represents the full model quite accurately. So instead of using time consuming full finite element model, the characteristics of the system could be determined by the state space matrices obtained from ANSYS and a fast model can be generated in Simulink and used instead of the full model.

It can be concluded from the above comparisons that the state space model computed from ANSYS using the first two modes by means of SPMWRITE command is a fast and accurate model to be used in the controller design studies.

Now this model will be updated so that the theoretical results will fit to the test data. Thereafter a controller will be designed for the updated model.

3.3 Test and Data Acquisition Over the Beam

3.3.1 Test Setup

The test setup is composed of the test structure, laser displacement sensor heads and controllers, strain gage conditioning units, piezoelectric voltage amplifiers, data acquisition (DAQ) card and input/output connection blocks with xPC target and host computers.

In data acquisition phase of the study, MATLAB xPC target is used. In the xPC target configuration, there is a host PC and a target PC. Host and target PC are interconnected via TCP/IP communication protocol. Host PC is the interface for the user. Target PC is the PC which communicates with the DAQ card. The DAQ card is National Instruments NI PCI 6289. This card is used in data acquisition and sending the output signals generated by xPC target to drive the piezoelectric patches via piezoelectric voltage amplifiers. A schematic view of the test setup is given in Figure 3-33. The test setup for the beam is installed in the Vibration Laboratory of Department of Mechanical Engineering in METU. Photos of the test setup are given in Figure 3-34 and Figure 3-35.

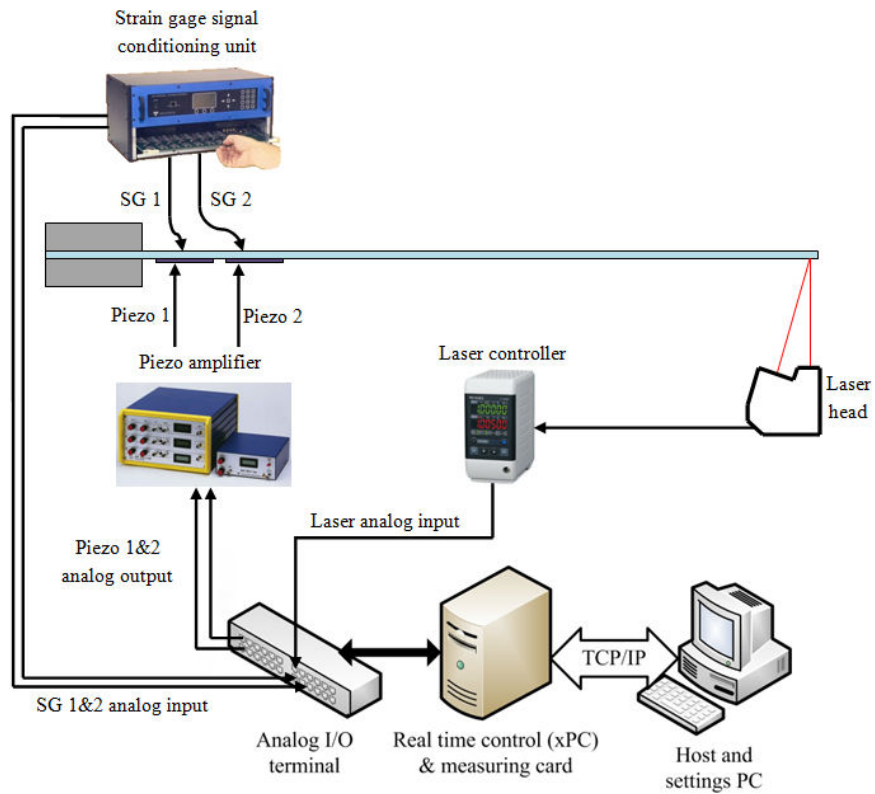


Figure 3-33. Test setup scheme

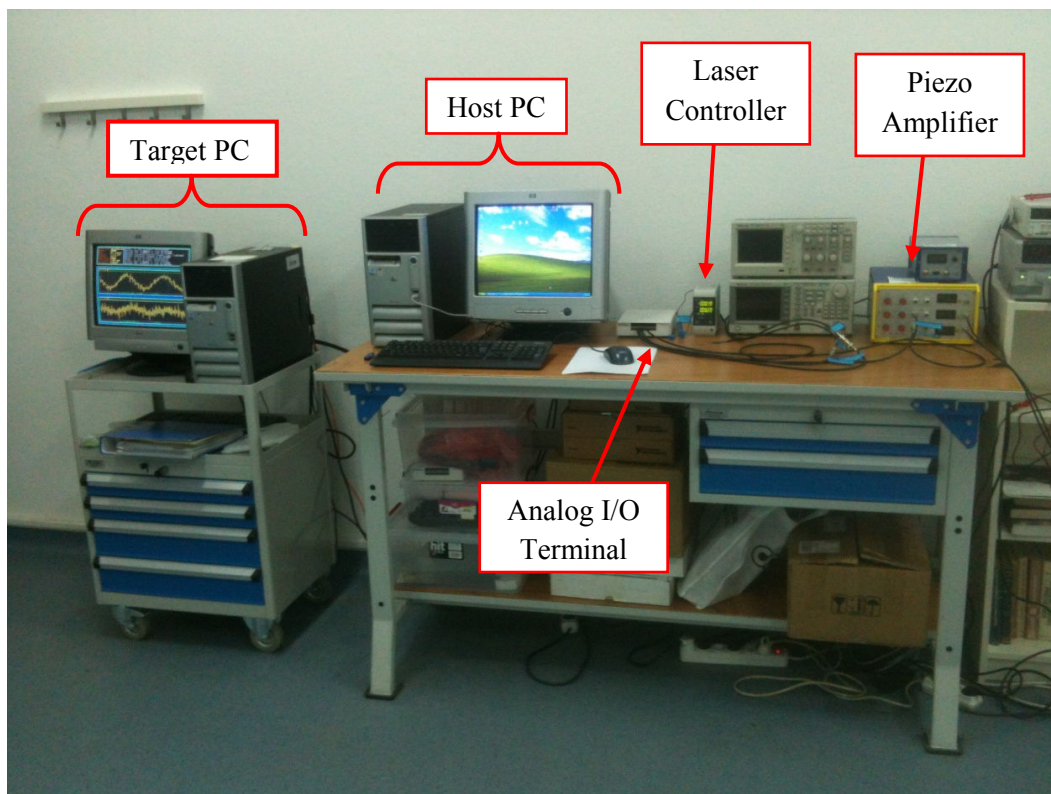


Figure 3-34. A photo of the test equipments in METU

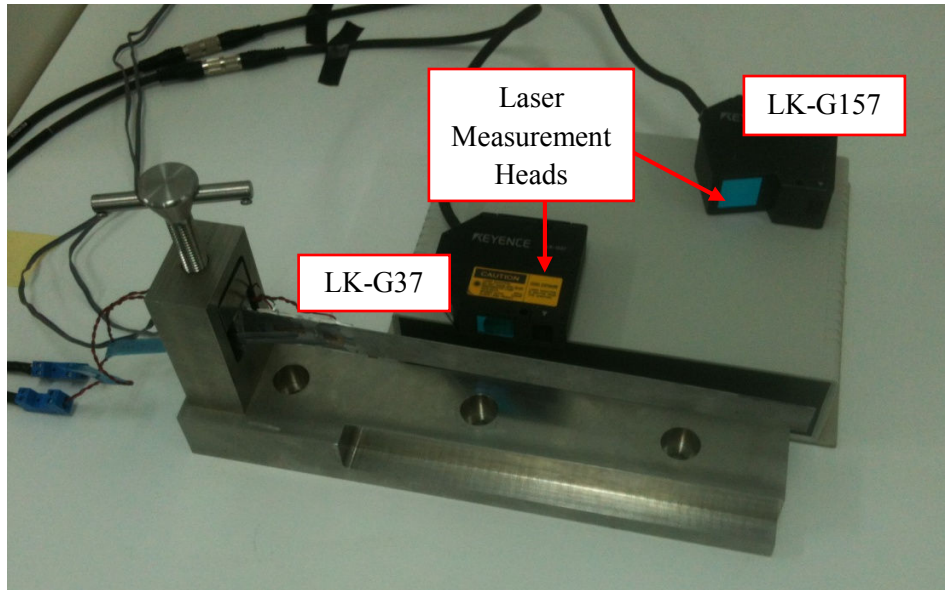


Figure 3-35. Test beam and laser displacement sensor heads

Keyence LK-G37 and LK-G157 type laser measurement heads are positioned for the ideal measurement distance to the test beam. The measurement signal output is taken in voltage terms from the Keyence LK-G3001V laser controller unit and connected to the analog input for the target PC. Photos of Keyence products are given in Figure 3-36.



Figure 3-36. Keyence laser displacement sensor and controller unit

For the strain gage measurements two separate quarter bridge configurations are used for two strain gages. Details of quarter bridge measurement and coefficients of conversion are given in Appendix A. The signal conditioning unit used in converting bridge measurement to volts is Micro Measurement's Model A2 and its photo is given in Figure 3-37.



Figure 3-37. Micro Measurement Model A2 Strain gage conditioning unit

The output signal is generated by the PCI card mounted on the target PC. Output signal is generated at the output port of the connecting block, however it is limited from -5V to +5V since it is generated by the card. Inherently this level of voltage is not enough to drive the piezoelectric patch actuators. Actuators require higher levels of voltage for significant levels of motion. For this purpose piezoelectric voltage amplifiers are required. The output port of the xPC signal is fed to the piezo amplifier and the output of the amplifier is connected to the electrodes of piezoelectric patch actuators. By the amplifier voltage signal from the output of the xPC target system is amplified to the meaningful levels for the piezoelectric actuators.

The piezoelectric voltage amplifier used is American Piezo Company's (APC) model SVR 350-bip bipolar voltage amplifier. This amplifier has three independent channels. The input voltage for this amplifier should be between -5V and +5V. The amplifier has the ability to increase the level of voltage 70 times, so its maximum

output can be between -350 V and +350 V. In this study to prevent any potential damage the input voltages for the piezoelectric patches are limited to 70V to be on the safe side. The amplifier has offset and gain knobs. The offset is set to zero, the gain is set to maximum and the input signal to the amplifier is limited to $\pm 1V$ in Simulink by a saturation block. Thus the operational voltages for the piezoelectric actuators is limited to 70V. A photo of SVR 350 bip amplifier is given in Figure 3-38.



Figure 3-38. APC SVR 350-bip piezoelectric voltage amplifier

The amplifier has also a monitor channel. This channel generates a signal which is 1/1000 of the voltage applied to the actuator. The monitor channel can also be used as a input for the DAQ card. Since it is 1/1000 of the applied voltage load to the actuator, it is safe to connect the monitor channel to the analog input port.

The duty of target PC in the system is to contain the NI's PCI card. PCI card is mounted inside the target PC. The connection block which serves as the analog input/output port is directly connected to the PCI card. All the output of the sensor's control units are connected to the analog input ports of the connection block.

Target PC is connected to the host PC via ethernet connection. The target PC is slave and the Host PC is the master. User interfaces with the host PC, and target PC realizes the data acquisition and control actions. In the target PC, only the MATLAB's xPC target software runs and no other operating system is required. However Windows operating system runs on the host PC. MATLAB and Simulink are installed on the host PC and the communication of target and the host are done by MATLAB and Simulink. A Simulink model can be operated by host PC after building it properly for the target PC. This is done by converting Simulink blocks to C codes by "incremental build" action in Simulink.

Communication of Simulink model and the input and output of the xPC target system is done by PCI card block in Simulink. These blocks serve as the gate between the real analog system and the digital controller in the Simulink environment. Input for the real system, which is the voltage input to the piezo amplifiers, is the output for the controller and the output of the real system, which is the output of the laser displacement sensor, is an input to the controller in Simulink environment. The digital to analog and analog to digital converter blocks for the PCI card are shown in Figure 3-39. These blocks carry out sampling of analog input signals and converting the digital output of the controller to analog signal to drive the piezoelectric voltage amplifier. They simply carry out digital to analog and analog to digital conversions. Note that the number of input and output channels can be increased via these blocks.



Figure 3-39. Simulink blocks for NI PCI card

Before designing the controller, the test setup will be used for data acquisition over the test structure so that the finite element model and thus the state space model could be updated for a more realistic one. Updating the model and generating a more accurate model has a key importance in the success of the designed controller.

3.3.2 Static Deflection for Applied Voltage Load

In the static deflection tests, constant voltage loads are applied on piezoelectric patch actuators #1 and #2 respectively, and beam deformation is measured in terms of tip deflection and strain at gage locations #1 and #2. In the static deflection tests, two input channels and two output channels are used. Output channels are used for driving piezoelectric patch #1 and #2 although only one patch is loaded at a time. However, since there are limitations of number on the measurement channels, static deflection tests are carried out in two parts. In the first part of the test, data acquisition from monitor channel of the piezoelectric voltage amplifier and output of laser displacement sensor is obtained. In this part of the test, applied voltage on the loaded piezoelectric patch, either piezo patch #1 or piezo patch #2, is measured together with the tip deflection. Tip deflection of the beam is measured by the laser displacement sensor. In the second part of the test, data acquisition from strain gage #1 and #2 is realized. In each part of the tests, each test is done twice for repeatability. Voltage load applied on the actuators and the data acquisition from various types of sensors in the static deflection tests are summarized in Table 3-6 and Table 3-7 for part 1 and for part 2 of static deflection tests respectively.

Table 3-6. Summary of input and output channels for part 1 of the tests

Test no	Voltage load on patch #1	Voltage load on patch #2	Data acquisition from input#1	Data acquisition from input#2
1.1	70V	0V	Monitor channel for piezo #1	Laser (tip displacement)
1.2	70V	0V	Monitor channel for piezo #1	Laser (tip displacement)
1.3	0V	70V	Monitor channel for piezo #2	Laser (tip displacement)

Table 3-6. Summary of input and output channels for part 1 of the tests**(Continued)**

1.4	0V	70V	Monitor channel for piezo #2	Laser (tip displacement)
1.5	-70V	0V	Monitor channel for piezo #1	Laser (tip displacement)
1.6	-70V	0V	Monitor channel for piezo #1	Laser (tip displacement)
1.7	0V	-70V	Monitor channel for piezo #2	Laser (tip displacement)
1.8	0V	-70V	Monitor channel for piezo #2	Laser (tip displacement)

Table 3-7. Summary of input and output channels for part 2 of the tests

Test no	Voltage load on patch #1	Voltage load on patch #2	Data acquisition from input#1	Data acquisition from input#2
2.1	70V	0V	Strain gage #1	Strain gage #2
2.2	70V	0V	Strain gage #1	Strain gage #2
2.3	0V	70V	Strain gage #1	Strain gage #2
2.4	0V	70V	Strain gage #1	Strain gage #2
2.5	-70V	0V	Strain gage #1	Strain gage #2
2.6	-70V	0V	Strain gage #1	Strain gage #2
2.7	0V	-70V	Strain gage #1	Strain gage #2
2.8	0V	-70V	Strain gage #1	Strain gage #2

In the static test, xPC target is used to generate the required signals. The offset of the amplifier is set to zero and 1V output signal is generated for 70V static tests and -1V output signal is generated for -70V static tests. At the beginning of the tests gain knobs for both piezo patches are set to zero location. After some time the gain knob of the related piezo patch is slowly turned up to its maximum, so the input signal is amplified 70 times. After the static deflection of the bam, the related knob is turned down and the voltage load on the beam is slowly removed. Reason for slow and gradual motion on the amplifier knob is to avoid the dynamic response of the structure. Simulink model used in part 1 of the static test is given in Figure 3-40 and the model used for part 2 of the tests is given in Figure 3-41. Note that the constants at the sink blocks are modified between the tests according to the voltage loads of the tests in order.

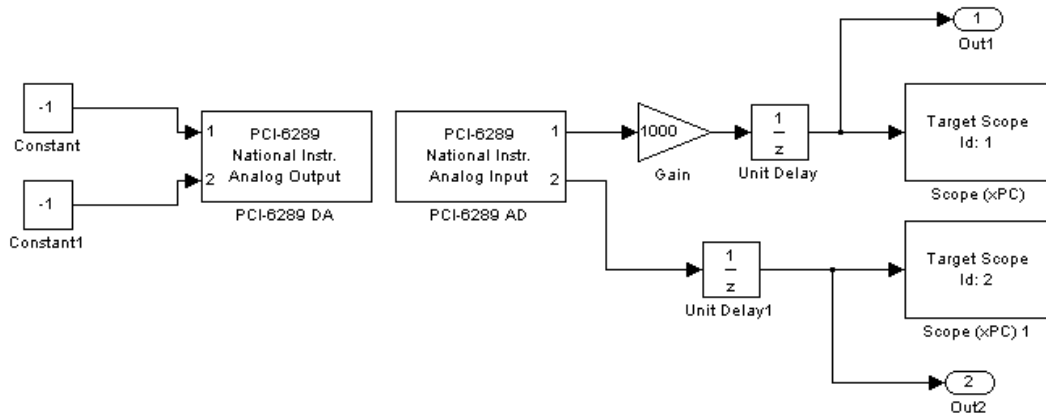


Figure 3-40. Simulink model on the Host PC used in static tests part 1

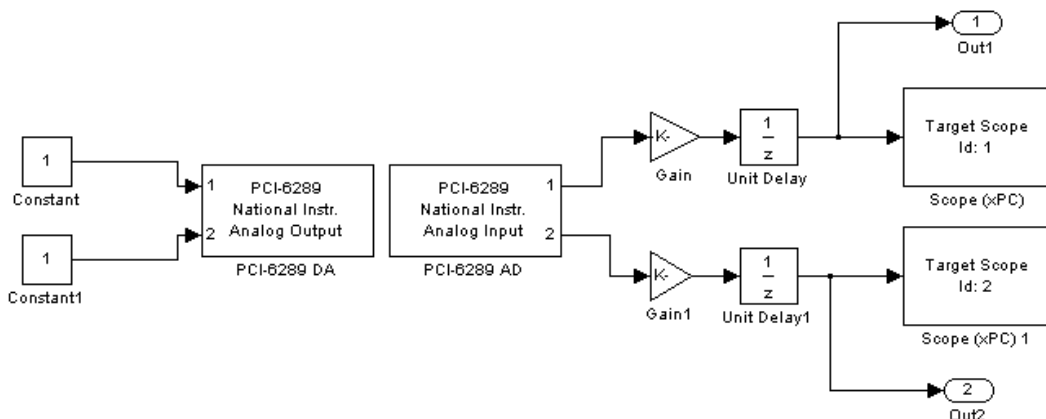


Figure 3-41. Simulink model on the Host PC used in static tests part 2

Data acquired in the first part of the static tests are given in figures from 3-42 to 3-49.

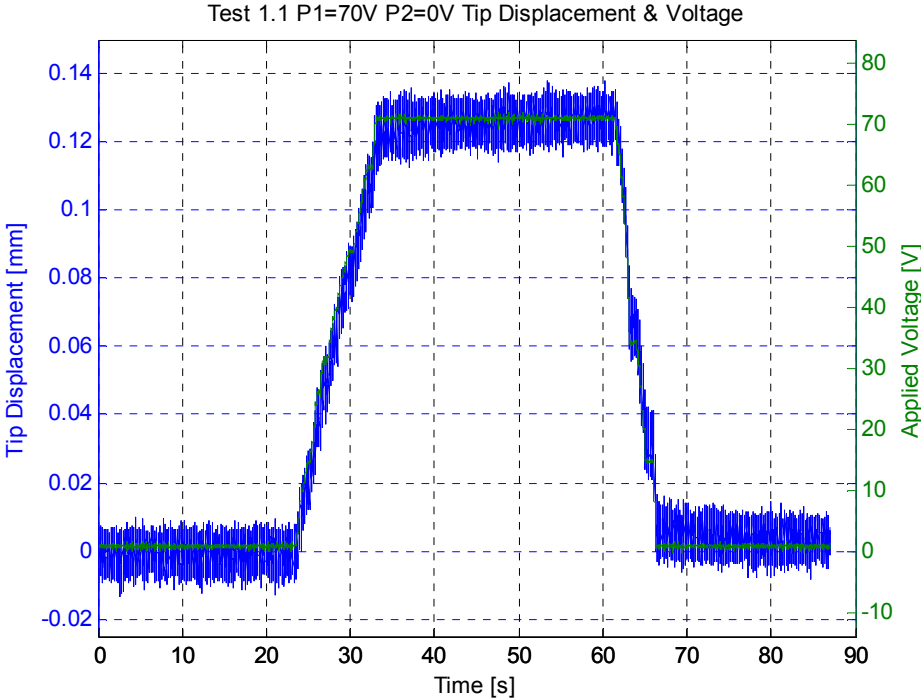


Figure 3-42. Data acquired at test 1.1, Tip displacement and voltage load

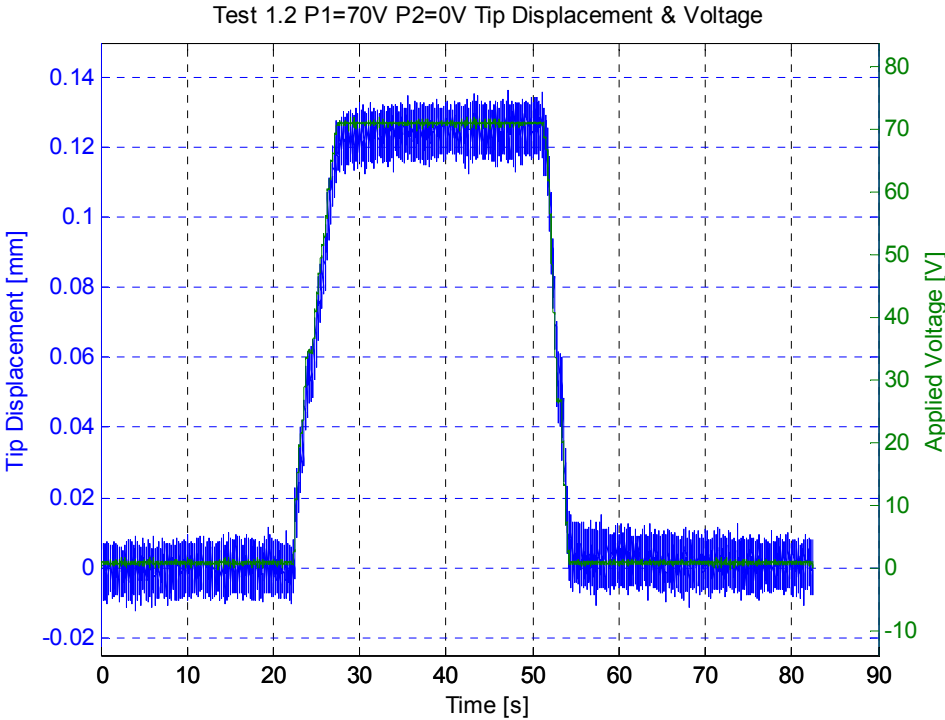


Figure 3-43. Data acquired at test 1.2, Tip displacement and voltage load

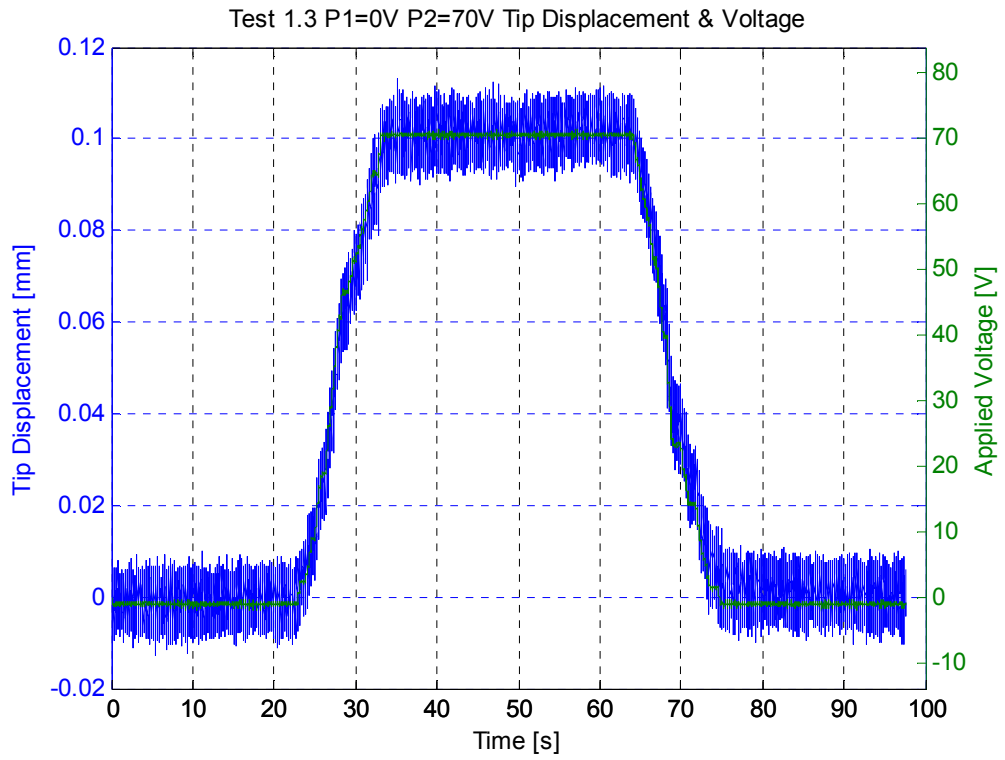


Figure 3-44. Data acquired at test 1.3, Tip displacement and voltage load

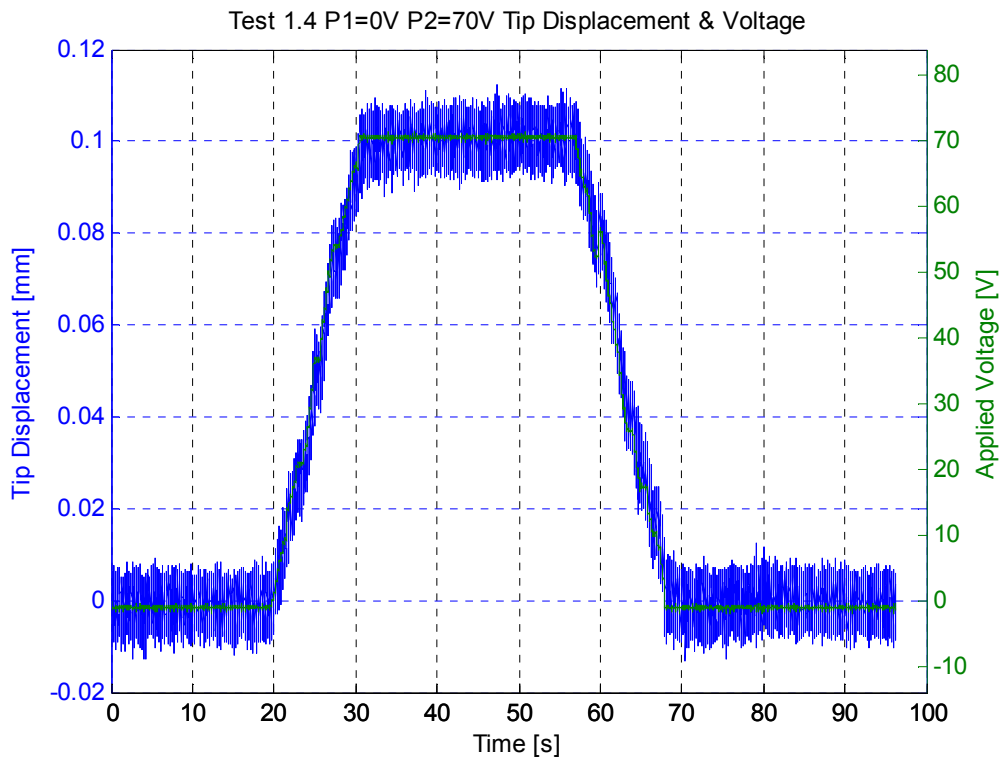


Figure 3-45. Data acquired at test 1.4, Tip displacement and voltage load

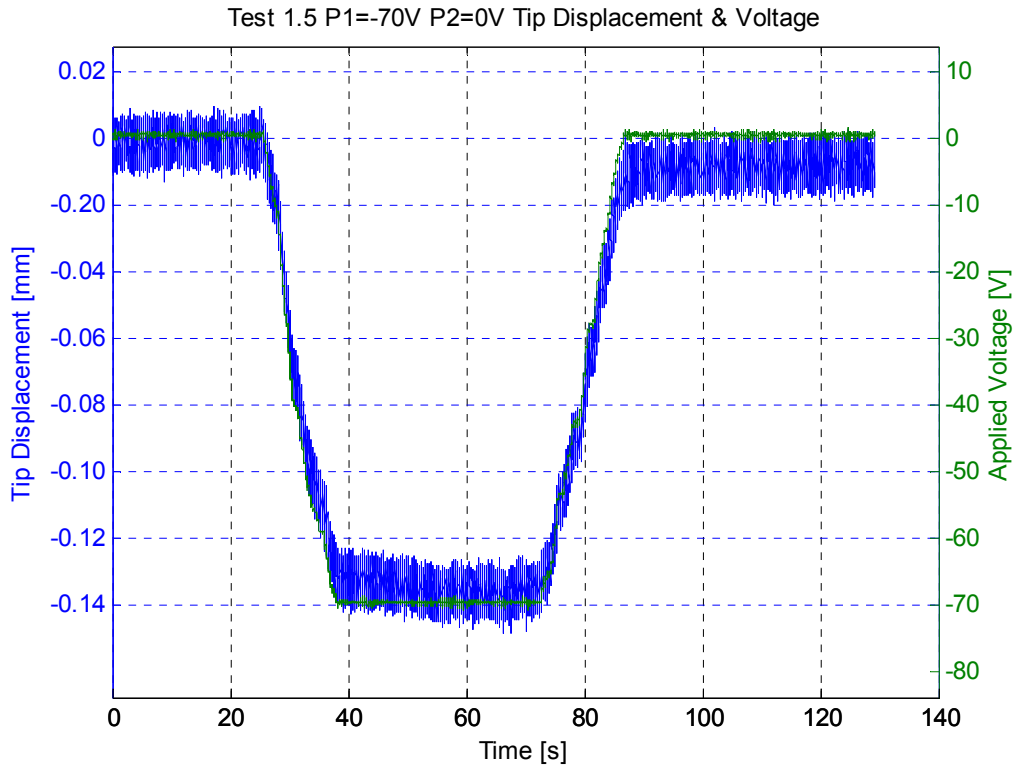


Figure 3-46. Data acquired at test 1.5, Tip displacement and voltage load

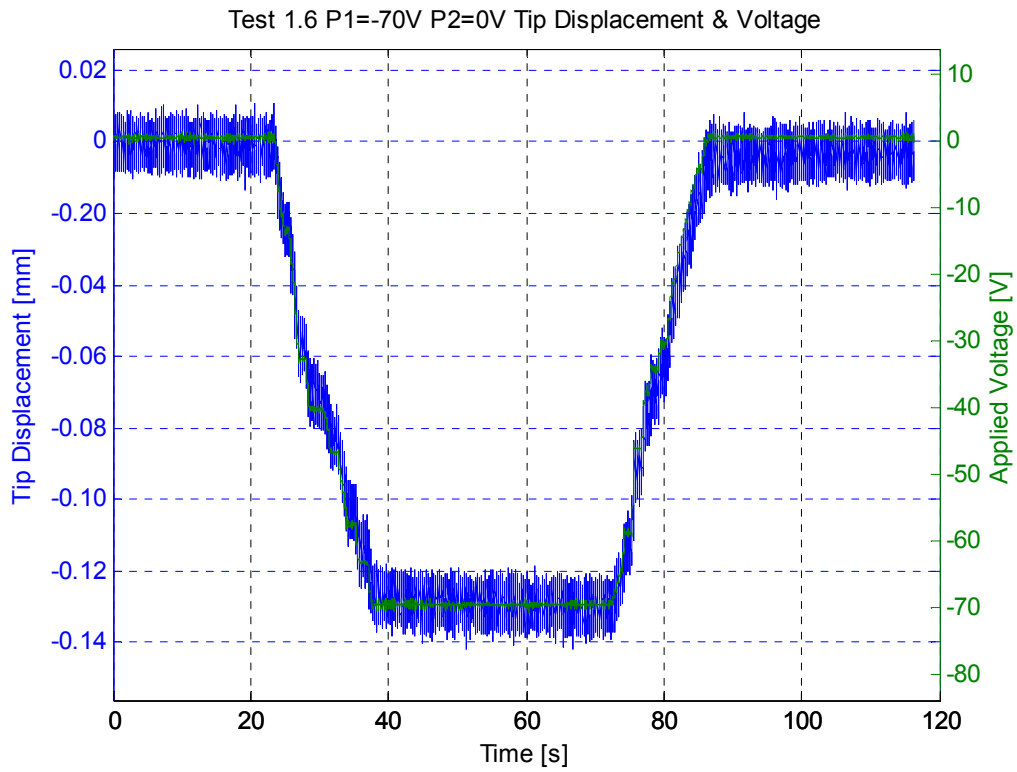


Figure 3-47. Data acquired at test 1.6, Tip displacement and voltage load

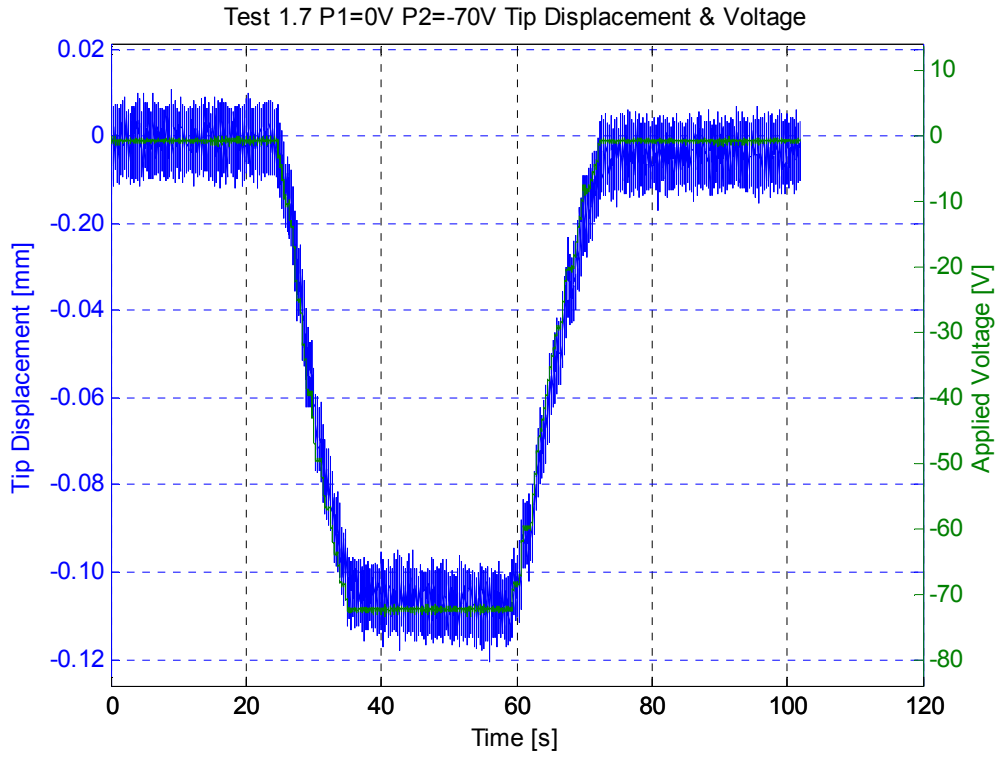


Figure 3-48. Data acquired at test 1.7, Tip displacement and voltage load

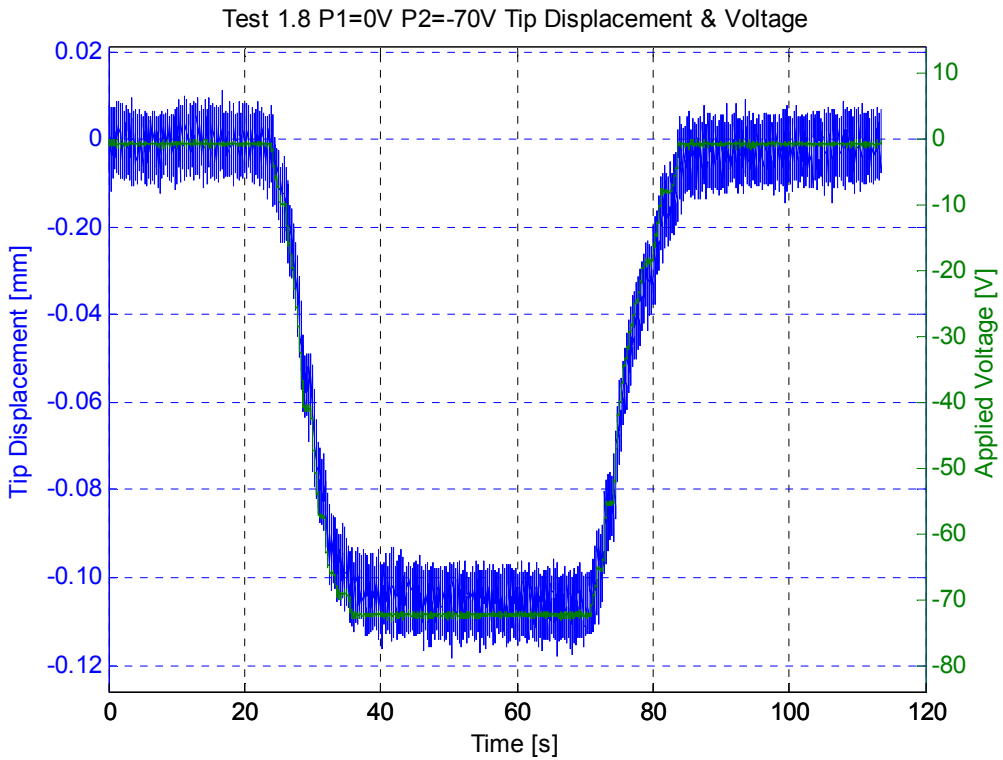


Figure 3-49. Data acquired at test 1.8, Tip displacement and voltage load

In strain gage measurements, the resistance change in the strain gage is read by using a quarter bridge. The strain gage is connected to Micro Measurement Model A2 conditioning unit, which forms the rest of the Wheatstone bridge. The bridge circuit generates an output voltage as a response to the resistance change in the strain gage as a response to the strain. The voltage output of the bridge circuit is amplified by a gain set by user at Model A2 conditioning unit. The strain measurement can be computed from the output voltage of the bridge circuit by a simple formula. For this compensation, a gain block is generated for the Simulink block in Figure 3-41 and a corresponding coefficient is entered so that the acquired data is in terms of mm/mm which is strain. Details are explained in Appendix A.

Results of the part 2 of the static tests are given in figures from 3-50 to 3-57.

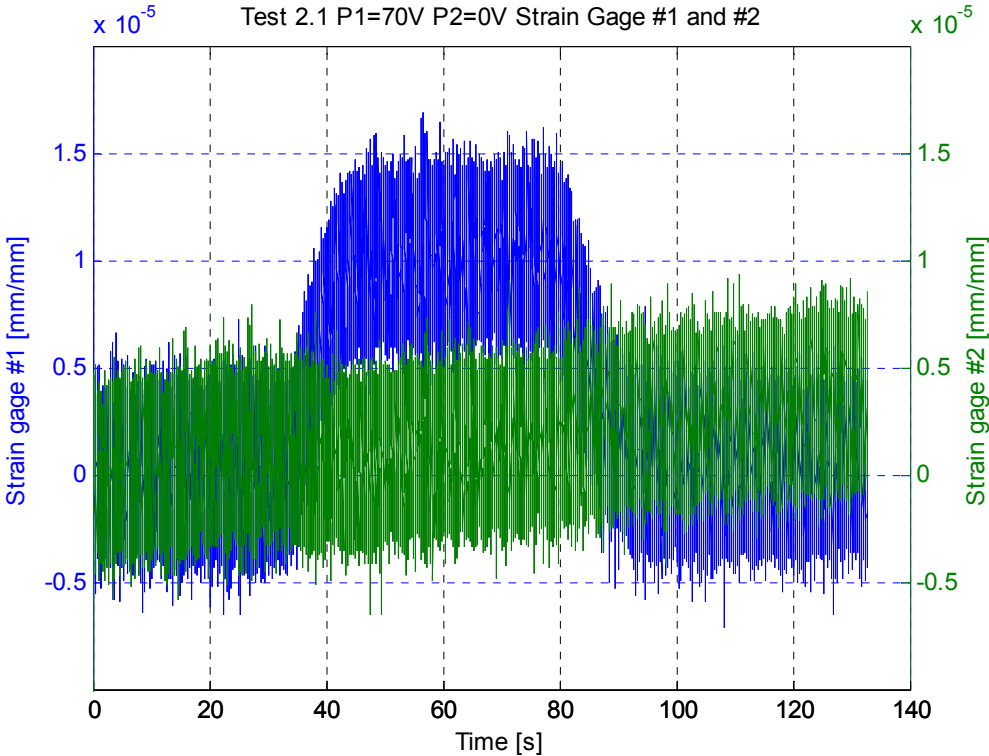


Figure 3-50. Data acquired at test 2.1, strain gage data #1 and #2 load

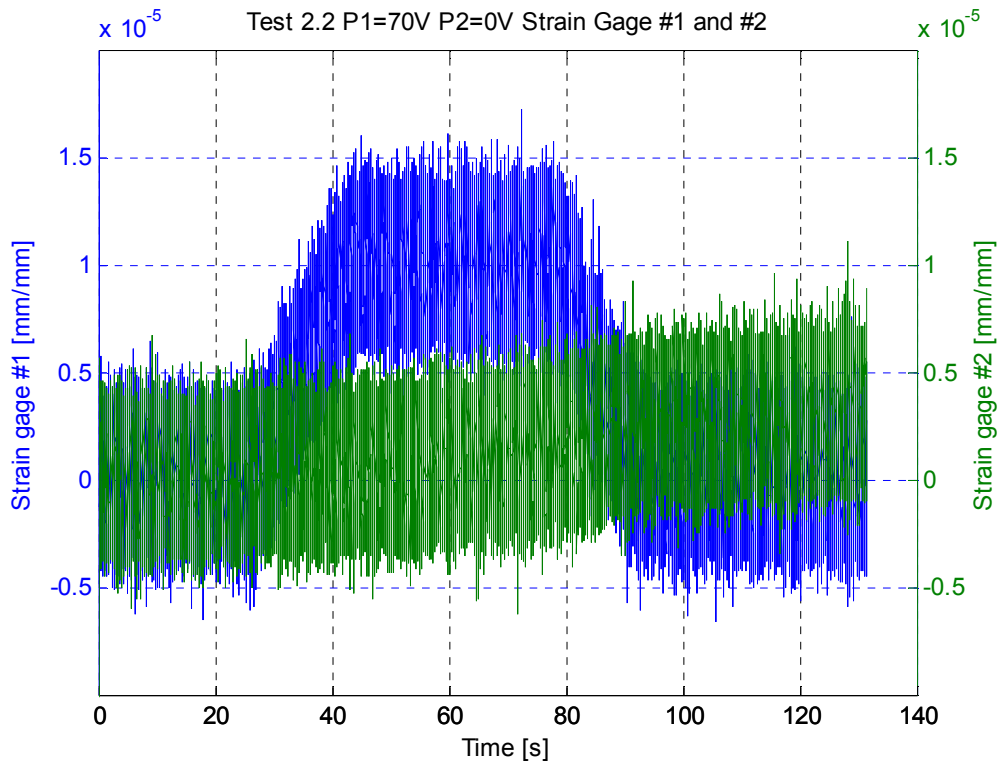


Figure 3-51. Data acquired at test 2.2, strain gage data #1 and #2 load

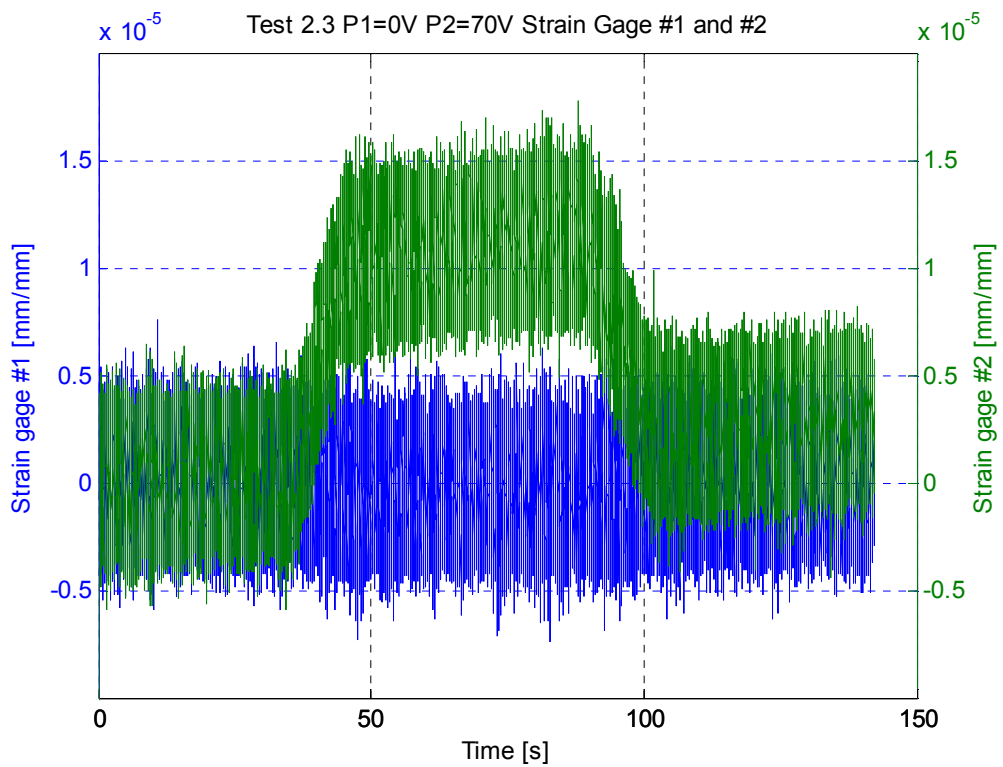


Figure 3-52. Data acquired at test 2.3, strain gage data #1 and #2 load

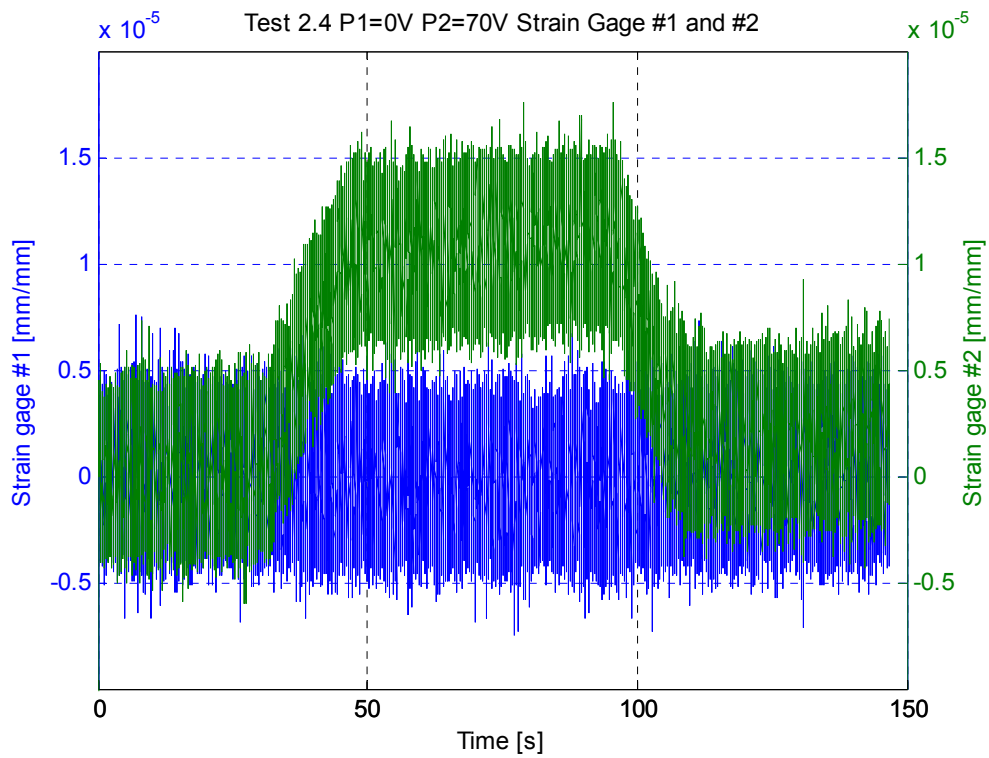


Figure 3-53. Data acquired at test 2.4, strain gage data #1 and #2 load

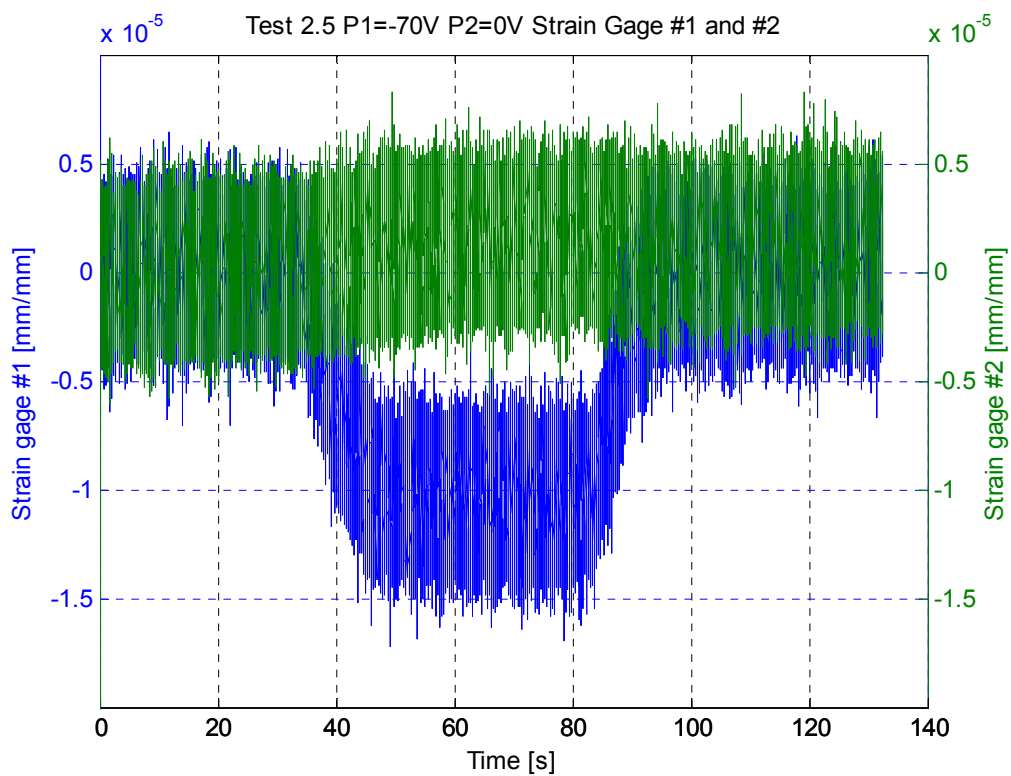


Figure 3-54. Data acquired at test 2.5, strain gage data #1 and #2 load

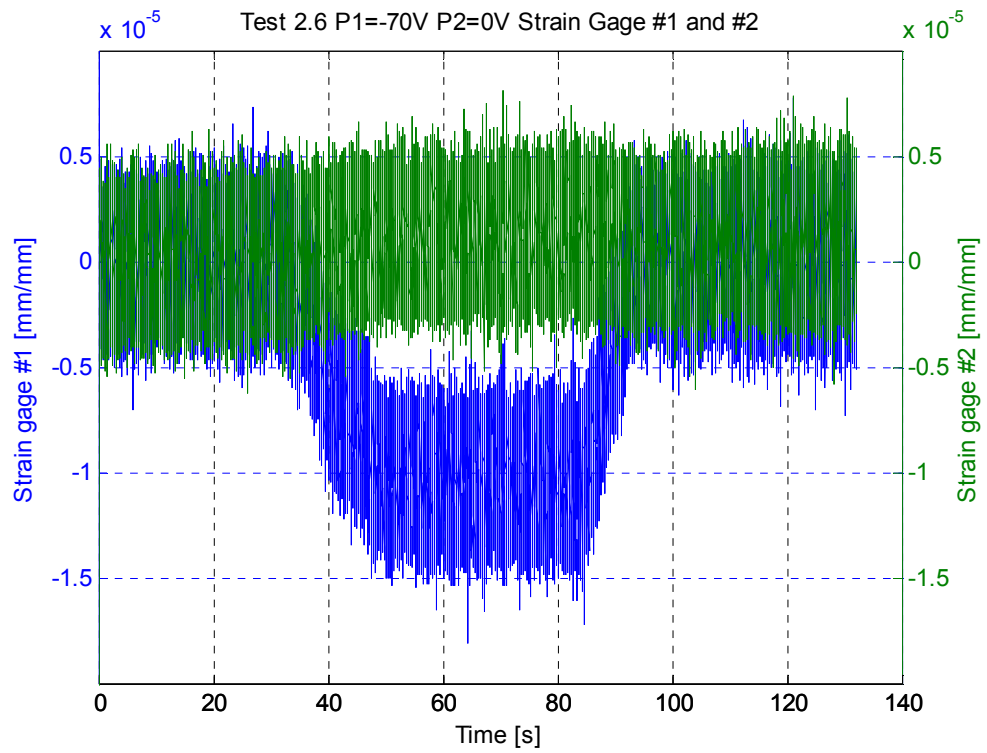


Figure 3-55. Data acquired at test 2.6, strain gage data #1 and #2 load

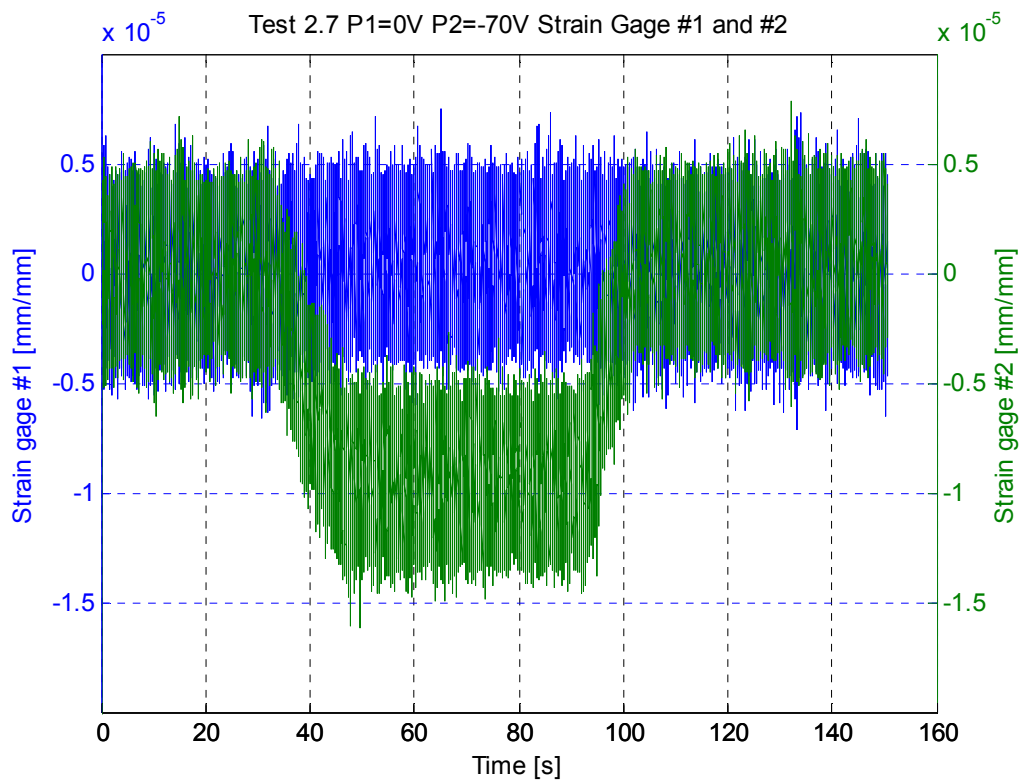


Figure 3-56. Data acquired at test 2.7, strain gage data #1 and #2 load

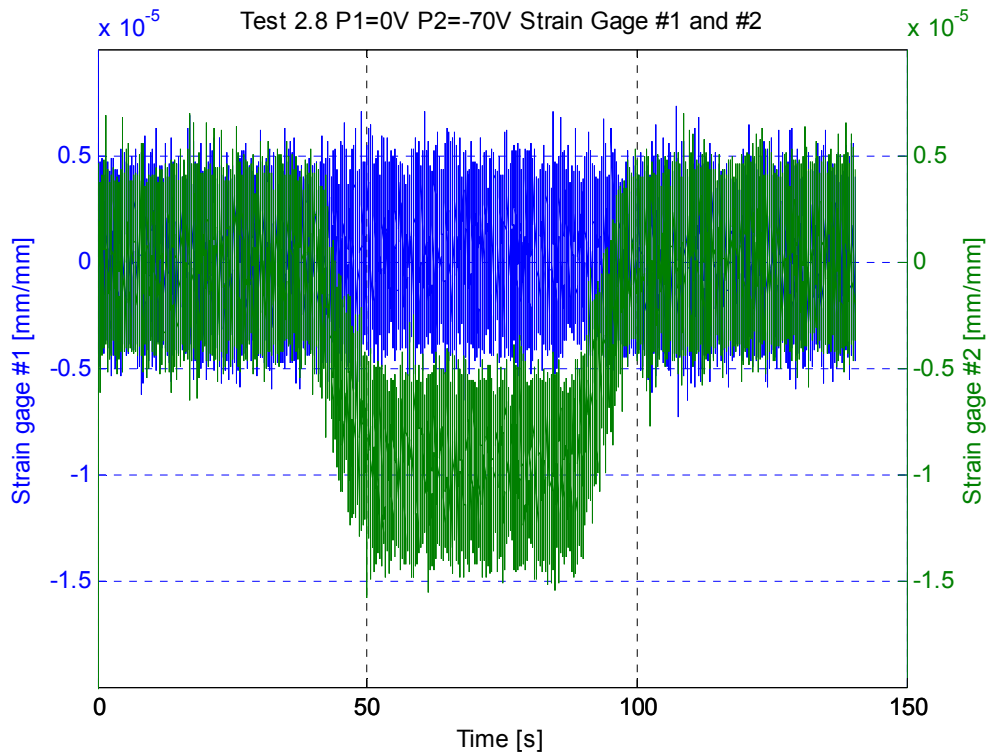


Figure 3-57. Data acquired at test 2.8, strain gage data #1 and #2 load

One thing to note in these measurements is that the measurements of the laser displacement sensor is much more precise than the measurements of strain gages considering the relative noises of the measurements.

3.3.3 Measurement of Voltage FRFs

In the beam model the inputs are the applied voltage across the electrodes of piezoelectric patches and the output is the deformation of the beam. The beam deformation is measured by means of strain gages and laser displacement sensors. The term voltage FRF (Frequency Response Function) refers to the FRF between a measurement over the beam (whether displacement or strain) and the applied input voltage to the piezo patches. FRFs are measured in the tests are given in Table 3-7.

Table 3-7. List of measured FRFs

Notation	Input	Output	Explanation
H_{p1d}	Piezo 1	Tip Deflection	FRF between piezo1 voltage and tip deflection
H_{p2d}	Piezo 2	Tip Deflection	FRF between piezo2 voltage and tip deflection
H_{p1s1}	Piezo 1	Strain @1	FRF between piezo1 voltage and strain1
H_{p1s2}	Piezo 1	Strain @2	FRF between piezo1 voltage and strain2
H_{p2s1}	Piezo 2	Strain @1	FRF between piezo2 voltage and strain1
H_{p2s2}	Piezo 2	Strain @2	FRF between piezo2 voltage and strain2

In the measurement of FRFs, MATLAB xPC Target is used in both data acquisition and generation the input signal for the piezoelectric patches. In the tests, due to the limitations of the number of input channels of the system, the data required for calculation of FRFs are obtained in two parts. In the first part of the data acquisition process, tests for the FRFs that include the tip deflection of the beam as output are carried out. In the second part, FRFs that include strain gage measurements as output are obtained. For the two different parts of the data acquisition process, two different Simulink models are used in the xPC Target system. Simulink model used in the first part of data acquisition is given in Figure 3-58 and the model used in the second part of the tests is given in Figure 3-59

In the generation of FRFs the voltage load applied as an input for piezoelectric patch actuator is measured as well as the output of the sensors. The first channel of the data acquisition block is allocated for the monitor channel of the piezoelectric voltage amplifier. The monitor channel gives the 1/1000 of the voltage output supplied to the piezoelectric patch actuator. By giving 1/1000 of the voltage used to drive the piezoelectric actuator to the monitor channel, the data acquisition instrument can safely record the applied voltage data to the actuator. In the recording, the output of the monitor channel is multiplied by 1000 in the Simulink diagram.

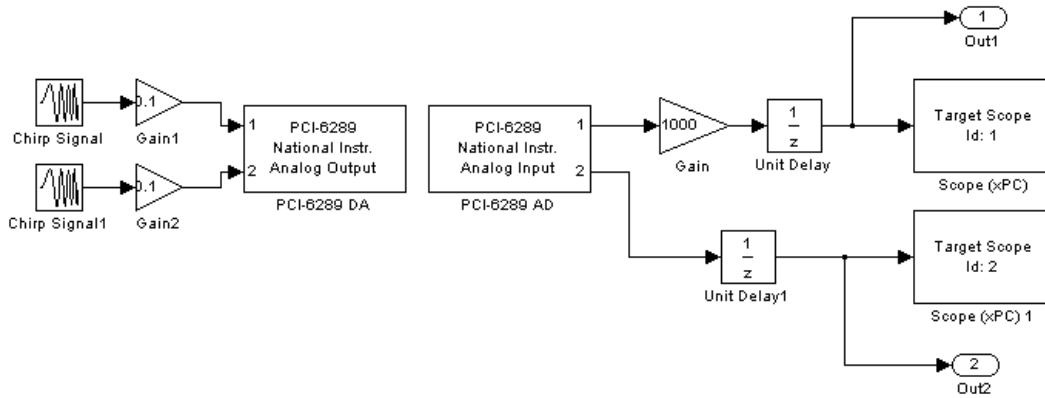


Figure 3-58. Simulink model on the Host PC used in dynamic tests part 1

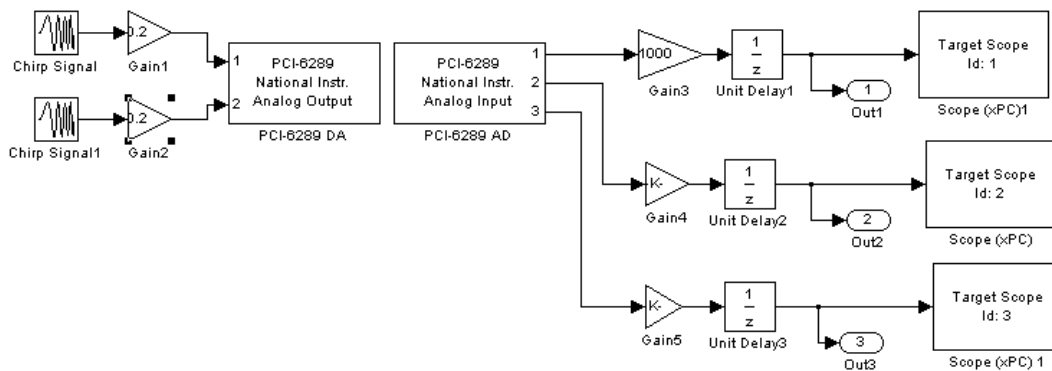


Figure 3-59. Simulink model on the Host PC used in dynamic tests part 2

In the measurement with strain gages, the output voltage of the strain gage conditioning unit is multiplied by a definite coefficient to calculate the strain. The calculation of the mentioned coefficient is based on strain gage formulas and it is explained in Appendix A in detail. This coefficient is included in the Simulink model in part 2 of the measurements.

In the tests, a chirp signal is generated in Simulink as an input for piezoelectric patches. The output signal of the chirp block is multiplied by a coefficient smaller than 1 for safety purposes. One piezoelectric patch is loaded at one time in the tests. Since a modal analysis of the beam has been carried out earlier, the natural frequencies for the first three bending modes of the beam are known to be 9.865 Hz,

56.65 Hz and 150.96 Hz. The fourth and the fifth modes of the system are lateral bending and torsion respectively and these modes are out of the consideration. Also these modes cannot be detected by the current sensor placement of the beam. Therefore in the test the excitation frequency is chosen to be starting from 0.1 Hz up to 165 Hz to capture first three modes of the beam. The chirp signal is desired to change 1Hz per second, so the target time is 165 seconds and the frequency at the target time is 165 Hz.

In order to obtain the FRF between the applied voltage and the tip displacement, both laser displacement sensor output channel and the monitor channel of the piezo amplifier are connected to the data acquisition system. Fast Fourier Transform (FFT) of both voltage data and tip displacement are taken. To formulate the voltage FRF between the tip displacement and the applied voltage to piezo patch #1, the equation below can be written:

$$H_{p1d}(\omega) = \frac{d(\omega)}{V_{p1}(\omega)} \quad (3.5)$$

In the equation above, $d(\omega)$ is the FFT of the tip displacement and $V_{p1}(\omega)$ is the FFT of the applied voltage to the piezo patch #1. Similarly the FRF between applied voltage to piezo patch #2 and the tip displacement can be formulated as shown below:

$$H_{p2d}(\omega) = \frac{d(\omega)}{V_{p2}(\omega)} \quad (3.6)$$

In this equation $V_{p2}(\omega)$ is the FFT of the applied voltage to piezo patch #2. In addition to tip displacements, strain gage data are acquired on the second part of the tests. Two strain gages are located at the back side of the beam in the locations corresponding to the mid points of the patch areas. The voltage FRF between the

applied voltage to the piezo patch#1 and the strain gage #1 is formulated as shown below:

$$H_{p1s1}(\omega) = \frac{s_1(\omega)}{V_{p1}(\omega)} \quad (3.7)$$

In this equation $s_1(\omega)$ is the FFT of the strain gage data. Similarly, the FRF between the applied voltage to piezo patch #1 and strain gage #2 is given below:

$$H_{p1s2}(\omega) = \frac{s_2(\omega)}{V_{p1}(\omega)} \quad (3.8)$$

The FFT of strain gage data acquired from strain gage #2 is denoted as $s_2(\omega)$. Similarly, FFT between applied voltage to piezo patch #2 and strain gage #1 is given below:

$$H_{p2s1}(\omega) = \frac{s_1(\omega)}{V_{p2}(\omega)} \quad (3.9)$$

Also the FFT between applied voltage to piezo patch #2 and strain gage #2 is given below:

$$H_{p2s2}(\omega) = \frac{s_2(\omega)}{V_{p2}(\omega)} \quad (3.10)$$

In part 1 of the tests, data acquired from the laser displacement sensor pointed to the tip of the beam and the monitor channel of the piezo amplifier channel used to drive piezo patch #1. A chirp signal is generated by Simulink from 0.1 Hz to 165 Hz increasing the frequency with a rate of approximately 1Hz per second in order to detect first three bending modes of the beam. Time data acquired from laser displacement sensor in the test for measuring H_{p1d} is given in Figure 3-60.

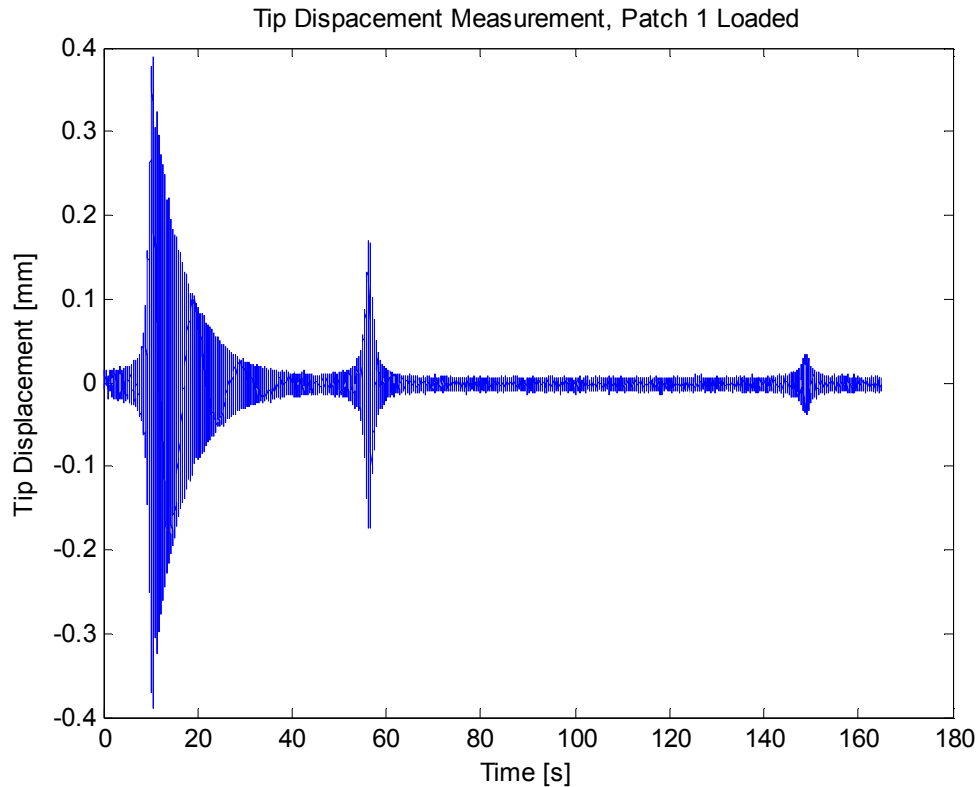


Figure 3-60. Tip displacement data acquired for H_{p1d} test

In Figure 3-60, the time values that the beam comes to resonance are apparent. Knowing the rate of the frequency sweep, one can guess the resonance frequencies. However the FFT related with the tip displacement signal will give a lot more information about the structure. In order to calculate the FRF over two points of a structure, one must measure the excitation signal. In this case, to calculate the voltage FRF for various sensors on a beam with piezoelectric actuators, the input voltage applied across the electrodes of piezoelectric patches should be acquired. The chirp signal applied to the piezo patch #1 over 165 seconds in the tests is given in Figure 3-61. For a better understanding of the chirp signal, the first 20 second of the applied voltage data is given in Figure 3-62.

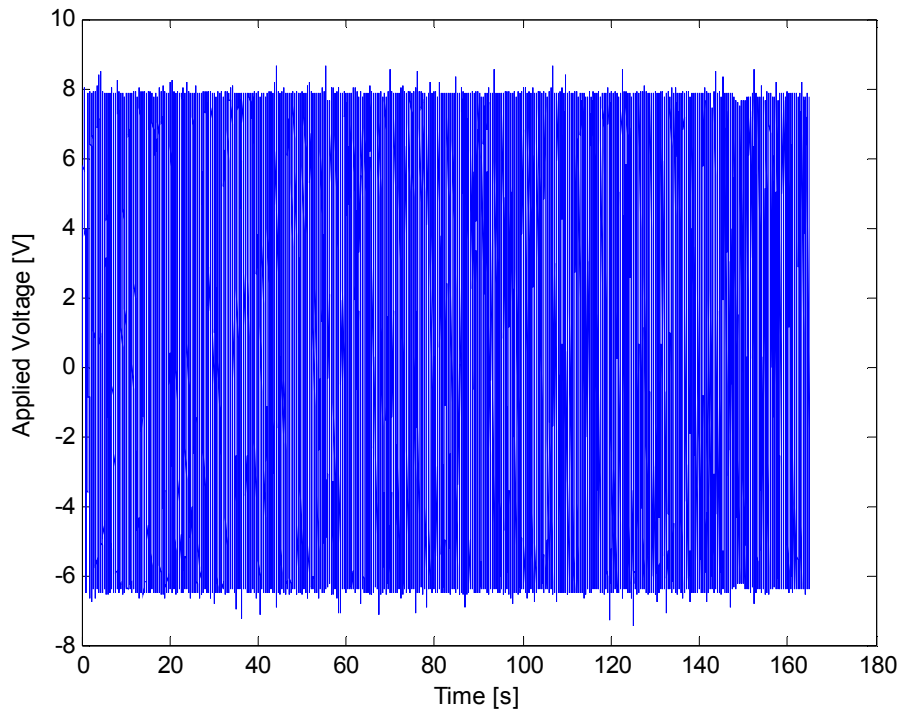


Figure 3-61. Voltage applied to piezo patch#1 in the test for H_{p1d}

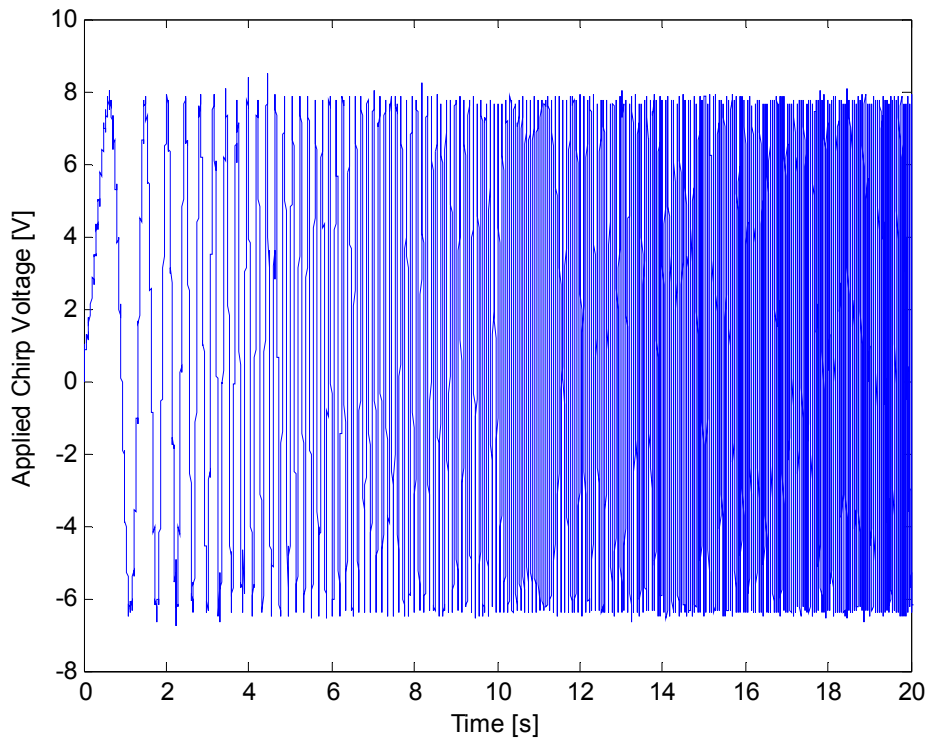


Figure 3-62. Chirp input voltage signal for first 20 seconds of H_{p1d} test

After data acquisition phase, the FRFs defined by equations from 3.5 to 3.10 are obtained and presented in terms of phase and amplitude. Voltage FRF between the applied voltage to piezoelectric patch#1 and the tip displacement of the beam measured by laser displacement sensor which is H_{p1d} is given in Figure 3-63.

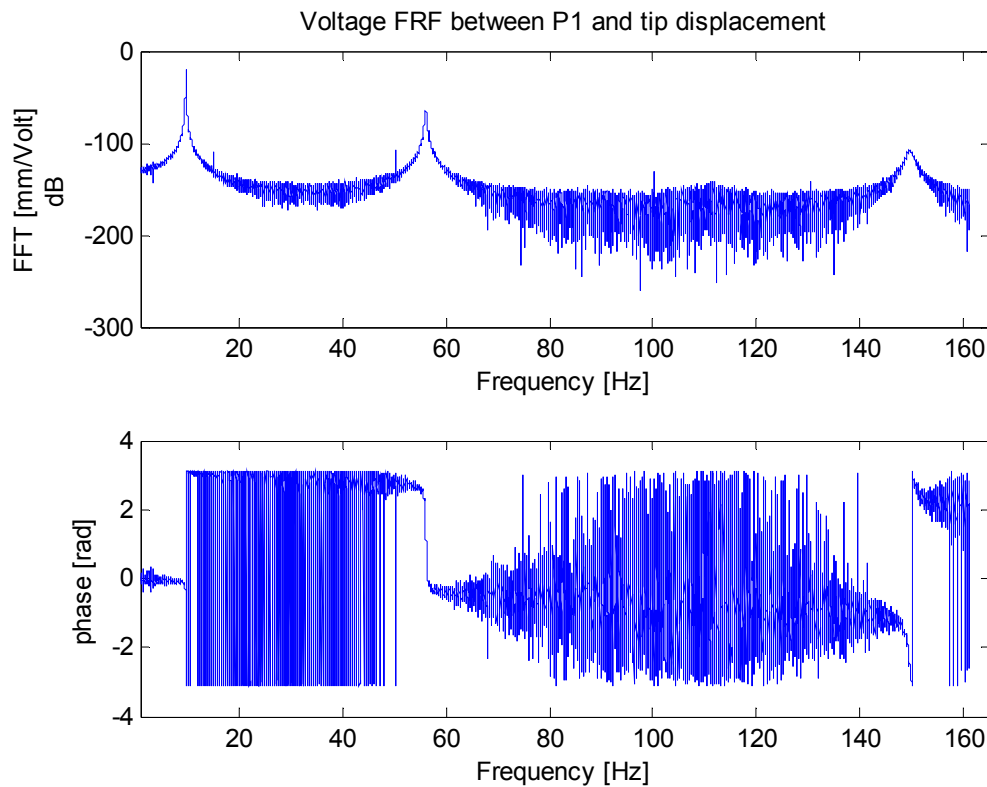


Figure 3-63. Voltage FRF between tip displacement and applied voltage to patch#1 (H_{p1d})

The voltage FRF of the beam is obtained by single test data. The first three resonances of the beam at 9.8 Hz, 55.9Hz and 149.1 Hz are distinctive from the FRF generated by single test data. Also phase changes π radians at frequencies where the system has a mode. However the sections of the FRF between resonant frequencies contains noise. The up and down lines at the phase plot at frequencies between resonances is because of the fact that the phase plot is limited between $-\pi$ and $+\pi$. By using multiple test data and averaging the result of each test, the noise that contaminates the FRF will cancel out since it has random characteristic. In Figure

3-64 voltage FRF between tip displacement and the applied voltage to piezoelectric patch is obtained again by using the average of 10 FRFs generated from 10 tests. The distinctive resonances are close to the previous FRF but the FRF computed by averaging 10 FRFs is much more smooth than the previous one.

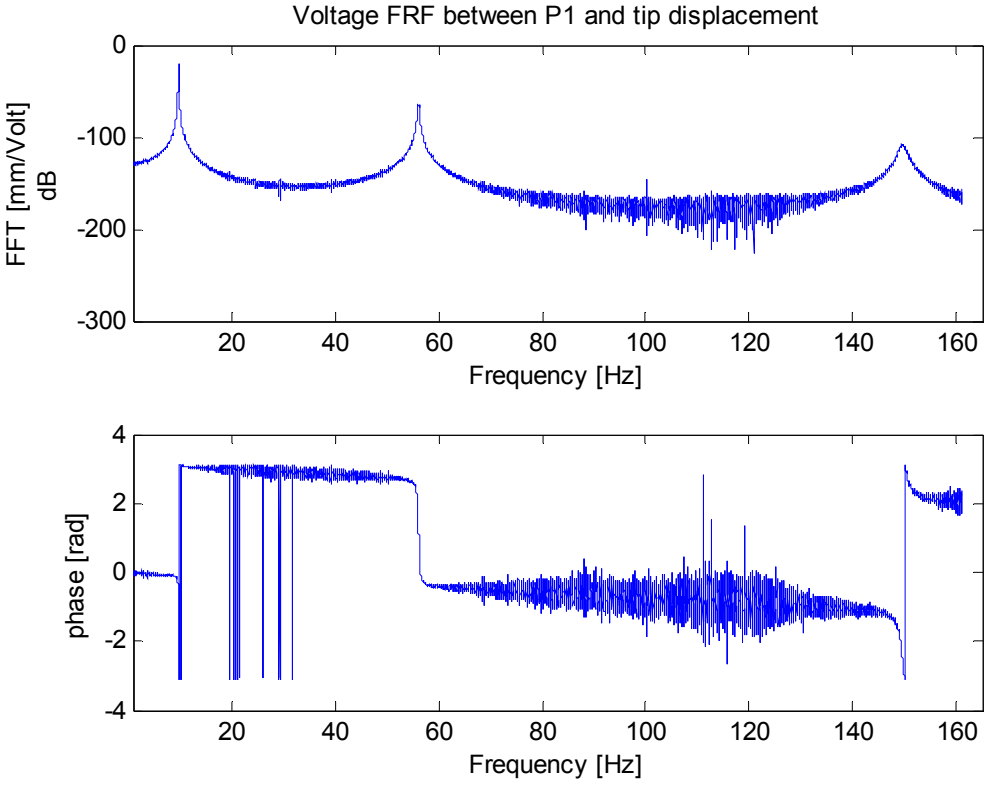


Figure 3-64. Voltage FRF between tip displacement and applied voltage to patch#1 (H_{p1d}) using 10 averages

Examining the plot for the voltage FRF between tip displacement and applied voltage to patch#1, the resonant frequencies of the FRF are spotted at 9.8 Hz, 56.2 Hz and 149.6 Hz. Comparison of these values with those found from finite element analysis is given in Table 3-8.

**Table 3-8. Comparison of resonant frequencies found by test
and modal analysis results**

Mode	Finite Element Result	Experimental Result	Difference (%)
1 st bending	9.865 Hz	9.8 Hz	0.6
2 nd bending	56.65 Hz	56.2 Hz	0.8
3 rd bending	150.96 Hz	149.6 Hz	0.9

The FRF between the applied voltage to piezoelectric patch#2 and the tip displacement of the beam measured by laser displacement sensor is given in Figure 3-65. For this case averaging of 10 FRFs obtained from 10 tests is also obtained. The voltage FRF between tip displacement and the applied voltage to patch#2 computed by the average of 10 tests is given in Figure 3-66. Although more measurements are required in this case, the peaks at resonance frequencies are distinct.

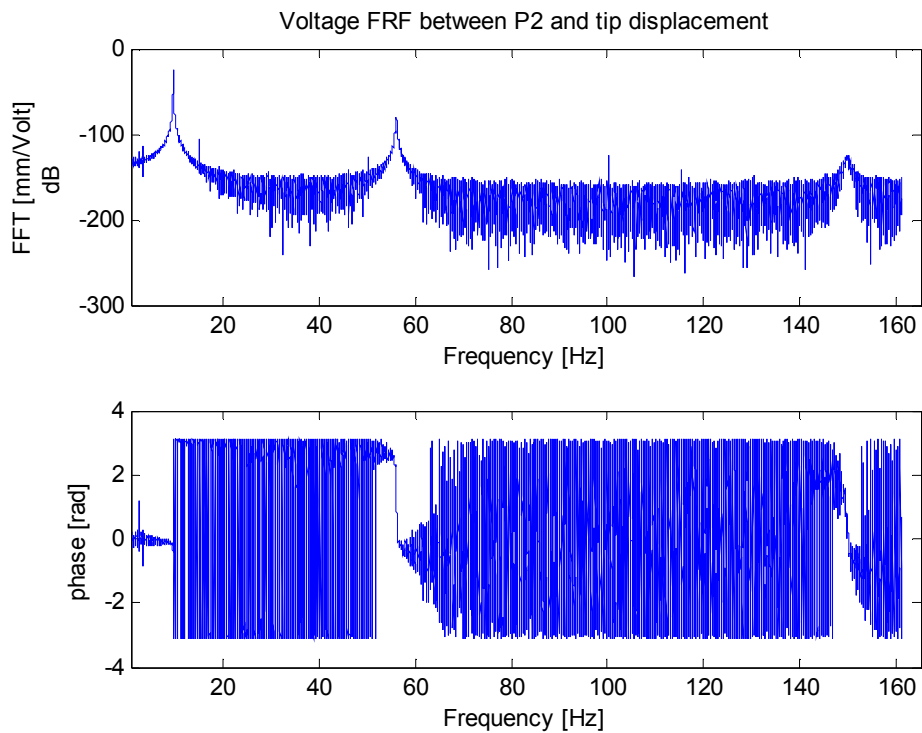


**Figure 3-65. Voltage FRF between tip displacement and
applied voltage to patch#2**

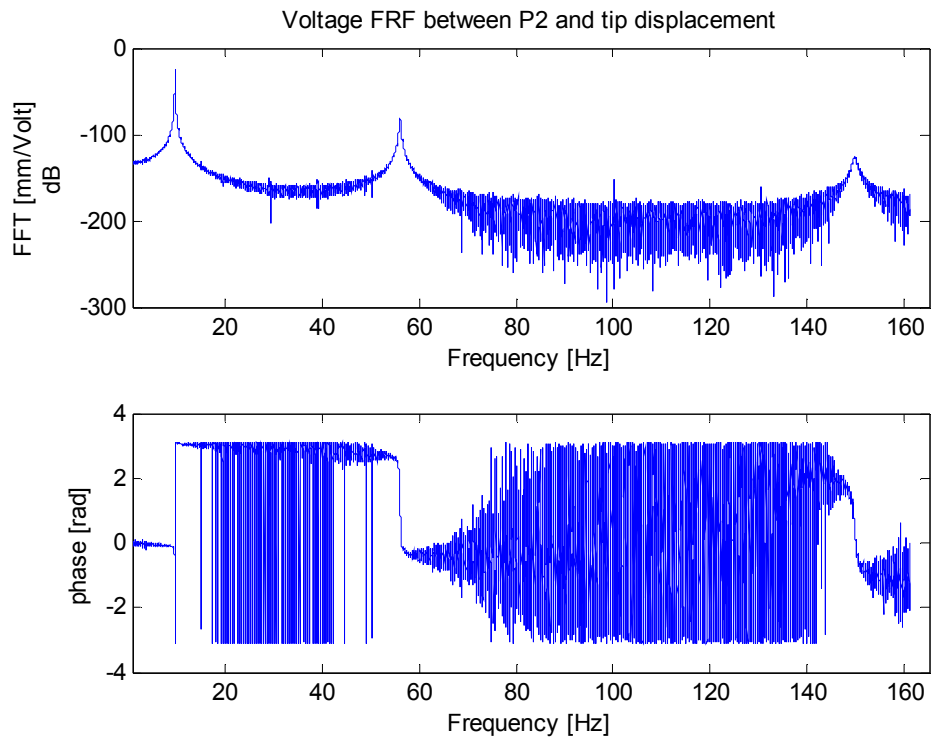


Figure 3-66. Voltage FRF between tip displacement and applied voltage to patch#2 using 10 averages

In addition to laser displacement sensor, strain gages are also used in the computation of FRFs. In the second part of the tests FRFs between strain gages and the applied voltages to piezoelectric patches are obtained. Taking the applied voltage to piezoelectric patch#1 as reference, voltage FRF between strain gage#1 and piezoelectric patch#1 (H_{p1s1}) and voltage FRF between strain gage#2 and piezoelectric patch#1 are obtained in the same test. The voltage FRF of $H_{p1s1}(\omega)$ is given in Figure 3-67 and the voltage FRF of $H_{p1s2}(\omega)$ is given in Figure 3-68. In the second test voltage FRFs between strain gages #1 and #2 and the applied voltage to piezoelectric patch#2 are obtained. The voltage FRF of $H_{p2s1}(\omega)$ is given in Figure 3-69 and the voltage FRF of $H_{p2s2}(\omega)$ is given in Figure 3-70.

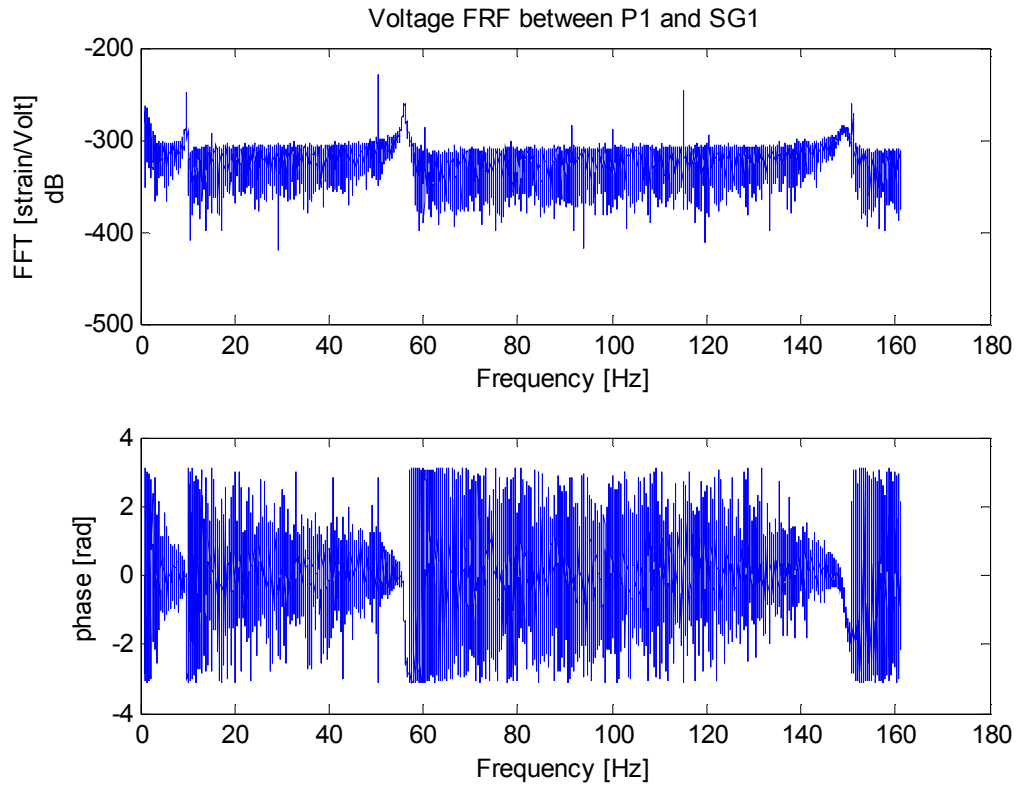


Figure 3-67. Voltage FRF between strain gage#1 and applied voltage to patch#1

As seen on the figures of strain gage FRFs, the resonant frequencies can be detected at 9.8 Hz, 56 Hz and 149.1 Hz. However the data contains much noise. The noise at 50Hz and its harmonics are visible in the amplitude plots, but it does not appear in phase plots as expected. Modes are detectable from the strain gage voltage FRF plots, but signal to noise ratio of strain gage data is quite low.

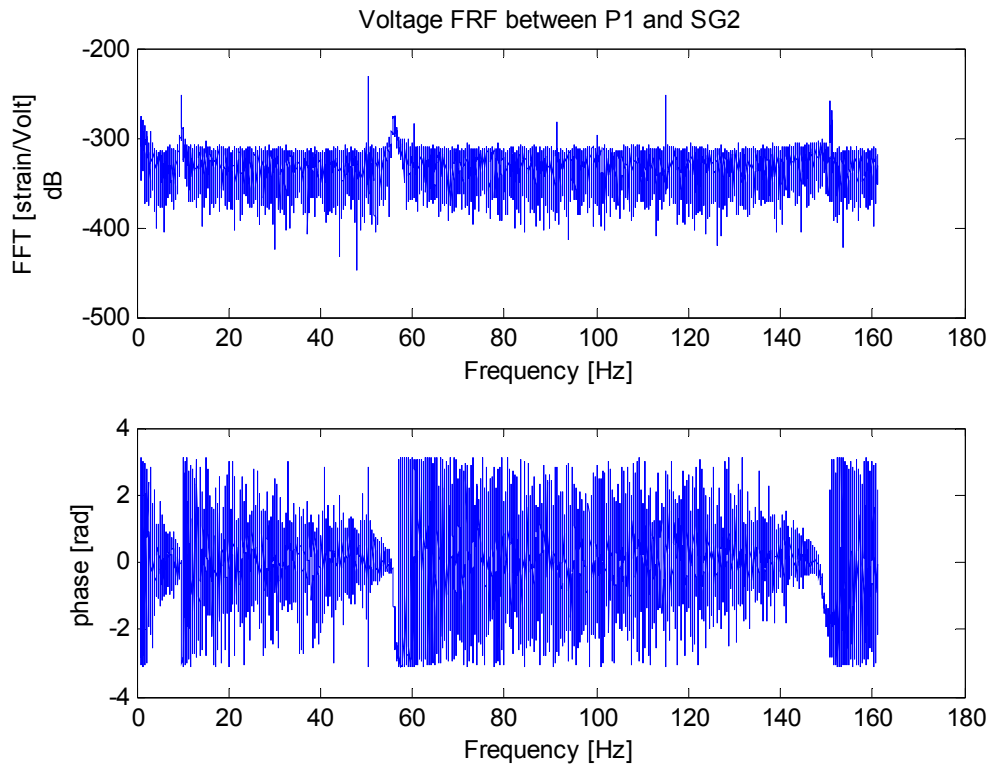


Figure 3-68. Voltage FRF between strain gage#2 and applied voltage to patch#1

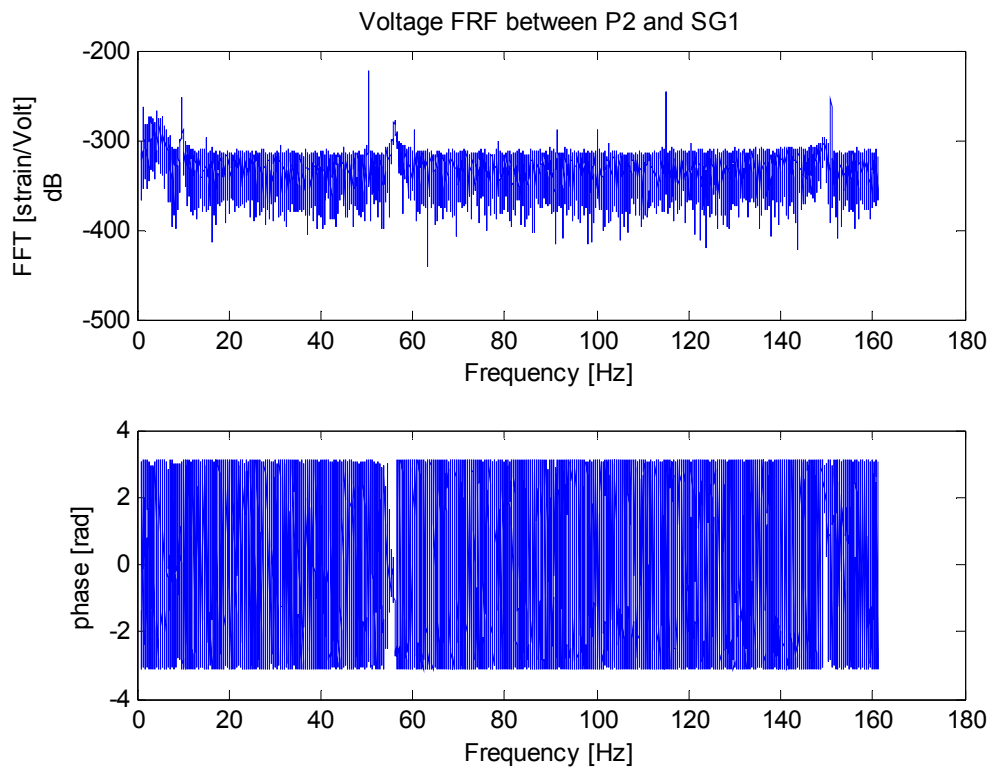


Figure 3-69. Voltage FRF between strain gage#1 and applied voltage to patch#2

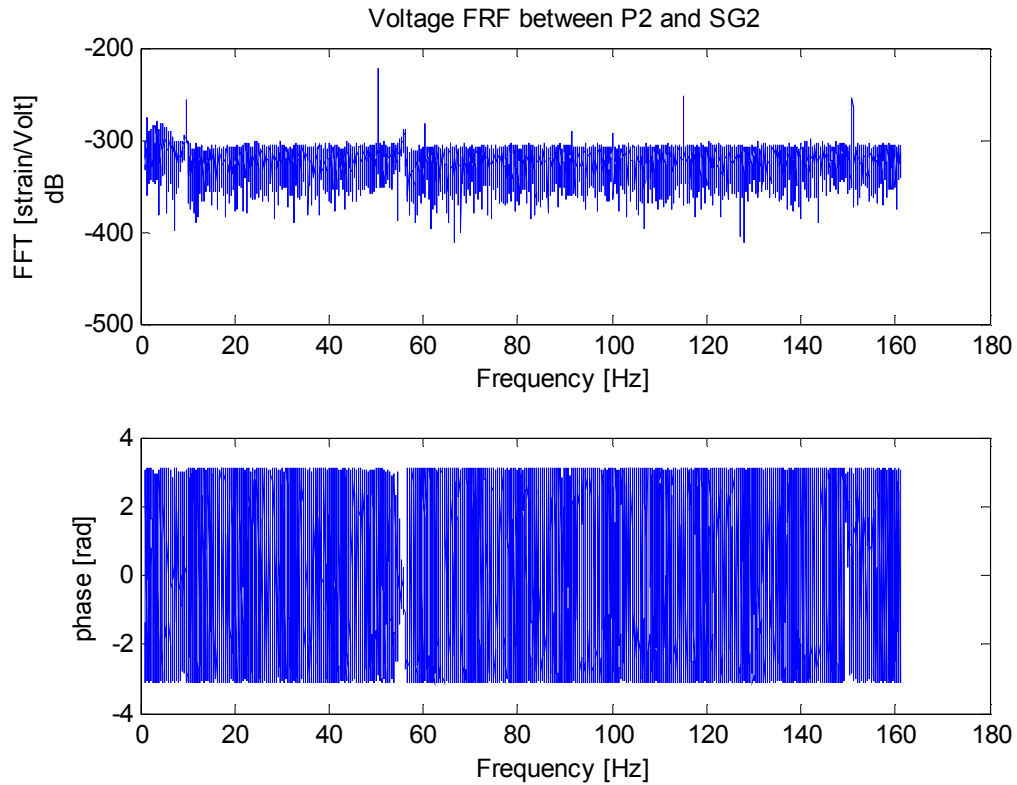


Figure 3-70. Voltage FRF between strain gage#2 and applied voltage to patch#2

By examining the data acquired by laser displacement sensor and the strain gages, laser displacement sensor is decided to be used as a part of feedback control system since it has higher signal to noise ratio than the strain gage.

Examining the FRF data gathered from laser displacement sensor and strain gages, it is decided to use the FRF data from laser displacement sensor to compare with the analysis results. Using the FRF of H_{pld} first three resonance frequencies can be compared with the results of modal analysis.

3.4 Updating FEM and State Space Model Using Test Data

The state space data is updated by using the test data in time domain. In updating process, the relevant model parameters are changed in ANSYS APDL code which builds the model and includes the SPMWRITE command in the end for extraction of A,B,C and D matrices. The APDL code used in building parametric beam model and extracting state space matrices is given in Appendix C. The state space matrices are used in Simulink for building the plant model to be controlled. This plant model can be tested by any input signal.

By updating piezoelectric coefficient d_{31} , and the damping ratio of the beam, it is possible to fit the test data with the state space model. By making tests over the beam, voltage FRF's are collected along with some time domain data. In this process, the input signal is applied to piezo patch#1. The Simulink model used in test and data acquisition is given in Figure 3-71. In the test the monitor channel of the piezo amplifier is connected to analog input #1 channel of the xPC Target system. Since the monitor channel gives 1/1000 of the voltage applied to the piezo actuator, this signal is multiplied by a gain of 1000 to acquire the applied voltage. The output of the laser displacement sensor pointing at the tip of the beam is connected to the analog input #2 channel and the measurement of SG#1 is connected to analog input #3 channel of the xPC Target system. The gain of strain gage channel is computed according to strain gage formulas given in Appendix A.

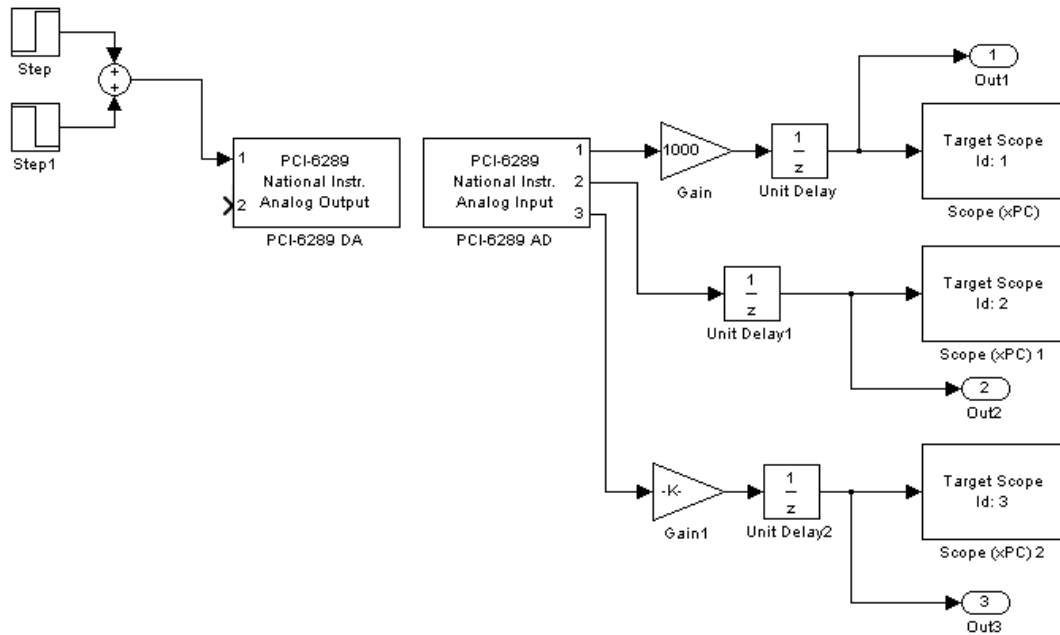


Figure 3-71. Simulink model used in data acquisition to test the model in time domain

To compare time domain results of the ANSYS model with the test data, Simulink model of the beam generated from the state space matrices from ANSYS are used. Using transient analysis of ANSYS for time response of the beam will be time consuming. Since it is shown in Chapter 3.2.4 that the transient analysis results are identical to the results obtained from the Simulink model, the state space matrices from ANSYS are directly entered into Simulink. The analysis model built using Simulink is given in Figure 3-72. Note that a band limited white noise source is added at the output of the model to simulate the sensor noise. The sensor noise will be added to the simulation results at the final step of the process of updating the model. In the model used to simulate the behavior of the beam, the input is the applied voltage to the piezo patch#1 and the output is the tip displacement.

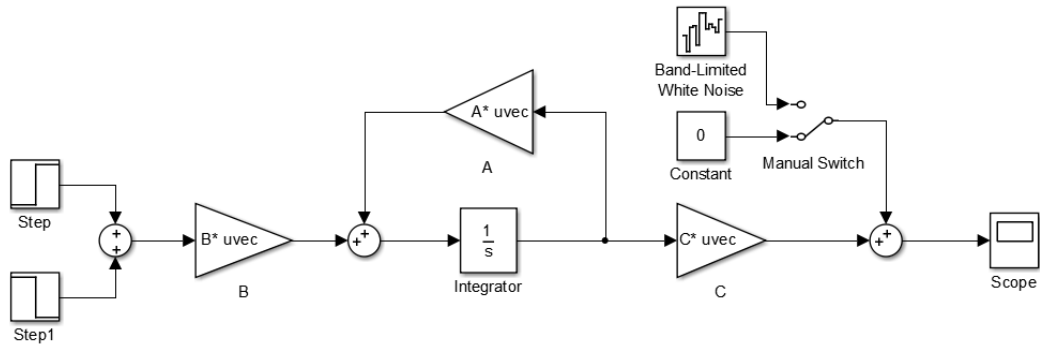


Figure 3-72. Simulink model used to test the simulation model to compare with the test data

In order to test the simulation model and the real life model, a test input is required. In Figure 3-73 the input voltage signals to be applied on the piezo patch#1 in simulation and test model are given. Note that the input for the test model contains some noise. The test and simulation runs for 165 seconds. In the 15th second a sudden voltage load of 70V is applied and kept until 70th second. At 70th second the voltage load is suddenly removed.

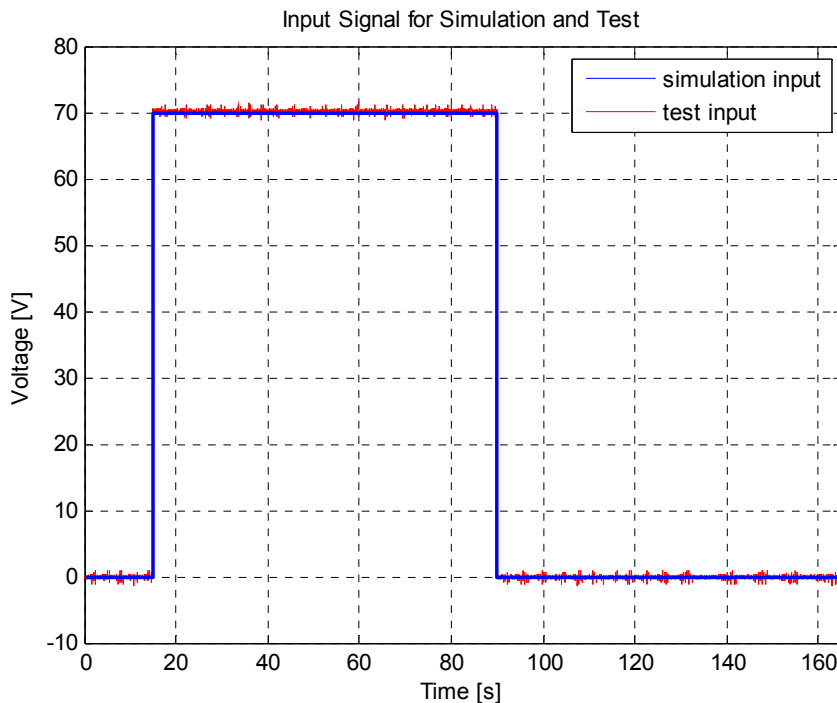


Figure 3-73. Voltage input used in simulation model and real life test model

After completion of data acquisition, the result of laser displacement sensor pointing at the tip of the beam is compared with the output of the simulation model. The comparison of the tip displacement results for test and simulation is given in Figure 3-74.

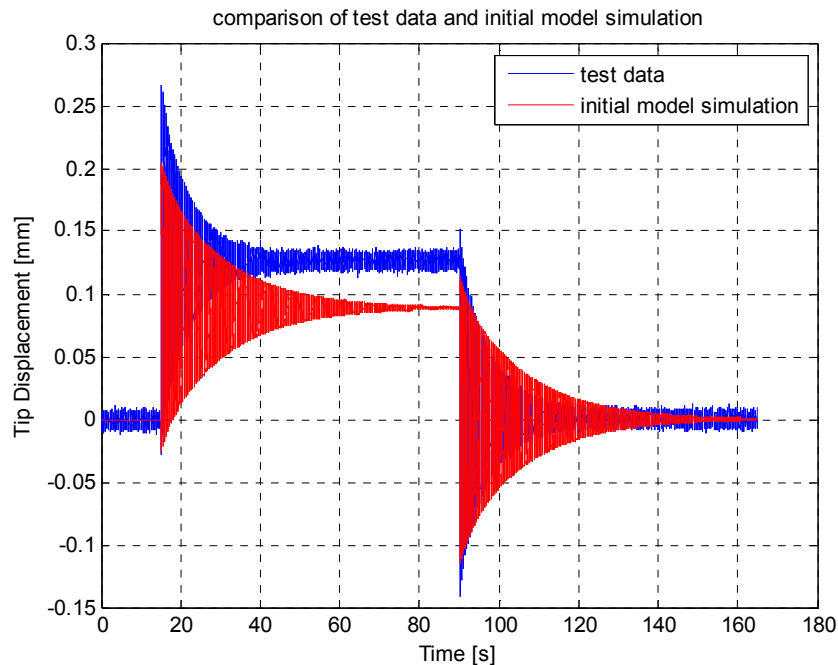


Figure 3-74. Comparison of results for the initial model and test result

By comparing the test results of the tip displacement with the simulation results of the initial model, and looking the results in detail as shown in Figure 3-75, it is seen that the peaks of two signals do not match after about 10-20 cycles. This is due to the fact that the first few resonant frequencies of the real life test model and the initial simulation model are close to each other but different in the 1/100's digit. To fit the resonant frequencies it is decided to play with the Young modulus of the steel which is the material of the beam since this material will have the largest effect on the resonant frequencies. The Young modulus of steel varies between 200 GPa and 210 GPa depending on the quality of the steel. After few simulations with different Young modulus values, the value for the model which fit best to the test data is found for 207 GPa. After finding the correct Young modulus, so the correct stiffness of the beam, other properties such as damping ratio and piezoelectric properties of the beam will be modified to make the model fit the test data.

From the comparison of the test data with the simulation results, it is observed that the steady state deflection values are different. These differences are also apparent when comparing the static analysis results in Chapter 3.2.2 and static deflection test results in Chapter 3.3.2. The static analysis result of tip deflection for an applied load of 70V is about 0.09mm, while the static deflection of the real beam when piezo patch#1 is loaded at 70V is measured to be about 0.13mm. It is understood from these results that the piezoelectric properties of the beam should be about %44 percent higher than the listed piezoelectric constants. To fit the analysis model with the test data, the d_{31} property of piezoelectric material APC 850 is entered as about 1.43 fold of the original value.

It is also seen from the above comparison that the initially assumed damping ratio of $\zeta = 0.001$ is lower than the actual value. Initially assumed damping ratio of simulation model can be updated by some trial and error. To fit the test data, several simulations are run and a proper damping ratio is found as $\zeta = 0.0022$.

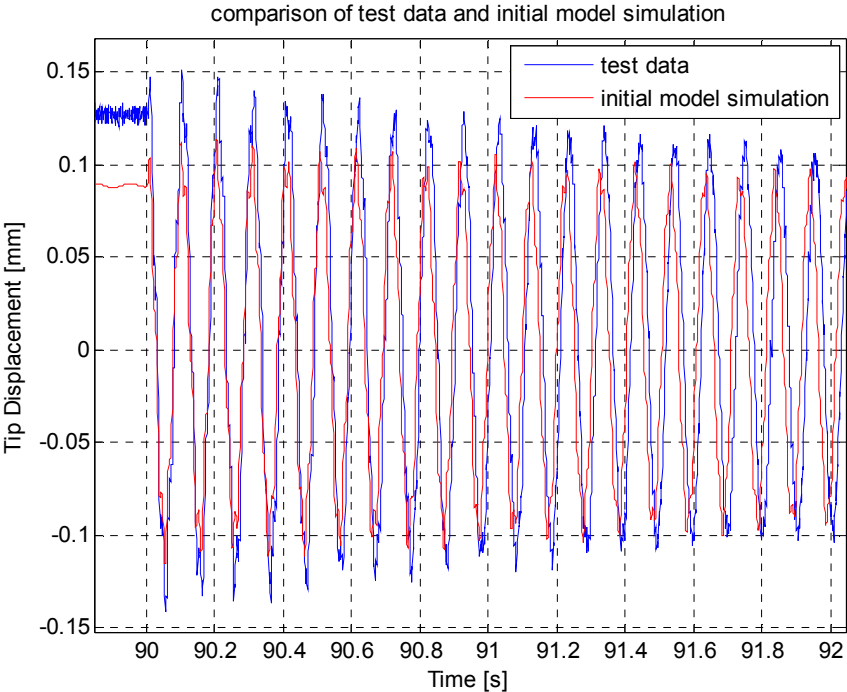


Figure 3-75. Comparison of results for the initial model and test result, detailed view

After setting proper values for the Young modulus of the steel, damping ratio of the structure, and piezoelectric constant d_{31} , the results of the simulation model computed using the state space matrices from ANSYS fits to the test data both in transient and steady state regimes. The comparison of the test data and the simulation results of the final model is given in Figure 3-76. The results of final updated model and the test data are also compared in detailed in Figure 3-77, which shows a pretty good match between the resonant frequencies of test and analysis models. As a final step of updating process, a random noise is added to the simulation results in comparison with test data.

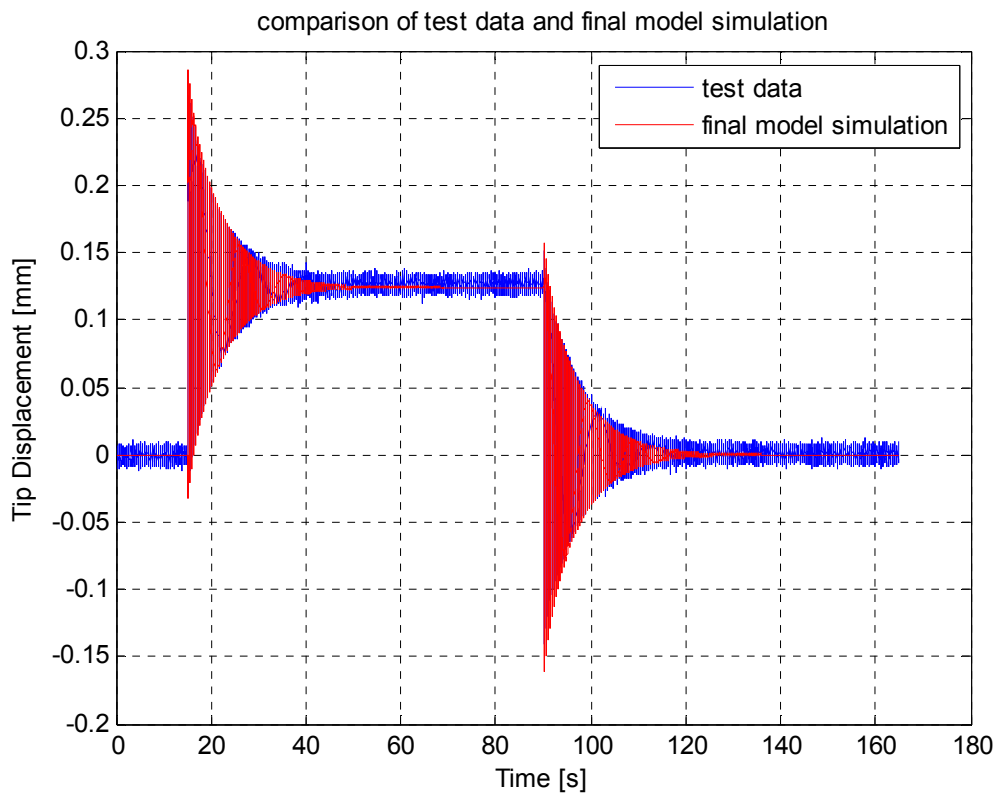


Figure 3-76. Comparison of test data with simulation of updated model

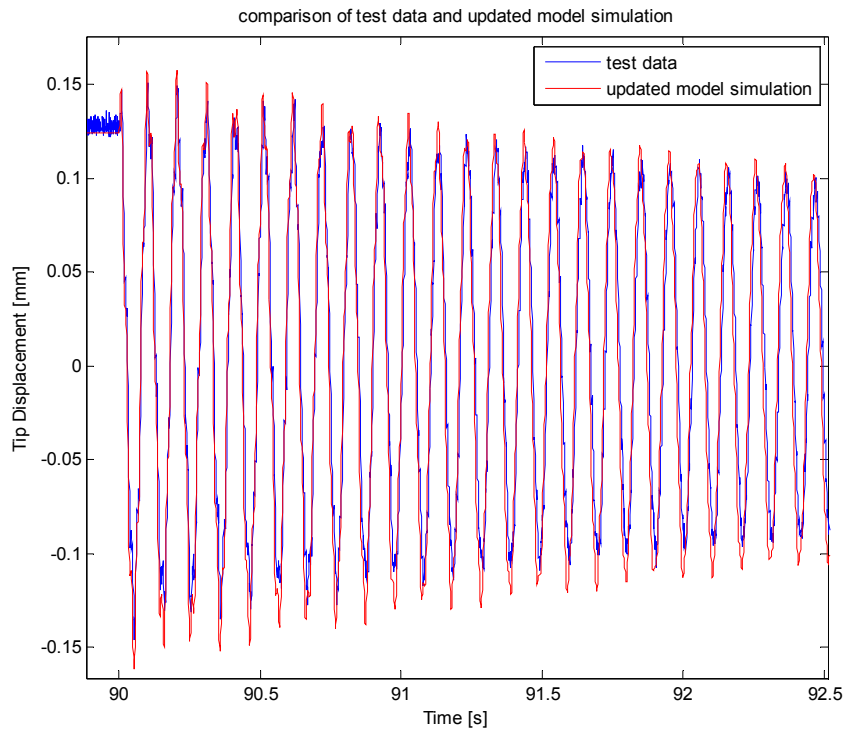


Figure 3-77. Comparison of test data with simulation of updated model, detailed view

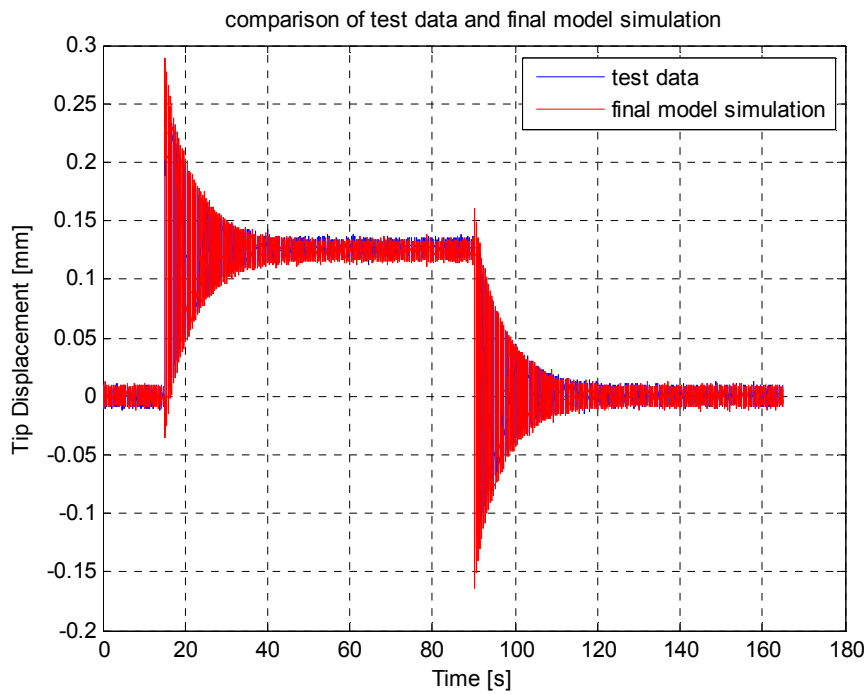


Figure 3-78. Comparison of test data with simulation of updated model with added noise

In test process, strain gage data is also acquired as well as laser displacement data. The data from strain gage #1 is given in Figure 3-79. It is seen that the dynamics of the beam is not captured by the strain gage.

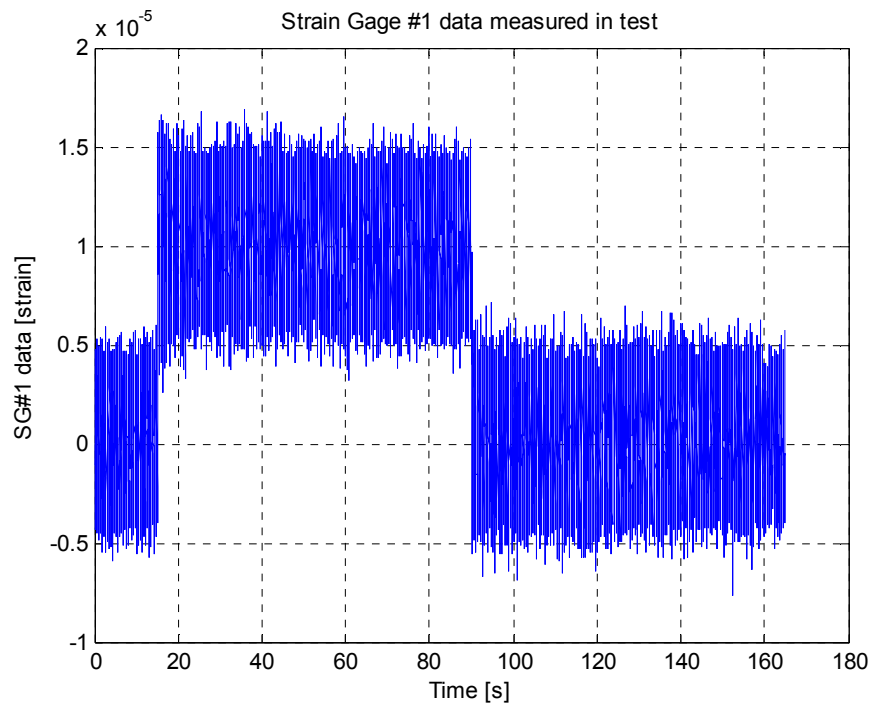


Figure 3-79. Data measured from strain gage #1 in the test

3.5 Controller Design and Simulations for the Updated Model

Having the model state space matrices (A,B,C and D) updated to fit the test data, the control simulation is expected to be more successful in predicting the controller parameters that will be useful in practical application.

The beam model in state space has the applied voltage at piezoelectric patch #1 across its electrodes. The input voltage is the input in the state space model, which is denoted as "u" in the equations. There is also a disturbance input which is taken as the force applied on the beam at its tip and it is denoted as "d". The output of the plant is taken as the tip displacement of the beam which is denoted as "y". The first two modes of the system are considered as the states of the system. Since there is no input which shows its effect directly in the output bypassing the system dynamics, D matrix will be zero. And since there is a disturbance input as force, the state space equations will be as given below

$$\dot{\mathbf{x}} = \mathbf{Ax} + \mathbf{Bu} + \mathbf{Ed} \quad (3.11)$$

$$y = \mathbf{Cx} \quad (3.12)$$

Note that details of modeling a vibratory system in state space is explained in Chapter 2.3. In that chapter, the calculation of A,B,C and E matrices are explained in detail.

A band-limited white noise block is added to the output of the plant to simulate the noise in the measurement of tip deflection by laser displacement sensor. The plant model, which has two inputs and one output is given in Figure 3-80.

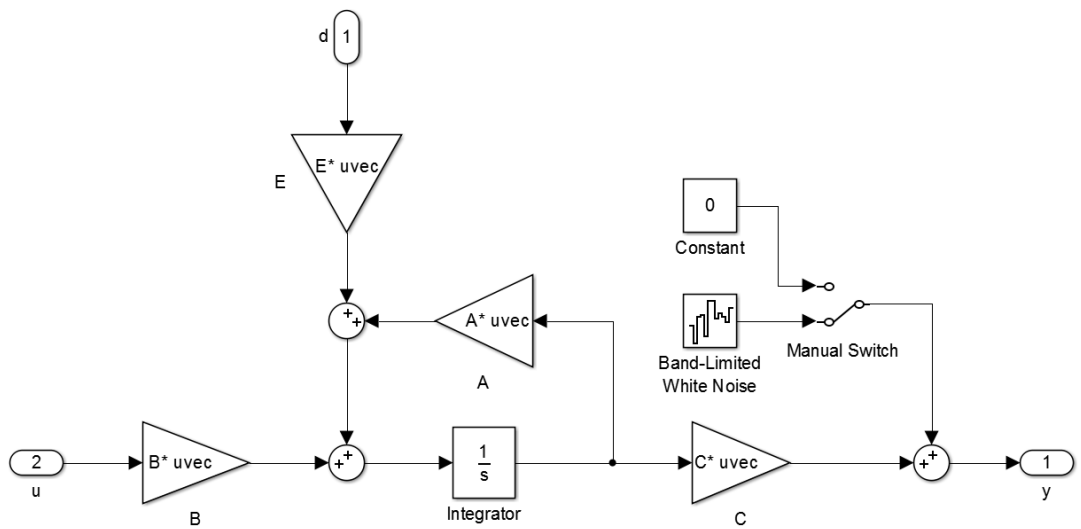


Figure 3-80. Plant model

A Proportional Integral Derivative (PID) controller is desired to be used for the system. Note that by the nature of controlling a real world system with the aid of a digital computer, the plant models should stay in the continuous domain (s domain), while the controller should be in the discrete domain (z domain). If a continuous controller is designed for a continuous plant in the simulation environment, there may be successful simulations, but the controller should be discretized before being loaded to the digital computer it will run on. Otherwise the parameters designed for the controller in the continuous domain will probably not fit to the parameters that work on a digital computer and control the system in real life. The simulation model used in tuning of control parameters is given in Figure 3-81.

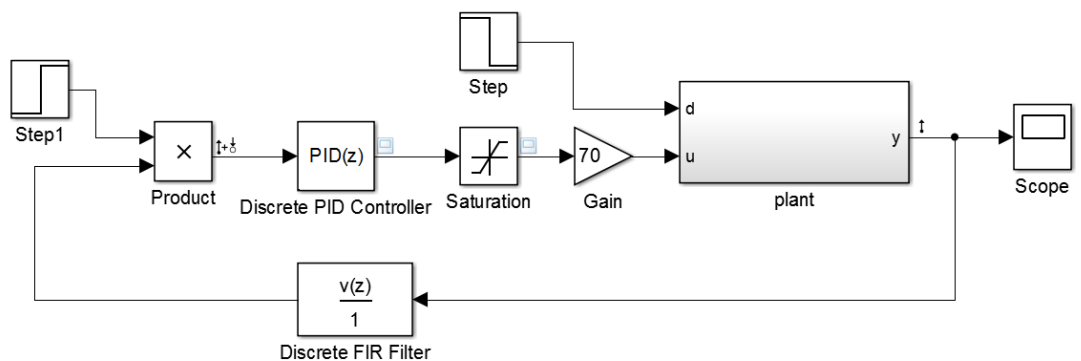


Figure 3-81. Simulink model of the PID controller simulation

In the simulation model, there is a two input single output plant, which is the model of the active beam. The input u is the control input voltage applied to the patch#1 and d is the disturbance input which is the deflection force applied at beam tip. The output y is the tip displacement of the beam and it is measured by laser displacement sensor. Keyence LK-G3001V laser controller unit has a built-in moving average for smoothing the displacement measurement and increase the stability of laser sensor. Moving average measurement mode is set to a value of 256 averages. In Simulink, the moving average feature of the laser sensor is created as discrete FIR filter. Moving average is generated by summing the previous samples with the current one and dividing the result by the number of samples included. When the input signal is entered in the filter, the signal is routed through a number of unit delays and a branch of signal is generated and added to the main stream. A block diagram of a moving average filter is given in Figure 3-82. Here $x[n]$ is the input signal and $y[n]$ is the output. The values of the gains depend on the number of averages included, so the value of each of the gain blocks is $(b_0, b_1, b_2, \dots, b_N)$ equal to $1/N$.

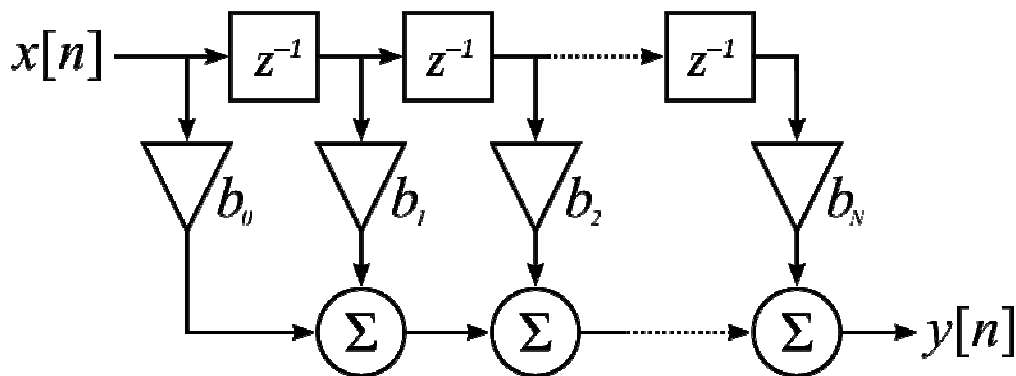


Figure 3-82. Block diagram of moving average

In the test model there is a saturation block added at the exit of the controller. The saturation block does not allow voltage outputs out of the bound of -1V to 1V. At the exit of the saturation block there is a gain block of 70V, which represents the piezoelectric voltage amplifier. By using saturation block, it is made sure not to send piezoelectric actuator more than 70V to ensure safe operation. The limit in the actuator voltage is also put in the simulation model.

The disturbance input for the model is decided to be a step input. It starts at time=0s as 0.1N and drops suddenly to zero at time = 60s. This force deflects the beam about 1.8mm. After about 30 seconds the beam settles to steady state condition. At 60th second the disturbance force is suddenly released and the beam is set to vibrate freely. There is another step input block in the model which is related to the control input. Until time = 60, the feedback coming into the controller block is kept zero. At time = 60s the controller is activated. By preparing model in a manner explained above, the condition of holding the beam and suddenly releasing is simulated. In the simulation first 60 seconds are for the beam without control and the next 60 seconds are for the beam with control.

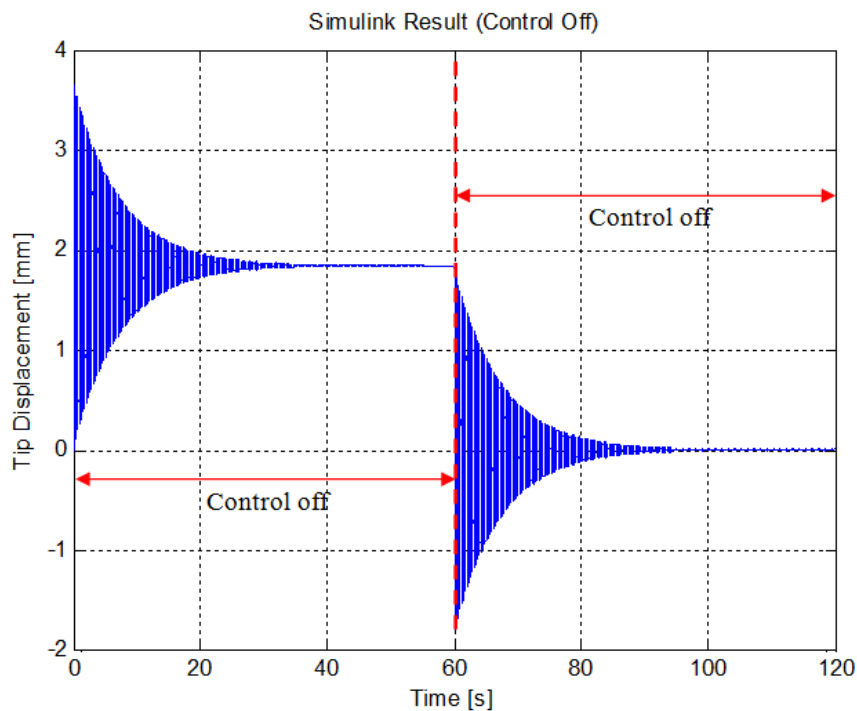


Figure 3-83. Beam simulation result without control

The controller is desired to be a PID controller. Simulating with different controller parameters and checking the result, it is observed that a P controller with a gain of $K_p = 3$ would be sufficient for control purposes. In Figure 3-84, the simulation result of the beam with control action is given. In Figure 3-85, the same simulation with added sensor noise is shown. The noise on the laser displacement sensor data does not affect the control action.

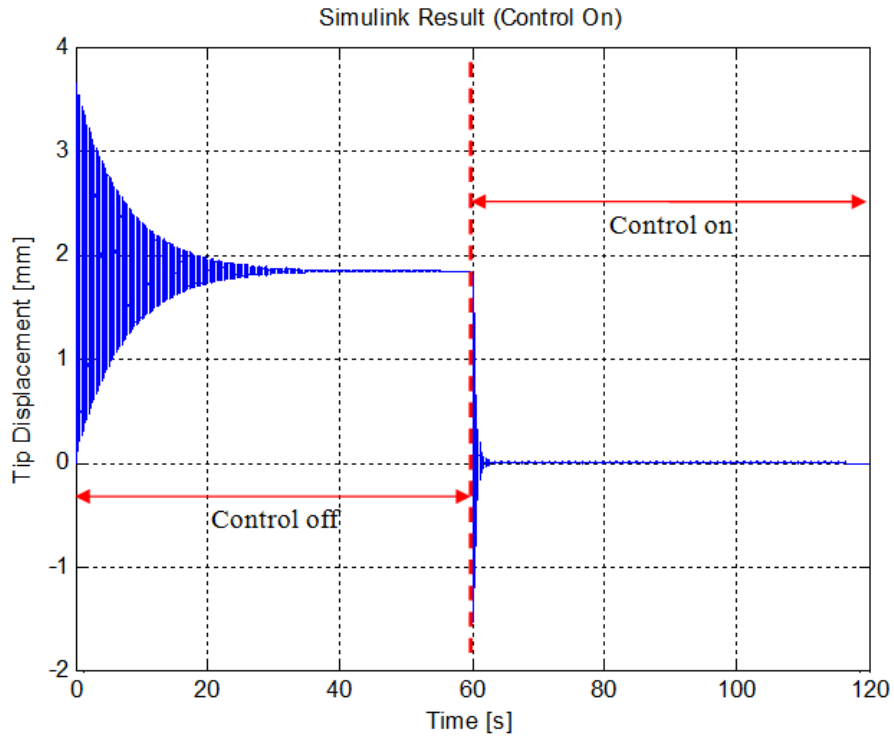


Figure 3-84: Beam simulation with control

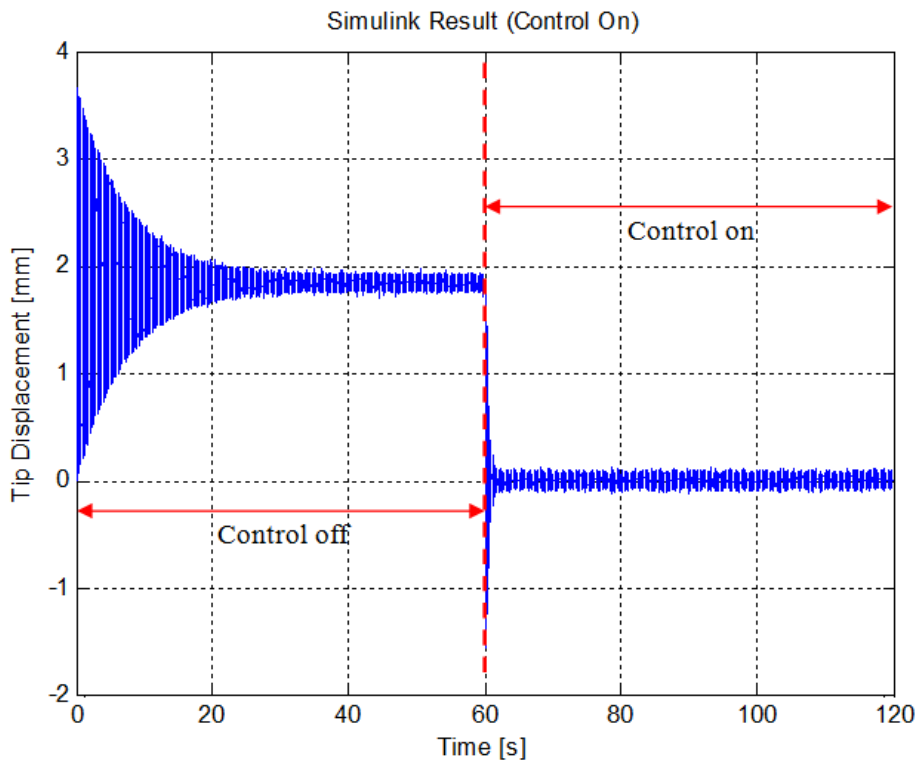


Figure 3-85. Beam simulation with control and with added noise

Pole placement method is another approach in controller design. In this approach, a controller is designed such that the input to the actuator is $\mathbf{u} = -\mathbf{K}\mathbf{x}$ where \mathbf{x} is the states of the system and \mathbf{K} is the controller matrix. That is why this type of control is called state feedback control. Details of this controller are explained in Chapter 2.7.

In the design of state feedback controller, the same plant model as in the PID control design is used. State feedback control requires that all the states of the system are known. However the states of the system are assigned to be the modal positions and velocities of the model and they cannot be measured physically. In the model the tip displacement is the only measured physical property. Here a virtual dynamic system needs to be coupled with the plant model to obtain the states of the system that are needed for the controller. That system is the observer and it is used to estimate the states of the system based on measurements of the sensors, which are the system outputs. The estimated states from the observer are input for the state feedback controller. At the exit of the controller there is a saturation block to limit the applied voltage to piezoelectric patches. In the simulation it is made sure that the voltage applied on the patch actuator does not exceed 70V. A tip force is applied on the beam as a step disturbance. Tip displacement of the beam is measured and the active vibration control system is designed to suppress the vibrations. The Simulink model of the whole system is given in Figure 3-86 and model of the observer is given in Figure 3-87.

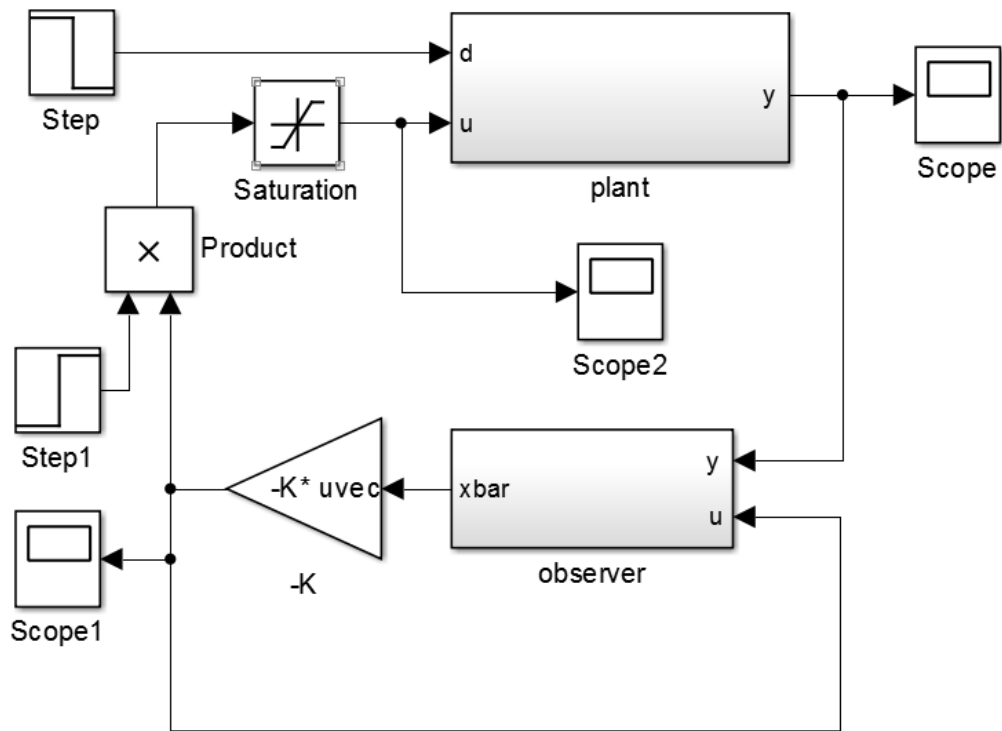


Figure 3-86. Simulink model for full state feedback control simulation

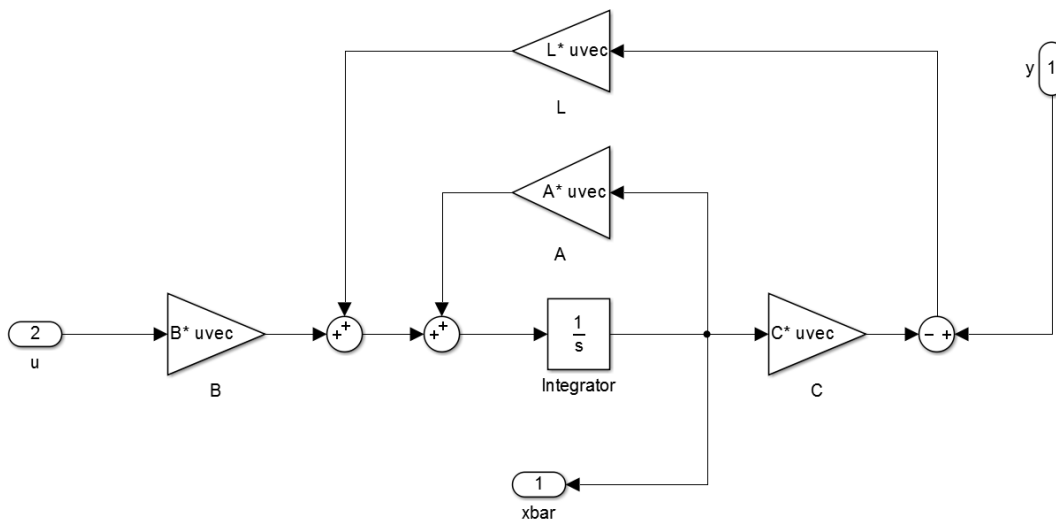


Figure 3-87. Observer model for full state feedback controller

On the observer model and the controller model, two blocks are unknown, namely the controller gain matrix \mathbf{K} , and the observer gain matrix \mathbf{L} . These blocks change

the performance of the controller and they are part of the controller design. According to the design requirements of the control system, the controller gain matrix \mathbf{K} and the observer gain matrix \mathbf{L} are designed.

After plant model is generated, the poles of the plant model are plotted in the s-plane. It is observed that the damping ratio of the poles of the original system is quite low, and the poles are close to the imaginary axis, which reduces the stability of the system and makes it very oscillatory. To improve the transient dynamics of the system and reduce the oscillations, the damping ratio of the system and so the closed loop poles should be increased. To increase the damping ratio of poles, they should be rotated towards the real axis and their distance to the origin should be kept the same as previous. The details of pole placement and observer design are given in Chapter 2.7. In this controller design the poles are placed to a location such that they make 45° with the real axis and their distance to the origin kept the same as previous. This does not change the natural frequencies of the closed loop system but makes it critically damped as desired. By placing the closed loop poles of the system to 45° location, the damping ratio of the poles of the system is increased to $\zeta = 0.707$. To calculate the controller matrix \mathbf{K} , MATLAB's "place" command is used. In "place" command, \mathbf{A} and \mathbf{B} matrices of the plant are supplied together with the desired pole locations. The plant poles and closed loop system poles are given in Figure 3-88.

In this system there is a state observer to estimate system states from measurements. Note that the details of observer design is given in Chapter 2.7. For a proper operation of observer, the observer poles should be 3 to 5 times faster than the system poles. So the observer poles are designed to be at 45° angle with the real axis but at a distance of 5 times more than the closed loop system poles. The observer matrix \mathbf{L} is calculated by MATLAB's "place" command supplying \mathbf{A}' and \mathbf{C}' and designed observer poles instead of \mathbf{A}, \mathbf{B} and closed loop system poles as in the controller design. The observer poles with the closed loop system poles and plant poles are given in Figure 3-89.

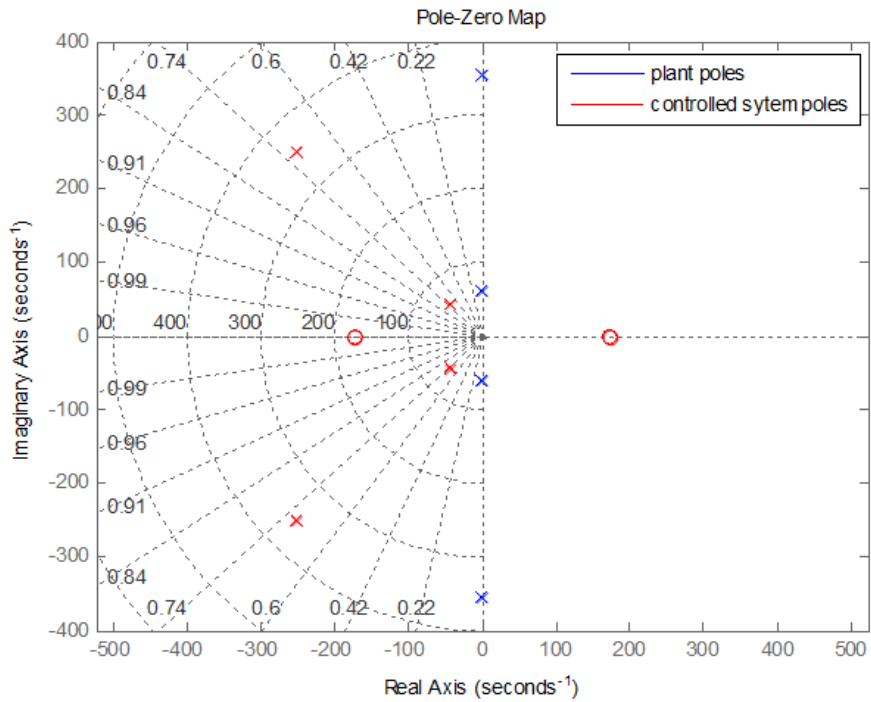


Figure 3-88. Uncontrolled plant poles and controlled system poles on s-domain

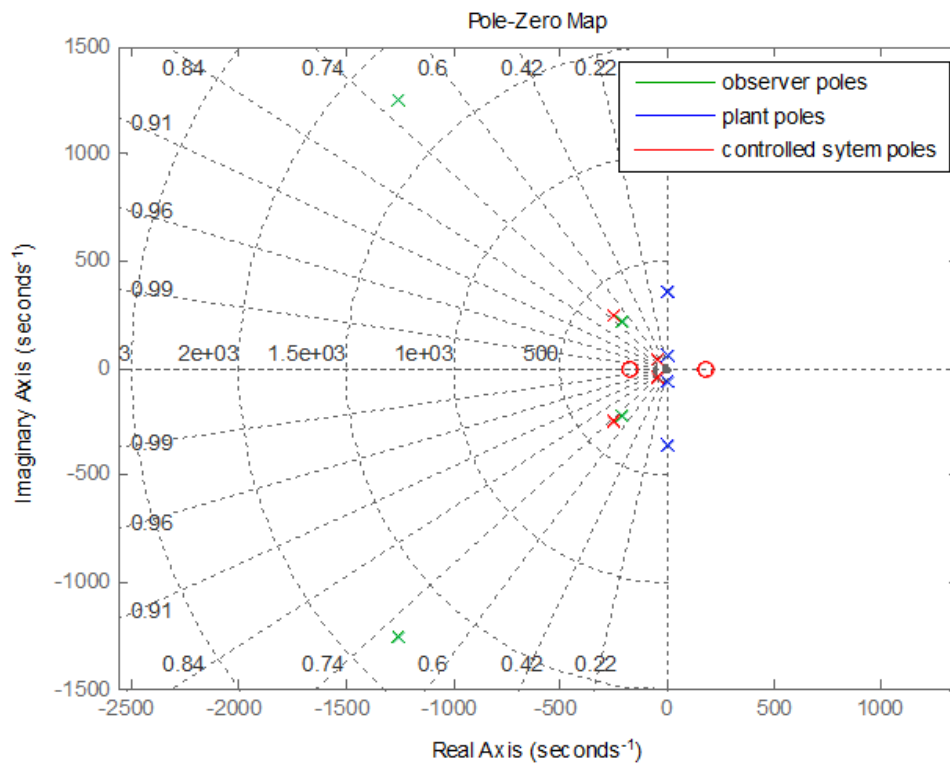


Figure 3-89. Observer poles, uncontrolled plant poles and controlled system poles on s-domain

Other than s-domain analysis, a frequency domain analysis of the designed control system is also made. The Bode plots of the original plant and the controlled system are given in Figure 3-90. Note that the first two resonances of the structure are suppressed by the active vibration control system. By this procedure active damping control is added to the structure.

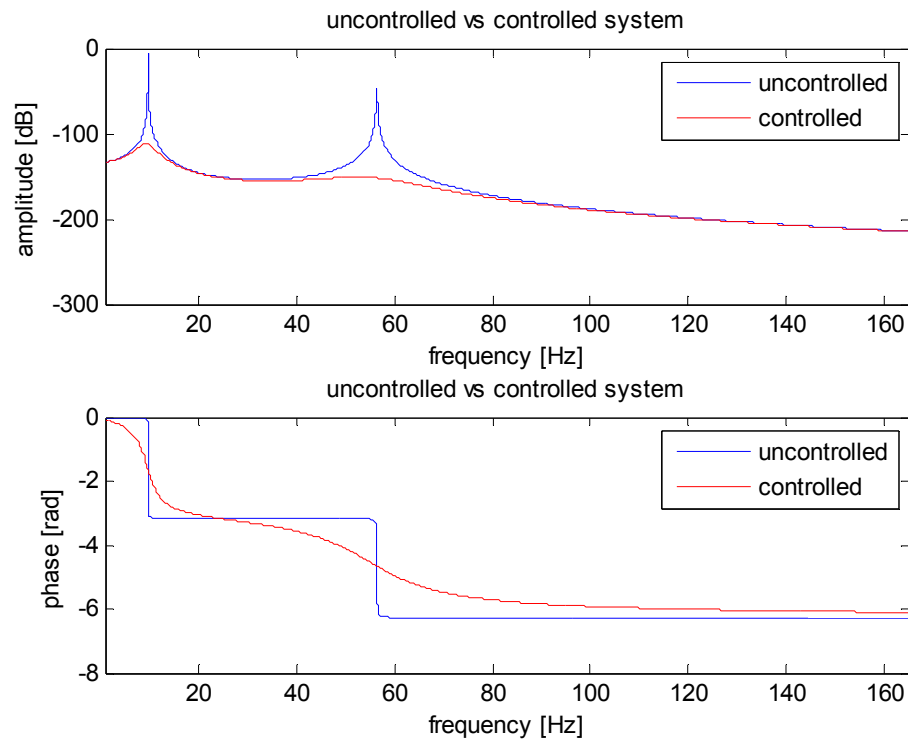


Figure 3-90. Frequency responses of uncontrolled and controlled models

As a final step of controller design, time domain analysis is carried out using Simulink. A step disturbance is applied to the system as force. The simulations run for two cases, with and without added noise. By this procedure robustness of the controller for the noise is tested. The effect of step disturbance on the output of the system for controlled and uncontrolled cases are simulated. In Figure 3-91 and in Figure 3-92 the simulation results without added sensor noise is given. In Figure 3-93 and in Figure 3-94 simulation results with added sensor noise is given. Note that the added noise to the sensor used in generating the feedback signal reduces the performance of the controller. It is observed that the controller in the case without

added noise suppresses the oscillations in 3 cycles, however in the case with added noise it takes 6 cycles for the controller to stop the oscillations.

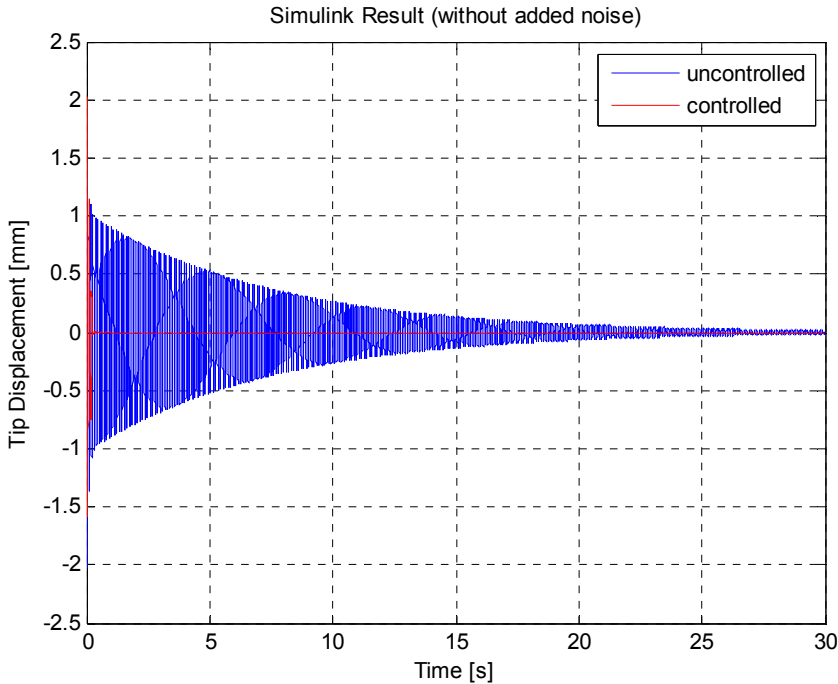


Figure 3-91. Simulation result without added noise

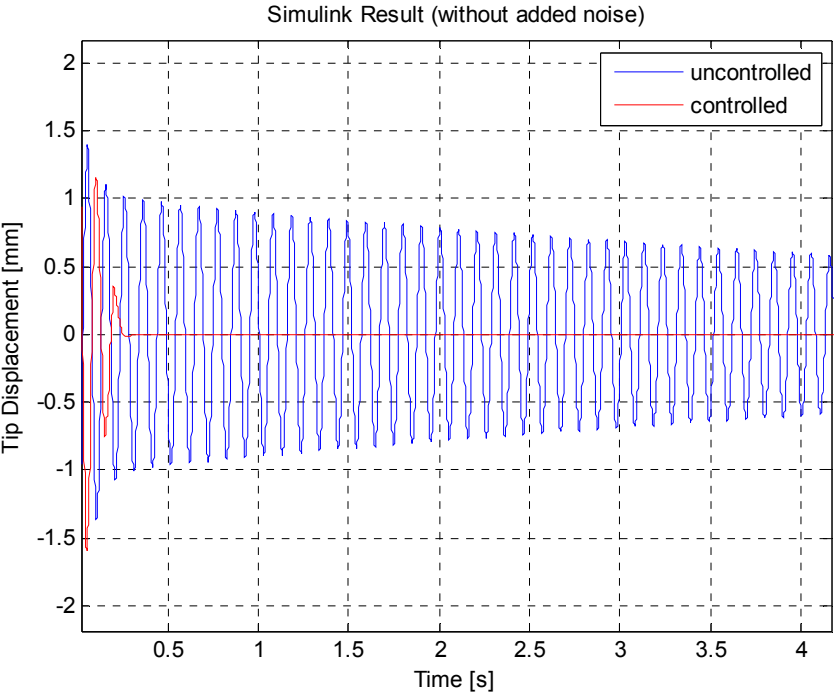


Figure 3-92. Simulation result without added noise, detailed view

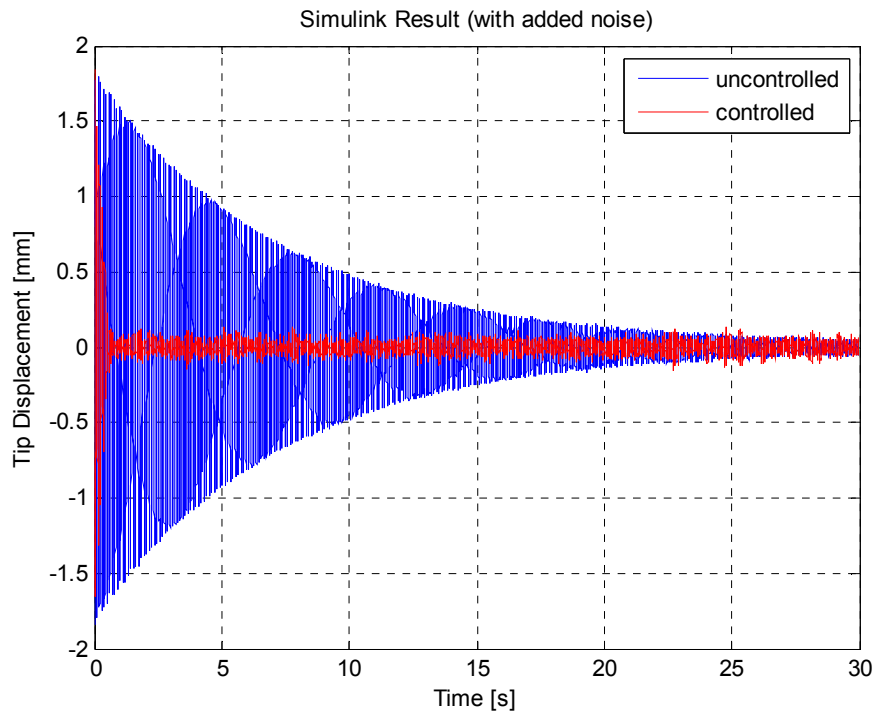


Figure 3-93. Simulation result with added noise

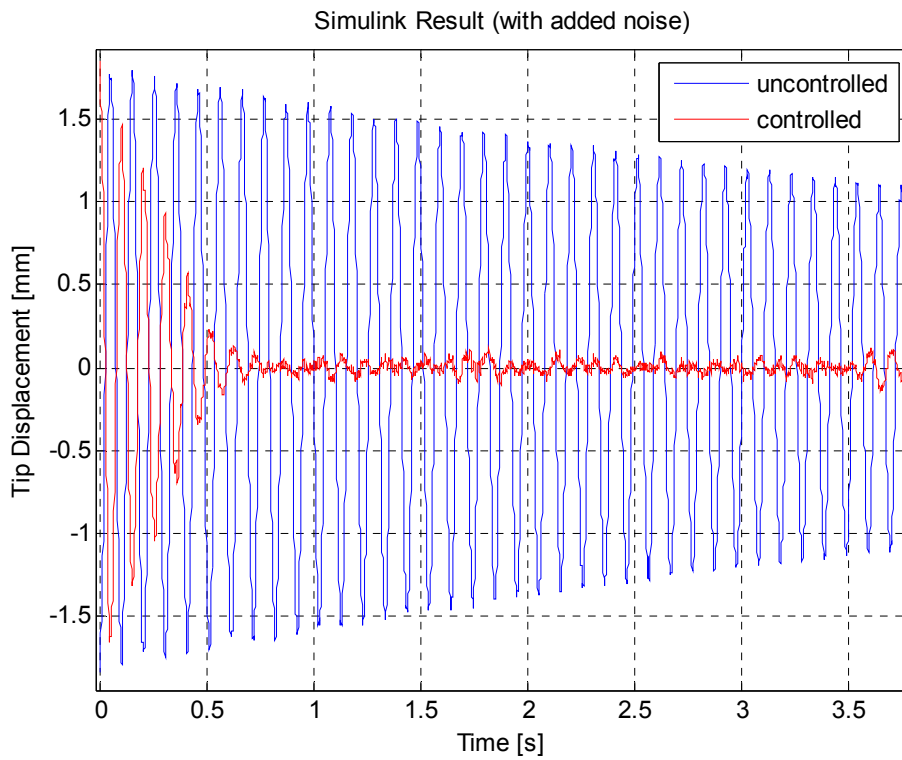


Figure 3-94. Simulation result with added noise, detailed view

3.6 Implementation of Controller to Beam Structure

As a final step of the active vibration control study of beam structure, the designed controller is implemented on the real life structure using MATLAB xPC Target. The Simulink model used in the control studies is given in Figure 3-95. A discrete PID controller is used with the parameters $K_p = 3$, $K_d = 0$ and $K_i = 0$ as in the design phase.

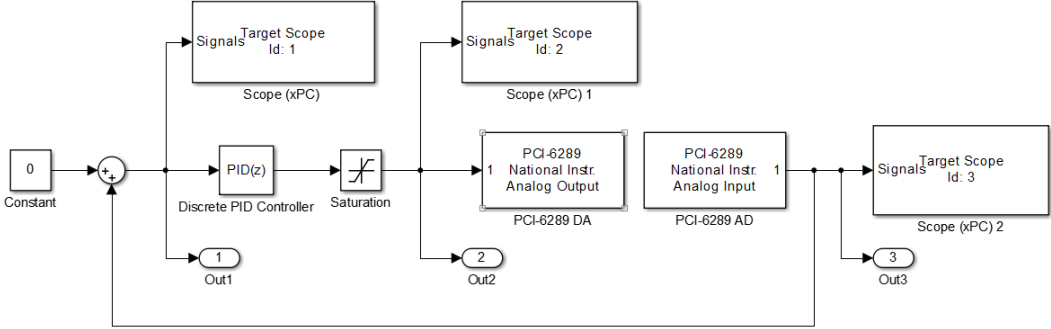


Figure 3-95. Simulink model used in PID control implementation

PID controller works with the same coefficients that are predicted in the design and simulation phase since the controller is designed in discrete domain in the first step. The result of implementation for the rejection of disturbance force is given in Figure 3-96.

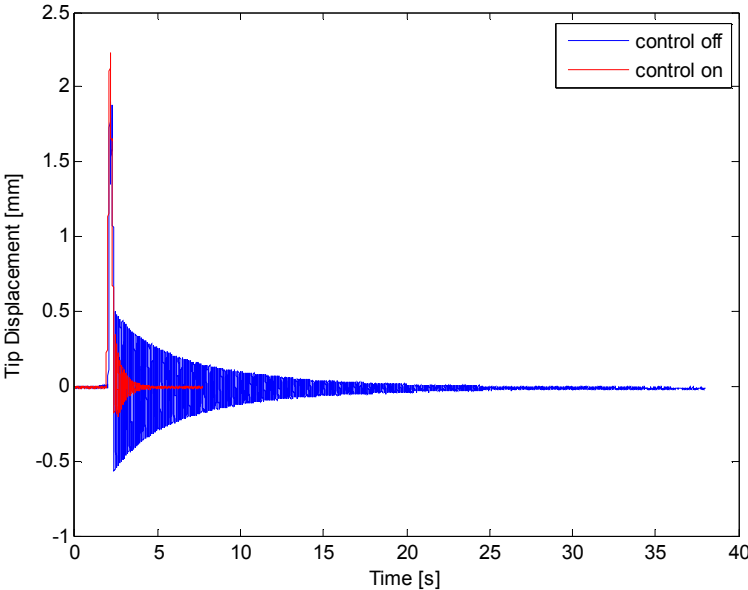


Figure 3-96. Result of PID implementation, test data

An interesting test to do is using one of the piezoelectric patches as the source of disturbance and trying to control the beam vibrations with the other patch. A sine input voltage signal at 9.8 Hz is applied to piezoelectric patch#2 as a source of disturbance and the patch#1 is connected to active vibration control system to suppress the effects from patch#2. Tip deflection of the beam measured by laser displacement sensor is used as feedback signal. In the test, the disturbance is applied first, and after reaching steady state, the controller is turned on with $K_p = 1$. After data acquisition for a while then the coefficient of P controller is increased to $K_p = 2$. This step by step procedure is kept until $K_p = 5$ after which the system starts to be unstable. In Figure 3-97 the tip deflection data of the beam is given until it becomes unstable. It is seen from the figure that after $K_p = 3$ the effect of controller does not increase much. That coefficient is kept as the coefficient for the P controller.

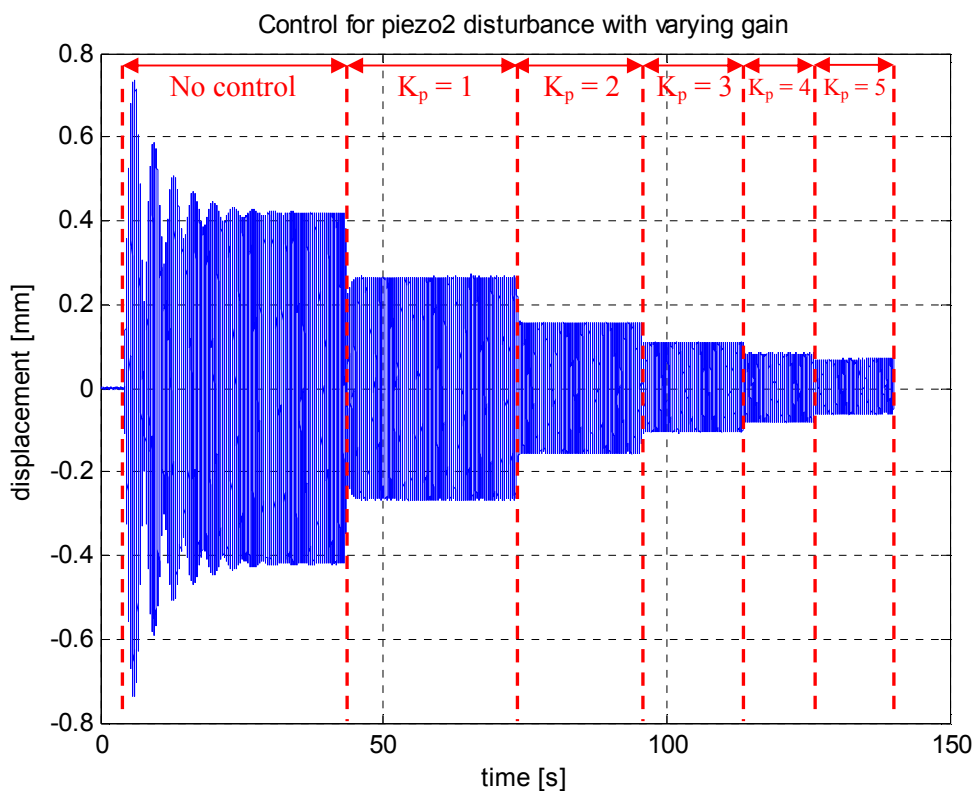


Figure 3-97. Control with piezo1 for disturbance from piezo2 with different controller gains

CHAPTER 4

ACTIVE VIBRATION CONTROL OF CYLINDER USING PIEZOELECTRIC PATCHES

4.1 Introduction

As a second part of active vibration control study a cylinder model is studied. The thickness of the cylinder changes in 4 levels along the length. Schematic representation of the dimensions of the cylinder is given in Figure 4-1.

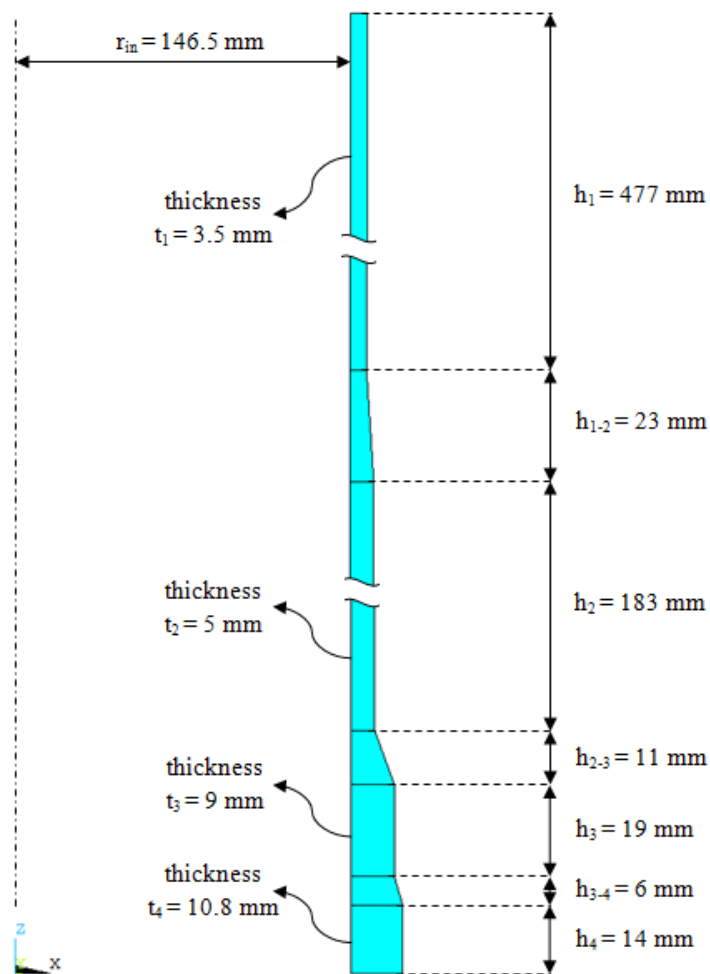


Figure 4-1. Dimensions of the cylinder

The hollow cylinder part is made of steel. The part is a seamless hollow tube and it is produced by a special technique called radial forging. The initial thickness of the cylinder is about 11mm. In radial forging, the inner diameter of the cylinder is supported by a mandrel and the thickness of the cylinder is reduced and the cylinder is elongated by means of radial rollers punching to the outer diameter of the cylinder in radial direction. This gives higher strength to the steel since it is manufactured by compression.

A photo of the real cylinder and a 3 dimensional solid model of the cylinder prepared in ANSYS are given in Figure 4-2.



Figure 4-2. Photo and 3-D model of the cylinder

For the cylinder structure to be used in active vibration control study, Physik Instrumente Dura Act type piezoelectric patches are planned to be used. Those type of patches are bendable, so they can be applied on curved surfaces. A photo of a Dura Act type piezoelectric patch is given in Figure 4-3 [55].



Figure 4-3. PI Dura Act type piezoelectric patch [55]

In this chapter of active vibration control study, same tools as in the beam study will be used. The most important difference between the beam and cylinder study is the placement of piezoelectric patches over the cylinder structure to control the desired modes. In cantilever beam structure it is obvious to place the actuator at the root, however mode shapes of the hollow cylinder are more complicated than the cantilever beam, so placement of patches requires additional analyses.

4.2 Finite Element Modeling of Cylinder with Piezoelectric Patches

Finite element model of the steel hollow cylinder and piezoelectric patch on it is generated in ANSYS using solid elements. Piezoelectric patches are modeled by SOLID 226 coupled field elements and steel cylinder is modeled by SOLID 186 elements. Both SOLID 226 and SOLID 186 are 20 node brick elements, and they have midside nodes so they can model the bending behavior quite well. Having 20 node element for both types of mesh serves the purpose of mesh connectivity. It is not preferred to use shell to solid coupling or any coupling equation between the steel cylinder and piezoelectric patch, so for the sake of mesh connectivity 20 node brick elements are used for both piezoelectric patch and steel cylinder. The mesh size chosen is ideal for this model for the analysis speed and accuracy considering usage of 20 node elements. The finite element model of the hollow cylinder with a piezoelectric patch has a total number of 7362 elements and 52049 nodes and is given in Figure 4-4.



Figure 4-4. Finite element mesh over the 3-D cylinder model

Cylinder part is made of steel and its material properties used in the analyses are given in Table 4-1.

Table 4-1. Material properties of steel

Elastic modulus	210×10^9 Pa
Poisson's ratio	0.3
Density	7850 kg/m^3

The material of the Dura Act piezoelectric patch used in this study is PIC 255 and its properties are given in Table 4-2 and Appendix B.

Table 4-2. Material properties of PIC 255

Density	7.800 kg/m ³
Piezoelectric constants	
d ₃₁	-1.8 x10 ⁻¹⁰ m/V
d ₃₃	4.00 x10 ⁻¹⁰ m/V
d ₁₅	5.50 x10 ⁻¹⁰ m/V
Elastic constants	
S ^E ₁₁	1.61 x10 ⁻¹¹ m ² /N
S ^E ₃₃	2.07 x10 ⁻¹¹ m ² /N
S ^E ₁₂	-5.70 x10 ⁻¹² m ² /N
S ^E ₁₃	-7.37 x10 ⁻¹² mm ² /N
S ^E ₄₄	4.49 x10 ⁻¹¹ mm ² /N
S ^E ₆₆	4.32 x10 ⁻¹¹ mm ² /N
Dielectric constants	
$\epsilon_{11}^T/\epsilon_0$	1650
$\epsilon_{33}^T/\epsilon_0$	1750
ϵ_0	8.85 x10 ⁻¹² F/m

The cylinder model weighted approximately 23 kg. In finite element model the cylinder is modeled to have free-free boundary conditions and laboratory test model rests on soft foam rubber sheets.

As an initial approximation, the damping ratio will be estimated as $\zeta = 0.001$ for the system.

4.3 Finite Element Analysis of the Cylinder Structure

4.3.1 Modal Analysis

Modal analysis is carried out as the first analysis of the cylinder. In the initial analysis, natural frequencies and mode shapes of the steel cylinder are computed. An important property of the cylinder is cyclic symmetry. Due to the symmetry, cylinder has double modes, modes that occur at the same frequency but with a symmetric

mode shape. Note that it is expected to have a slight change of the natural frequencies of the cylinder after placing a piezoelectric patch. Adding a patch will disturb the cyclic symmetry, so the natural frequencies of double modes will not be exactly at the same frequency. The natural frequencies of first ten modes of the cylinder are listed in Table 4-3.

Table 4-3. Analysis results of the cylinder model

Mode number	Natural frequency (Hz)
1	114.80
2	114.80
3	204.06
4	204.06
5	313.88
6	313.88
7	484.74
8	484.74
9	589.13
10	589.13

In the modal analysis of the cylinder to obtain the first ten modes, breathing modes are encountered. Those 10 modes are double modes and mode shapes are given in Figure 4-5, Figure 4-6, Figure 4-7, Figure 4-8 and Figure 4-9.

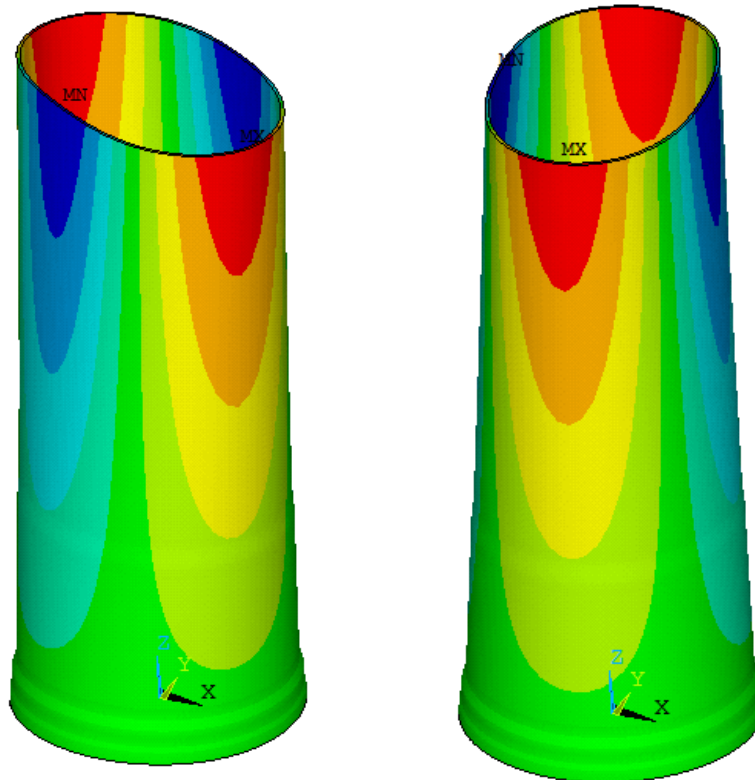


Figure 4-5. 1st and 2nd mode shapes

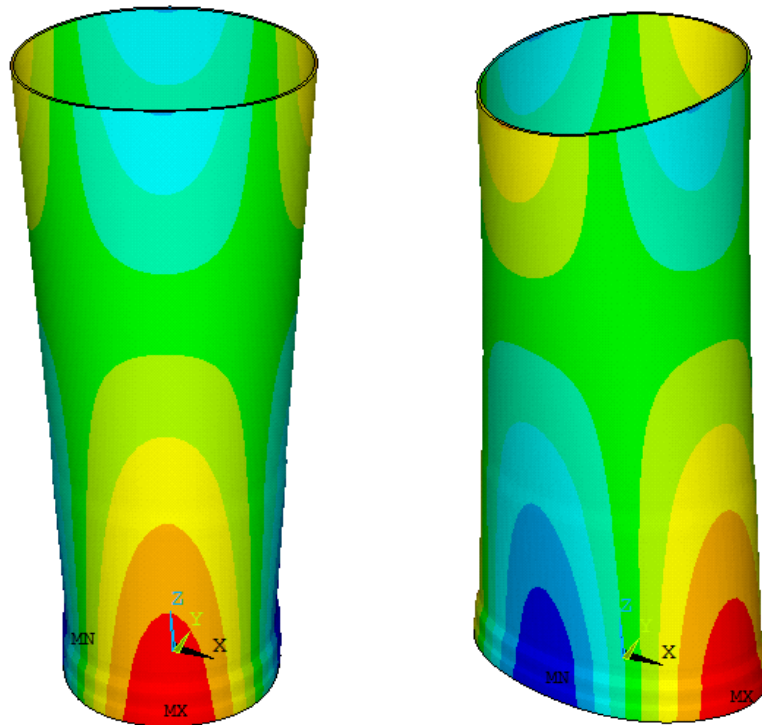


Figure 4-6. 3rd and 4th mode shapes

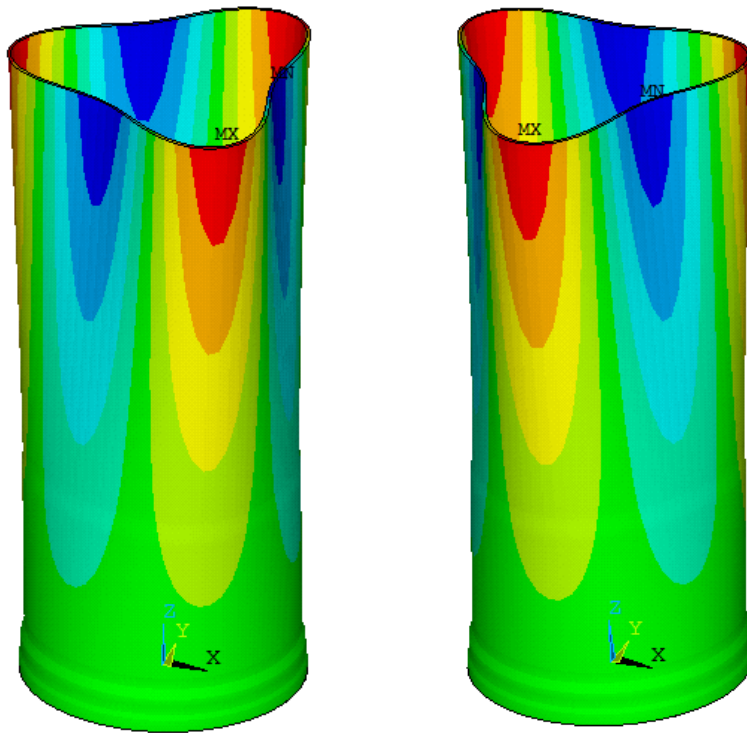


Figure 4-7. 5th and 6th mode shapes

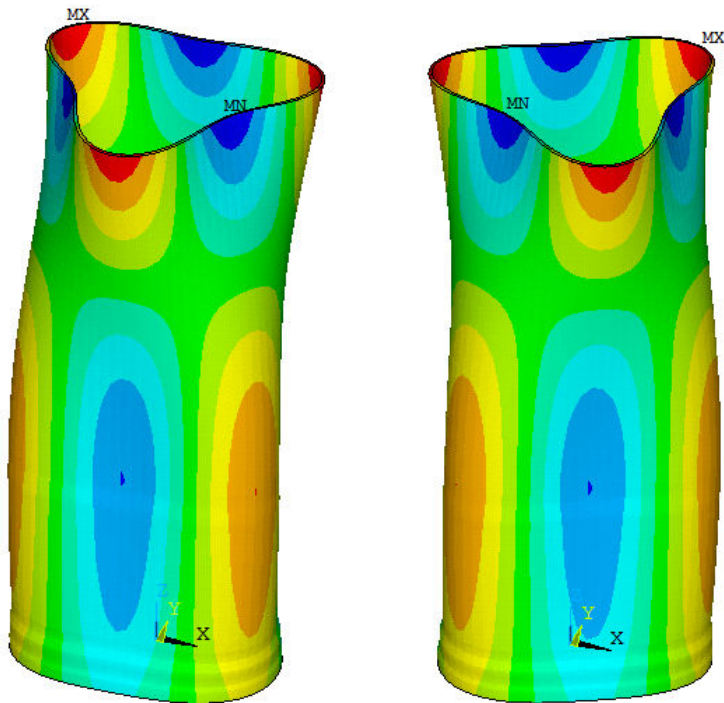


Figure 4-8. 7th and 8th mode shapes

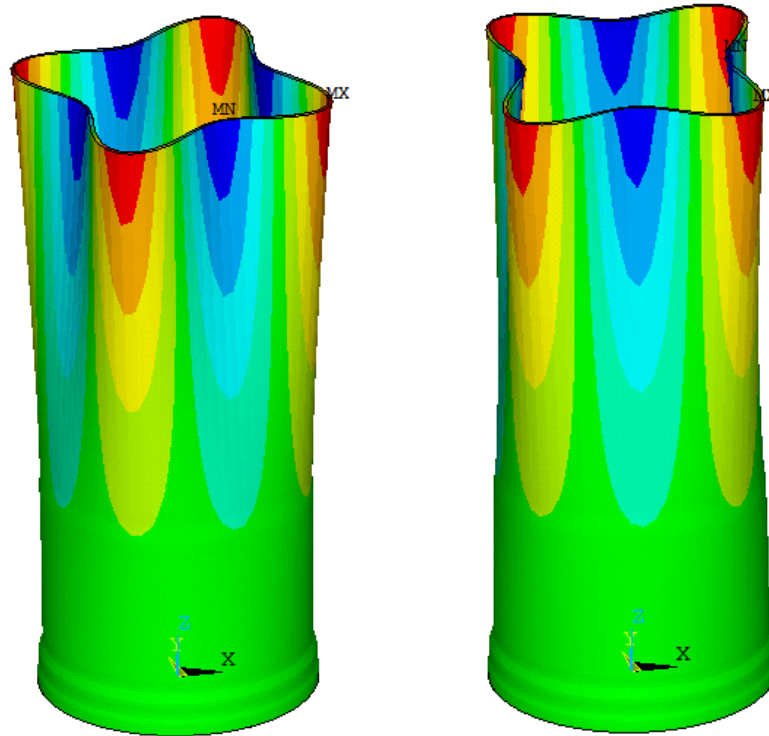


Figure 4-9. 9th and 10th mode shapes

It is expected to have approximately 1 Hz increase in the natural frequencies of the cylinder structure with a piezoelectric patch due to stiffening effect of the added piezoelectric material. However the increase in each natural frequency is not exactly known without determining the patch location.

4.3.2 Static Analysis

After modal analysis, a static analysis is desired to be made over the cylinder with an added piezoelectric patch for curiosity. For this purpose a piezoelectric patch actuator is placed on an arbitrary location over the cylinder and 150V static voltage load is applied between its electrodes. Deformation in the radial direction is plotted over the 50000 times exaggerated deformed shape of the cylinder in Figure 4-10.

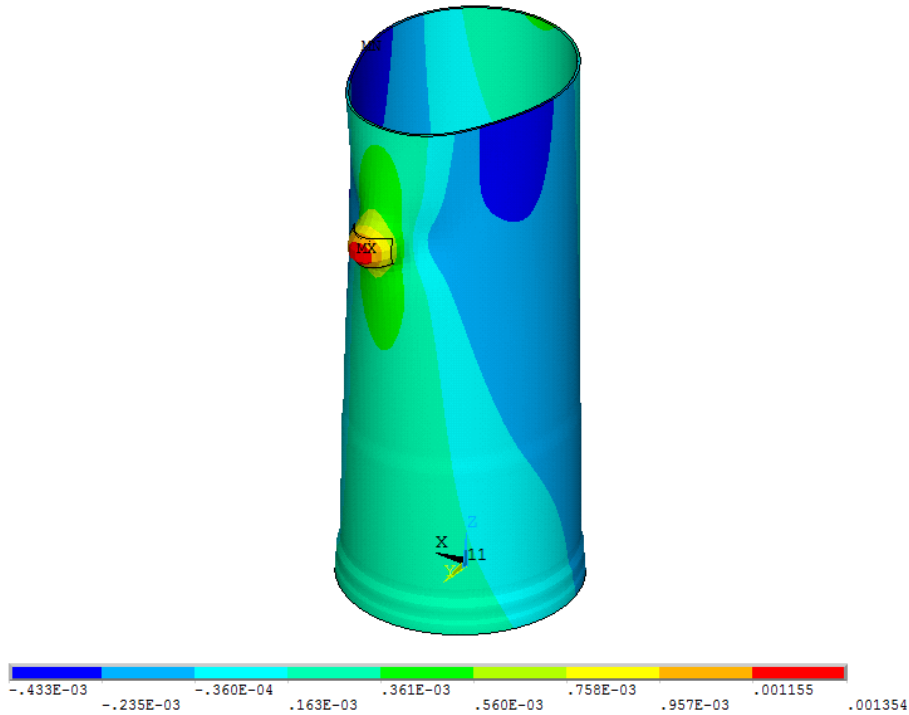


Figure 4-10. Result of static analysis over the cylinder

4.4 Placement of Piezoelectric Patches by Controllability Concepts

ANSYS Parametric Design Language (APDL) is a handy finite element tool in design problems where programming skills are required. In the optimal placement of piezoelectric patch actuator problem, the optimal location is selected based on the controllability Gramian of the resulting system. Each model with a different piezoelectric patch actuator is a different system. The best location is the one that results with a system whose controllability Gramian is the highest. For this, state space matrices of different systems with possible piezoelectric patch actuator locations should be computed. In this study ANSYS APDL is used to model different systems with piezoelectric patch actuators at different locations. After modeling APDL is again used to compute the state space matrices of each possible system with different patch locations. State space matrices of each system corresponding to different patch locations are taken by MATLAB. Controllability Gramian matrices of the corresponding systems and eigenvalues of those matrices are computed for each possible actuator location using MATLAB. According to a placement criterion, optimal actuator location for target modes is obtained.

The possible locations for piezoelectric patch actuators are defined on the portion of the cylinder with a 3.5mm thickness. This portion of the cylinder is further divided into volumes for proper mesh generation in ANSYS. After this volume division, the outer surface of the cylinder is also divided in areas. A piezoelectric patch can be placed on any of these areas on the outer surface of the cylinder. The portion of the cylinder is divided into 18 in radial direction and 15 in axial direction. Those divisions are decided considering the size of the piezoelectric patch and the dimensions of the cylinder. In total it makes 270 possible piezoelectric patch actuator locations. In the patch actuator placement, a coordinate system is used over the cylinder so that Q denotes the radial position and H denotes the axial position of the patch over the cylinder. Orientation of Q and H positions over the cylinder is shown in Figure 4-11. Note that Q and H coordinates are defined over the cylinder section with 3.5 mm thickness.

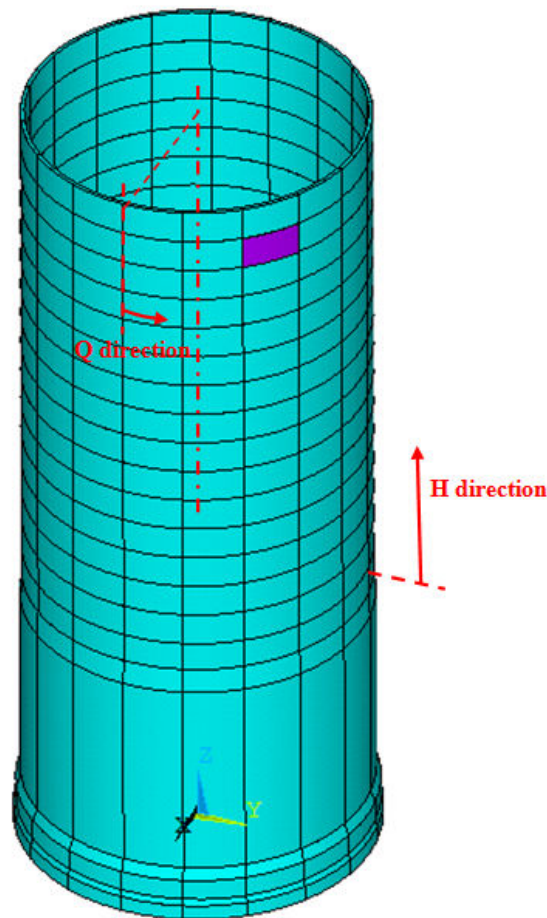


Figure 4-11. Cylinder structure with divided volumes and a patch actuator

In Chapter 2.5 detailed theoretical information is given about the piezoelectric patch actuator placement using a placement criteria based on the eigenvalues on controllability Gramian matrices. In this study the target modes are decided as 1st, 2nd, 5th and 6th modes. Any other modes can also be selected.

In the calculation, as a result of the modal analysis by ANSYS, the radial angles of motion of the breathing modes are at some fixed angles. However, the deflection shapes of the cylinder breathing modes depend on the orientation of the excitation force. This is a unique property of structures with cyclic symmetry. As an example to illustrate this phenomenon, one can consider the 1st mode shape calculated from ANSYS. If the task is finding the optimal piezoelectric patch location to control 1st mode of the cylinder excited by a force in X direction, then the current orientation of mode shape coming directly from ANSYS will lead to wrong results. Reason of the wrong calculation is that the orientation angle of the 1st mode shape coming from ANSYS is any angle, but in reality the deflection shape of the 1st mode of the cylinder excited as a result of a force in X direction will make 0 degrees with the X axis. In Figure 4-12, the above explanation is illustrated by plotting the top views of the deformed cylinder models. In Figure 4-12 - a) top view of the 1st mode shape of the cylinder computed by ANSYS is given. Note that the orientation of motion is not aligned with any coordinate axis. If the problem is finding the best locations to control the vibrations as a response to a force in X direction, then one should align the 1st mode shape coming from ANSYS to obtain the 1st deflection shape as given in Figure 4-12 - b).

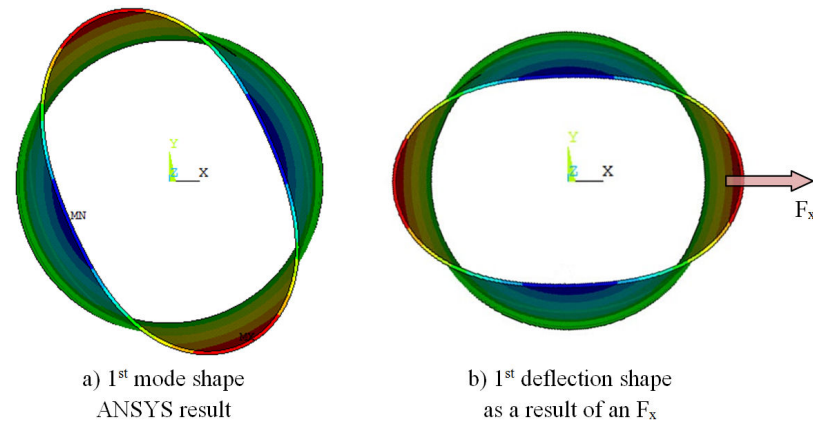


Figure 4-12. Example of the difference between mode shapes and deflection shapes in cylinder, a) 1st mode shape, b) 1st deflection shape for F_x

When working with structures with perfect symmetry, it is expected to have two orthogonal mode shapes at exactly the same frequency. This is called "double modes". In this case the nodal lines of those modes move according to the excitation force direction. In real life, when working with cylinders that are not tuned, the natural frequencies of "double modes" are slightly separated and the nodal lines of those modes are fixed [56]. In the case of cylinder with imperfections, the direction of motion of the double modes depend on the imperfection of the structure. A good practice is to conduct tests to obtain the deflection shapes of the cylinder in the operational conditions. If the cylinder will be subjected to loads in X direction, then a modal test can be conducted in which the cylinder is excited in X direction to obtain correct orientation of the mode shapes for the breathing modes. The example is given for the 1st mode shape, but alignment should be done for the modes that are subject to active vibration control. In this study the mode shapes of the cylinder to be controlled will be aligned for a disturbance force applied in X direction.

After maintaining proper alignment for the modes to be controlled for an external force in X direction, the placement criteria of possible piezoelectric patch actuators are calculated according to the criteria given in Equation 2.26 which is based on the eigenvalues of controllability Gramian matrices of each systems. Note that system output matrix C is not required in the calculation of controllability Gramian matrix as in Equation 2.25. System matrix A and input matrix B is required for this task. As a

result of this computation, best locations of piezoelectric patches are $Q = 3, H = 14$ and $Q = 12, H = 14$. Those two best places are on the opposite sides of each other over the cylinder. The placement criteria of all possible patch actuators are plotted in Q and H coordinates in Figure 4-13.

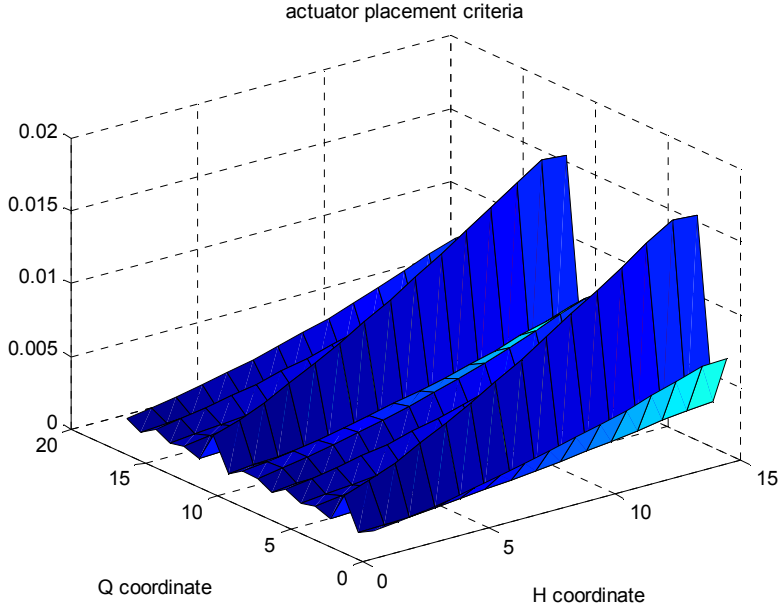


Figure 4-13. Piezoelectric patch actuator placement criteria according to coordinates

4.5 Mathematical Model Using State Space Matrices

Finite element model of the steel cylinder with piezoelectric patch is used in order to obtain the mathematical model of the structure. SPMWRITE command of ANSYS APDL is a good way to calculate the state space matrices of the system. As studied before in Chapter 3 for modeling beams with piezoelectric patches, the mathematical model of the cylinder with a piezoelectric patch actuator can be obtained by calculating the state space matrices of the system from ANSYS SPMWRITE command.

In active vibration control of the cylinder structure, the best type of sensors to detect the motion of the cylinder are piezoelectric patches in sensor mode. So the control system will be designed for piezoelectric patch sensors.

It is desired to use collocated sensor/actuator pair for active vibration control purpose. There will be one piezoelectric patch actuator on the outer surface of the cylinder and there will be one piezoelectric patch sensor on the inner surface, just behind the actuator. The voltage generated between the electrodes of the piezoelectric sensor is linearly related to the strain that the piezoelectric material is subjected to, according to piezoelectric constitutive equations of the linear piezoelectric model, which is described in Chapter 2.2.

ANSYS SPMWRITE command is the method used in computing system matrix A , and input matrix B so far. However the output matrix C , cannot be directly computed using SPMWRITE, since this command does not have the ability to give VOLT or CHARGE as output. Unfortunately the only types of outputs supported by SPMWRITE are translations and rotations of nodes. An assumption should be made to use displacements instead of the voltage output of the piezoelectric patch. Tangential relative displacement of the inner surface of the cylinder will be used as output instead of voltage readout. The model will be generated so that the control input is the piezoelectric patch at the optimal location calculated before. The disturbance input is the point force applied on the outer rim of the cylinder in the direction of X axis. The output of the system is the relative tangential motion of the nodes on the inner surface corresponding to the piezoelectric patch sensor location.

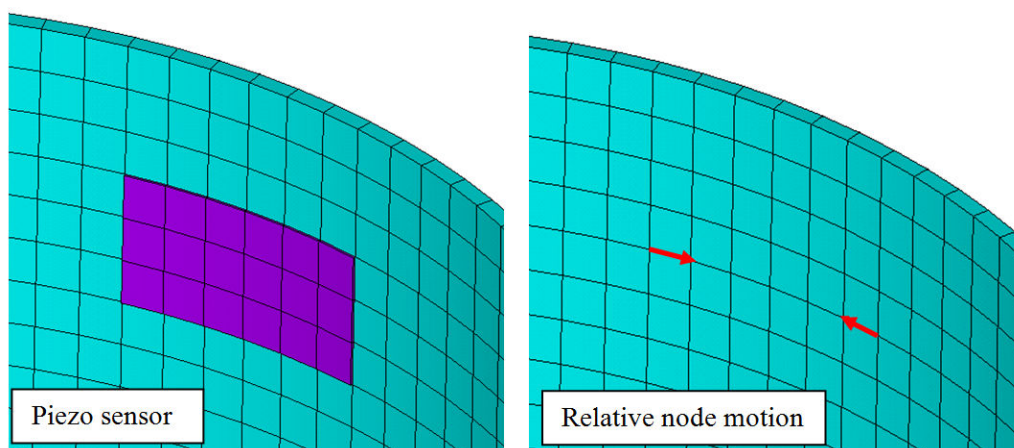


Figure 4-14. Relative tangential motion of the nodes corresponding to piezo sensor

The system model generated has the same architecture as in the one generated for the beam in Chapter 3. There is one control input, one system output and one disturbance input. The pole zero plot of the transfer function between control input and the system output is given in Figure 4-15 and the frequency response of this system is given in Figure 4-16.

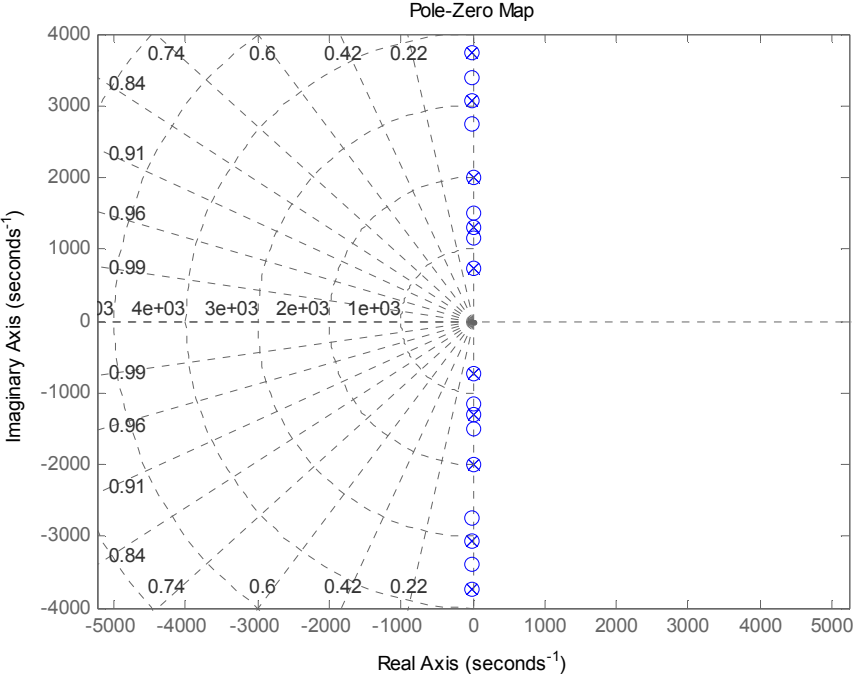


Figure 4-15. Pole-Zero plot of the plant

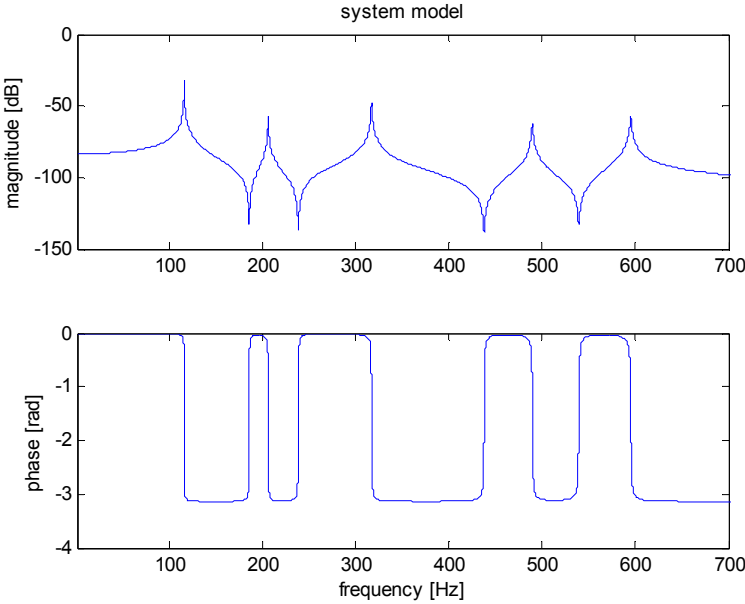


Figure 4-16. Frequency response of the system

Note that since the sensor and the actuator are collocated, the frequency response of the system shows drive point FRF characteristics.

4.6 Controller Design and Simulations

In the efforts for designing controllers for the plant, the method that is tried first is the pole placement. In this method, the system poles are moved to desired location by the proper design of the controller. This design method is used for beam geometry in Chapter 3 before and it will be used in a similar logic as before.

In this study it is desired to control 1st, 2nd, 5th and 6th vibration modes of the cylinder. Each vibration mode has a pair of complex poles symmetric with respect to the real axis on s-plane. The aim of active vibration control study is moving the system poles to locations that they will have more damping.

Although it is desired to stop the vibrations for 4 modes, it can be hard to control the vibrations of modes with high natural frequency. In pole placement the poles of the observer should be 3-5 times faster than the poles to be controlled. Poles with high natural frequency are already away from the origin of the s-plane. Placing 3-5 times faster observer poles will result in a very fast dynamic system in overall. This will require design of a system with very high sampling rate, which will bring many problems such as high frequency noise and instability problems. The system is designed to control 1st and 2nd modes. The pole zero map of the dynamic system is given in Figure 4-17 and the frequency response of the system is given in Figure 4-18.

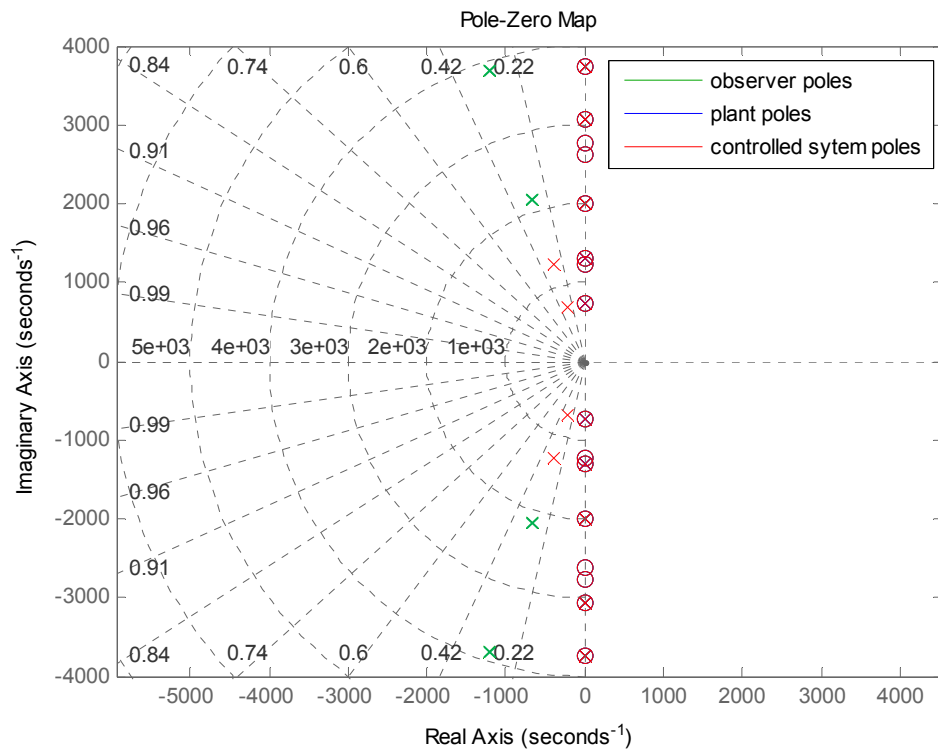


Figure 4-17. Pole zero plot of the plant, observer and the controlled system

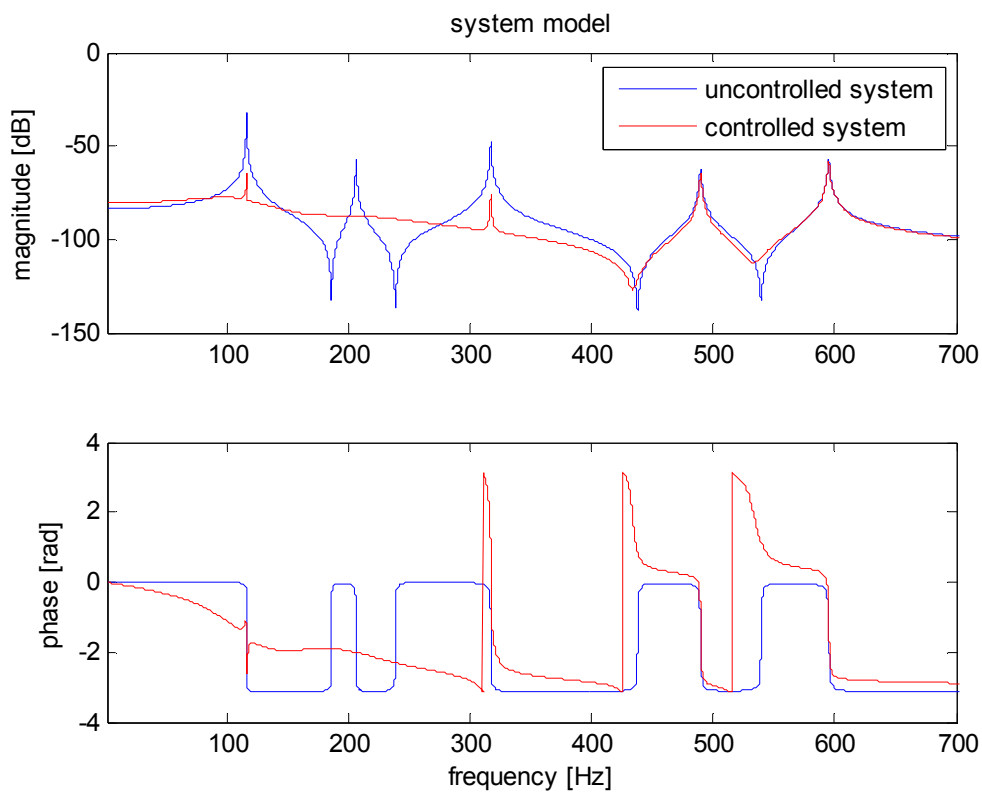


Figure 4-18. Frequency response on uncontrolled and controlled systems

Pole placement method can be hard to implement and may require many number of sensors and actuators for control purposes since in this system an observer is employed to estimate system states. If more sensors are used, then the success of the observer to estimate the states will increase.

Another way to control the vibrations of systems is called Positive Position Feedback (PPF) control. In PPF control, each mode is controlled separately, by filters that are tuned to the natural frequencies of each mode. In PPF control the filter designed to control n^{th} mode is given as follows

$$f_n(s) = \frac{K_n}{1 + 2\zeta_n\omega_n s + \omega_n^2} \quad (4.1)$$

In the equation above, ω_n is the natural frequency of the target mode, ζ_n is the damping ratio and K_n is the gain of the PPF controller for the target mode. In this control strategy, different controller gains can be assigned to different modes. In this control study, 1st, 2nd, 5th and 6th modes are desired to be controlled. Four PPF controllers are designed with natural frequencies tuned to each mode. A damping ratio of $\zeta = 0.1$ is assigned for all PPF controllers. The Simulink model constructed for PPF control is given in Figure 4-19 and the simulation result for disturbance rejection performance of the system is given in Figure 4-20.

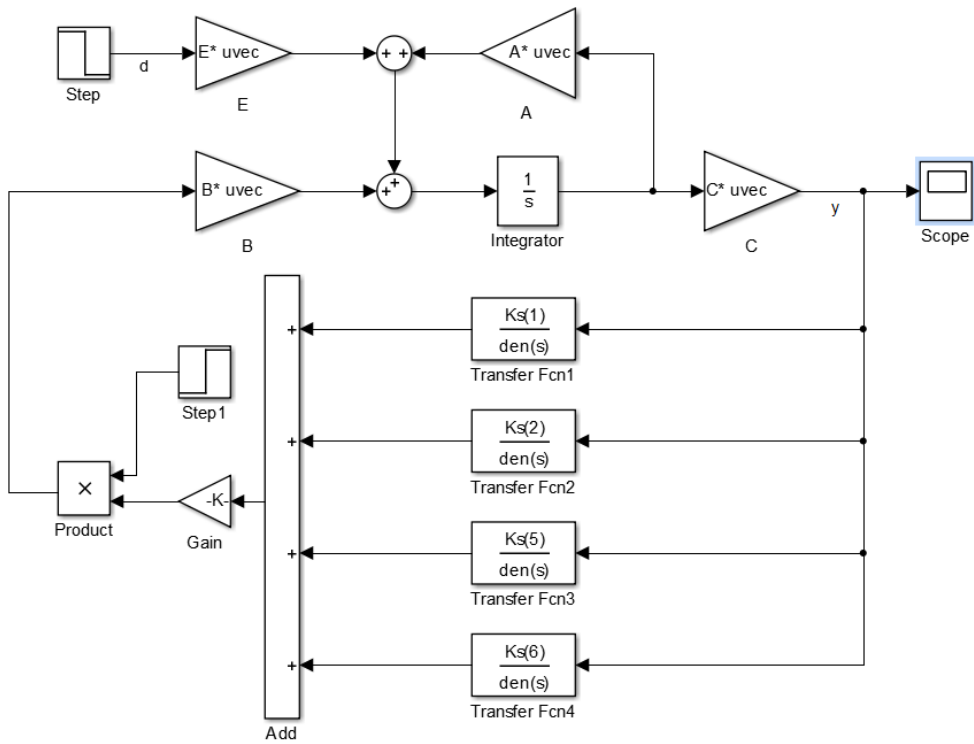


Figure 4-19. Simulink block diagram of the system with PPF control

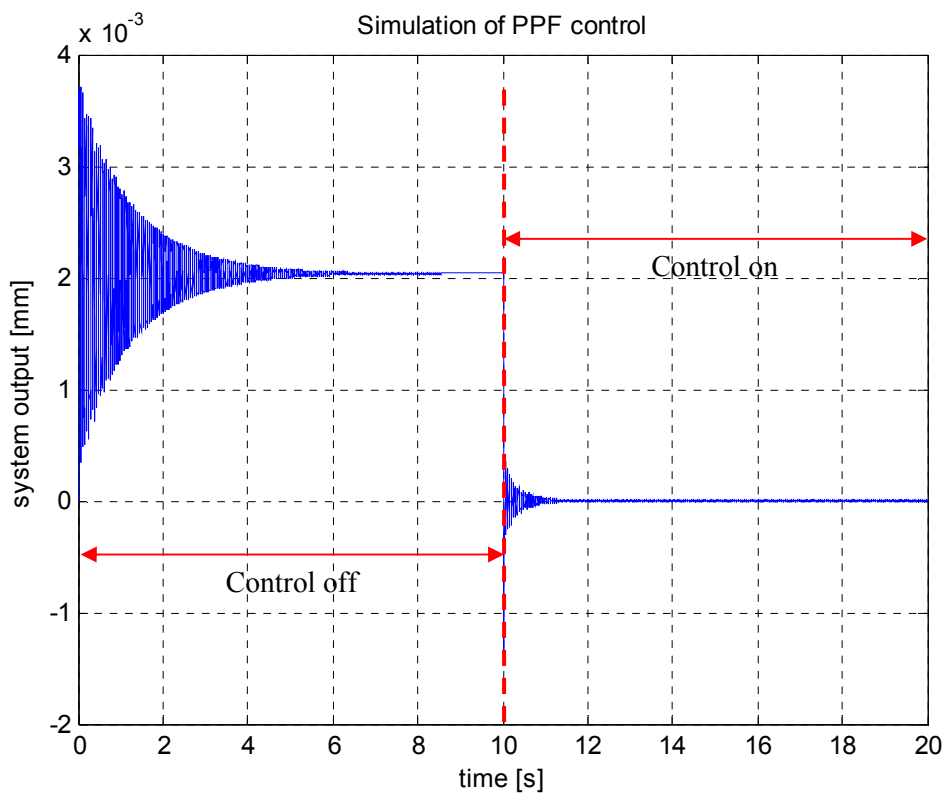


Figure 4-20. Simulation of PPF control

After designing a controller for the best actuator location, a verification of the best location is made. For this purpose, the PPF controller designed for the best actuator is kept fixed and the plant model used in the simulation is changed. In each simulation a different plant model corresponding to a different actuator location is used with the same controller. Note that since collocated sensor approach is employed, the piezoelectric sensor is also moved together with the actuator, however the location of the disturbance force is kept fixed. In the simulations the best piezoelectric actuator location is found at $Q = 3$ and $H = 14$, the second best actuator location is found at $Q = 6$ and $H = 14$ and finally the worst actuator location is at $Q = 8$ and $H = 1$. Results of the simulations done with different actuator locations and the same controller is given in Figure 4-21. Note that the performance of the system when the sensor is in the best location and in the second best location are close to each other, however when the actuator is at the worst location, the performance of the control system is reduced noticeably.

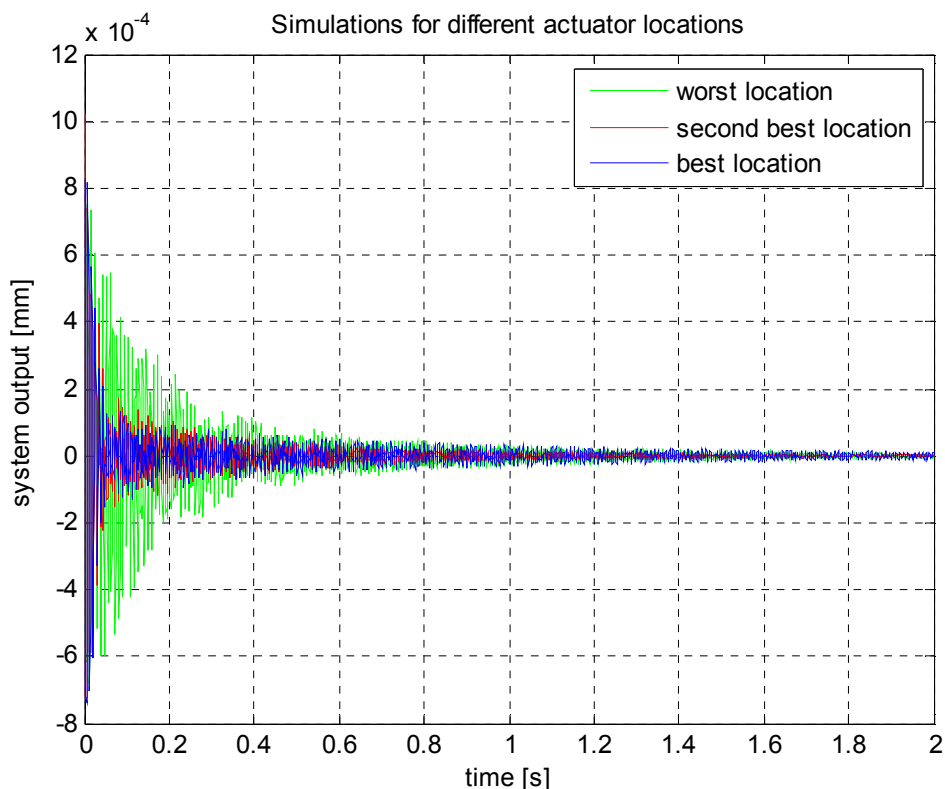


Figure 4-21. Simulation for piezoelectric actuators at different locations

FFT of the simulations with different actuator locations is also computed and given in Figure 4-22. On the FFT plot it is seen that the performance of the controller at worst location is the worst of all for all modes. The performance of the system when the controller is at the best location is lower than the performance of the system for the second best controller location for 1st and 2nd modes (see Figure 4-23). However for 5th and 6th modes the situation is different. For those modes the performance of the control system is the highest when the actuator at the best location (see Figure 4-24). This result is not surprising since in placement criteria a balanced formulation is used to find the location of the actuator that can control all the modes of interest.

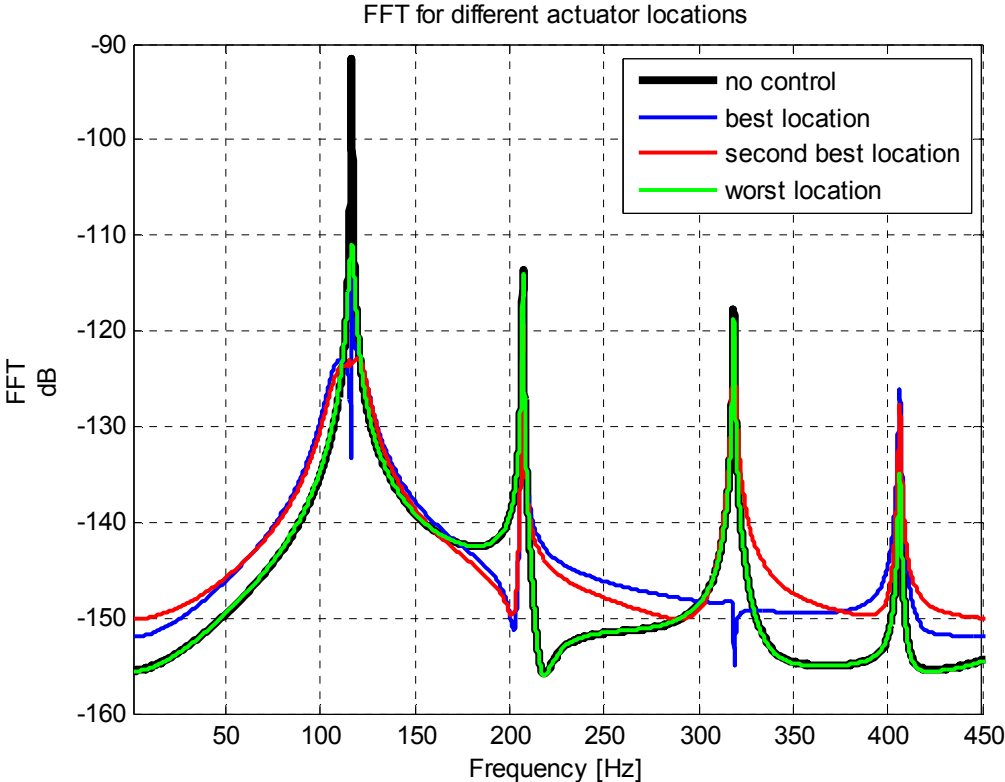


Figure 4-22. FFT of the response for different actuator locations

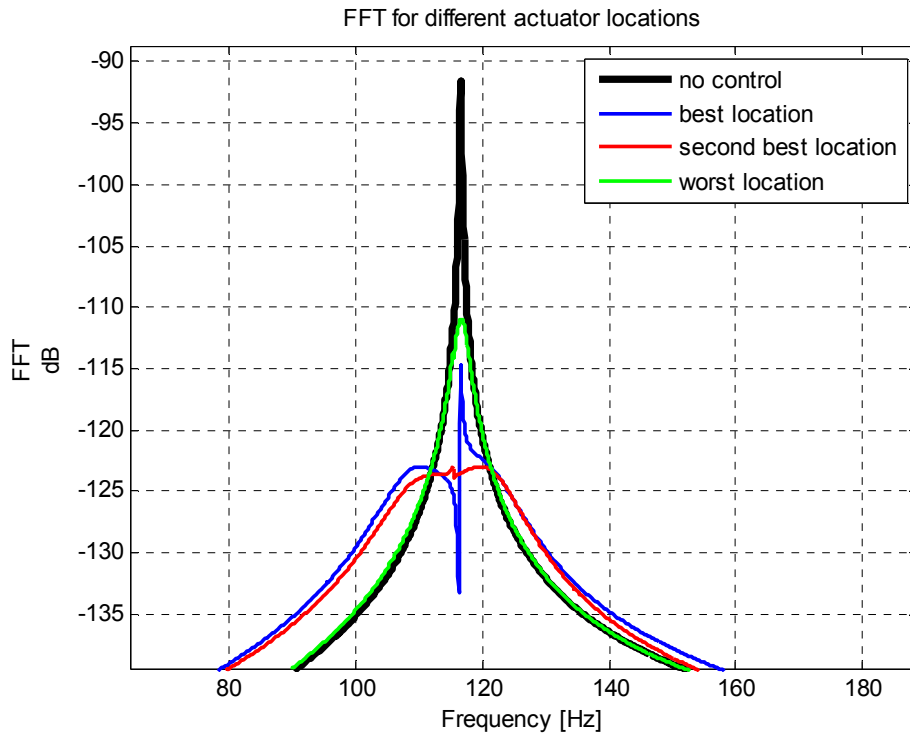


Figure 4-23. FFT of the response for different actuator locations, 1st and 2nd mode, zoomed

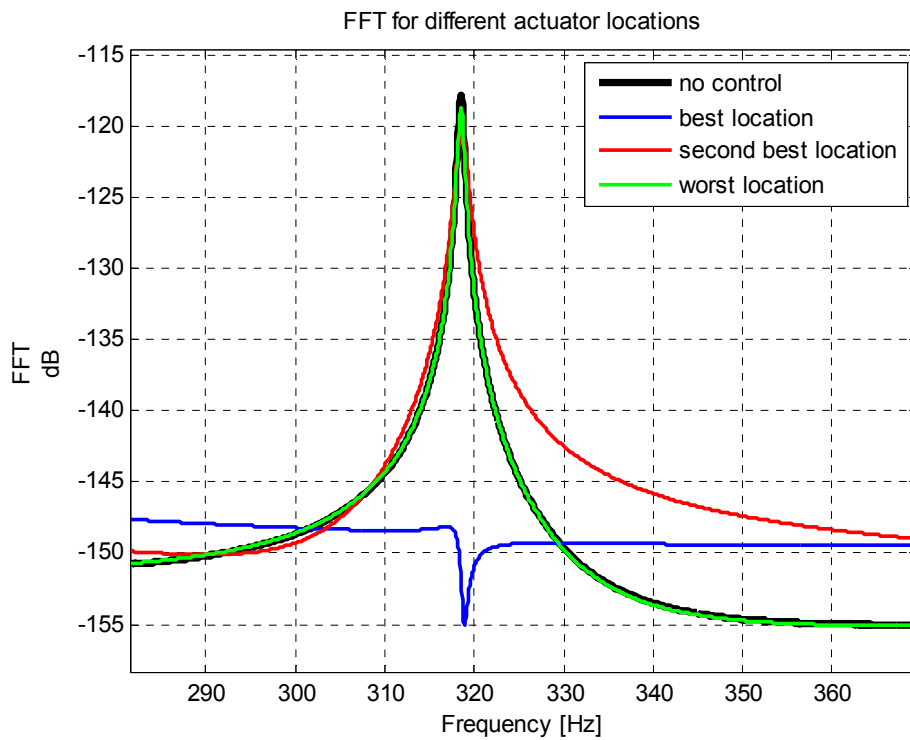


Figure 4-24. FFT of the response for different actuator locations, 5th and 6th mode, zoomed

4.7 Verification by Tests

Real life test model in the laboratory is used for verification purposes of the finite element model. The test setup used in beam studies is also used for the cylinder. The cylinder part is in free - free boundary condition. To simulate this condition cylinder is put on soft rubber foam sheets. Photo of the test setup and the cylinder installed in Roketsan is given in Figure 4-25.



Figure 4-25. Test setup and the cylinder in Roketsan

A Dura Act piezoelectric patch is glued on the outer surface of the cylinder. This piezoelectric patch will be driven by the piezoelectric amplifier. Unlike the beam study, Dura Act patches are already electrically isolated from the surface that they are glued, so a relatively thin glue layer exists between the patch and the cylinder.



Figure 4-26. Piezoelectric patch on the outer surface of the cylinder

Unlike the beam, the cylinder structure is thick and stiff. Its vibratory motion could not be detected using strain gages. Laser displacement sensors could not be used in cylinder case since the displacement of the cylinder is much smaller than that of the beam and the cylinder is in free - free boundary condition. Sensor types that can be used on the cylinder are piezoelectric patches and accelerometers. ICP accelerometers are also piezoelectric based, so similar types of sensors in principle can be used on cylinder.

Collocated piezoelectric patch sensor and actuator pair is desired to be used over the cylinder. A piezoelectric patch is glued on the inner surface of the cylinder corresponding to position just behind the patch on the outer surface. The patch on the outer surface is used as actuator and the one on the inner surface is used as sensor. A PCB model 352A24 teardrop single axis accelerometer is also placed at one corner of the piezoelectric actuator on the outer surface of the cylinder. Photo of piezoelectric patch sensor on the inner surface is given in Figure 4-27 and the photo of the accelerometer at the corner of the actuator on the outer surface is given in Figure 4-28.



Figure 4-27. Piezoelectric patch on the inner surface of the cylinder



Figure 4-28. Accelerometer placed at the corner of the piezoelectric actuator

All data acquisition and actuator diving tasks are done using NI-PCI-6289 DAQ card mounted on the target PC in the xPC target system. Accelerometers and piezoelectric patches are sensor that do not have ground connection, so those types of sensors are called "floating" sensors. When using floating sensors, they should be used in differential signal configuration. However in beam study, laser displacement sensor is used in single ended signal configuration. Another adjustment done in order to obtain healthy measurement with the accelerometer is using PCB model 480E09 signal conditioning unit to feed the internal circuit of the ICP accelerometer. Since NI-PCI-6289 DAQ card does not have the ability to feed ICP sensors, it is impossible to obtain correct ICP accelerometer measurements without using the signal conditioner. Photo of PCB model 480E09 signal conditioning unit is given in Figure 4-29.



Figure 4-29. PCB model 480E09 signal conditioning unit

As in the beam study, a chirp signal is generated to drive the piezoelectric patch actuator and data is acquired by the accelerometer and piezoelectric patch sensor. A 70V sinusoidal chirp signal starting at 0.1 Hz at the beginning and moving up 450 Hz in 450 seconds is used. Chirp signal moves approximately 1 Hz in 1 second in a linear manner. Total duration of the signal is 450 seconds. Level of the voltage on the piezoelectric actuator is given constant by the command, however the level of the voltage read from the piezoelectric amplifier as the applied voltage increases as the cylinder goes through a resonance. Monitor channel of the amplifier gives 1/1000 of the voltage applied to piezoelectric actuator for safety purposes of the readout equipment. This voltage is measured from the monitor channel of the amplifier and multiplied with 1000 in Simulink and represented as piezoelectric drive voltage. Voltage applied to piezoelectric patch actuator is given in Figure 4-30. Voltage read from piezoelectric patch sensor is given in Figure 4-31 and voltage readout from the accelerometer is given in Figure 4-32. Note that the voltage levels of the sensor channels increase as the cylinder goes through resonances.

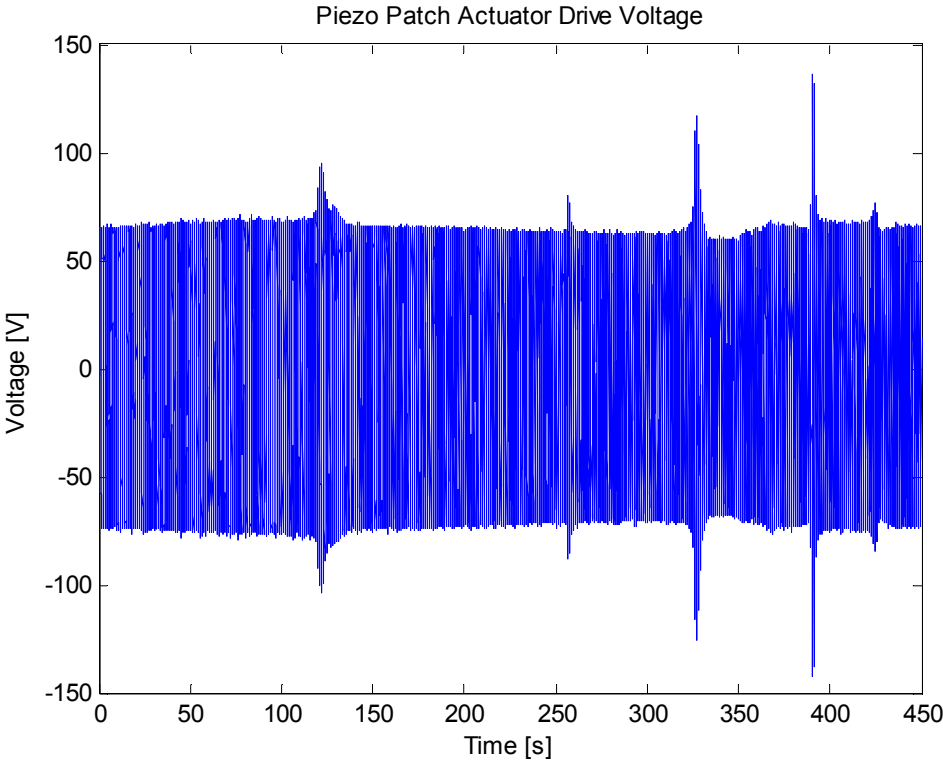


Figure 4-30. Voltage applied to piezoelectric patch actuator from the amplifier as drive voltage

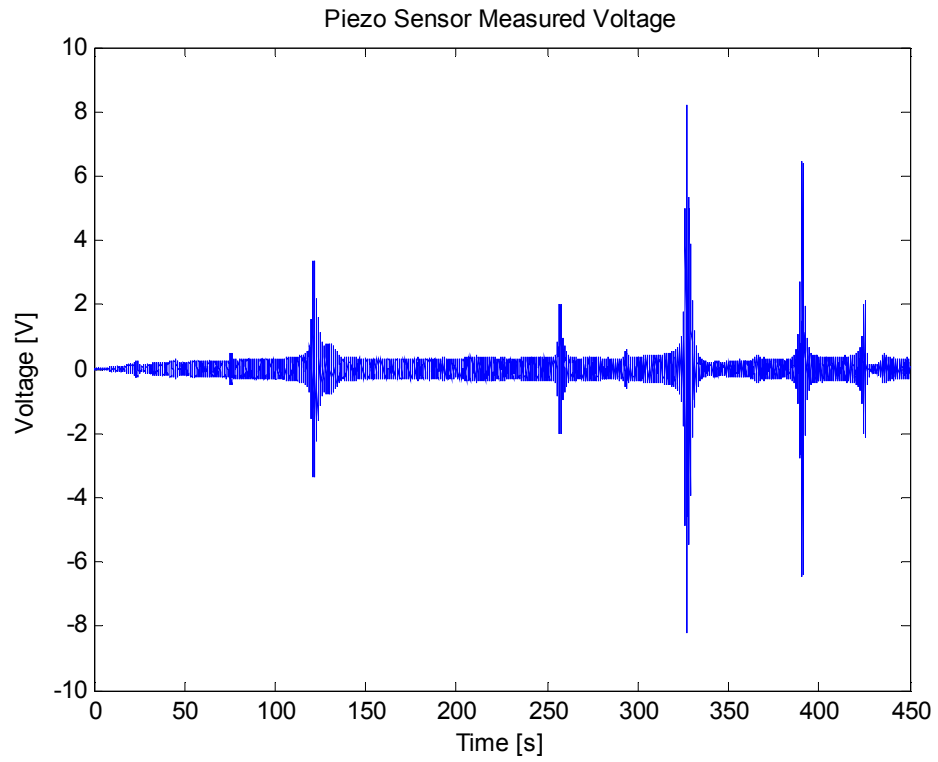


Figure 4-31. Voltage read from piezoelectric patch sensor

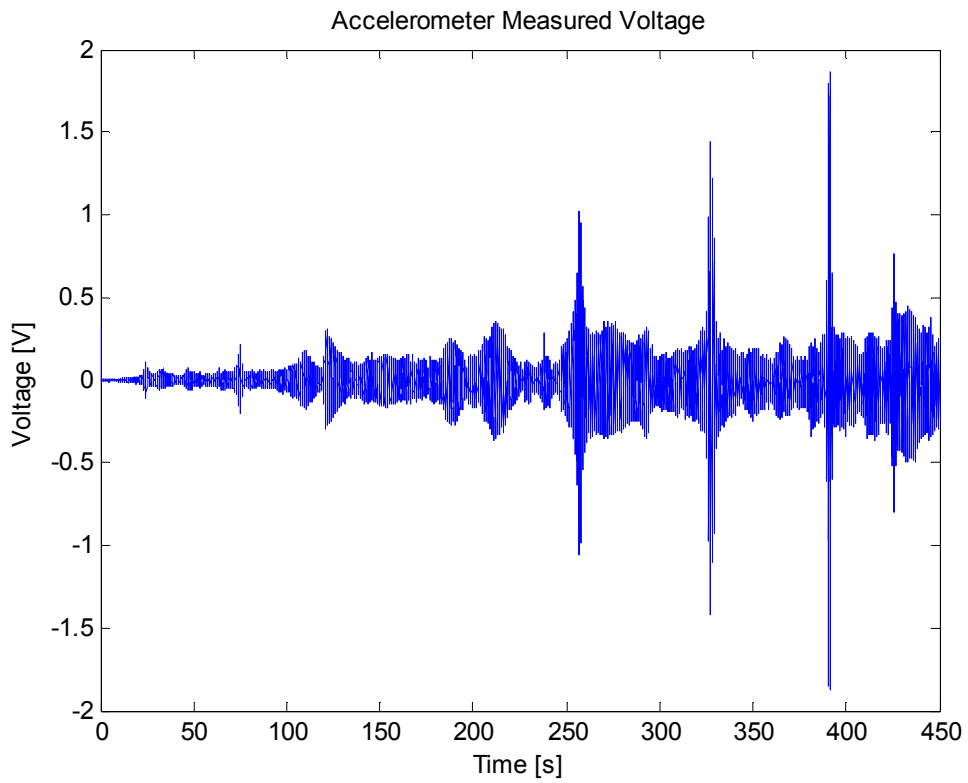


Figure 4-32. Voltage read from accelerometer

Using time domain data, the frequency content of those signals can be computed. The drive voltage to piezoelectric actuator is taken as reference channel. Piezoelectric patch sensor and accelerometer voltage readout channels are taken as measurement channels. By computing FFT's of measurement channels and the reference channel and dividing the FFT's of measurement channels to the FFT of the reference channel, transfer functions between the measurements and reference can be computed, as done in the beam study in Chapter 3. Transfer function (TF) between piezoelectric patch sensor and piezoelectric patch actuator is given in Figure 4-33 and TF between accelerometer and piezoelectric patch actuator is given in Figure 4-34. Note that those TF's are computed using only 1 chirp signal data. The accuracy of those results will increase by using more averages. Also note that the noise on the piezoelectric patch sensor data is much less than the noise on the accelerometer data.

In addition to xPC target system, LMS SCADAS Recorder 07 Data Acquisition System is also used in data acquisition over the cylinder. This system is a more advanced data acquisition system with a more professional and dedicated software to data acquisition and processing, LMS Test Lab. In the measurement with LMS a random voltage load of approximately maximum 160 Volt magnitude (55 Volt RMS) is generated and applied to the piezo actuator and data acquired from piezo sensor with a maximum of approximately 5 Volt and RMS of 1.1 Volt. Acquired time data of 100 seconds is given in Figure 4-35. Using this time data a transfer function is computed in LMS Test Lab using time blocks of 1 second and overlap of %50. As an average of 200 blocks, the transfer function between piezoelectric patch sensor and actuator is generated more accurately than done by single chirp data. Transfer function from LMS using random data of 100 seconds is given in Figure 4-36.

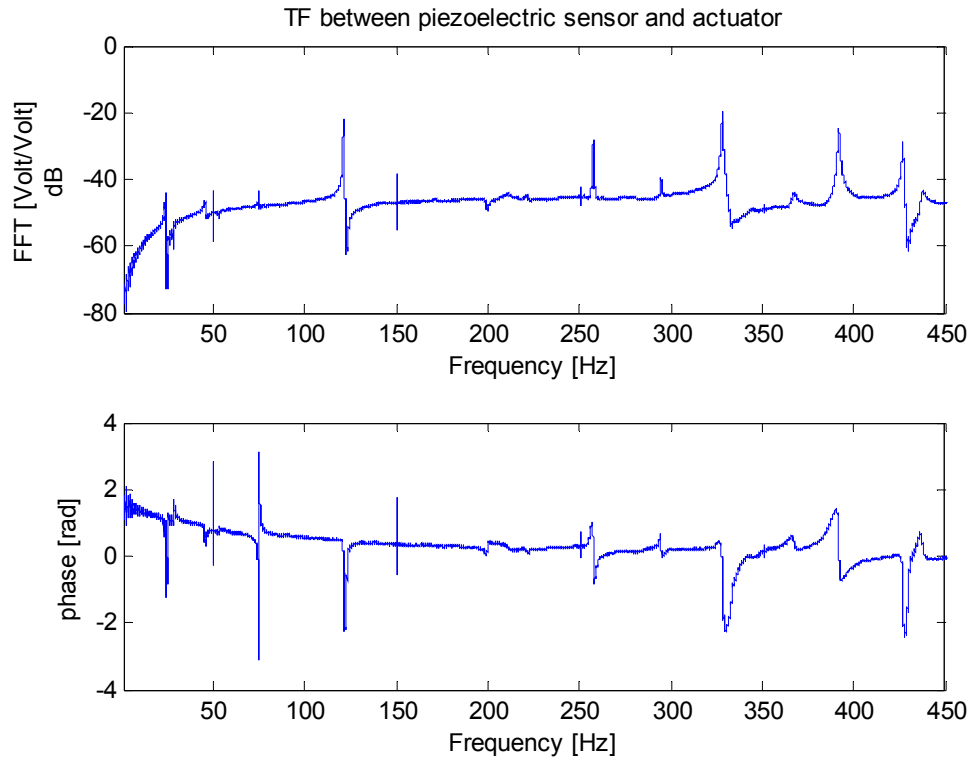


Figure 4-33. TF between piezoelectric patch sensor and actuator

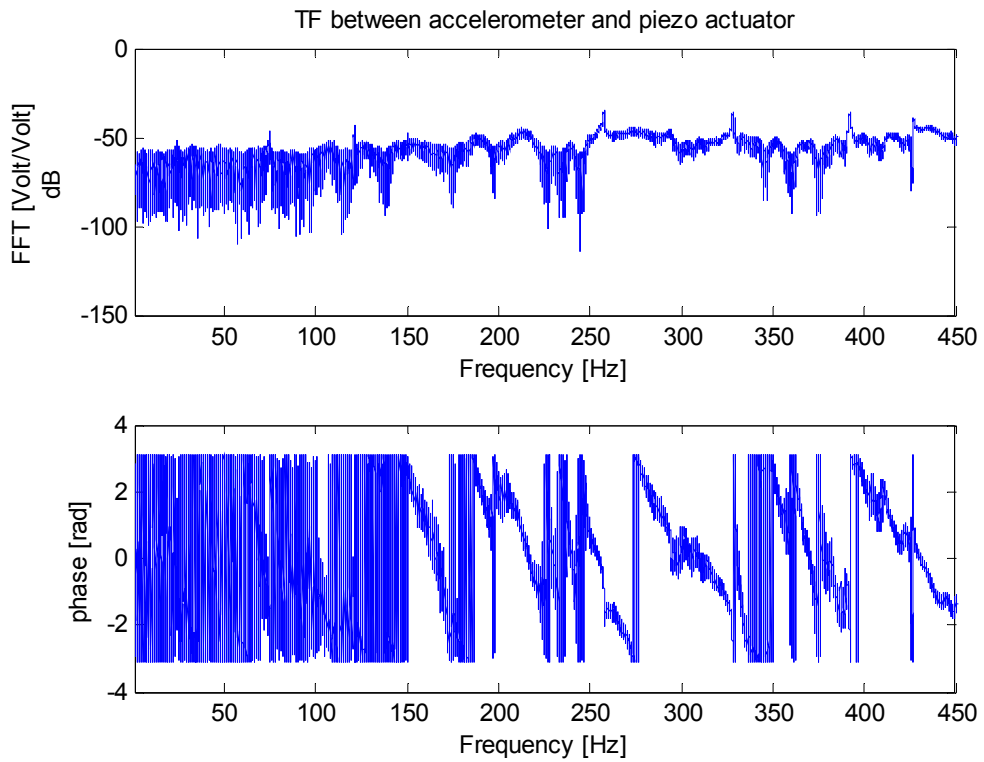


Figure 4-34. TF between accelerometer and piezoelectric patch actuator

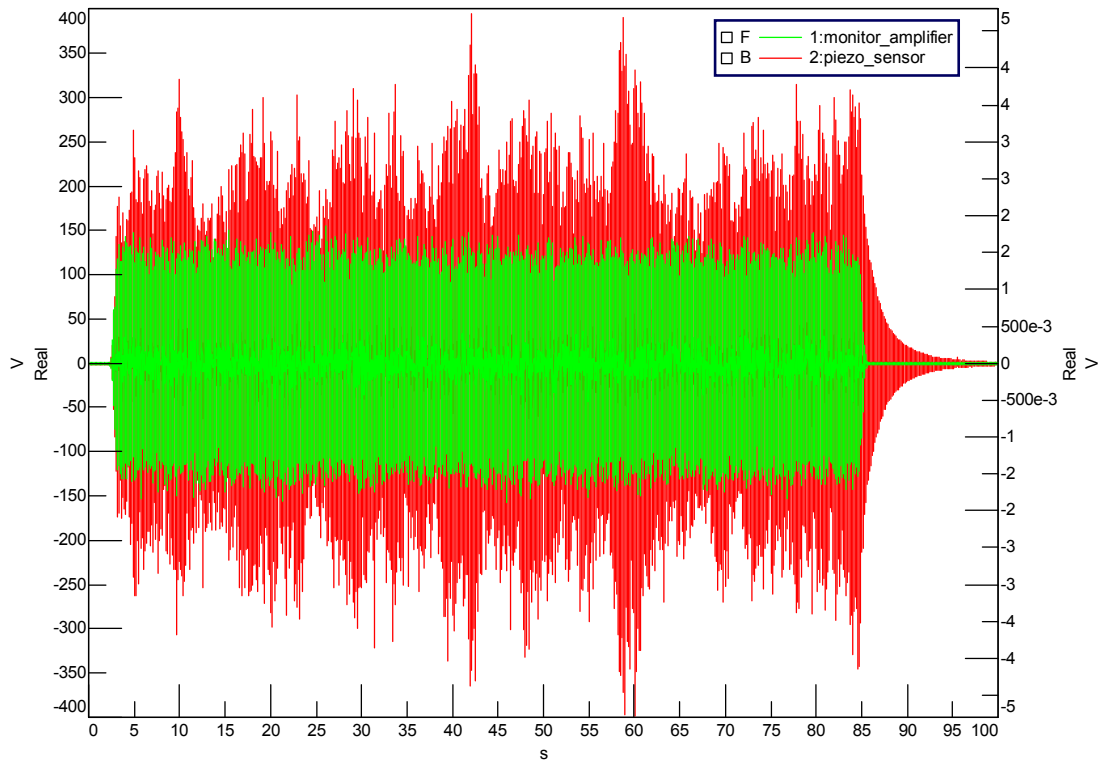


Figure 4-35. Time data acquired by LMS

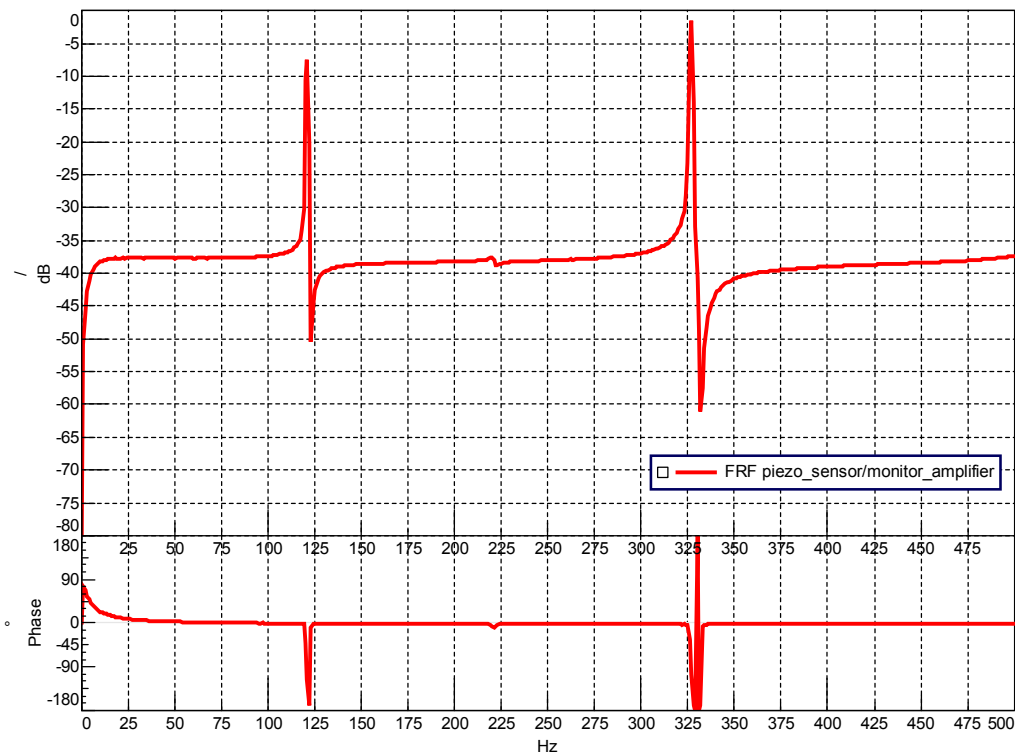


Figure 4-36. TF between piezoelectric patch sensor and actuator using 200 averages, LMS result

A modal test with impact hammer is carried out on the cylinder using LMS Test Lab. In the modal test 12 accelerometers are placed on the upper outer rim of the cylinder to detect the breathing modes. In modal test B&K type 8200 impact hammer is used with 12 single axis accelerometers. Photo of the impact hammer is given in Figure 4-37 and photo of the modal test accelerometers on the cylinder is given in Figure 4-38.



Figure 4-37. B&K 8200 impact hammer



Figure 4-38. Accelerometers placed on the cylinder for modal test

In modal test, cylinder is excited at point 1 in radial inward direction by hitting with the hammer. Mode shapes obtained from the modal test are given in Figure 4-39, Figure 4-40, Figure 4-41, and Figure 4-42.

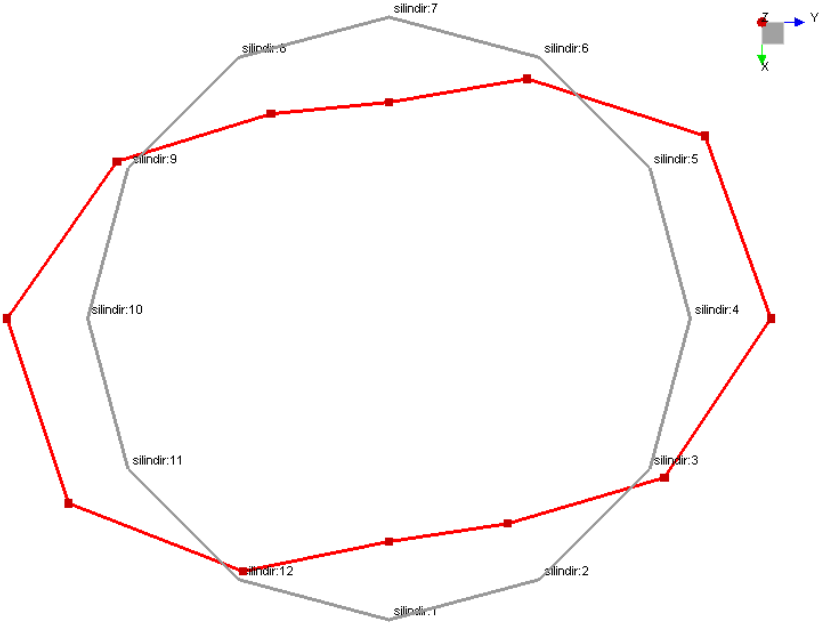


Figure 4-39. 1st mode shape, test result

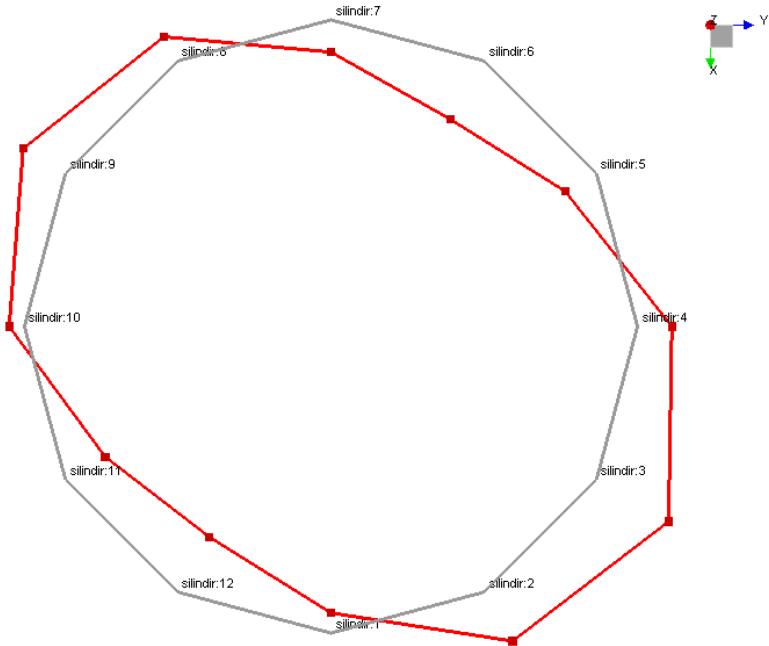


Figure 4-40. 2nd mode shape, test result

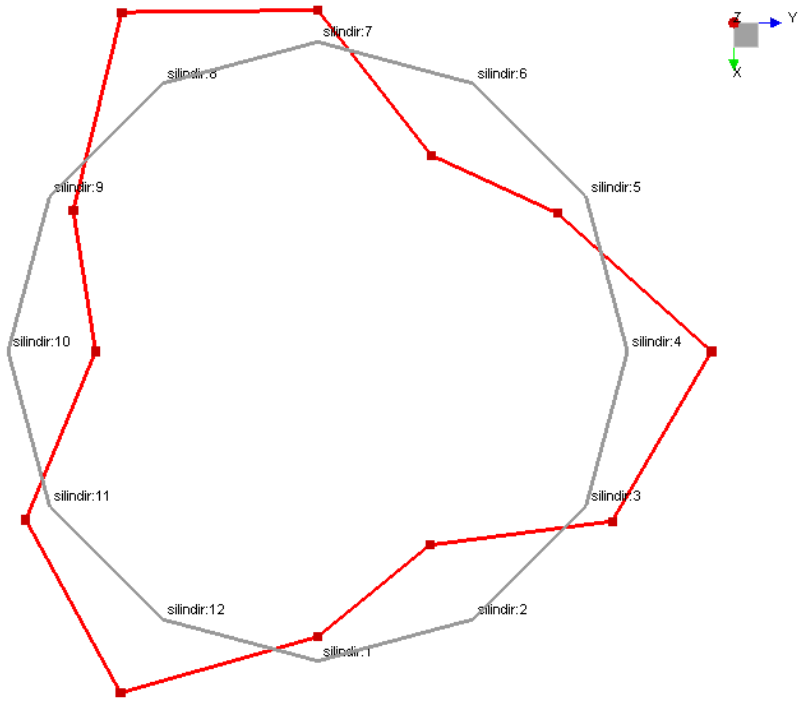


Figure 4-41. 5th mode shape, test result

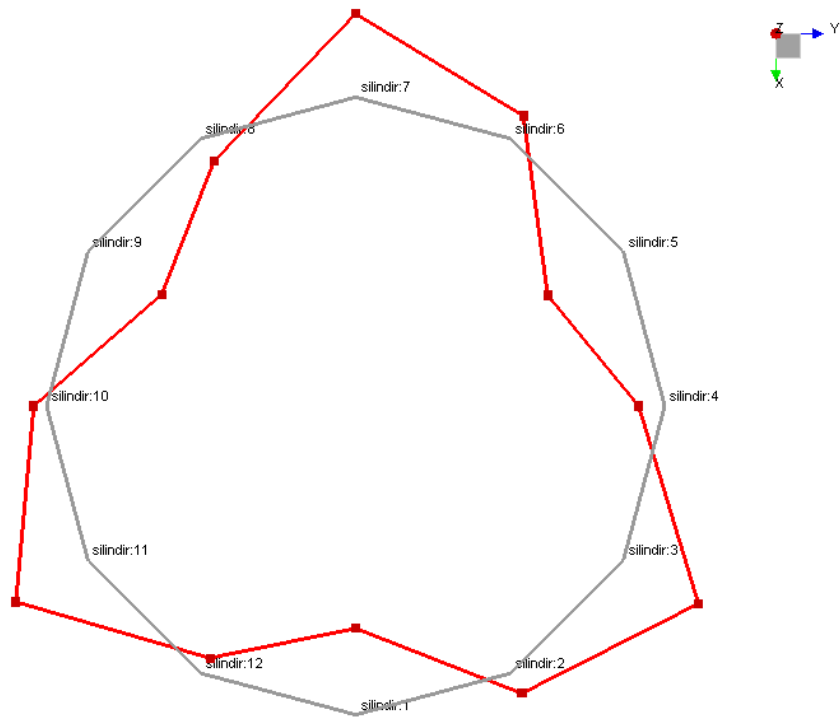


Figure 4-42. 6th mode shape, test result

1st, 2nd, 5th and 6th mode shapes from the analysis are obtained by using the accelerometers on the upper outer rim of the cylinder in modal test. It is not worth the trouble to detect 3rd and 4th modes by tests. By using more accelerometers on lower outer rim of the cylinder and exciting the cylinder from lower points, those modes can be detected as well. However, considering the active vibration control study scenario of this study, 1st, 2nd, 5th and 6th modes are found to be sufficient. To verify findings of the modal test, auto Modal Assurance Criteria (MAC) values are computed in LMS Test Lab for the four modes detected by test. It shows in the MAC graph in Figure 4-43 that a quite good job is done in the modal test since the similarity of different mode shapes are very low and the mode shapes are orthogonal.

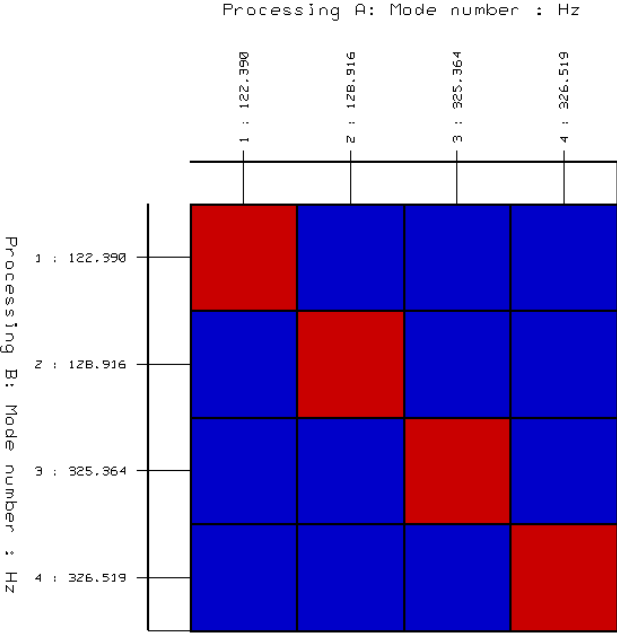


Figure 4-43. Auto MAC values of modes obtained from LMS

Natural frequencies from test and analysis are compared in Table 4-4. By this comparison, it is seen that the difference between natural frequencies are about 5 percent except at the 2nd mode. Note that 5 percent is an acceptable difference between finite element analysis results and test results considering differences in the analysis model and real life test model. Real model is made by radial forging and this increases the stiffness, and so the natural frequency of the cylinder. There is also another point to note: The real life model is not tuned. The double modes of the

cylinder as a result of cyclic symmetry are not exactly at the same frequency due to mistuning of the part. This can be result of cutting process after radial forging. Since the part is not tuned its nodal points and the mode shapes for breathing modes should be fixed. If the cylinder was "perfectly tuned" then its vibration mode shapes and location of nodal points would depend on the excitation force direction and location. However in this case the mode shapes are defined due to imperfection of the cylinder and they are fixed. The level of excitation at each mode depends on the direction of excitation force.

Table 4-4. Comparison of natural frequencies from test and analysis

Mode Number	Natural Frequency Analysis Result (Hz)	Natural Frequency Test Result (Hz)	Percent Difference (%)
1	114.8	122.4	6.2
2	114.8	128.9	10.9
5	313.8	325.4	3.5
6	313.8	326.5	4

As a final part of this study positive position feedback controller is successfully implemented over the cylinder by using one piezoelectric patch sensor and actuator pair. The positive position filter target frequencies are set to the natural frequencies of the cylinder measured by modal test. This is one of the differences between the PPF controller in design stage and the one used in the implementation. Another difference between the controller in design and the implementation is that the designed controller is in the continuous domain (s-domain) and the one in the implementation is in the discrete domain (z-domain). PPF filters are designed at the target frequencies of the real cylinder and those filters are transformed in discrete domain using MATLAB's "c2d" command and "tustin" transformation option. This is the recommended discrete domain transformation method when the model has important frequency domain properties [57]. Simulink model used in the implementation of PPF controller is given in Figure 4-44.

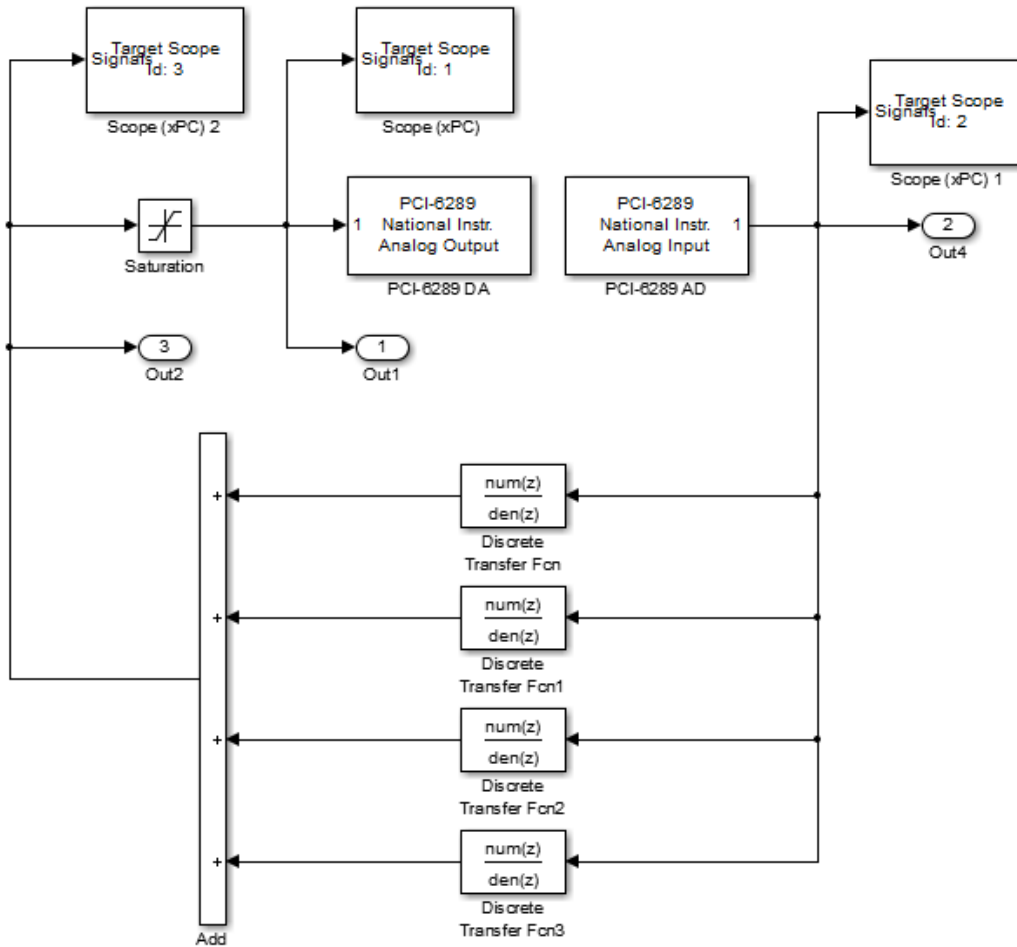


Figure 4-44. Simulink block diagram of the cylinder test model

There is another difference to consider between the test and analysis models is the orientation of the mode shapes. Recall that mode shapes were required to be aligned according to excitation force before making further analysis for optimal patch placement, since the cylinder breathing mode shapes from ANSYS are not aligned. Actually a best practice in this case should be making a modal analysis on the real cylinder part and in this test exciting the structure from the point where the excitation force will be applied on. Later the mode shapes of the analysis results should be aligned according to test results.

The angular differences between mode shapes are shown in Figure 4-45, Figure 4-46, Figure 4-47 and Figure 4-48 side by side. If there is a big misalignment, then mode shapes should be aligned and placement criterion should be computed afterwards. It

can be seen that the 1st mode shape of the analysis is 90 degrees rotated version of the 2nd mode shape in test. Also the 2nd mode shape of analysis is 90 degrees rotated version of the 1st mode shape. This case is also valid for the 5th and the 6th mode shapes. Therefore the optimal locations calculated in the analysis should be rotated about 90 degrees in Q coordinate. So the best location is Q = 7 and H = 14 and the worst actuator location is Q = 12 and H = 14.

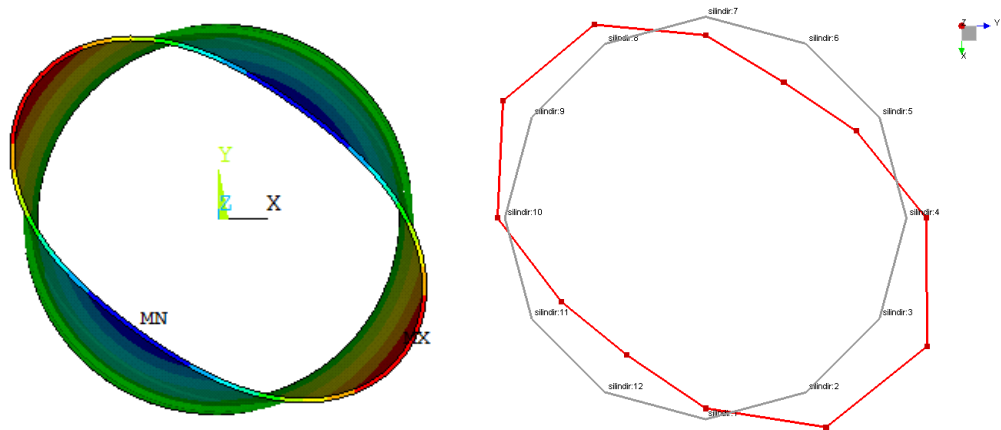


Figure 4-45. 1st mode shape from analysis, 2nd mode shape from test

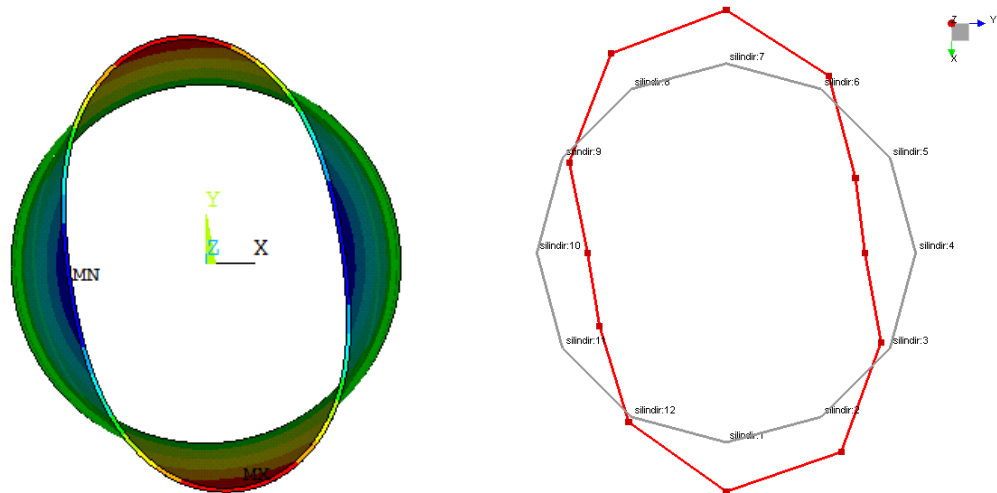


Figure 4-46. 2nd mode shape from analysis, 1st mode shape from test

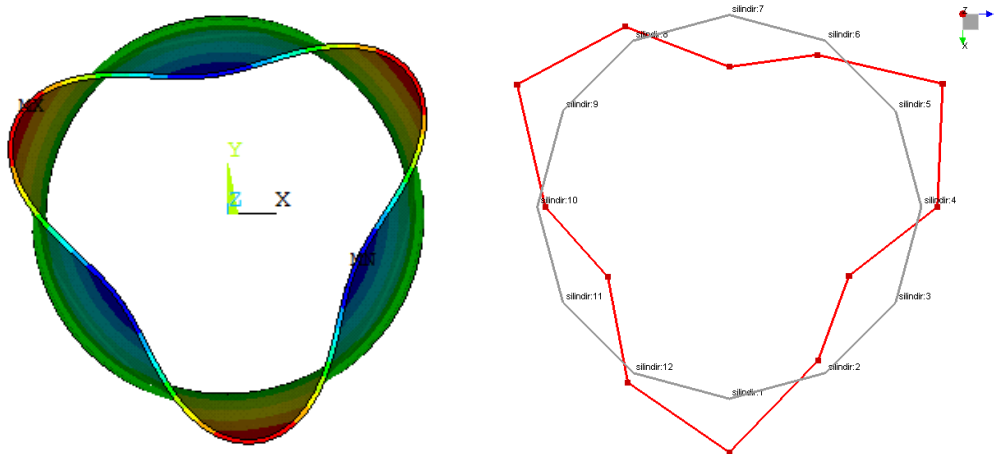


Figure 4-47. 5th mode shape from analysis, 6th mode shape from test

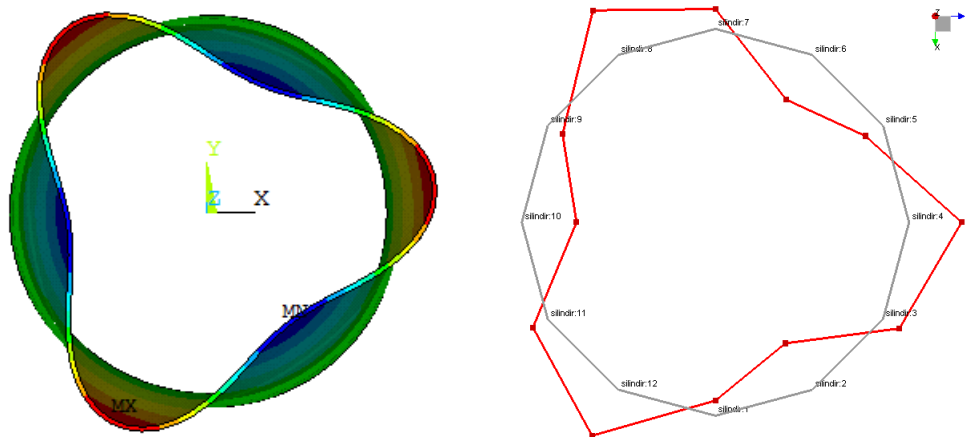


Figure 4-48. 6th mode shape from analysis, 5th mode shape from test

The best actuator locations calculated by analysis are updated according to the modal test results. After finding the best location piezoelectric patches are glued on the cylinder. Tests for trial of the controller performance are carried out. As a first test, the cylinder is hit and the controller is turned on while the cylinder is still vibrating. Results of this test in the form of sensor voltage is presented in Figure 4-49. Note that the cylinder vibrations are stopped shortly after the control system is turned on. As another test, the free vibration of the cylinder when the controller is off is compared with the free vibrations of the cylinder when the controller is on. This comparison is given in Figure 4-50. Effectiveness of the controller can be seen from this figure.

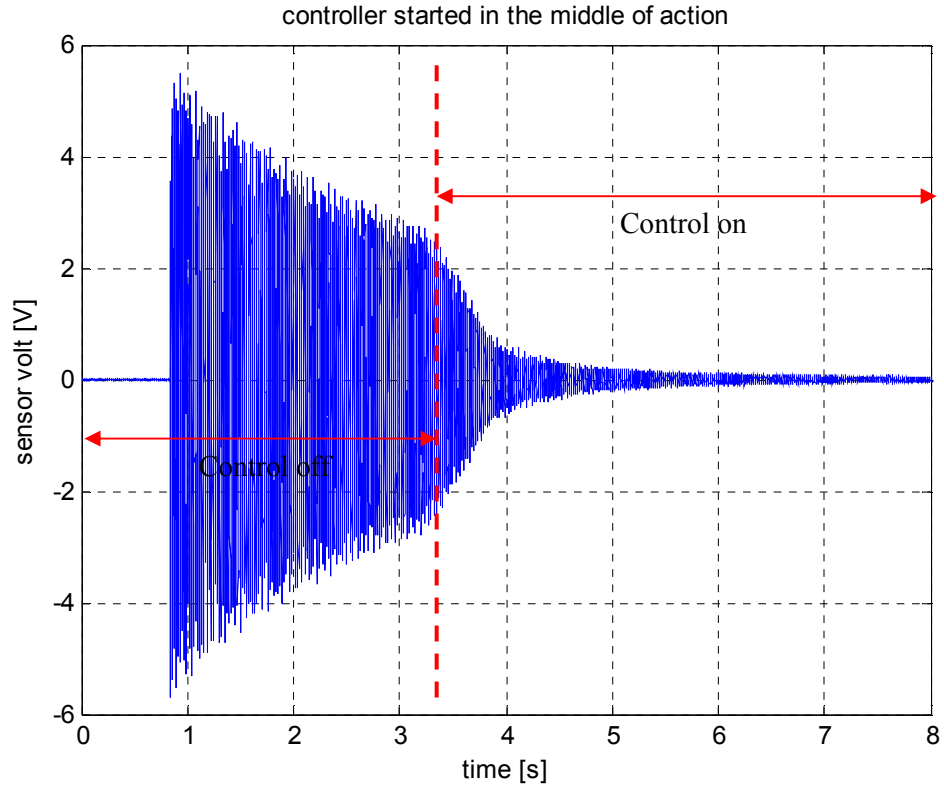


Figure 4-49. Controller started in the middle of cylinder motion

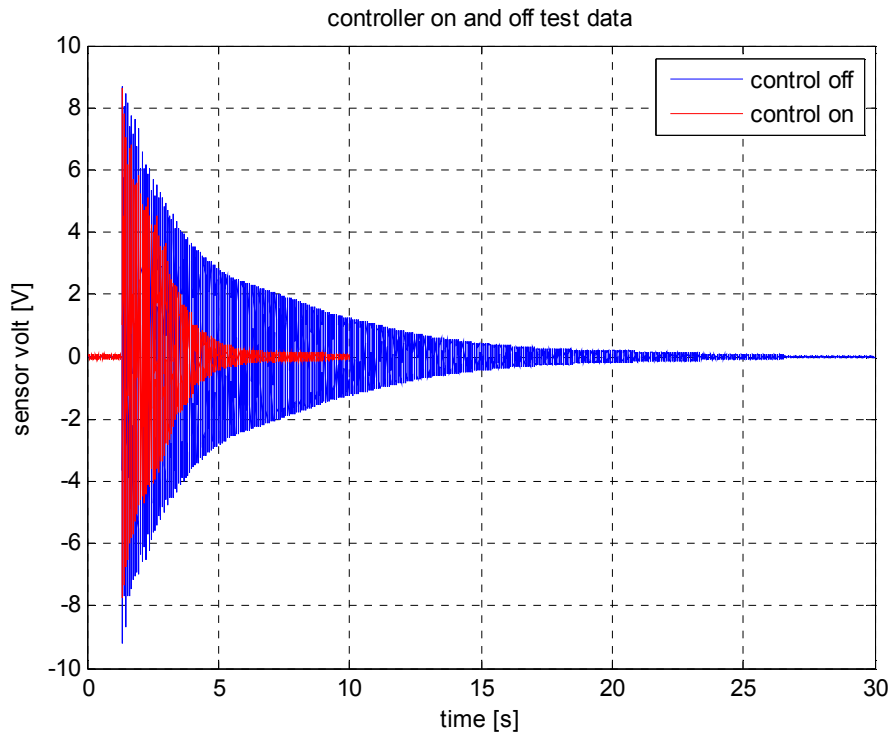


Figure 4-50. Cylinder sensor measurements for control off and control on

The effectiveness of the placement of actuators is also verified experimentally. A piezoelectric patch actuator and sensor couple were placed on $Q = 7$ and $H = 14$. To see the effectiveness of patch placement, an experimental comparison between the responses for best and worst actuator locations is desired to be tested. The worst location for the actuator is $Q = 12$ and $H = 1$. However for practical purposes, instead of $Q = 12$ and $H = 1$, $Q = 12$ and $H = 14$ is tested as worst location. Thus, the piezoelectric patch is not required to be removed, and the tests can be completed by only changing the impact location on the cylinder. The result of this comparison is given in Figure 4-51.

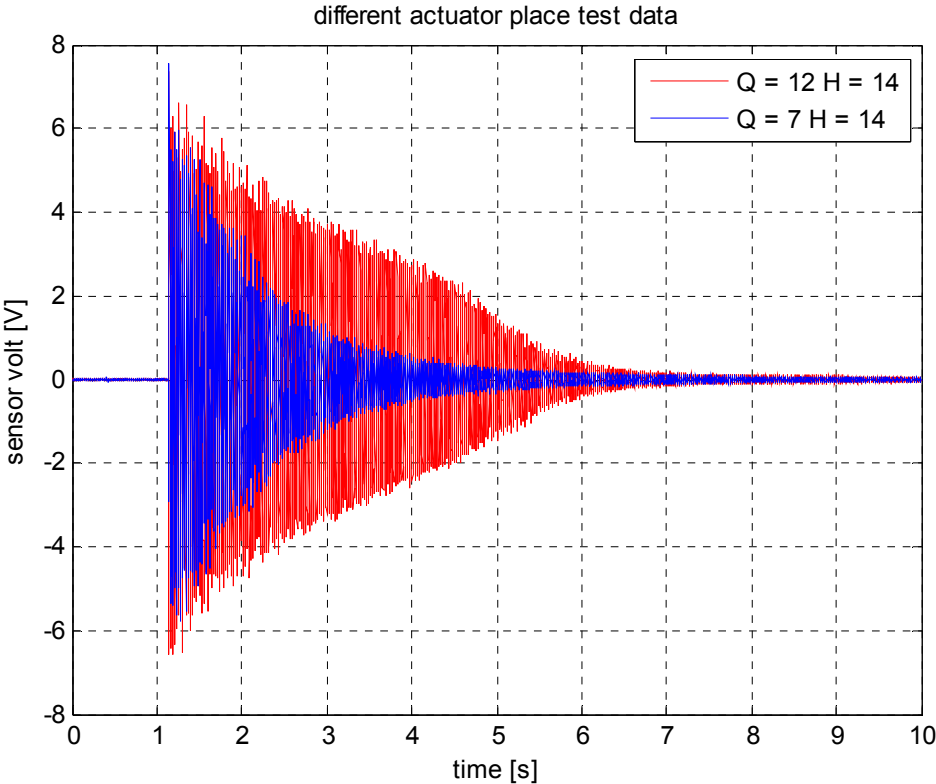


Figure 4-51. Cylinder sensor measurements for different actuator locations

CHAPTER 5

SUMMARY AND CONCLUSIONS

This study is carried out in order to gain theoretical and practical knowledge on active vibration control using piezoelectric patches. In the first chapter an introduction to active vibration control by piezoelectric materials is made by presenting the examples of active vibration control solutions applied to engineering structures used in aerospace namely aircraft wings and fins, helicopter rotor blades and turboprop engine propellers, missile airframe and launch vehicle payload adapters. In addition to complex engineering structures, active vibration studies are also carried out for simpler geometries such as beams, plates and shells in order to obtain basic knowledge about active vibration control. An introduction to this type of studies is made by giving an example study on cylinder structures.

In the second chapter of this study, information about piezoelectric materials are given, from definition of piezoelectricity to definition of material properties and modeling of piezoelectric materials. Information about different types of piezoelectric actuators and their potential is also presented. After giving information about piezoelectric materials and actuators, theoretical information about active vibration control is given. Concepts of modeling a vibratory system in state space, controllability, observability and pole placement are discussed. The placement criterion used in finding optimum piezoelectric patch locations based on the eigenvalues of the controllability Gramian matrix is introduced.

Third chapter of the study is dedicated to active vibration control of a cantilever beam structure with piezoelectric patches. A cantilever beam has simple mode shapes and it is obvious to place piezoelectric patch actuators close the root of the beam to control its vibrations. At first the cantilever beam to be studied is manufactured and then two piezoelectric patches were glued close to the root of the

beam on one face of the beam side by side. Then the beam with piezoelectric patches is modeled in ANSYS. A full model is created, by also modeling the piezoelectric elements in finite element environment. Static analyses are carried out by applying voltage load to piezoelectric patch actuators and beam deflections as a response to the loads are recorded. Modal analysis is done on the beam to obtain the dynamics of the structure. Based on those analyses, mathematical model of the beam that will be used in control simulations is generated in MATLAB/Simulink environment. The input of the beam is the control voltage applied to piezoelectric patch actuator, whereas the output of the beam is taken as the tip displacement. The mathematical model is a reduced state space vibratory model of the beam and the frequency response of this model is the transfer function between the voltage applied to piezoelectric actuator and the beam tip displacement. By this procedure a simple and fast model of the beam is generated to be used in the controller design simulations. The reduced mathematical model is verified by comparing the step response of the model with the ANSYS full transient analysis results. Frequency response of the reduced model is also compared with the ANSYS full harmonic analysis results. By these comparisons it is concluded that the reduced mathematical model can accurately replace the full finite element model. Without using a simple model and instead by only using time consuming finite element simulations, it would be practically impossible to develop a proper controller.

In the next step of the beam studies, static and dynamic tests are done on the beam to verify and update the generated finite element model. The dynamic behavior of the beam model showed a good agreement with the test results for the initially set of parameters, so only slight changes were required to be done on the finite element model to match the test results. For the static behavior d_{31} parameter of piezoelectric actuator is needed to be updated to fit the analysis results of the model with the test data. After updating finite element model the mathematical model to be used in controller design simulations is also updated. By this approach the controller will be developed for the updated model and the controller is supposed to work without any further modifications.

The controller design is made for the updated model by simple PID control and by pole placement methods. Both controllers offered sufficient results of disturbance rejection in the simulation. The PID control designed for the beam is implemented in real life, and experimentally it is illustrated that it works successfully as it is designed.

In the fourth chapter of this study active vibration control of a hollow cylinder is studied. In the third chapter, finite element analysis, testing, modeling and control strategies were developed for simple beam structure. Cylinder studies are presented as the extensions of the beam studies. In active vibration control of cylinder structure, the main difference (compared with active vibration control of beams) is the requirement of optimal piezoelectric patch actuator placement study for desired mode shapes. Mode shapes of a cylinder are much more complex than those of cantilever beam. It is important to find the optimum piezoelectric patch actuator locations in the active vibration control of cylinder. Placing piezoelectric patch actuators to the locations where the strain energy is the highest is a fast and practical method, however things can get complicated when multiple modes are desired to be controlled with a single patch. A patch placement routine based on controllability Gramian matrices and the mode shapes of the modes to be controlled is employed. In this routine ANSYS is used to obtain system matrices of the cylinder, and MATLAB is used in the computation of the controllability Gramian matrices and patch placement criteria. In this analysis an important point to note is that for cylinder structures that are perfectly tuned, there are two vibration modes exactly at the same frequency and the position of nodal lines of those mode shapes depend on the direction of the excitation force for breathing modes. Therefore one should keep this fact in mind and consider the excitation force direction and align the mode shapes accordingly in the placement procedure since the locations of nodal points of mode shapes depend on the excitation force direction.

After discussing how to find the optimum place for given piezoelectric patch, mathematical model of the cylindrical structure with piezoelectric patch is generated using a similar method as in the beam study. Controller design by using pole

placement is employed to control desired vibration modes of the cylinder. Positive Position Feedback control strategy is also employed in designing a separate controller to decrease the vibrations of target modes. In this point, the effect of patch placement is shown by simulations using the same controller for models with different patch locations. It is shown in the simulations that the actuator performance comes out to be better when the patch is placed by using a balanced patch placement criterion between the modes to be controlled. After simulations, experimental studies are carried out to verify the finite element analysis results. In the experimental studies piezoelectric patch sensor and accelerometers on the cylinder structure are used in data acquisition. Modal test by impact hammer is made and mode shapes and natural frequencies of the test cylinder are determined. Then, the mode shapes of the analysis results are aligned according to test results and the optimum patch locations are updated according to the mode shapes obtained by modal test. The designed PPF controller is also updated for the actual natural frequencies of the cylinder. PPF controller is successfully implemented and the vibrations of the cylinder is damped by active vibration control method. The placement of piezoelectric patch actuator is also verified by tests. In this study it is shown that multiple vibration modes of a hollow cylinder can be controlled by using a collocated piezoelectric patch sensor and actuator pair. The effect of piezoelectric patch placement is also demonstrated experimentally.

In this thesis active vibration control of a hollow cylinder is studied both theoretically and experimentally primary goal being to find the best location for the piezoelectric patch actuators to minimize the vibrations. As a future work, this study can be applied to one of real life engineering structures with a cylindrical shape.

REFERENCES

1. Bisplinghoff, R. L., Ashley, H., and Halfman, R. L., (1955) *Aeroelasticity*, Dover.
2. Kandagal, S. B., Venkatraman, K., (2006) Piezo-actuated Vibration and Flutter Control. *Defence Science Journal*, 56 (4), 615-626.
3. Hanagud, S., Bayon de Noyer, M., Luo, H., Henderson, D., Nagaraja, K.S., (1999) Tail Buffet Alleviation of High Performance Twin Tail Aircraft Using Piezo- Stack Actuators. In: *Proceedings of AIAA/ASME/ASCE/AHC Structures, Structural Dynamics and Materials Conference, St. Louis, MO, U.S.A.*
4. Facciano, A. B., Moore, R. T., Hlavacek, G. J., Seasley, C. D., (2011) *missile airframe and structure comprising piezoelectric fibers and method for active structural response control*. United States Patent US 8,049,148 B2 (Patent).
5. Evert, M. E., Janzen, P. C., Anderson, E. H., (2004) Active Vibration Isolation System for Launch Load Alleviation. In: *Proceedings of Smart Structures and Materials 2004: Industrial and Commercial Applications of Smart Structures Technologies, March 2004, San Diego, CA.*
6. Konstanzer, P., Enenkl, B., Aubourg, P. A., Cranga, P., (2008) Recent advances in Eurocopter's passive and active vibration control. In: *Proceedings of American Helicopter Society 64th Annual Forum, April 29 – May 1, 2008, Montréal, Canada.*
7. Bachmann, F., (2012) *Integration of Monolithic Piezoelectric Damping Devices into Adaptive Composite Structures*, Ph.D. thesis, ETH Zurich.

8. Kolonay, R. M., (2001) *Computational Aeroelasticity*. [Presentation] RTA-NATO The Applied Vehicle Technology Panel, Ankara, October 1-5.
9. Browning, J. S., (2009) *F-16 Ventral Fin Buffet Alleviation Using Piezoelectric Actuators*, M.Sc. thesis, Wright-Patterson Air Force Base Ohio.
10. Shetaa, E. F., Moses, R. W., Huttshell, L. J., (2006) Active smart material control system for buffet alleviation. *Journal of Sound and Vibration* 292, 854–868.
11. Maucher, C., Grohmann, B., Janker, P., Altmikus, A., Jensen, F., Baier, H., (2007) Actuator Design for the Active Trailing Edge of a Helicopter Rotor Blade. In: *In 33rd European Rotorcraft Forum, Kazan, Russia*.
12. Jaenker, P., Kloeppe, V., Konstanzer, P., Maier, R., (2008) Piezo Active Vibration and Noise Control in Helicopters. In: *26th International Congress of the Aeronautical Sciences, Alaska, USA*.
13. Jackson, P. B., (2010) Overview of Missile Flight Control Systems. *Johns Hopkins Apl. Technical Digest*, 29 (1).
14. Sohn, J. W., Choi, S.-B., Lee, C. H., (2009) Active vibration control of smart hull structure using piezoelectric composite actuators. *Smart Materials Structures*, 18.
15. Kwak, M. K., Heo, S., Jeong, M., (2009) Dynamic modeling and active vibration controller design for a cylindrical shell equipped with piezoelectric sensors and actuators. *Journal of Sound and Vibration*, 321, 510–524.

16. Jyoti, A. K., (2008) *Modeling and Analysis of PZT Micropower Generator*, Ph.D. thesis, Auburn University AL, USA.
17. Jordan, T.L., Ounaies, Z., (2001) *Piezoelectric Ceramic Characterization*, ICASE Report No. 2001-28.
18. Piezo Systems Inc. (2013) *History of Piezoelectricity*. [Online]. Available from: <http://www.piezo.com/tech4history.html> [Accessed 1st December 2013].
19. Özgen, O. G., (2011) *Introduction to Smart Structures and Materials*. [Lecture] METU Ankara.
20. Applied Piezo Foundation (2013) *Poling Treatment*. [Online]. Available from: <http://www.applied-piezo.com/about-piezo-technology/poling-treatment> [Accessed 1st December 2013].
21. Physik Instrumente (2009) *Piezoelectrics in Positioning: Tutorial on Piezotechnology in Nanopositioning Applications*, Karlsruhe, Germany.
22. APC International Ltd. (2013) *Piezoelectricity*. [Online]. Available from: <https://www.americanpiezo.com/knowledge-center/piezo-theory/piezoelectricity.html> [Accessed 1st December 2013].
23. READE Advanced Materials (2013) *Lead Zirconate Titanate (PZT)*. [Online]. Available from: <http://www.reade.com/products/41-titanate-compounds-powder/284-lead-zirconate-titanate-powder-pzt-lead-zirconate-titanate-lead-zirconium-titanate-lead-titanate-zirconate-plumbum-zirconate-titanate-cas-12626-81-2> [Accessed 1st December 2013].
24. HyperPhysics (2013) *Work and Voltage: Constant Electric Field*. [Online]. Available from: <http://hyperphysics.phyastr.gsu.edu/hbase/electric/elewor.html> [Accessed 1st December 2013].

25. Piezo Systems Inc. (2013) *Introduction to Piezo Transducers*. [Online]. Available from: <http://piezo.com/tech2intropiezotrans.html> [Accessed 1st December 2013].
26. Piezo Systems Inc. (2013) *Standard Quick Mount Piezoelectric Sensors*. [Online]. Available from: <http://www.piezo.com/prodbg7qm.html> [Accessed 1st December 2013].
27. Sensor Technology Ltd. (2009) *Product Overview*. Ontario, Canada.
28. Physik Instrumente (PI) GmbH & Co.KG (2013) *Piezo Tutorial*. [Online]. Available from: http://www.physikinstrumente.com/tutorial/4_28.html [Accessed 1st December 2013].
29. Noliac A/S (2013) *Plate Stacks, Standard Product*. [Online]. Available from: http://www.noliac.com/Plate_stacks-59.aspx [Accessed 1st December 2013].
30. Cedrat Technologies (2013) *Amplified Piezoelectric Actuators*. [Online]. Available from: <http://www.cedrat-technologies.com/en/mechatronic-products/actuators/apa.html> [Accessed 1st December 2013].
31. Smart Material Corp. (2013) *Macro Fiber Composite (MFC)*. [Online]. Available from: <http://www.smart-material.com/MFC-product-main.html> [Accessed 1st December 2013].
32. Physik Instrumente (PI) GmbH & Co.KG (2013) *Piezo Actuator Catalog Site, Piezo Tube Actuators*. [Online]. Available from: http://www.physikinstrumente.com/tutorial/4_28.html [Accessed 1st December 2013].

33. Wikimedia Commons (2009) *Inchworm Motors*. [Online]. Available from:http://commons.wikimedia.org/wiki/File:Inchworm_Motor.jpg [Accessed 1st December 2013].
34. ANSI/IEEE (1987) 176. *IEEE Standard on Piezoelectricity*, New York, IEEE.
35. ANSYS, Inc, (2009) *Theory Reference for the Mechanical APDL and Mechanical Applications*, Canonsburg, PA.
36. Imaoka, S., (1999) *ANSYS Tip of the Week: Conversion of Piezoelectric Material Data*, Collaborative Solutions Inc. Memo Number STI45:000509C.
37. Physik Instrumente (PI) GmbH & Co.KG (2013) *Orthogonal system describing the properties of a poled piezoelectric ceramic*. [Online]. Available from:<http://physikinstrumente.com/en/products/primages.php?sortnr=400600.05&picview=2> [Accessed 1st December 2013].
38. ANSYS, Inc, (2010) *ANSYS Mechanical APDL Element Reference*, Canonsburg, PA.
39. Gencoglu, C., Özgüven, H. N., (2013) Optimal Placement of Piezoelectric Patches on a Cylindrical Shell for Active Vibration Control. In: *Proceedings of IMAC 2013 Conference, Los Angeles, CA*.
40. ANSYS, Inc, (2011) *ANSYS 14.0 Help Theory Reference*, Canonsburg, PA.
41. Meirovitch, L., (2001) *Fundamentals of Vibration*. McGraw Hill International Edition.
42. Ogata, K., (2002) *Modern Control Engineering, 4th Edition*. Prentice-Hall, Inc.

43. Gupta, V., Sharma, M., Thakur, N. (2010) Optimization Criteria for Optimal Placement of Piezoelectric Sensors and Actuators on a Smart Structure: A Technical Review. *Journal of Intelligent Material Systems and Structures* (21), 1227-1243.
44. Hac, A., Lui, L. (1993) Sensor and Actuator Location in Motion Control of Flexible Structures. *Journal of Sound and Vibration* (167), 239-261.
45. Jha, A. K., & Inman, D. J. (2003) Optimal Sizes and Placements of Piezoelectric Actuators and Sensors for an Inflated Torus. *Journal of Intelligent Material Systems and Structures* (14), 563-576.
46. Leleu, S., Abou-Kandil, H. and Bonnassieux, Y. (2000) Piezoelectric Actuators and Sensors Location for Active Control of Flexible Structures. In: *Proceedings of the IEEE International Measurement Technology Conference, Baltimore, Maryland, USA pp. 818–823.*
47. Peng, F., Ng, A., Hu, Y.-R., (2005) Actuator Placement Optimization and Adaptive Vibration Control of Plate Smart Structures. *Journal of Intelligent Material Systems and Structures* (16), 263-271.
48. Bruant, I., Gallimard, L., & Nikoukar, S. (2010) Optimal Piezoelectric Actuator and Sensor Location for Active Vibration Control, Using Genetic Algorithm. *Journal of Sound and Vibration* (329), 1615-1635.
49. Hardt, D., (2004) *Analysis and Design of Feedback Control Systems*. [Lecture] Massachusetts Institute of Technology Department of Mechanical Engineering, Fall 2014.
50. Messner, B., Tilbury, D., Hill, R., Taylor, J. D., (2012) *Control Tutorials for MATLAB and Simulink*. [Online]. Available from: <http://ctms.engin.umich.edu/CTMS/> [Accessed 10th December 2013].

51. Lewis, F. L., (2001) *State Observer and Regulator Design*. [Lecture] University of Texas Arlington.
52. Vaccaro, R. J., (2012) *Linear Control Systems Lecture Notes: Rules for Selecting Pole Locations*. [Lecture] University of Rhode Island.
53. Lüleci, İ. F., (2013) *Active Vibration Control of Beams and Plates by Using Piezoelectric Patch Actuators*, M.Sc. thesis, METU Ankara.
54. Dassault Systemes (2013) *Rayleigh Damping*. [Online]. Available from: http://help.solidworks.com/2012/English/SolidWorks/cworks/Rayleigh_Damping.htm [Accessed 10th December 2013].
55. Physik Instrumente (PI) GmbH & Co.KG (2013) *P-876 Dura Act Transducer* [Online]. Available from: <http://www.physikinstrumente.com/en/products/prdetail.php?sortnr=101790> [Accessed 10th December 2013].
56. Ewins, D. J., (2000) *Modal Testing Theory Practice and Application Second Edition*, Research Studies Press LTD.
57. The Math Works, Inc, (2013) *MATLAB Help R2013a*, Massachusetts, USA.
58. Kyowa Electronic Instruments Co. Ltd., (2013) *What is a strain gage? Introduction to Strain Gages*, Tokyo, Japan

APPENDIX A

QUARTER BRIDGE STRAIN GAGE MEASUREMENT WITH SINGLE STRAIN GAGE

Strain gage is a sensor that measures the strain of the surface it is applied on by measuring change of resistance of the wire coil of the strain gage. Each strain gage has a property called the gage factor which relates the strain of the gage and the resistance difference of the strain gage and it is given as follows

$$\frac{\Delta R}{R} = K_s * \varepsilon \quad (\text{A.1})$$

In the above equation ΔR is the resistance change as a response to strain, R is the resistance of the gage, K_s is a constant called gage factor and ε is the strain [58].

Strain gages are used with Wheatstone bridge circuits for measuring change in their resistances. A single strain gage can be used in quarter bridge formation as shown in Figure A-1 [58].

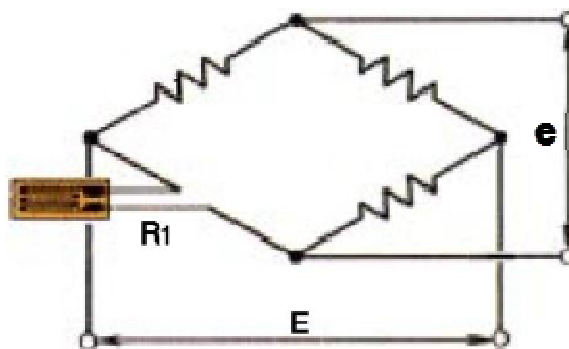


Figure A-1. Quarter bridge Strain Gage [58]

In the bridge circuit E is the applied excitation voltage applied to circuit and e is the measured output voltage from the circuit. By the equation given below, strain can be derived from the voltage measurements of bridge circuit [58].

$$E = \frac{1}{4} K_S * \varepsilon * E \quad (A.2)$$

In this study gage factor of the strain gage used is 2.1 and resistance of the strain gage is 350Ω .

APPENDIX B

MATERIAL PROPERTIES

Material and piezoelectric properties of APC 850 is given below

APC Material:	840	841	850	855	880
Navy Equivalent	Navy I	--	Navy II	Navy VI	Navy III
Relative Dielectric Constant					
K^T	1250	1350	1900	3300	1000
Dielectric Dissipation Factor (Dielectric Loss(%))*					
$\tan \delta$	0.40	0.35	1.40	1.30	0.35
Curie Point (°C)**					
T_c	325	320	360	250	310
Electromechanical Coupling Factor					
k_p	0.59	0.60	0.63	0.68	0.50
k_{33}	0.72	0.68	0.72	0.76	0.62
k_{31}	0.35	0.33	0.36	0.40	0.30
k_{15}	0.70	0.67	0.68	0.66	0.55
Piezoelectric Charge Constant (10^{-12} C/N or 10^{-12} m/V)					
d_{33}	290	300	400	630	215
$-d_{31}$	125	109	175	276	95
d_{15}	480	450	590	720	330
Piezoelectric Voltage Constant (10^{-3} Vm/N or 10^{-3} m²/C)					
g_{33}	26.5	25.5	24.8	21.0	25.0
$-g_{31}$	11.0	10.5	12.4	9.0	10.0
g_{15}	38.0	35.0	36.0	27.0	28.0
Young's Modulus (10^{10} N/m²)					
Y_{11}^E	8.0	7.6	6.3	5.9	9.0
Y_{33}^E	6.8	6.3	5.4	5.1	7.2
Frequency Constants (Hz*m or m/s)					
N_L (longitudinal)	1524	1700	1500	1390	1725
N_T (thickness)	2005	2005	2040	2079	2110
N_F (planar)	2130	2055	2080	1920	2120
Density (g/cm³)					
ρ	7.6	7.6	7.6	7.7	7.6
Mechanical Quality Factor					
Q_m	500	1400	80	65	1000

Figure B-1. Material and piezoelectric properties of APC 850

Glue used when attaching APC piezoelectric patch to the steel beam is 3M Scotch-Weld DP 760 and its Young's Modulus for different temperatures is given in Figure B-2.

Compression strength (MPa)	Young's modulus (MPa)
23 +/- 2°C : 78.8	23 +/- 2°C : 5972
80 +/- 2°C : 48.7	80 +/- 2°C : 4930
120 +/- 2°C : 36.8	120 +/- 2°C : 3633
150 +/- 3°C : 24.2	150 +/- 3°C : 2350

Figure B-2. Young modulus of Scotch Weld DP 760 glue

In PI Dura Act piezoelectric actuator, PIC 255 piezoelectric material is used and its properties is given in Figure B-3.

	PIC151	PIC153	PIC255/252	PIC050
Physical and Dielectric Properties				
Density ρ [g/cm ³]	7.80	7.60	7.80	4.70
Curie temperature T_c [°C]	250	185	350	>500
Relative permittivity in the polarization direction $\epsilon_{33}^T/\epsilon_0$ Perpendicular to the polarization ϵ_{11}/ϵ_0	2400	4200	1750	60
	1980		1650	85
Dielectric loss factor $\tan \delta$ [10^{-3}]	20	30	20	<1
Electro-Mechanical Properties				
Piezoelectric deformation coefficient, piezo modulus*				
d_{31} [pm/V]	-210		-180	
d_{33} [pm/V]	500	600	400	40
d_{15} [pm/V]			550	80
Acousto-Mechanical Properties				
Elastic compliance coefficient				
s_{11}^E [10^{-12} m ² /N]	15.0		16.1	
s_{33}^E [10^{-12} m ² /N]	19.0		20.7	
Mechanical quality factor Q_m	100	50	80	

Figure B-3. Material and piezoelectric properties of PIC 255

APPENDIX C

ANSYS APDL CODES

Code used in generating beam finite element model

```
FINISH
/CLEAR
/PREP7

!Voltage
Volt1 = 1
Volt2 = 0

!Dimensions
beam_dim_x = 315
beam_dim_y = 24
beam_dim_z = 1
beambase_dim_x = 35
piezo1_dim_x = 25
piezo1_dim_y = beam_dim_y
piezo1_dim_z = 0.5
piezo1_base_x = 9
piezo1_base_y = (beam_dim_y-piezo1_dim_y)/2
epoxy_dim_z = 0.25
piezo2_dim_x = 25
piezo2_dim_y = beam_dim_y
piezo2_dim_z = 0.5
piezo2_base_x = 39
piezo2_base_y = (beam_dim_y-piezo1_dim_y)/2
```

sg1_base_x = 20

sg2_base_x = 50

!Geometry

BLOCK,0,beam_dim_x,0,beam_dim_y,0,beam_dim_z,

BLOCK,-beambase_dim_x,0,0,beam_dim_y,0,beam_dim_z,

BLOCK,piezo1_base_x,piezo1_base_x+piezo1_dim_x,piezo1_base_y,piezo1_base_y+piezo1_dim_y,beam_dim_z,beam_dim_z+epoxy_dim_z

BLOCK,piezo1_base_x,piezo1_base_x+piezo1_dim_x,piezo1_base_y,piezo1_base_y+piezo1_dim_y,beam_dim_z+epoxy_dim_z,beam_dim_z+epoxy_dim_z+piezo1_dim_z

BLOCK,piezo2_base_x,piezo2_base_x+piezo2_dim_x,piezo2_base_y,piezo2_base_y+piezo2_dim_y,beam_dim_z,beam_dim_z+epoxy_dim_z

BLOCK,piezo2_base_x,piezo2_base_x+piezo2_dim_x,piezo2_base_y,piezo2_base_y+piezo2_dim_y,beam_dim_z+epoxy_dim_z,beam_dim_z+epoxy_dim_z+piezo2_dim_z

wpro,,90.000000

wpof,,piezo1_base_x

VSBW,ALL

wpof,,sg1_base_x-piezo1_base_x

VSBW,ALL

wpof,,piezo1_base_x+piezo1_dim_x-sg1_base_x

VSBW,ALL

wpof,,piezo2_base_x-piezo1_base_x-piezo1_dim_x

VSBW,ALL

wpof,,sg2_base_x-piezo2_base_x

VSBW,ALL

wpof,,piezo2_base_x+piezo2_dim_x-sg2_base_x

VSBW,ALL

wpro,,-90.000000,

wpof,,beam_dim_y/2

VSBW,ALL

WPCSYS,-1
VGLUE,ALL

!Element

ET,1,SOLID186
KEYOPT,1,2,1
KEYOPT,1,3,0
KEYOPT,1,6,0
ET,2,SOLID226,110
KEYOPT,2,1,1001
KEYOPT,2,2,0
KEYOPT,2,4,0
KEYOPT,2,6,0
KEYOPT,2,9,0
KEYOPT,2,10,0

!Material

MPTEMP,1,0
MPDATA,EX,1,,207000
MPDATA,PRXY,1,,0.3
MPDATA,DENS,1,,7.85e-9

!Piezo Properties APC 850

TB,ANEL,2,1,,0
TBDATA,1,1.203462e+05,7.517913e+04,7.509007e+04
TBDATA,7,1.203462e+05,7.509007e+04
TBDATA,12,1.108671e+05
TBDATA,16,2.257336e+04
TBDATA,19,2.105263e+04
TBDATA,21,2.105263e+04
TB,PIEZ,2
TBDATA,3,-1.884532e-02

```

TBDATA,6,-1.884532e-02
TBDATA,9,6.801787e-03
TBDATA,14,1.242105e-02
TBDATA,16,1.242105e-02
EMUNIT,EPZRO,8.850000e-12
MP,PERX,2,1.071930e+03
MP,PERY,2,1.071930e+03
MP,PERZ,2,5.278673e+02
MP,DENS,2,7.600000e-09

```

!Epoxy Properties

```

MPDATA,EX,3,,6000
MPDATA,PRXY,3,,0.35
MPDATA,DENS,3,,1.2e-9

```

!Mesh

```

ESIZE,beam_dim_z*2
VSEL,S,LOC,Z,0,beam_dim_z
VATT,1,,1,0
VSEL,S,LOC,Z,beam_dim_z,beam_dim_z+epoxy_dim_z
VATT,3,,1,0
VSEL,S,LOC,Z,beam_dim_z+epoxy_dim_z,beam_dim_z+epoxy_dim_z+piezo1_dim_z
VATT,2,,2,0
ALLSEL,ALL
VSWEEP,ALL

```

!Boundary Condition

```

ASEL,S,LOC,Z,0
ASEL,A,LOC,Z,beam_dim_z
ASEL,R,LOC,X,-beambase_dim_x,-beambase_dim_x/2
CM,boundary,AREA

```

```

ALLSEL,ALL
ASEL,S,LOC,Z,beam_dim_z+epoxy_dim_z
ASEL,R,LOC,X,piezo1_base_x,piezo1_base_x+piezo1_dim_x
CM,electrode1,AREA
ASEL,S,LOC,Z,beam_dim_z+epoxy_dim_z
ASEL,R,LOC,X,piezo2_base_x,piezo2_base_x+piezo2_dim_x
CM,electrode2,AREA
ASEL,S,LOC,Z,beam_dim_z+epoxy_dim_z+piezo1_dim_z
ASEL,R,LOC,X,piezo1_base_x,piezo1_base_x+piezo1_dim_x
CM,ground1,AREA
ASEL,S,LOC,Z,beam_dim_z+epoxy_dim_z+piezo2_dim_z
ASEL,R,LOC,X,piezo2_base_x,piezo2_base_x+piezo2_dim_x
CM,ground2,AREA
ALLSEL,ALL
DA,boundary,UX,0
DA,boundary,UY,0
DA,boundary,UZ,0
NodeTip = NODE(beam_dim_x-6,beam_dim_y/2,beam_dim_z)

```

```

!Analysis
/SOLU
ANTYPE,2
EQSLV,SPAR
MXPAND,2,,0
LUMPM,0
PSTRES,0
MODOPT,LANB,2,0,0,,OFF
MODCONT,ON
DMPRAT, 0.0022
DA,electrode1,volt,1
DA,electrode2,volt,0
DA,ground1,volt,0

```

```
DA,ground2,volt,0
```

```
ALLSEL,ALL
```

```
SOLVE
```

```
FINISH
```

```
!Writing State Space Matrices
```

```
/POST1
```

```
*DIM,OUTPUT,,1,2
```

```
OUTPUT(1,1) = NodeTip
```

```
OUTPUT(1,2) = 3
```

```
*DIM,OUTPUTLAB,CHAR,1
```

```
OUTPUTLAB(1) = 'BeamTip'
```

```
*DIM,INPUTLAB,CHAR,1
```

```
INPUTLAB(1) = 'pizeo1'
```

```
SPMWRITE,MODAL,,,INPUTLAB,OUTPUT,OUTPUTLAB,,,0
```

Code used in cylinder geometry

```
FINISH
```

```
/CLEAR
```

```
/PREP7
```

```
Q = 1
```

```
H = 1
```

```
!DIMENSIONS
```

```
rin = 146.5
```

```
t1 = 3.5
```

```
t2 = 5
```

```
t3 = 9
```

```
t4 = 10.8
```

```
tp_1 = 0.5
```

tp_2 = 0.5
h1 = 477
h12 = 23
h2 = 183
h23 = 11
h3 = 19
h34 = 6
h4 = 14
nseg = 18
hseg = 15
hp = 30
hall = h1+h12+h2+h23+h3+h34+h4

!ELEMENT TYPE

ET,1,SOLID186

ET,2,SOLID226,1001

!MATERIAL PROPERTIES

!MATERIAL1: STEEL

MPTEMP,1,0

MPDATA,EX,1,,210E3

MPDATA,PRXY,1,,0.33

MPDATA,DENS,1,,7.85E-9

!MATERIAL2: PZT

TB, ANEL,2 , 1 , 0

TBDATA, 1, 9.6903E+04 , 7.0017E+04 , 7.0017E+04

TBDATA, 7, 1.2276E+05 , 7.6462E+04

TBDATA, 12, 1.2276E+05

TBDATA, 16, 2.2272E+04

TBDATA, 19, 2.3148E+04

TBDATA, 21, 2.2272E+04

TB, PIEZ, 2

```

TBDATA, 1, 0.0138
TBDATA, 4, -0.0071
TBDATA, 7, -0.0071
TBDATA, 11, 0.0119
TBDATA, 18, 0.0119
EMUNIT, EPZRO, 8.85E-12
MP, PERX,2 , 857
MP, PERY,2 , 929
MP, PERZ, 2 , 929
MP, DENS,2 , 7.8E-09

```

!GENETRAING GEOMETRY

```

CSYS,1
K,1,rin,0,h1+h12+h2+h23+h3+h34+h4
K,2,rin+t1,0,h1+h12+h2+h23+h3+h34+h4
K,3,rin+t1,0,h12+h2+h23+h3+h34+h4
K,4,rin+t2,0,h2+h23+h3+h34+h4
K,5,rin+t2,0,h23+h3+h34+h4
K,6,rin+t3,0,h3+h34+h4
K,7,rin+t3,0,h34+h4
K,8,rin+t4,0,h4
K,9,rin+t4,0,0
K,10,rin,0,0
K,11,0,0,0
K,12,0,0,h1
LSTR,1,2
LSTR,2,3
LSTR,3,4
LSTR,4,5
LSTR,5,6
LSTR,6,7

```

```

LSTR,7,8
LSTR,8,9
LSTR,9,10
LSTR,10,1
AL,ALL
VROTAT,1,,,,,11,12,360,nseg,
wpof,,,h4
VSBW,ALL
wpof,,,h34
VSBW,ALL
wpof,,,h3
VSBW,ALL
wpof,,,h23
VSBW,ALL
wpof,,,h2
VSBW,ALL
wpof,,,h12
VSBW,ALL
wpof,,,h1-hseg*hp
VSBW,ALL
*DO,i,1,hseg-1
wpof,,,hp
VSBW,ALL
*ENDDO
wpof,,,hp*(H-hseg)
CYL4,0,0,rin+t1,(360/nseg)*(Q-1),rin+t1+tp_1,(360/nseg)*Q,hp
WPAVE,0,0,0
VGLUE,ALL

!MESHING
VSEL,S,LOC,Z,hall-h1,hall-hp*hseg
CM,h_bottom1,VOLU

```

```

ALLSEL,ALL
VSEL,S,LOC,Z,hall-h1-h12,hall-h1
CM,h_bottom12,VOLU
ALLSEL,ALL
VSEL,S,LOC,Z,hall-h1-h12-h2,hall-h1-h12
CM,h_bottom2,VOLU
ALLSEL,ALL
VSEL,S,LOC,Z,hall-h1-h12-h2-h23,hall-h1-h12-h2
CM,h_bottom23,VOLU
ALLSEL,ALL
VSEL,S,LOC,Z,hall-h1-h12-h2-h23-h3,hall-h1-h12-h2-h23
CM,h_bottom3,VOLU
ALLSEL,ALL
VSEL,S,LOC,Z,hall-h1-h12-h2-h23-h3-h34,hall-h1-h12-h2-h23-h3
CM,h_bottom34,VOLU
ALLSEL,ALL
VSEL,S,LOC,Z,0,h4
CM,h_bottom4,VOLU
ALLSEL,ALL
VSEL,S,LOC,Z,hall-hp*hseg,hall
VSEL,R,LOC,X,rin,rin+t1
CM,piezo_1_vol,VOLU
ALLSEL,ALL
VSEL,S,LOC,Z,hall-hp*hseg,hall
VSEL,U,LOC,X,rin,rin+t1
CM,h_cyl,VOLU
ALLSEL,ALL
VATT,1,,1,,
CMSEL,S,piezo_1_vol
VATT,2,,2,,
ALLSEL,ALL
CMSEL,S,h_cyl

```

```

ASLV,R
LSLA,R
LSEL,R,LOC,Z,hall-hp/4,hall
LSEL,U,LOC,X,rin+0.1*t1,rin+0.9*t1
LESIZE,ALL,,6,,1,,1,
ALLSEL,ALL
ESIZE,t1*4
VSWEEP,ALL
NROTAT,ALL
ALLSEL,ALL
LOCAL,11,1,0,0,0,0,0
CMSEL,S,piezo_1_vol
ESLV,S
CM,piezo_1_ele,ELEM
EMODIF,piezo_1_ele,ESYS,11
ALLSEL,ALL
CSYS,1

!DEFINE ELECTRODES
CMSEL,S,piezo_1_vol
ASLV,R
ASEL,R,LOC,X,rin,rin+t1
ASEL,R,LOC,Z,hall+(H-0.75-hseg)*hp,hall+(H-0.25-hseg)*hp
CM,ground_1_area,AREA
ALLSEL,ALL
CMSEL,S,piezo_1_vol
ASLV,R
ASEL,R,LOC,Z,hall+(H-0.75-hseg)*hp,hall+(H-0.25-hseg)*hp
ASEL,R,LOC,X,rin+t1+0.75*tp_1,rin+t1+tp_1
CM,electrode_1_area,AREA
ALLSEL,ALL
TIP = NODE(rin,0,hall)

```

```
!ANALYSIS
/SOLU
ANTYPE,2
EQSLV,SPAR
MXPAND,12,,,0
LUMPM,0
PSTRES,0
MODOPT,LANB,12,2,1000,,OFF
MODCONT,ON
DMPRAT, 0.001
DA,electrode_1_area,VOLT,1
DA,ground_1_area,VOLT,0
ALLSEL,ALL
SOLVE
FINISH
```

APPENDIX D

IMAC 2013 PAPER

Optimal Placement of Piezoelectric Patches on a Cylindrical Shell for Active Vibration Control

Caner Gencoglu^{1,2}

H. Nevzat Özgüven¹

¹Department of Mechanical Engineering, Middle East Technical University, Ankara,
Turkey

²Roketsan Inc. PO Box 30, 06780, Elmadag, Ankara, Turkey

ABSTRACT

Piezoelectric materials have proven themselves to be used as actuators for active vibration control. In this study, the active vibration control of a cylindrical shell by means of piezoelectric actuators is investigated. As the most important stage of controlling the vibrations, this paper focuses on the optimal placement of piezo patch actuators. It is aimed in this study to determine the optimum locations of piezo patches on a cylindrical shell by using finite element model of the system. In optimization, the spillover effects, which are caused by accidentally excited higher modes of the structure are also taken into account.

Keywords: Piezoelectric patches, active vibration control, cylindrical shell vibrations, actuator placement, spillover

1. INTRODUCTION

Piezoelectric materials have proven themselves to be used as actuators for active vibration control of lightweight and flexible structures in recent years. Lightweight and flexible structures are mostly used in space applications. Reducing the mass of the structure due to weight limitations also reduces its stiffness, making low frequency vibrations a problem for the structure. Piezoelectric actuators which have low mass, high bandwidth quick response, low cost and ease of mounting are good candidates for solution of vibration problem (Peng, Ng, & Hu, 2005). Considerable research effort has been spent in recent years in active vibration control via piezoelectric materials.

Piezoelectric materials are applied as surface mounted patches from the early years of active vibration control studies starting from Crawley and de Luis in 1987 (Crawley & de Luis, 1987). Beam and plate geometries are studied by many researchers. In the active vibration control problem of structures, placement of actuators has always played an important role. Misplaced actuators may cause lack of controllability and stability (Bruant, Gallimard, & Nikoukar, 2010). This led researchers to work in the field of optimal placement of actuators in active vibration control problems. Gupta et al. prepared a comprehensive review in the subject of optimal placement of actuators and sensors on smart structures (Gupta, Sharma, & Thakur, 2010). However, their study covered beam and plate geometry. Although cylinder geometry is commonly used in engineering structures, studies on active vibration control of cylindrical structures with piezoelectric patches are very limited (Sohn, Choi, & Kim, 2011).

In the optimal actuator placement problem, several approaches have been used. Hac and Lui used controllability gramian matrices in the calculation of optimal placement of actuators (Hac & Lui, 1993). Bruant et al. used controllability gramians as optimization criteria and genetic algorithm as search method (Bruant, Gallimard, & Nikoukar, 2010). Peng used ANSYS substructuring tool in the finite element model reduction (Peng, Ng, & Hu, 2005).

In this study the optimal placement of piezoelectric patch actuators on a cylindrical shell is investigated. The system is modeled by using finite elements (FE), and model reduction, similar to the one used by Peng. After the model reduction and formulation of superelements, effect of piezoelectric material at each possible patch location is calculated by applying unit voltage to each patch and carrying out static analysis. Then, structural matrices required in the computation of controllability gramian matrix are obtained. Alternatively, static analysis can be carried out for a limited number of patch locations and a search method such as genetic algorithm can be used to find optimal locations; however this approach has the risk of having non-convergence. When calculating the optimal placement for actuators the spillover effects, which are caused by accidentally excited higher modes of the structure are also taken into account. The method used in this study does not take the orientation angles of piezoelectric patches into account. Mass and stiffness effects of the actuators are neglected in this study since actuators are thin compared to host structure. Perfect bonding is assumed between piezoelectric patch and host structure.

2. METHODOLOGY

The equation of motion for a dynamic system with piezoelectric actuators on its surface can be written as follows:

$$\mathbf{M}\ddot{\mathbf{r}} + \mathbf{C}\dot{\mathbf{r}} + \mathbf{K}\mathbf{r} = \mathbf{P}\mathbf{V} \quad (1)$$

where \mathbf{r} is the displacement vector for the degrees of freedom of interest, \mathbf{M} is mass matrix, \mathbf{C} is damping matrix and \mathbf{K} is stiffness matrix, \mathbf{V} is a vector containing the applied voltage information, and \mathbf{P} is the piezoelectric coupling matrix which relates the applied voltage to the piezoelectric patch and the force applied on the structure by the actuator.

For this structure, proportional damping is assumed, so that damping matrix can be expressed as the linear combinations of stiffness and mass matrices:

$$\mathbf{C} = \alpha \mathbf{M} + \beta \mathbf{K} \quad (2)$$

Equation (1) can be written in modal domain as shown below:

$$\bar{\mathbf{M}}\ddot{\boldsymbol{\eta}} + \bar{\mathbf{C}}\dot{\boldsymbol{\eta}} + \bar{\mathbf{K}}\boldsymbol{\eta} = \bar{\mathbf{P}}\mathbf{V} \quad (3)$$

where $\boldsymbol{\eta}$ is the vector of modal coordinates, $\bar{\mathbf{M}}$ is modal mass matrix, $\bar{\mathbf{C}}$ is modal damping matrix, $\bar{\mathbf{K}}$ is modal stiffness matrix and $\bar{\mathbf{P}}$ is piezoelectric coupling matrix transformed into modal domain. The matrices in modal domain can be expressed as follows:

$$\bar{\mathbf{M}} = \boldsymbol{\phi}^T \mathbf{M} \boldsymbol{\phi} \quad (4)$$

$$\bar{\mathbf{C}} = \boldsymbol{\phi}^T \mathbf{C} \boldsymbol{\phi} \quad (5)$$

$$\bar{\mathbf{K}} = \boldsymbol{\phi}^T \mathbf{K} \boldsymbol{\phi} \quad (6)$$

$$\bar{\mathbf{P}} = \boldsymbol{\phi}^T \mathbf{P} \quad (7)$$

Here $\boldsymbol{\phi}$ is the mass normalized modal matrix. Now the system equations can be represented in state space.

$$\begin{aligned} \dot{\mathbf{x}} &= \mathbf{A}\mathbf{x} + \mathbf{B}\mathbf{u} \\ \mathbf{y} &= \mathbf{C}\mathbf{x} + \mathbf{D}\mathbf{u} \end{aligned} \quad (8)$$

where

$$\begin{aligned} \mathbf{x} &= [\boldsymbol{\eta} \quad \dot{\boldsymbol{\eta}}]^T \\ \mathbf{u} &= \mathbf{V} \end{aligned} \quad (9)$$

$$\begin{aligned} \mathbf{A} &= \begin{bmatrix} \mathbf{0} & \mathbf{I} \\ -\bar{\mathbf{M}}^{-1}\bar{\mathbf{K}} & -\bar{\mathbf{M}}^{-1}\bar{\mathbf{C}} \end{bmatrix} & \mathbf{B} &= \begin{bmatrix} \mathbf{0} \\ \bar{\mathbf{M}}^{-1}\bar{\mathbf{P}} \end{bmatrix} \\ \mathbf{C} &= [\mathbf{I}] & \mathbf{D} &= [\mathbf{0}] \end{aligned} \quad (10)$$

Here \mathbf{x} is the state vector. Conversion of system equations into state space allows calculation of the controllability gramian matrix of the system. By controllability gramian matrix, one can obtain information about how easy it is to control the states of the system. The controllability gramian matrix is the measure of controllability of a system and defined as follows (Jha & Inman, 2003):

$$\mathbf{W}_c(t_1) = \int_0^{t_1} e^{\mathbf{A}t} \mathbf{B} \mathbf{B}^T e^{\mathbf{A}^T t} dt \quad (11)$$

In this equation $\mathbf{W}_c(t_1)$ is the controllability gramian matrix at time t_1 . In this problem, states of the system are defined by modal coordinates. So each of the diagonal element of the controllability gramian matrix gives information about the effort to be spent to control the corresponding particular mode of the system. For example, having a higher value for the controllability gramian for a mode means less effort to be spent to control that particular mode. By comparing the controllability gramian values of a system with different piezoelectric actuator locations, the best actuator location to control vibrations of the system can be determined.

Spillover problem may emerge when controlling real structures by means of feedback control. When modeling a vibrating structure, only a limited number of modes are included in the model, and higher modes are usually truncated. When trying to implement feedback control, the high frequency modes may be accidentally excited. As also noted by Bruant et al., only in few papers spillover effects are considered when placing actuators (Bruant, Gallimard, & Nikoukar, 2010). In the placement criterion, the modes which are not taken into account when designing the feedback controller should also be considered as the ones not to be excited. According to this criterion, actuators should be placed such that they control the desired modes and they do not excite the selected higher modes which are not controlled.

The placement criterion J to control first N modes is stated as follows (Hac & Lui, 1993):

$$J = \frac{1}{\sigma(\lambda_i)} \left(\sum_{i=1}^{2N} \lambda_i \right)^{2N} \sqrt{\left(\prod_{i=1}^{2N} \lambda_i \right)} \quad (12)$$

where λ_i are the eigenvalues of controllability gramian matrix and $\sigma(\lambda_i)$ is the standard deviation of λ_i . A higher J value for a possible patch location means that

this location is a better place for actuator placement. In this criterion, having high values of summation of eigenvalues of controllability gramian matrix leads to high controllability. Same amount of controllability for each mode is desired, so by means of multiplication of eigenvalues and division by the standard deviation of eigenvalues make each mode equally controllable (Jha & Inman, 2003).

By using this criterion, locations that will control all the desired modes can be determined. However spillover effects are not considered in this criterion. As a modification to this, it is suggested not to excite the high order modes that are not included in the system model. To achieve this, the criterion is modified as follows (Hac & Lui, 1993):

$$J = \frac{1}{\sigma(\lambda_i)} \left(\sum_{i=1}^{2N_m} \lambda_i \right)^{2N_m} \sqrt{\left(\prod_{i=1}^{2N_m} \lambda_i \right)} - \gamma \frac{1}{\sigma(\lambda_i)} \left(\sum_{i=2N_m+1}^{2N_m+2N_u} \lambda_i \right)^{2N_u} \sqrt{\left(\prod_{i=2N_m+1}^{2N_m+2N_u} \lambda_i \right)} \quad (13)$$

Here N_m is the number of modes used in the system model (modes used in the feedback controller) and N_u is the number of high order modes which are not included in the control system model but considered for spillover effects, and γ is the weighting constant. If the control system works up to 1000 Hz, then number of modes of system up to 1000 Hz is equal to summation of N_m and N_u . For instance, if the structure has 14 modes up to 1000 Hz and if we are interested in controlling the first 4 modes then N_m is 4 and N_u is 10.

3. APPLICATION TO CYLINDER GEOMETRY

A hollow cylinder of 200 mm inner diameter and 600mm length and 2 mm thickness is taken as the host structure. The cylinder is made of aluminum and one end of the cylinder is fixed to a rigid wall. PZT 4 piezoelectric patches of 1 mm thick are glued on the outside wall of the cylinder. The actuators will be in unimorph operation mode. A perfect bonding between piezoelectric patch and the host structure is assumed.

To obtain the optimal locations of piezoelectric patch actuators on a cylindrical shell, the shell structure is divided into sectors. Each sector is a possible location for a patch actuator. In radial direction, the possible patch location covers 22.5 degree of a circle. In length, the cylinder is divided into 12 equal pieces. Dividing the cylindrical shell into sectors for possible patch actuator location generates a grid over the cylinder. The grid is composed of the corners of each sector. In the calculation of mass, stiffness, damping and piezoelectric matrices, the degrees of freedoms taken from finite element mesh are the radial coordinates of grid points since in cylinder structure, radial modes (breathing modes) are the modes of interest. The divided sectors of the cylindrical shell (possible piezoelectric patch locations) are shown in Figure 1.

After the cylinder geometry is formed, a proper mesh is generated over the cylinder. For the aluminum cylinder SOLID 186, for piezoelectric patch SOLID 226 type elements are used. One end of the cylinder is constrained in all degrees of freedom. The mesh with the boundary condition is shown in Figure 2.

For the material properties used in the analysis, the piezoelectric properties of PZT 4 (Navy Type 1) are taken. Material properties of the host structure and the active element used in this study are listed in Table 1.

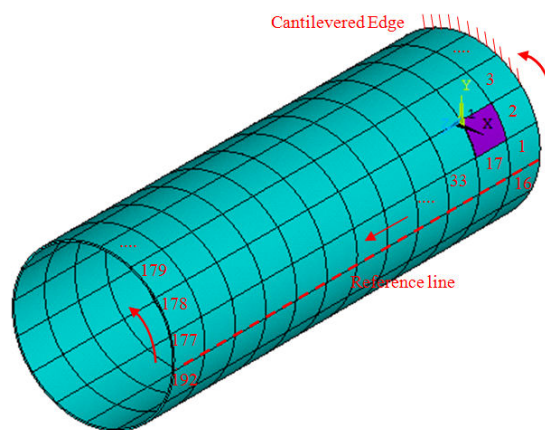


Figure 1: Cylindrical shell geometry divided into sectors

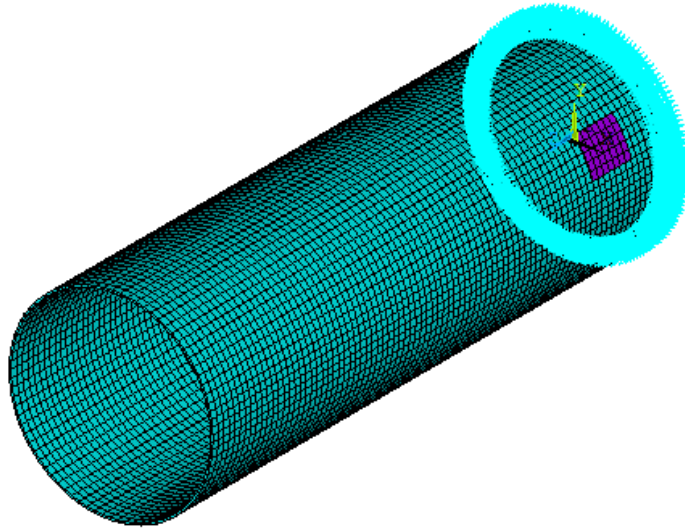


Figure 2: Mesh generated over the cylinder

Table 1: Material Properties

Host Structure: Aluminum	
Young's modulus	70 GPa
Poisson's ratio	0.33
Density	2700 kg/m ³
Active Material: PZT 4	
Density	7500 kg/m ³
d ₃₁	-1.23*10 ⁻¹⁰ m/V
d ₃₃	2.89*10 ⁻¹⁰ m/V
d ₁₅	4.96*10 ⁻¹⁰ m/V
s ^E ₁₁	1.23*10 ⁻¹¹ ms ² /kg
s ^E ₃₃	1.55*10 ⁻¹¹ ms ² /kg
s ^E ₁₂	-4.05*10 ⁻¹² ms ² /kg
s ^E ₁₃	-5.31*10 ⁻¹² ms ² /kg
s ^E ₄₄	3.90*10 ⁻¹¹ ms ² /kg
s ^E ₆₆	3.27*10 ⁻¹¹ ms ² /kg
K ^T ₁₁	1475 (ε ^T ₁₁ /ε ₀)
K ^T ₃₃	1300 (ε ^T ₃₃ /ε ₀)
ε ₀	8.85*10 ⁻¹² F/m

The generated mesh is used in the analyses; however, the radial deflection results are collected only at the nodes which are located at the corner of each sector. In other words, the results at the grid nodes are taken into consideration. These coordinates are selected as master degrees of freedom (dofs) in ANSYS substructuring analysis. In the calculation of mass, stiffness, damping and piezoelectric matrices, radial degree of freedom of grid points are considered.

The equation of motion of the cylinder is expressed in terms of the master dofs chosen. Therefore, firstly the reduced mass, damping and stiffness matrices and the piezoelectric matrix are calculated. Then the system is expressed by state space representation to calculate the controllability gramian for the vibratory system,

In calculation of piezoelectric matrix, a solid in the shape of piezoelectric patch actuator is placed on one of the possible actuator locations and piezoelectric material properties are attributed on that solid. After generating the structure, 1V is applied on the outer surface and 0V is applied on the inner surface of the patch actuator. A static analysis is done for each possible patch locations and deformations of the nodes on the grid in radial direction are collected to form a column of P matrix. A sample static analysis result with one piezoelectric patch on the cylinder surface is shown in Figure 3. Then the geometry is re-created by the APDL macro, but this time the patch is moved to the next location. The procedure is continued until a single patch has moved to each possible location. In this case P is a 192 by 192 matrix, since there are 192 master dofs and 192 possible patch locations. In static case, equation (1) reduces to $\mathbf{Kr}=\mathbf{PV}$ from which piezoelectric matrix can be calculated.

The reduced mass and stiffness matrices obtained by substructuring analysis are reordered according to the degrees of freedom numbers of the grid. Damping matrix is calculated from mass and stiffness matrices by assuming proportional damping. Here, proportional structural damping is assumed; so that $\alpha=0$ and $\beta=1\times 10^{-6}$. The piezoelectric matrix is calculated for each possible patch location. Therefore, the corresponding column of P matrix is taken when calculating controllability gramian for each possible piezoelectric patch actuator location. At each possible patch

location, a new system model is generated in state space according to Eq.(8) and Eq.(10). Then the controllability gramian matrix for each of those systems is computed using MATLAB. Another approach would be carrying out static analysis for a limited number of patch locations and using a search method such as genetic algorithm to find optimal locations. However, such approaches may have the drawback of having non-convergence.

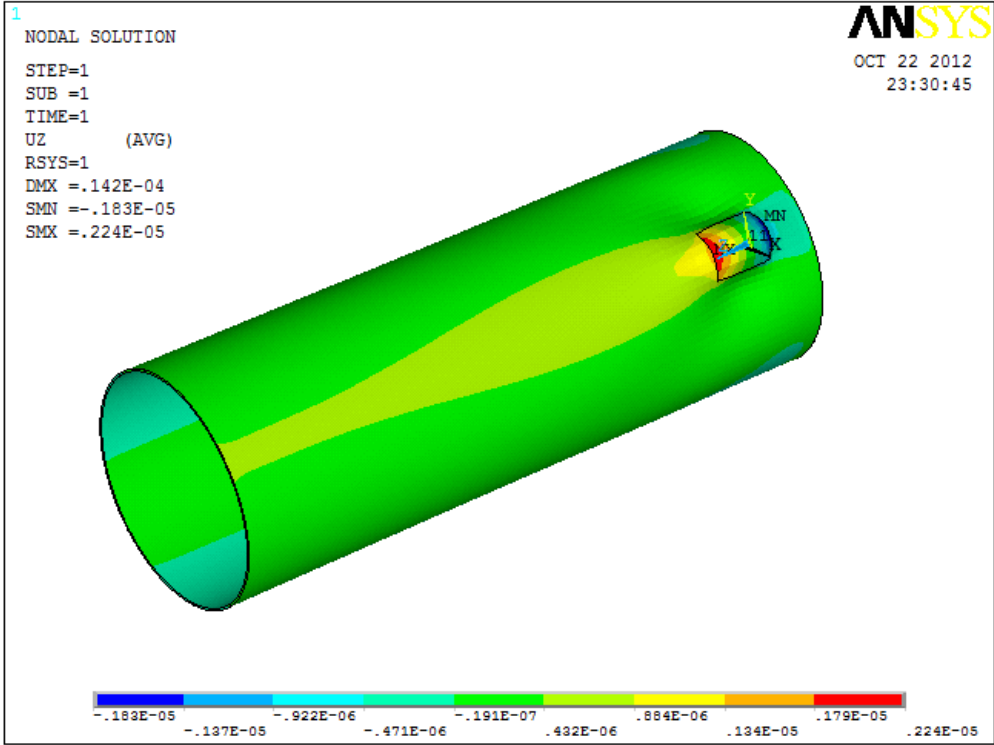


Figure 3: Static analysis for one possible piezoelectric patch location on the cylinder

In finding the optimum patch locations for the cylindrical structure considered, the modes of the cylinder up to 1000 Hz are taken into consideration. The first 14 natural frequencies of the structure are given in Table 2. Note that in this calculation, the slight changes in the natural frequencies of the host structure due to the existence of PZT patches are ignored.

Table 2: Natural frequencies of the host structure

Mode Number	Natural Frequency (Hz)
1	216.4
2	216.4
3	379.4
4	379.4
5	476.5
6	476.5
7	615.6
8	615.6
9	708.8
10	708.8
11	787.7
12	787.7
13	897.4
14	897.4

In this application the first 4 modes of the cylindrical structure are selected to be controlled. The corresponding mode shapes are given in Figure 4 and Figure 5.

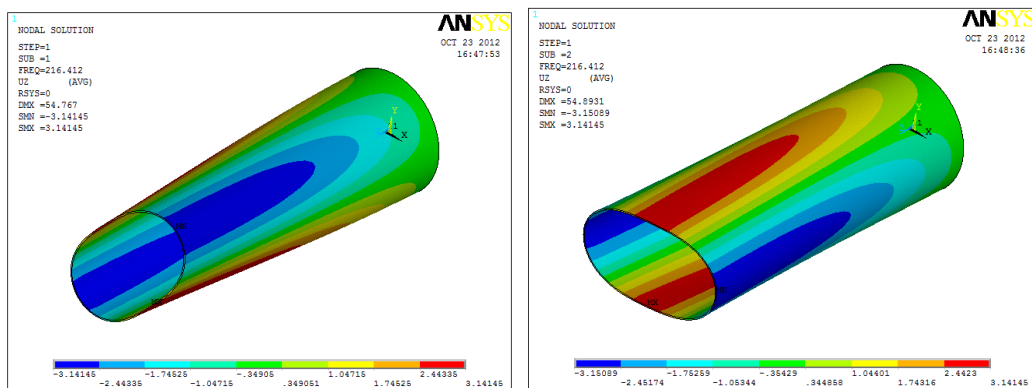


Figure 4: First two modes of the structure

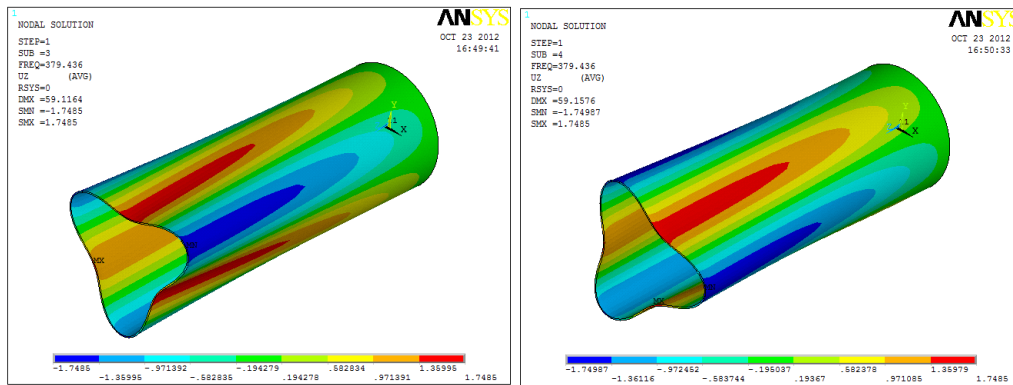


Figure 5: 3rd and 4th modes of the structure

In this active vibration study, a feedback controller with a frequency band up to 1000 Hz is chosen to be used. In order to avoid spillover effects for the higher modes of the structure up to 1000 Hz, the criterion of placement is constructed such that the modes to be controlled are the first four modes (216.4 Hz and 379.4 Hz) and modes which are not controlled, but also not to be excited while controlling the first four modes are 5th to 14th modes. The placement criterion values calculated at each possible patch location are shown in Figure 6. The locations with high placement criterion values are optimal locations for patch placement. The best locations are found to be 163 and 171 from this figure. These locations are close to the free edge, and they are equally spaced on the periphery of the cylinder. The second best locations are found as 179 and 187 which are at the free edge and equally spaced on the periphery as in the previous case. It should be noted here that the best patch location on one periphery of the cylinder depends on the orientation of the mode shape and the orientation of the grid formed over cylinder.

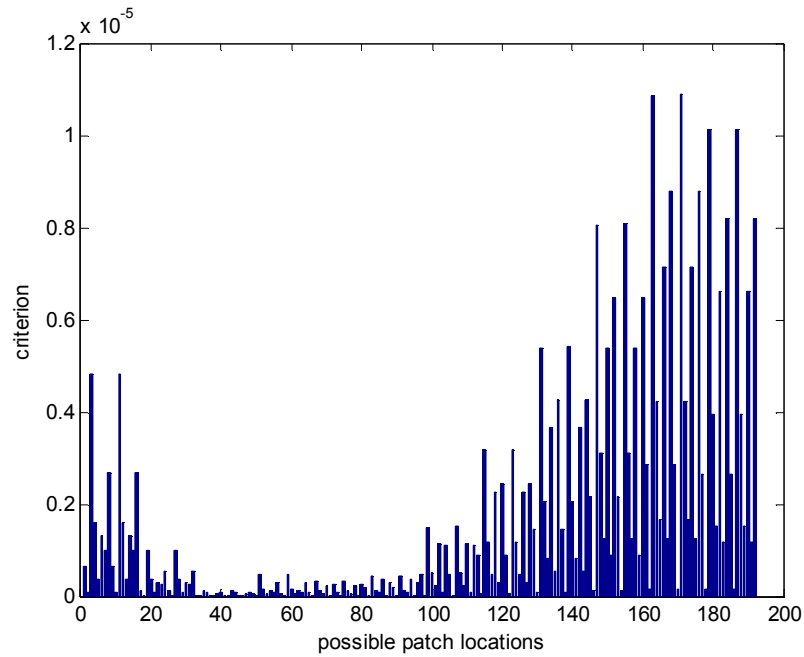


Figure 6: Placement criterion values at possible patch locations

In order to demonstrate the effect of active vibration control with piezoelectric patches which are placed at the best and second best locations, three analyses are carried out. In the first analysis no actuator is placed on the cylinder and a force of 100 N is applied on the free edge of the cylinder in 3 o'clock direction and then suddenly released. The point where the force is applied is shown in Figure 7. The free vibration response of the cylinder at the point where the force is applied is calculated by transient vibration analysis. In the second and third analyses, the same initial disturbance is given and the vibration responses of the same point are computed. However, in these analyses the piezoelectric patch is used and a closed loop control system is employed. The displacement of the point where 100 N force is applied is taken as the feedback signal of the controller. A simple proportional controller with a gain of 20000 is used. In the second analysis the piezoelectric patch is placed at location 163 (one of the best locations) and in the third analysis it is placed at location 179 (one of the second best locations). The output signal of the controller is used as the voltage input for the piezoelectric patch actuator. In the implementation of control system in the transient analyses, an APDL macro is used (Karagülle, Malgaca, & Öktem, 2004). The time domain results of the three transient

analyses are given in Figure 8, and the results in frequency domain are given in Figure 9.

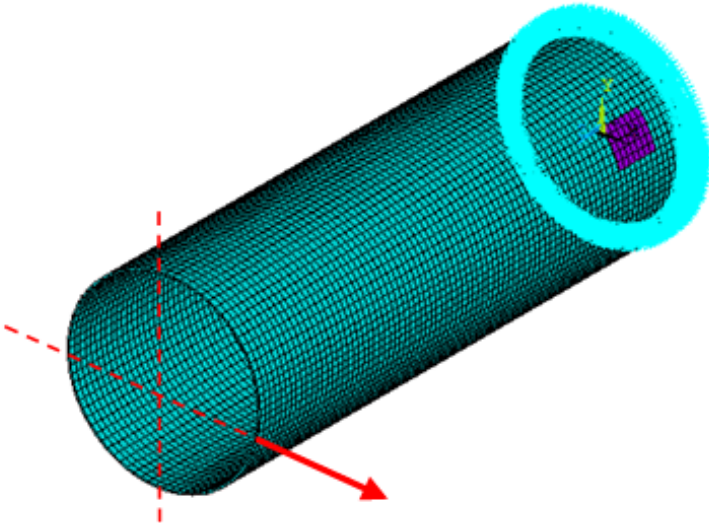


Figure 7: Application point of 100 N force

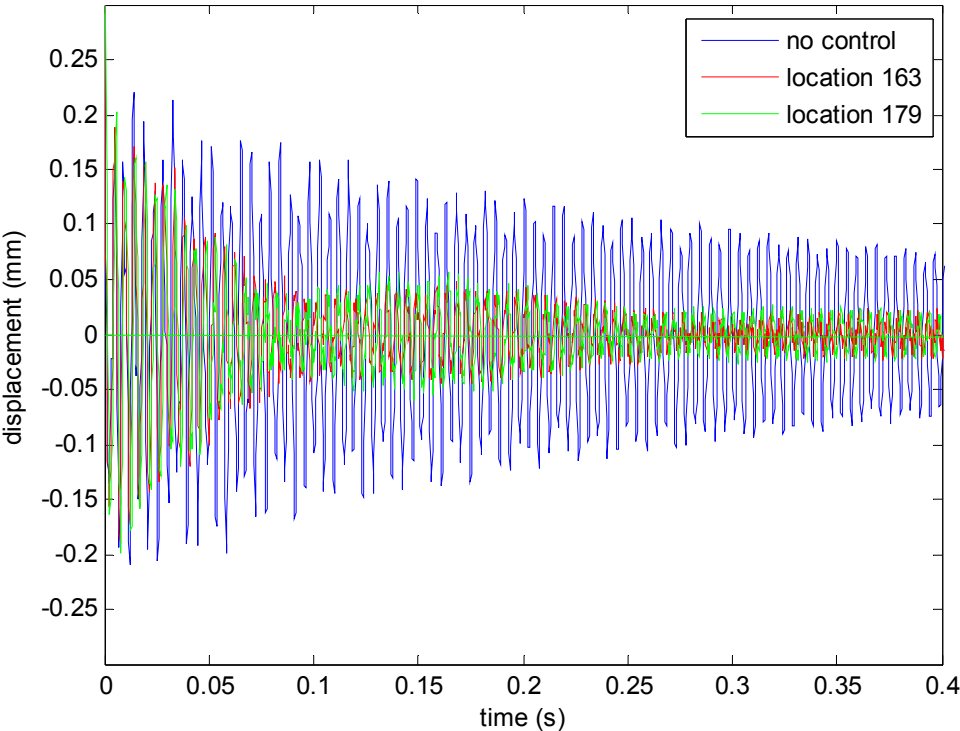


Figure 8: Time domain responses

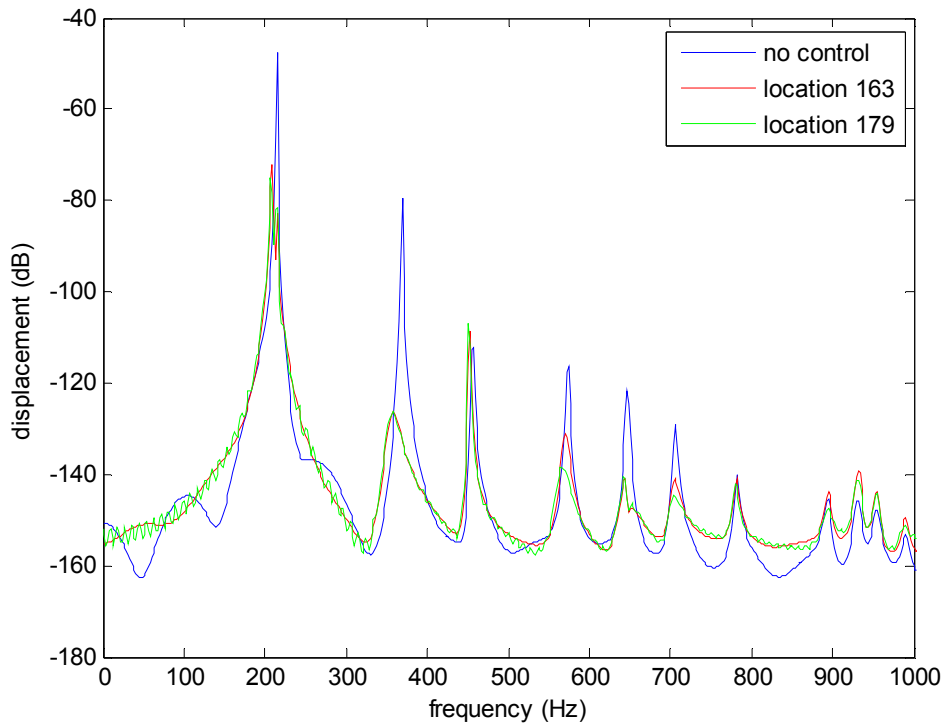


Figure 9: FFT of time domain responses

From Figure 9 it can be observed that the approach is successful in reducing vibration response in the first four modes by also avoiding the spillover effects in most of the higher modes.

4. CONCLUSION

In this study, optimum placement of piezoelectric patch actuators for active vibration control of cylindrical shell structures is studied. The approach employed in finding best piezoelectric patch locations is based on controllability gramian of the structure calculated for each possible actuator location. In order to find the best actuator locations to control a desired number of modes, and not to cause spillover due to certain high order modes, a modified placement criteria is utilized. The approach suggested is employed to control the first four modes of a cantilevered cylindrical shell and at the same time not to cause spillover at higher modes until 1000 Hz. The best and second best locations are determined for an example problem, and the transient responses of the system are calculated with and without active vibration control. It is observed in this application that the approach is successful in reducing

vibration response in the first four modes, as planned, by also avoiding the spillover effects in most of the higher modes.

REFERENCES

Bruant, I., Gallimard, L., & Nikoukar, S. (2010). Optimal Piezoelectric Actuator and Sensor Location for active vibration control, using genetic algorithm. *Journal of Sound and Vibration* (329), 1615-1635.

Crawley, E.F., & de Luis, J. (1987). Use of Piezoelectric Actuators as Elements of Intelligent Structures. *AIAA Journal* (25), 1373-1375.

Gupta, V., Sharma, M., & Thakur, N. (2010). Optimization Criteria for Optimal Placement of Piezoelectric Sensors and Actuators on a Smart Structure: A Technical Review. *Journal of Intelligent Material Systems and Structures* (21), 1227-1243.

Hac, A., & Lui, L. (1993). Sensor and Actuator Location in Motion Control of Flexible Structures. *Journal of Sound and Vibration* (167), 239-261.

Jha, A. K., & Inman, D. J. (2003). Optimal Sizes and Placements of Piezoelectric Actuators and Sensors for an Inflated Torus. *Journal of Intelligent Material Systems and Structures* (14), 563-576.

Karagülle, H., Malgaca, L., & Öktem, H. F. (2004). Analysis of Active Vibration Control in Smart Structures by ANSYS. *Smart Materials and Structures* (13), 661-667.

Peng, F., Ng, A., & Hu, Y.-R. (2005). Actuator Placement Optimization and Adaptive Vibration Control of Plate Smart Structures, *Journal of Intelligent Material Systems and Structures* (16), 263-271.

Sohn, J. W., Choi, S.-B., & Kim, H. S. (2011). Vibration Control of Smart Hull Structure with Optimally Placed Piezoelectric Composite Actuators. *International Journal of Mechanical Sciences* (53), 647-659.